Assembly and Charge Transport in Interfacial Polymeric and Supramolecular Thin Films

Qiang Zeng B.Sc. (Hons.)

A Thesis presented at Dublin City University
for the Degree of Doctor of Philosophy

Supervisors
Prof. Robert J. Forster
and
Dr. Tia E. Keyes

School of Chemical Science
Dublin City University

November 2008

This thesis is dedicated to my parents and Shuoshuo.

ACKNOWLEDGMENTS

First and foremost, I would like to express my gratitude to my supervisor Prof. Robert J. Forster and Dr. Tia E. Keyes for their continuous support, encouragement and attention to detail throughout my research.

I would to thank all the members in our research group who I have had the pleasure of working with over the years. Thank for their encouragement and help. In particular, I would like to thank Dr. Andrea McNally for helpful advice and patience with my questions.

I wish to thank to the technical staff of the school of chemical science at DCU for their help over the year. Special thanks to Calum and David at University of Limerick for help with TEM.

I would like to acknowledge the staff of BDI for their help advice and the use of the facilities.

I wish to thank to the chemistry postgrads and postdocs whom I have had the pleasure of knowing. Also, a special thank you, and apologies, to anyone I have forgotten.

Finally, thanks to all my friends in Ireland and China for their support during all the years.

DECLARATION

I certify that this thesis, which is submitted for the requirement of the award of doctor of philosophy, is entirely of my own research work carried out at Dublin City University and has not been taken from the work of other, save and to the extent that such work has been cited and acknowledged within the text of my work.

Qiang Zeng

Assembly and Charge Transport in Interfacial Polymeric and Supramolecular Thin films

A novel metallopolymer [Ru(terpy)(box) PVP_{20}]PF_6 has been successfully synthesised and the photonic and electrochemical properties of this metallopolymer is reported, where terpy is $2,2^{'}:6^{'},2^{''}$-terpyridine, box is 2-(2-hydroxyphenyl)benzoxazole and PVP is poly(4-vinyl)pyridine in which one in every twenty of the monomer units is labelled with the ruthenium complex. Cyclic voltammetry and Raman spectroscopy reveal that oxidation of the ruthenium metal centre is electrochemically reversible at approximately +0.400 V and the phenolate ligand based oxidation is irreversible at +0.800 V, vs. Ag/AgCl. These redox processes are associated with a reversible colour changes from wine red (reduced) to red orange (mixed composition) then to light green (oxidized) in the visible region and an irreversible change in the near-IR region, respectively. The rate determining step of the metallopolymer film switching has been investigated by using scan rate dependent cyclic voltammetry under semi-infinite linear diffusion conditions in aqueous lithium perchlorate. These data yield a maximum value of $3.6\pm0.2\times10^{-13}$ cm^2 s^{-1} for the homogeneous charge transport diffusion coefficient, D_{CT}, which weakly depends on counterion availability and limited by the rate of segmental polymer chain motion necessary to bring adjacent centres sufficiently close to allow electron transfer to occur.

Monolayers of di-6^A,6^D-deoxy-6-(4-pyridylmethyl)amino-β-cyclodextrin, β-CD-$(4\text{-py})_2$, have been formed on platinum electrodes and backfilled with 1-nonanethiol. Their electrochemical behaviours have been investigated using cyclic voltammetry and impedance. The binding of [$Os(CAIPA)_2Cl_2$] guest molecules to CD in the backfilled monolayer results in the increase of capacitance from 3.2 to 4.9 $\mu F/cm^2$ and rate of charge transfer due to their redox activity, where CAIPA is 2-(4-carboxyphenyl)imidazo[4,5-f][1,10]-phenanthroline-1-adamantylamine.

Also, β-CD-$(4\text{-py})_2$ monolayer-protected gold nanoparticles multilayer via cyclodextrin-adamantane host –guest interaction, where [$Os(CAIPA)_3$]$(ClO_4)_2$ complex is the linker bridge and redox label, has been formed and characterized by spectroscopic and microscopic techniques. The redox labels within the multilayer show the well-defined and diffusion-like voltammetric responses in aqueous $LiClO_4$. The values of homogeneous charge transport diffusion coefficient, D_{CT}, are obtained as $(6.1\pm0.6)\times10^{-11}$ cm^2 s^{-1} and $(6.5\pm0.4)\times10^{-11}$ cm^2 s^{-1} for oxidation and reduction of the redox labels in the AuNPs multilayer, respectively. These values are somewhat smaller than those obtained in the label complex film as the orientation and the spatial location of the linkers were changed due to host-guest inclusion resulting in a longer pathway for electron transport through the multilayer. Moreover, this observation has been confirmed by the electronic conductivity experiment using interdigitated array electrodes (IDAs).

Finally, nanocomposite materials have be prepared by blending the metallopolymer and gold nanoparticles with controlled fraction. The improvement of charge transport efficiency compared to the parent metallopolymer is due to the presence of the gold nanoparticles. This observation is also confirmed by the dry state IDAs measurements.

TABLE OF CONTENTS

List of Figures

Chapter 1. 1

Chapter 2. 59

CHAPTER 1

Theoretical Framework
And
Literature Survey

1.1 ELECTROCHROMIC MATERIALS FOR DISPLAY APPLICATION

1.1.1 Introduction

Would it be fashionable if contrast or colour of your sunglasses could be changed by pushing a button? Electrochromic materials have been widely available in some applications, e.g. in cars as rear-view mirrors to increase driving safety and in architecture as colouration controlled windows to cut out solar infrared and save working environment costs.

Numerous chemical materials exhibit redox states with distinct electronic (UV/visible) absorption spectra. Where the switching of redox states generates new or different absorption bands, the material is said to be electrochromic [1,2,3,4]. The colour change can be between a transparent ('bleached') state and a coloured state, or between two coloured states, or more than two colour states [2]. By selective absorption or transmission of light by a material, the light energy impinging upon the observer can be modulated [1]. For electrochromic (EC) materials, such colour can arise from either a moderate-energy internal electronic excitation or an intervalence optical charge transfer where the chemical species has two centres of differing valence or oxidation state [2,3,4].

In 1953, Kraus first described electrochromism of tungsten oxide films in his unpublished laboratory report [3]. Interest in electrochromism was brought to public attention and increased after Deb's publication on amorphous and crystalline tungsten oxide films at Cyanamid Corp in 1969 [5]. Since then, interest in EC materials, both in the liquid and in the solid state, from both academia and industry has continued both because of fundamental interest and commercial applications [6,7,8].

The most common commercial applications of EC materials in devices include, electrochromic sunglasses, electrochromic strips used as battery "state-of-charge" indicators [9,10], and anti-glare car rear-view mirrors [4,11]. Company such as Gentex Corporation has commercialized electrochromic auto-dimming mirrors as rear-view visors for the automobile industry to increase driving safety by eliminating accident causing glare. Proposed applications include 'smart windows' (based on modulation of either the transmitted or reflected solar radiation) for use in cars and in buildings [11], re-usable price labels, protective eyewear, controllable aircraft canopies, glare-reduction system for offices, sensor tag [12,13], food freshness monitoring devices [14], camouflage materials, spacecraft thermal control, and controllable light-reflective or light-transmissive display devices for optical information and storage [15].

1.1.2 Families of Electrochromic Materials

EC materials can be divided into different families due to their difference in optical states, solubility, or chemical properties. There are three main types of electrochromic material in terms of their electronically accessible optical states [16]. The first type are materials that switch between at least one coloured and one transparent (‘bleached’) state, where the chromophore only absorbs in the UV region. Such materials are especially useful for absorption/transmission type applications such as smart windows and optical shutters [2,3,4]. Electrochromes with two distinctive coloured states are classified as a second type of electrochromic material. Such EC materials lack a transparent state but are useful for display applications where different colours are desired from different redox states [16]. A third type addressed here are electrochromes where more than two colour states are accessible. These EC materials are considerably rarer, but are valuable in display applications [2], especially for three colour electrochromism with red, green and blue states since all other colours can be obtained according to colour mixing theory [17] if these three primary colours are available.

Recently a few groups have been interested in the electrochromic properties of some chemical species in the near infrared (NIR) [18,19] and thermal infrared [20]. Compared to the colours in visible region, ‘colours’ in these situations can mean response of detectors to these electromagnetic regions, not human eyes [21]. The NIR region, typically from 800 to 2000 nm, is of particular significance because telecommunications frequencies lie in the 1300 to 1550 nm region, at which silica optical fibres are most transparent. Such wavelengths are used for propagation of signals through fibre-optic networks [19,22].

EC materials also can be classified as three basic types based on their solubility [2]. In a particular electrolyte solution, EC materials, which are soluble in both reduced and oxidized states, belong to the first type. The second type of EC materials are soluble in one redox state, but generate a solid thin film on the surface of an electrode. For the third type EC material, both redox states are solid and studied as thin films on electrode surfaces. No extra charge injection is needed to retain the electrochromic state when the second and the third types EC materials are oxidized or reduced. However, it is necessary to keep current flowing for the first type EC materials until the whole solution is totally electrolyzed because the new electrochromic state of an EC material diffuses in the solution away from the electrode surfaces [2].

1.1.3 Chemical Classes of Electrochromic Materials

There is a vast number of chemical species that show electrochromic properties [2,23]. Metal oxide systems [2,3], such as WO_3, NiO, MoO_3, IrO_2 or Co_2O_3, exploit the colour change of a layer of a transition metal oxide deposited on a transparent conductive electrode. The transition metal oxide film can be electrochemically switched to a redox state which has an intense electronic absorption band due to optical intervalence charge transfer [2,3].

Among EC materials, Prussian blue [iron(III) hexacyanoferrate(II)] is the prototype for of a number of polynuclear transition metal hexacyanometallates which form an important class of insoluble mixed valance compounds and contain two oxidation states with the possibility of charge/electron transfer between them [23,24]. Since the colourations of Prussian blue and tungsten trioxide are anodic and cathodic, respectively, these two materials can be used together in a single EC device so that their electrochromic reactions (Equation 1.1.1 and Equation 1.1.2) are complementary [3,23].

$$[Fe^{3+}Fe^{2+}(CN)_6]^- + e^- \rightarrow [Fe^{2+}Fe^{2+}(CN)_6]^{2-} \qquad \textbf{(1.1.1)}$$

$$WO_3 + x(M^+ + e^-) \rightarrow M_xW^{4+}_{(1-x)}W^{5+}_xO_3 \qquad \textbf{(1.1.2)}$$

Other EC materials include organic small molecules, such as the bipyridilums (viologens). Of their three redox states (Figure 1.1.1), viologens are colourless in the stable dicationic state. Reductive one electron transfer can result in the formation of a highly coloured and exceptionally stable radical cations [23,24,25,26].

Conducting polymers are another class of organic EC materials e.g. poly(thiophene), poly(aniline), and poly(pyrrole). They have attracted significant interest due to their ease of processability, rapid response time and high optical contrasts [16]. In their oxidised forms, conducting polymers are 'doped' with counter anions (p-doping) and possess a delocalised π-electron band structure. The colourations of these EC materials arise from the energy gap between the highest occupied π electron band (valence band) and the lowest unoccupied band (the conduction band) [23, 27]. Finally, transition metal coordination complexes based on metallopolymers are potentially useful electrochromic materials because of their intense colouration and redox reactivity [15]. The EC effects and colour control of such metallopolymers will be detailed in the following section.

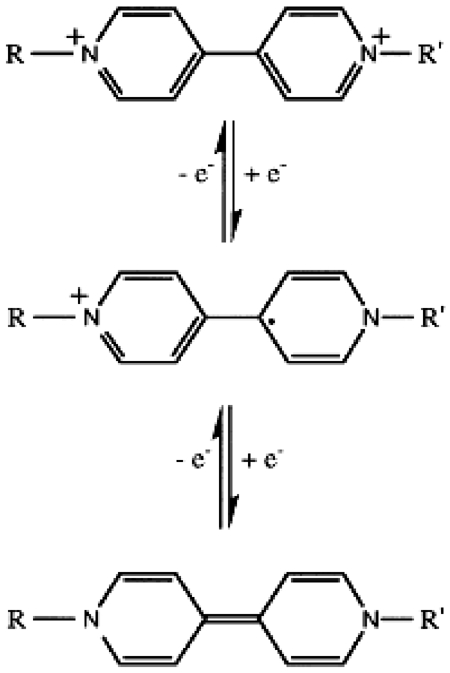

Figure 1.1.1. The three common viologen redox states. From ref [26]: R. J. Mortimer. Electrochim. Acta 44 (1999) 2971.

1.1.4 Metallopolymers

Metallopolymers are characterized by the presence of specific spatially and electrostatically isolated electrochemically active site. Electroactivity in the metallopolymer is highly localized with respect to voltage. A metallopolymer consists of a redox active transition metal based pendant group, which is covalently bound to a polymer backbone. This polymer backbone may or may not be electroactive.

The chromophoric properties of metallopolymers typically arise from low energy metal-to-ligand charge transfer (MLCT), inter-valence CT, intraligand excitation and related visible region electronic transitions. Significantly, these transitions depend upon oxidation or reduction of the transition metal coordination complex because valence electrons are involved in these transitions. Transition metal coordination complexes are directly used in solution-phase electrochromic devices, because of their spectroscopic and redox properties. However, their metallopolymer systems have potential value in all-solid-state systems, which have been described for the preparation of thin-film metallopolymers [26,27]. Moreover, metallopolymer thin films play an important role in the area of chemically modified electrodes, which are especially important for developing some sensor systems [28]. A few typical metallopolymer monomers are shown in Figure 1.1.2.

1

2

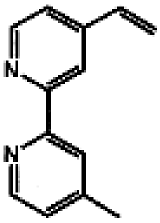

3

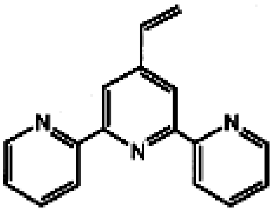

Figure 1.1.2. Structures of metallopolymer polymerisable ligands. 1 is 4-vinyl-pyridine, 2 is 4-vinyl-4′-methyl-2,2′-bipyridine, and 3 is 4′-vinyl-2,2′:6′,2″-terpyridine. From ref [26]: R. J. Mortimer. Electrochim. Acta 44 (1999) 2971.

1.1.4.1 Ruthenium Polypyridyl Complexes

The best known examples of transition metal coordination complexes used in metallopolymers include the $[M^{II}(bpy)_3]^{2+}$ (M=iron, ruthenium, osmium; bpy=2,2′-bipyridine) series. Ruthenium, coordinated to a polypyridyl ligand, is one of the most widely studied and best understood transition metals and Ru(II)-polypyridine complexes have attracted the attention of several research groups because of a unique combination of ground and excited state properties [29,30,31,32]. Because of their versatile photophysical properties, Ru(II)-polypyridine complexes have potential applications in photo-molecular devices [31], photocatalysis [33], and artificial photosynthesis [34].

$[Ru(bpy)_3]^{2+}$ is the most fully studied Ru polypyridine complex. The basic ligand field model for ruthenium polypyridyl complexes and the possible orbital transitions are shown in Figure 1.1.3. There are four transitions may occur. They are 1). Ligand centred (LC) or intraligand (IL), which are equivalent to that observed for the free ligand; 2). Metal to ligand charge transfer (MLCT), where the metal centre is formally oxidised and the ligand is reduced; 3). Metal centred (MC or dd) where a transition is from the formally non-bonding t_{2g} to the anti-bonding e_g orbitals; and 4). Ligand to metal charge transfer (LMCT) where the ligand is oxidised and the metal reduced in the excited state. Other transitions not shown in Figure 1.1.3 are ligand-to-ligand (LLCT) and metal-to-metal inter-complex charge transfer (MMCT).

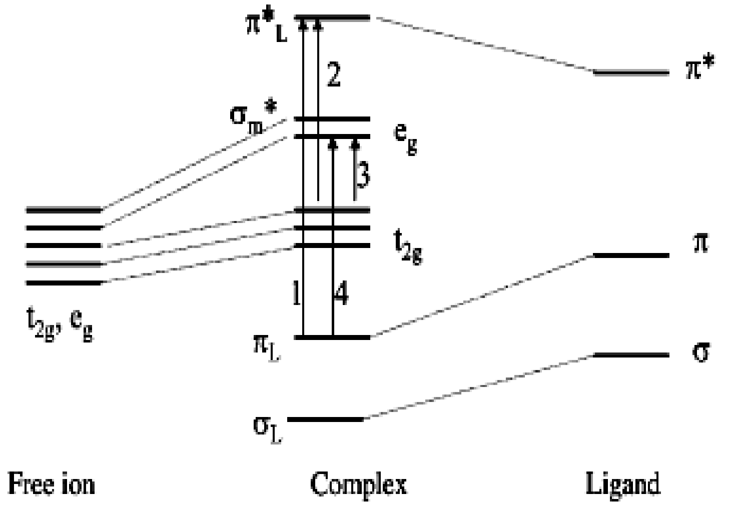

(1) ππ* (LC); (2) dπ* (MLCT); (3)dd* (MC); (4) πd* (LMCT)

Figure 1.1.3. Energy level diagram showing the relative position of metal and ligand orbitals and possible electronic transitions for a Ru complex in an octahedral ligand field.

As shown in Figure 1.1.4(a), the absorption spectrum of $[Ru(bpy)_3]^{2+}$ is dominated by an intense band in the visible region, at 450 nm. This band is associated with a metal to ligand charge transfer (MLCT), which is due to promotion of an electron from a π_M metal orbital to the π_L^* ligand orbitals. Transitions between the ligand π-bonding and π^* anti-bonding orbital labelled π-π^* or ligand centred transitions (LC) usually lie at higher energies at 185 and 285 nm. In addition, transitions such as promotion of an electron from a metal t_{2g} to an e_g orbital are possible and such d-d or metal centred transition (MC), which gives rise to weak absorption bands at 322 and 344 nm [35]. We might regard the full t_{2g} orbitals as the highest occupied molecular orbitals (HOMO). Due to a strong crystal field, the lowest unoccupied molecular orbital (LUMO) in this complex is a vacant π anti-bounding orbital. Therefore, the lowest energy electronic transition is a metal to ligand charge transfer, which can be considered as metal centre oxidation and a ligand reduction [35,36]. The electronic state manifolds of $[Ru(bpy)_3]^{2+}$ are illustrated in Figure 1.1.5. For low spin Ru^{2+} complexes the ground electronic state is of singlet multiplicity, hence only transitions to singlet-excited states are formally allowed. The lowest excited state is a ^{3}MLCT excited state and emission is at 620 nm as shown in Figure 1.1.4(b). Its population by inter system crossing made possible by spin orbit coupling with heavy Ru atom. In Figure 1.1.5, the large energy gap between the lowest excited states and the ground state allows radiative processes (phosphorescence) to compete with non-radiative ones. Population of ^{3}MC states following MLCT excitation by internal conversion from the ^{3}MLCT to the ^{3}MC excited states, can lead to non-radiative decay and also lead to ligand-loss photochemistry.

As shown in Figure 1.1.6, the oxidation potential in the $[Ru(bpy)_3]^{2+}$ occurs at +1.3 V vs. NHE (NHE = normal hydrogen electrode) and involves the removal of one electron from a metal centred orbital. Reduction of $[Ru(bpy)_3]^{2+}$ takes place on the bpy based ligand π^* orbital at negative potential –1.29 V vs NHE. The $[Ru(bpy)_3]^{2+}$ excited state is both a more powerful oxidant (0.83 V vs NHE) and reductant (-0.79 V vs NHE) than the ground state. This property can be rationalized by considering the excited state to be a combination of Ru^{3+} and a bpy^- radical anion. The excited state can be intercepted with quenchers to generate the long-lived oxidant $[Ru(bpy)_3]^{3+}$ or reductant $[Ru(bpy)_3]^+$.

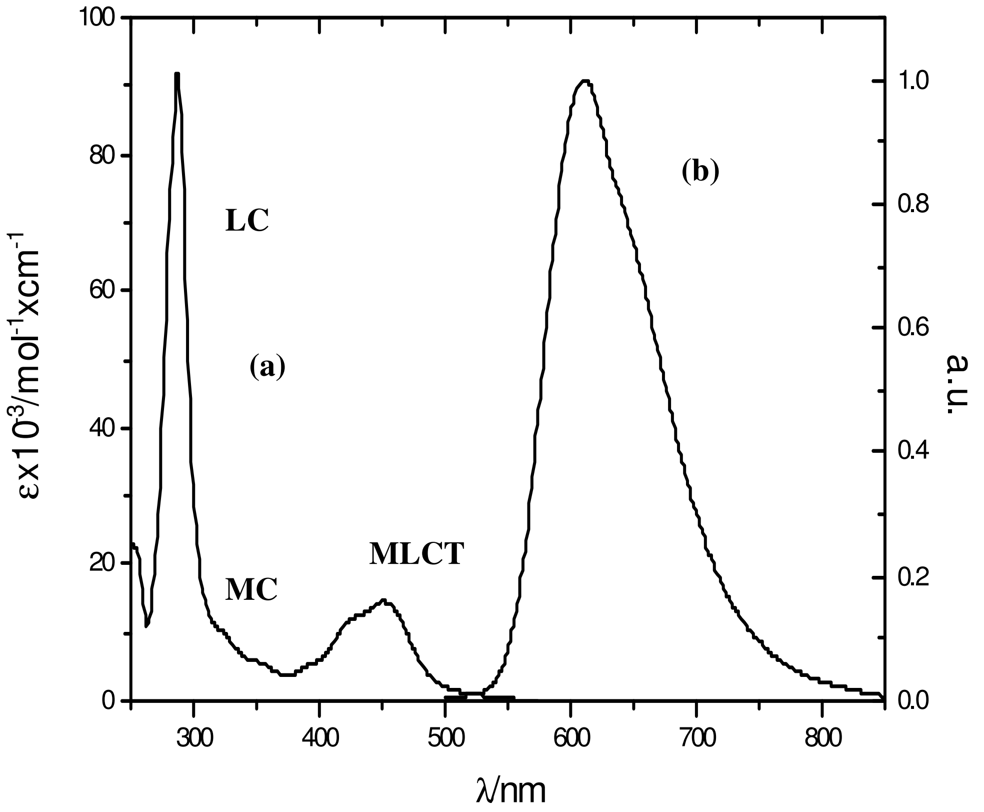

Figure 1.1.4. Absorption (a) and emission spectra (b) of $[Ru(II)(bpy)_3]^{2+}$, at room temperature in acetonitrile solution.

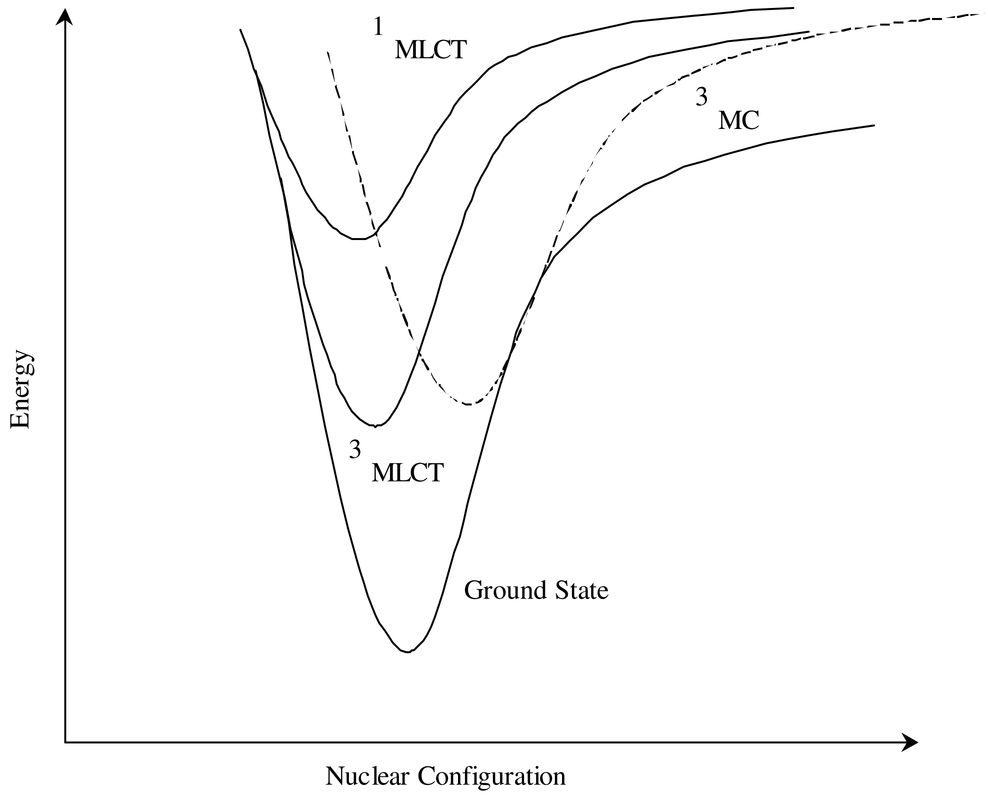

Figure 1.1.5. Ground and excited state PE curves for $[Ru(bpy)_3]^{2+}$ complexes.

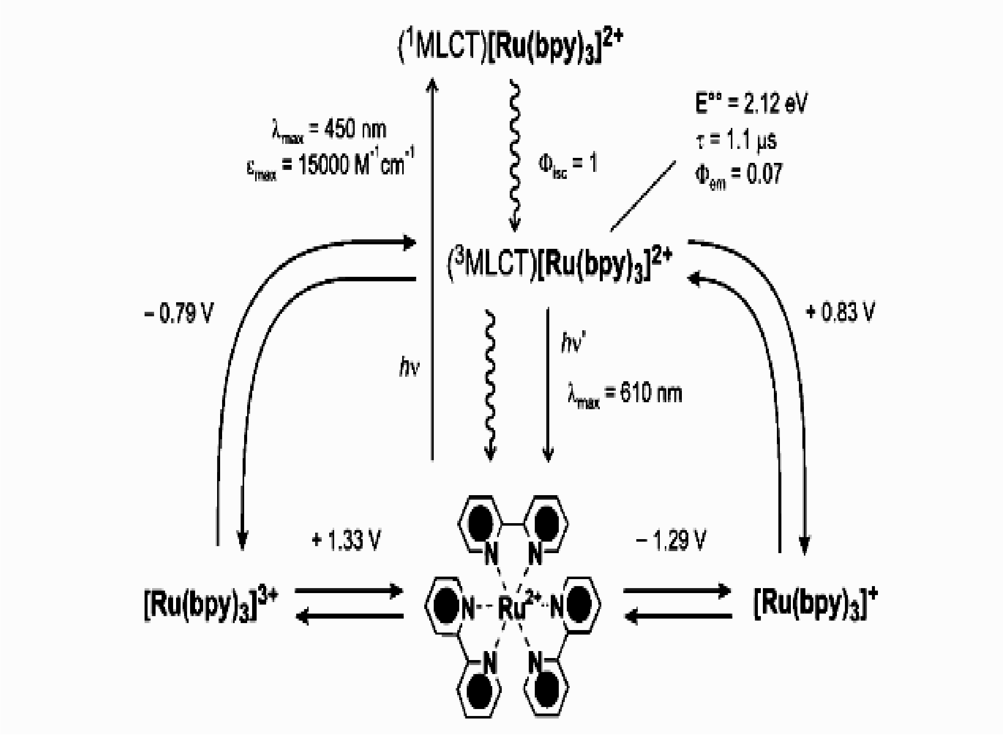

Figure 1.1.6. Photophysical and redox properties of the complex $[Ru(II)(bpy)_3]^{2+}$.

1.1.4.2 Ruthenium- O^- Complexes Coordinated Quinoid Ligands

For ruthenium polypyridyl complexes containing phenolate donors, the strong σ-donating nature of the ligand increases electron density at the metal site. These complexes have attracted significant interest because of their rich optical spectroscopy with transitions frequently extending to the NIR and their rich redox chemistry based on both the metal and ligand at relatively low potentials. In general, phenolate donor ligands oxidize after the ruthenium site and therefore permit metal addressability whilst the ligand is a reduced state [37,38,39]. As the ligand electrochemistry may be complicated by coupled chemical reactions the ability to reversibly address the metal, which leads to significant optical changes at a low potential is an advantage for any electrochromic application. A feature of oxygen-coordinated ruthenium polypyridyl complexes is the general lack of luminescent excited states [37,38,39,40,41]. The reason for this observation is low-lying donor or acceptor states on the non-innocent oxygen bearing ligand.

The interest in phenolate donors is based on the following observation. First, as strong σ donors, they are capable of increasing the photochemical stability of Ru^{2+} complexes while simultaneously extending the visible absorbance range of the complex through ILCT transitions. Second, although significant research has been dedicated to catecholate and quinone based Ru O-O and O-N bound complexes, the influence of the reduced ligand on the metal redox levels is not clear in these systems because the ligand oxidation is more facile than metal. The higher oxidation potentials of the phenolate described here, allows the metal oxidation to be investigated in the presence of a reduced phenolate ligand. Third, a feature of O bound catecholate and quinoid ligands seems to be significant metal-ligand orbital mixing, which can lead to very intense optical transitions.

1.1.5 Fundamentals of Electrochromism

For commercial applications, electrochromic materials must demonstrate key performance characteristics [2]. These electrochromic performance parameters include electrochromic contrast, coloration efficiency, switching speed, stability, and optical memory [16].

Electrochromic contrast is perhaps the key factor in evaluating an EC material. It is a percent transmittance change ($\Delta\%T$) at a specified wavelength where the electrochromic material obtains the highest optical contrast. For some applications, it is more useful to report a contrast over a specified range rather than a single wavelength. For example, to ensure that glazing is adequately transmitting for night driving, frontal automotive glazing must be 70% transmitting [42]. As shown in Fig 1.1.7, the Gentex window based on the electrochromic polymer gels is dimmed from 80% transmission to 4% when it is switched off and on at particular applied potential [11] giving it useful for daytime “off” and nightime “on” states.

Colouration efficiency is used to measure the power requirements of an electrochromic material. It measures the amount of optical density change induced as a function of the injected/ejected electronic charge (Q_d). It is given by Equation 1.1.3.

$$\eta = \log[T_b / T_c] / Q_d \qquad \textbf{(1.1.3)}$$

where η (cm^2/C) is the coloration efficiency at a given wavelength and T_b and T_c are the bleached and colored transmittance values, respectively. The relationship between η and the Q_d can be used to evaluate the reaction coordinate of the coloration process, or the η values can be reported at a specific degree of coloration for practical purposes.

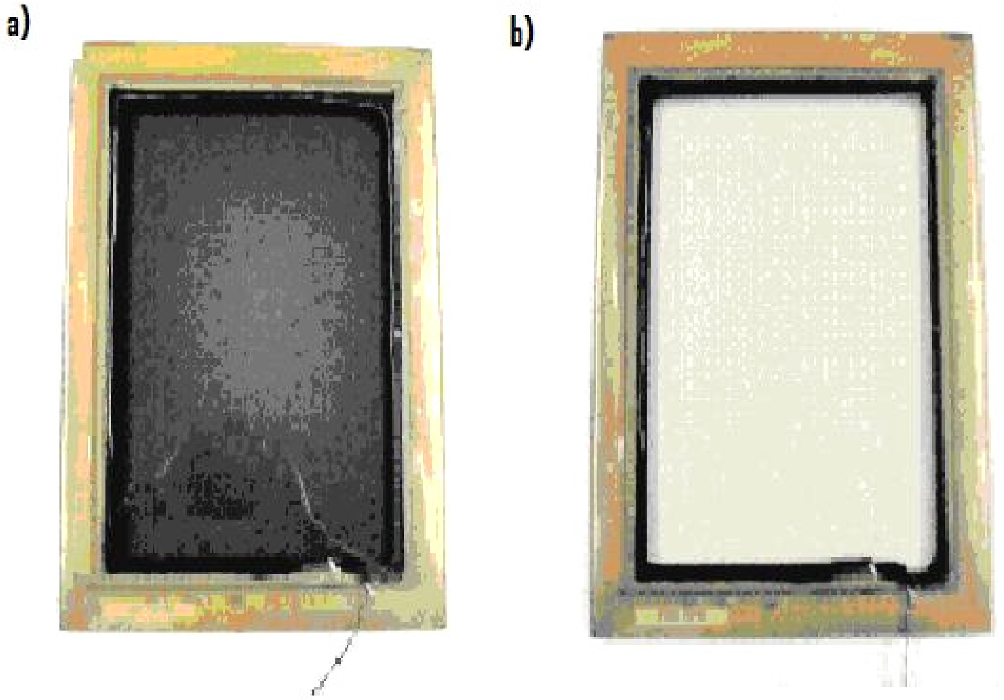

Figure 1.1.7. Close-up of Gentex window based on the electrochromic polymer gels: a) potential on; b) potential off. From ref [11]: D. R. Rosseinsky, R. J. Mortimer. Adv. Mater. 13 (2001) 783.

Switching speed is defined as the time required for the colouring/bleaching process of an electrochromic material. It is an important factor for application in display devices. The switching speed of electrochromic materials depends on several factors such as the ionic conductivity of the electrolyte, ion diffusion in thin films, the magnitude of the applied potential, the film thickness, and the morphology of the thin film.

The stability of electrochromic materials is dictated by the electrochemical stability as the degradation of the active redox couple results in the loss of electrochromic contrast and hence the performance of the EC material. Common degradation pathways include irreversible oxidation/reduction at extreme potentials, iR loss of the electrode or the electrolyte, side reactions due to the presence of water or oxygen in the cell, and heat release due to the resistive parts in the system. For the new electrochromic material introduced in the following chapter, strong switching stabilities of at least 1.5 h repetitive electrochemical cycling when coated on 3mm glassy carbon electrode were observed.

Optical memory is defined as the time the EC material retains its absorption state after termination of current. It is one of the benefits of using an EC material in a display as opposed to a light-emitting material.

1.1.6 Electrochromic Device

An electrochromic device (ECD) is simply constructed in a ‘sandwich’ like two-electrode system, in which two electrochromic electrodes are separated by a solid or liquid electrolyte, and colour changes take place on charge/discharge electrochromic electrodes by application of an appropriate electrical potential. Figure 1.1.8 illustrates an electrochromic device configuration [43].

Electrochromic films are coated onto conductive, transparent glass, such as tin-doped indium oxide (ITO), or transparent conductor films, which are formed on glass or flexible polyester foil, to form electrochromic electrodes [23,27,43]. These electrochromic electrodes used in ECDs can work either in the absorptive/transmissive or reflective mode. In absorptive/transmissive type devices, the counter electrode substrate also has to be transparent ITO glass, with the counter electrode chemical species being either colourless in its redox forms or electrochromic in a complementary mode to the electrochromic material. For a reflective ECD, the counter electrode can be of any material with a suitable reversible redox reaction [23]. Electrolyte can be organic or inorganic. However, the ions contained in the electrolyte should be small in order to optimise their mobility [43].

An electrochromic device for practical application should display sharp contrast, provide fast switching, and offer long-term stability. Self-assembly leads the possibility to obtain an organized and thermodynamically stable monolayer by chemisorption on a suitable substrate. In this way, some electrochromic materials can form self-assembled monolayer [43] or immobilized host-guest inclusions with suitable host monolayer on an electrode to create electrochromic electrode, which may offer higher stability and short response time due to the specific properties of the structure of the monolayer. This method can be also combined with nano materials i.e. gold nanoparticles to obtain the nano-crystalline electrochromic electrode, where electrochromic materials contained monolayer can be formed on the surface of gold nanoparticles [1]. The properties of electrical conductivity, plasmon enhanced optical absorption, and fast interfacial electron transfer offered by the gold nanoparticles allows the nano-crystalline electrochromism to be with sharp contrast and fast switching rate and very useful in the application of electrochromic device. In the following sections, these fundamental concepts and properties of supramolecular chemistry, interfacial self-assembled monolayer, and surface protected gold nanoparticles will be reviewed.

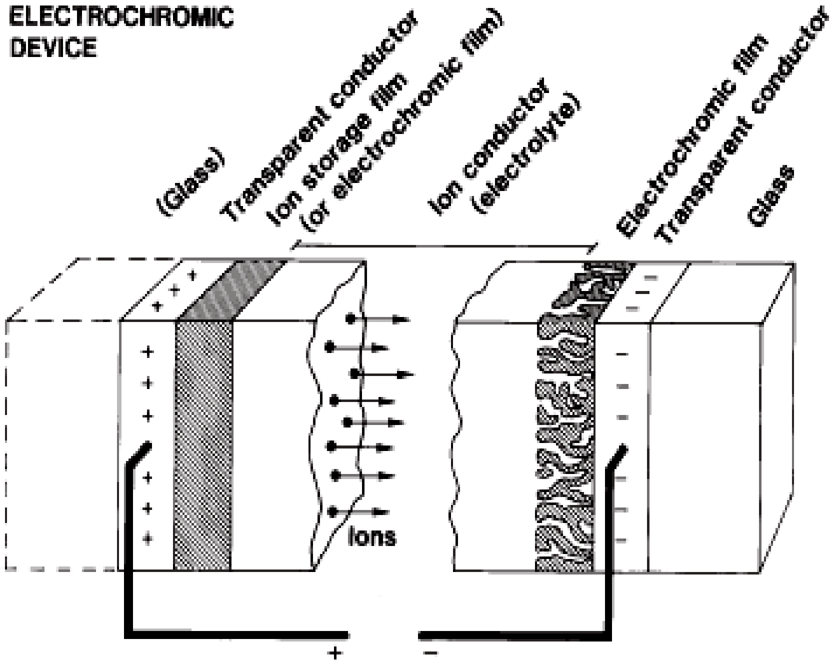

Figure 1.1.8 Schematic diagram of an electrochromic device (ECD) suitable for a transmissive light-modulation application. From ref [43]: G. A. Niklasson, C. G. Granqvist, J. Mater. Chem. 17 (2007) 127.

1.2 SUPRAMOLECULAR CHEMISTRY AND INTERFACIAL SELF-ASSEMBLED MONOLAYER

1.2.1 Supramolecular Chemistry

The early concepts of supramolecular chemistry can be described as 'chemistry beyond the molecule', 'the chemistry of the non-covalent bond', or 'on-molecular chemistry', and even date back to the late 19th century with the origin of the 'lock and key' mechanism of biological catalysis introduced by Emil Fischer in 1894 [44]. The modern concept of supramolecular chemistry was proposed by Jean-Marie Lehn [45], who won the Nobel Prize for work in this area in 1987, as the 'chemistry of molecular assemblies and of the intermolecular bond'.

At the beginning, supramolecule was a term mainly used to describe a host-guest system linked by non-covalent interaction. As highlighted in Figure 1.2.1, this kind of definition emphasises the relationship between molecular and supramolecular chemistry in terms of both structures and function. However, the area of supramolecular chemistry rapidly evolved to encompass molecular devices and molecular assembles. Therefore, Lehn added a further functional definition for supramolecular chemistry: 'Supramolecular chemistry aims at developing highly complex chemical systems from components interacting by non-covalent intermolecular force' in 2002 [46]. The current emphasis is thus on increasing complexity and, hence, increasingly sophisticated functionality, and on the information stored in molecular [47].

In general, complex chemical systems of supramolecules arise from aggregation of a number of components by non-covalent interaction. These components come together to form a larger entity with properties derived from each component. As shown in Figure 1.2.2, such supramolecular systems can be host-guest type, in which one molecule encapsulates the other, or they can involve complementary self-assembly, in which the components have a similar size and there are no hosts or guests [47].

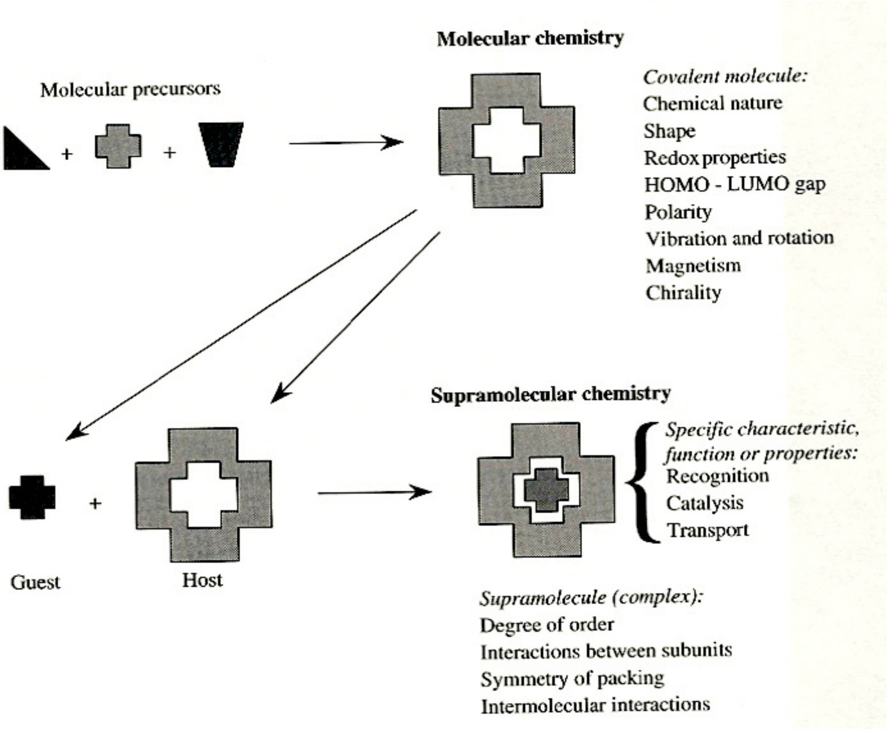

Figure 1.2.1. Comparison between the scope of molecular and supramolecular chemistry according to Lehn. From ref [45]: J.-M. Lehn. Angew. Chem. Int. Ed. Engl. 27 (1988) 90.

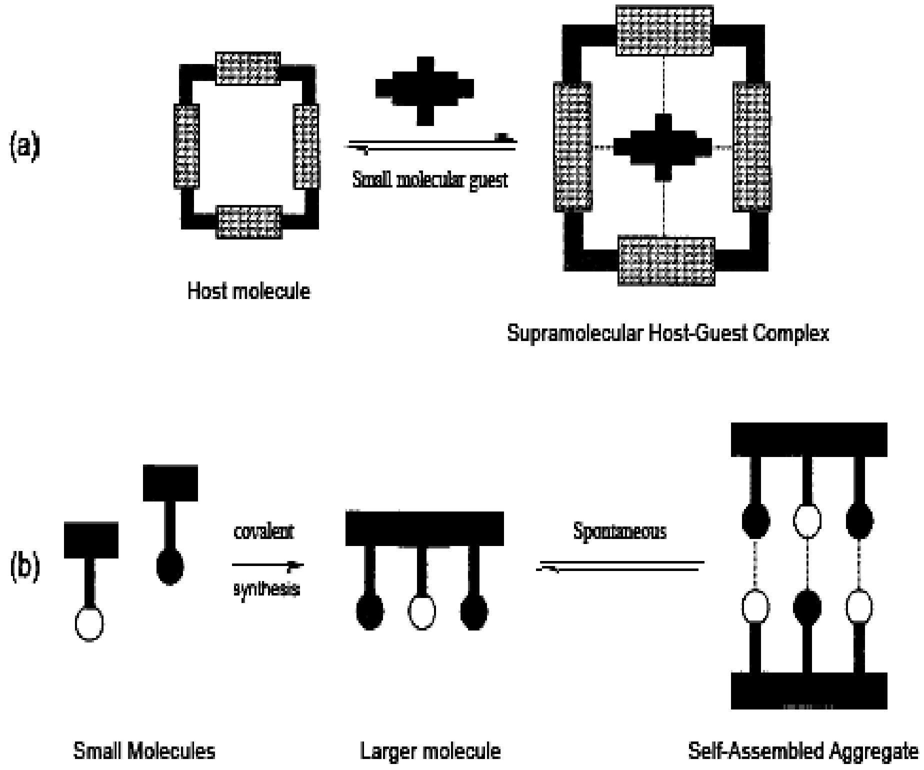

Figure 1.2.2. A complex supramolecular system (a) Host-gust complexation and (b) Self-assembly between complementary species. From ref [47]: J. L. Atwood, J. W. Steed. Encyclopaedia of Supramolecular Chemistry. Taylor & Francis Group. Boca Raton, 2004.

1.2.2 Host-Guest Chemistry

A supramolecule or a 'host-guest' complex is produced when a 'host' molecule binds a 'guest' molecule by non-covalent forces. The definition of host-guest complex was introduced by Donald Cram [48] who shared the 1987 Nobel Prize in Supramolecular in the following way:

> " Complexes are composed of two or more molecules or ions held together in unique structural relationships by electrostatic forces other than those of full covalent bonds...molecular complexes are usually held together by hydrogen bonding, by ion pairing, by π-acid to π-base interactions, by metal-to-ligand binding, by van der Waals attractive forces, by solvent reorganising, and by partially made and broken covalent bonds (transition states)…High structural organisation is usually produced only through multiple binding sites…A highly structured molecular complex is composed of at least one host and on guest component…A host-guest relationship involves a complementary stereoelectronic arrangement of binding sites in host and guest…The host component is defined as an organic molecule or ion whose binding sites converge in the complex…The guest component as any molecule or ion whose binding sites diverge in the complex…"

Commonly, the host is a large molecule or aggregate such as an enzyme or synthetic cyclic compound possessing a sizeable, central cavity and the guest may be a monatomic cation, a simple inorganic anion, or a more sophisticated molecule such as a hormone, pheromone or neurotransmitter [49]. Some well studied host-guest complex examples are crown ether-metal cation supramolecules bound by ion-dipole interaction, spherand-alkyl ammonium cation by hydrogen bonding, cyclodextrin-organic molecule by hydrophobic/van der Waals forces, and calixarene-organic molecule by van der Waals/crystal packing [49]. Among the host molecules, crown ethers are one of the simplest and most ubiquitous macrocyclic host molecules in supramolecular chemistry. For the discovery of the crown ethers [50], Charles Pederson shared the Nobel Prize in Chemistry in 1987 with Cram and Lehn.

Crown ethers (Figure 1.2.3) are highly flexible organic ring compounds and consist of at least 12 atoms in the cycle, containing oxygen, nitrogen, sulphur, or other heteroatoms. In crown ethers, the oxygen heteroatom is intended to bind alkali metals. Nitrogen is usually incorporated bind to transition metals. Moreover, crowns containing sulphur atoms in the donor array favour transition over alkali metal ions. These heteroatoms are separated by ethylene units or more complex structures such as 1,2-dihydroxybenzene, which is an O-C-C-O unit fused to a benzene ring.

The earliest and most studied properties of crown ethers is their ability to complex cations [51,52,53]. The crown ether host molecule is a unimolecular solvation gradient, because the exterior of alkyls are hydrophobic and the interior of heteroatoms are hydrophilic. 18-crown-6 is the more fully understood crown ether molecule [54,55]. A host-guest complex of 18-crown-6 can be formed by fitting an appropriately sized cation into the macrocycle. If the diameters of the macrocycle and cation are identical, the cation is typically embedded within the macrocycle. If the diameter of macrocycle is larger than the cation, the macrocycle may pucker so that donor-group-to-ion contacts are optimised. When the diameter of macrocycle is smaller than the cation, the cation may sit on the macrocycle or be sandwiched between two macrocycles.

Organic cations can also fit in crown ethers, in which the oxygen atoms may function as π-bond acceptors. In particular, alternate oxygen atoms in 18-crown-6 are positioned to form hydrogen bond via $N\text{-}H\cdots O$ with an ammonium ion or amine ligand on a metal [56]. In general, a number of factors affect the selectivity of a host molecule for a specific guest. For crown ethers, the most relevant are [49]:

1. Size match between host cavity and guest cation.
2. Number of donor atoms. Larger crown ethers bind more strongly to metal cations as long as all of the donor atoms can fit around the metal.
3. Solvation of cation and ligand. The solvation free energy increases in the order $K^+ < Na^+ < Ca^{2+}$, hence less energy is required to desolvate K^+ in order to bind it.

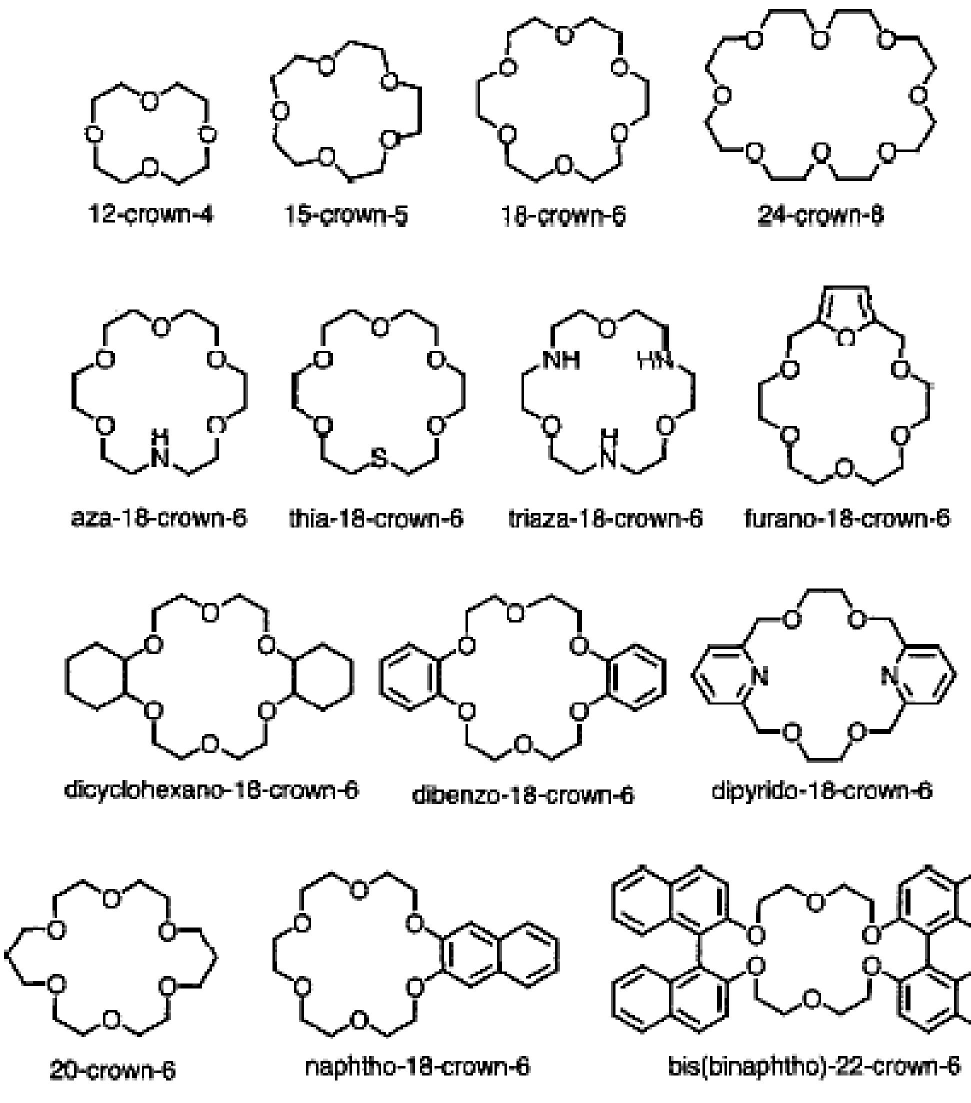

Figure 1.2.3. The crown ethers and their semi-systematic names. From ref [47]: J. L. Atwood, J. W. Steed. Encyclopaedia of Supramolecular Chemistry. Taylor & Francis Group. Boca Raton, 2004.

1.2.3 Cyclodextrins

A cyclodextrin (CD) is a cyclic oligomer of α-D-glucose formed by the action of certain enzymes on starch. The discovery of CDs dates back to 1891 by Villiers [57]. However, the first detailed description of the preparation and isolation of CDs was made by Schardinger in 1903 [58]. CDs have become the most widely used host molecules to form host-guest type inclusion complexes. As shown in Figure 1.2.4, the most common CDs contain six, seven, and eight glucose unites and are named as α-CD, β-CD, and γ-CD, respectively. Larger CDs, such as those with up to 13 glucose units, have also been identified and isolated but currently have little value in terms of application [59,60]. Larger CDs are not commercially available as they are produced by the glucosyltransferases in only very small amounts and the purification is difficult. Also, it is not yet clear whether the larger CDs can form inclusion complexes because their molecular shapes are very different compared to the shapes of the smaller CDs and their structures are relatively rigid even in solution [59]. CDs composed of less than six glucose units are not known to exist due to steric hindrance and the 6-fold character of the starch helix [61,62]. All the glucose unites in the CD molecules are connected with glycosidic α-1,4 bonds. This formation gives the CD a truncated cone shaped molecular structure with the narrower side cavity by the primary 6-hydroxy and the wider side cavity formed by the secondary 2- and 3-hydroxyl groups (Figure 1.2.5) [63]. Unlike crown ethers, the interior of the cavity is non-polar and relatively hydrophobic compared to water, while the external faces are hydrophilic. These features arise because the non-bonding electron pairs of the glycosidic oxygen bridges face toward the inside of the cavity and produce high electron density. Also, the hydrogen bonding between the 2-hydroxyl and the 3-hydroxyl groups of adjacent glucose units in the CD molecular ring makes the CD molecule rigid.

As shown in Figure 1.2.5, the inner dimensions of the cavities in three major CDs are dictated by the number of glucose units and vary from 5 to 10 Å, and the depth of these cavities is about 8 Å. These internal cavities allow for the inclusion of a wide range of guest molecules, ranging from polar compounds such as alcohols, acids, amines, and small inorganic anions to apolar compounds such as aliphatic and aromatic hydrocarbons [64]. The driving forces for the inclusion between hydrophobic CD cavity and guests include van der Waals forces, hydrophobic interaction, electronic effects, and steric factors [65]. Most CD applications involve the consequence of the inclusion complexation between CDs and appropriate guest molecules. These applications include artificial enzymes, sensors, drug formulations, cosmetics, food technology, and textiles [47,49,60,65].

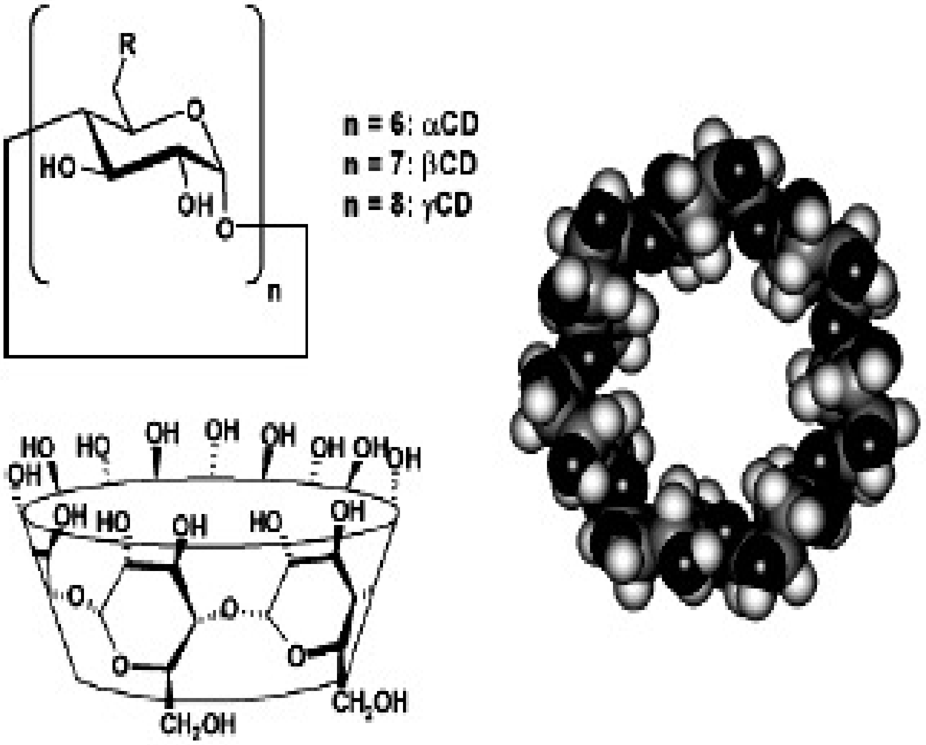

Figure 1.2.4. Structure of cyclodextrins. From ref [60]: R. Villalonga, R. Cao, A. Fragoso. Chem. Rev. 107 (2007) 3088.

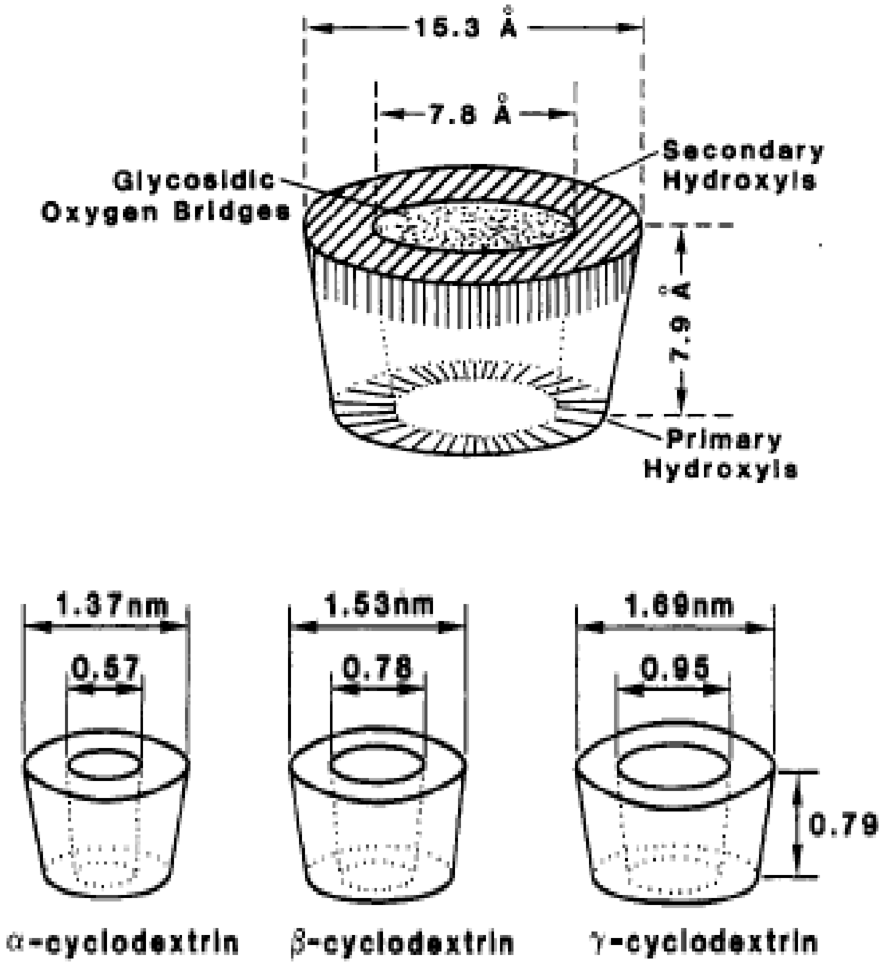

Figure 1.2.5. Functional structural of β-CD and molecular dimension of different cyclodextrins. From ref [63]: S. Li, W. C. Purdy. Chem. Rev. 92 (1992) 1457.

In aqueous solution, complex formation between a CD host molecule and a guest molecule is a dynamic equilibrium process. This process is described by Equation 1.2.1 [49]:

$$CD + G \leftrightarrow CD - G \qquad \textbf{(1.2.1)}$$

where G is the guest molecule and CD-G is the inclusion complex. Therefore, the stability of the inclusion complex can be described in terms of the association constant, *K*, as shown in Equation 1.2.2:

$$K = \frac{[CD - G]}{[CD][G]} \qquad \textbf{(1.2.2)}$$

A number of factors affect the stability of CD inclusion complex. Among these factors, the most important are the size and polarity of the guest molecules, and the medium [63]. For guest molecules, their size must match the size of the CD cavity to form a fully included complex and their polarity should be less than water. The stability also strongly depends on the nature of the medium used for inclusion. Complexation is more perfect in the presence of water. However, the complexation in an organic solvent is generally weak. The solubility of the guest in solvent is also important. Moreover, the stability of CD inclusion complex decreases with increasing temperature and can be improved by chemically modifying the CD molecules by substituting the primary or secondary hydroxyl groups [63].

The CDs are not electroactive, but they can form inclusion complexes with some suitable redox active organometallic guests. This observation has been detailed in numerous reports [66,67,68]. The CD can associate with an organometallic complex as a second-sphere ligand (Figure 1.2.6 a), a first- and second-sphere ligand (Figure 1.2.6 b), a first-sphere ligand and a transient second-sphere ligand (Figure 1.2.6.c), or a transient second-sphere ligand (Figure 1.2.6.d). The most common complexation is where the CD acts as a second-sphere ligand by non-covalently binding one of the first-sphere ligands of the metal centre.

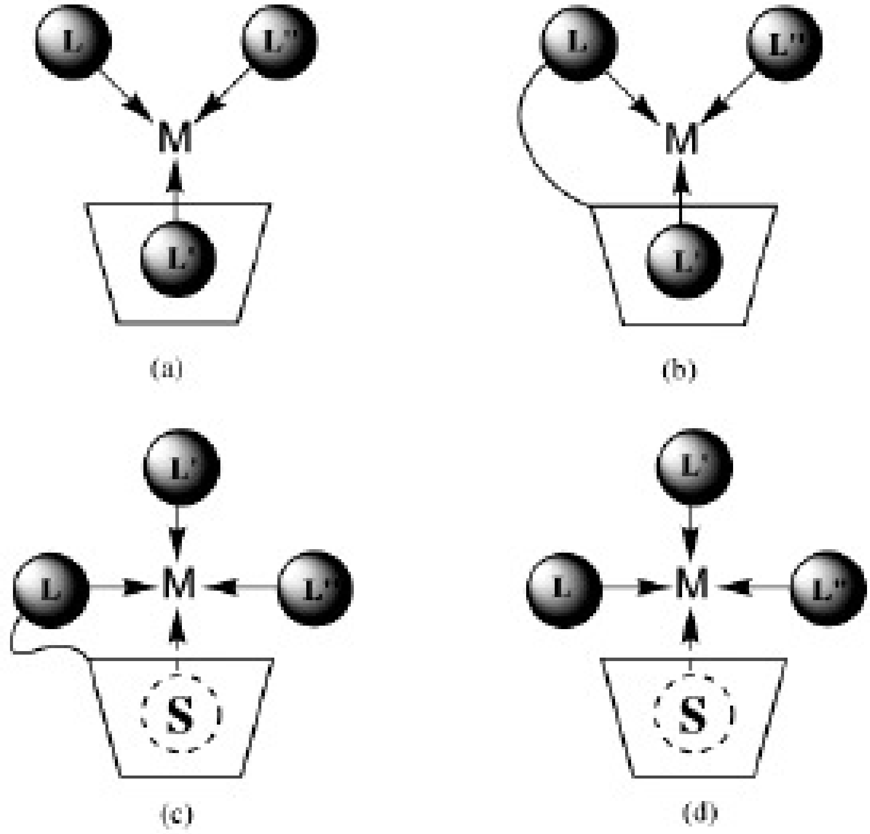

Figure 1.2.6. Four types of adducts when a CD host molecule complexation of an organometallic complex, where L is a normal ligand and S is a transient ligand. From Ref [68]: F. Hapiot, S. Tilloy, E. Monflier. Chem. Rev. 106 (2006) 767.

Osa and co-workers demonstrated the inclusion of ferrocenecarboxylic acid in β-CD [69]. The association constant of this inclusion system was determined as 2200 M^{-1} using cyclic voltammetry. This formal potential shifted in a positive direction upon inclusion in the CD cavity as the included ferrocene is harder to oxidise. However, no evidence was found to show that the oxidized form of ferrocene was bound by CD host molecule to form an inclusion complex. Similar results were found in CD complexation of other ferrocene derivative [70], viologens [71], and cobaltocenium derivatives [70d,72] by Kaifer's research group. These findings suggest that electron transfer from the inclusion complex must be thermodynamically or kinetically hindered. The charged states of guest molecules can decrease their affinity for the CDs and therefore inhibit inclusion. However, an important distinction can be made between the ferrocene-based guests and those containing viologens or cobaltocenium moieties [67]. For ferrocene guests, the molecular recognition forces can be deactivated electrochemically as the most stable state of ferrocene molecules is their neutral state, while viologens or cobaltocenium derivatives require electrochemical activation to trigger inclusion complexes of CDs because their most stable states are in their charged forms.

1.2.4 Self-Assembled Monolayers

In order to prepare organized monolayer assemblies, two common methods have been exploited respectively, Langmuir-Blodgett and self-assembly methods [49]. In the Langmuir-Blodgett (LB) method, amphiphilic molecules are mechanically compressed into an organized film at the air-water interface to form a monolayer or multilayer. By contrast, the self-assembly method takes advantage of strong chemisorption through chemical bonding or a large number of weak and/or moderate interactions to spontaneously generate the organized interfacial structures [73]. This approach provides unique opportunities to increase fundamental understanding of self-organization, structure-property relationships, and interfacial phenomena [74]. Well-defined and accessible interfacial structures are good model systems for studies of physical chemistry and statistical physics in two-dimensions, and the crossover to three dimensions.

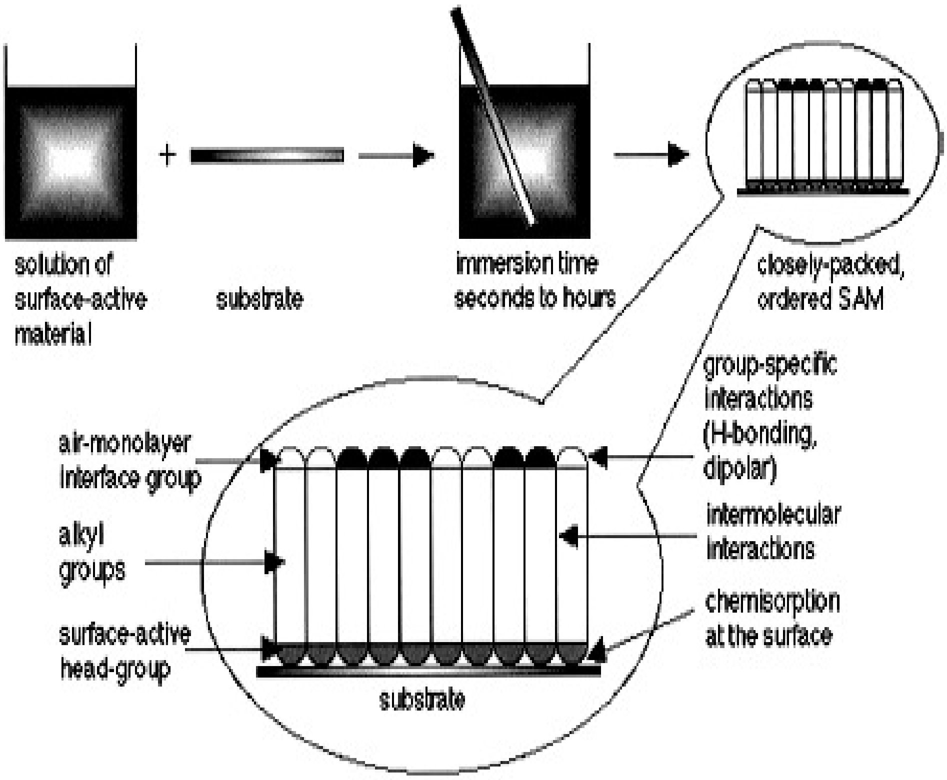

Figure 1.2.7. Formation of self-assembled monolayer. From ref [74]: A. Ulman. Chem. Rev. 96 (1996) 1533.

As illustrated in Figure 1.2.7 closely-packed self-assembled monolayers (SAMs) are organic assemblies formed by simply immersing an appropriate substrate into a solution of the surface-active material. The driving force for the spontaneous formation of the two-dimensional assembly includes chemical bond formation of molecules with the surface and intermolecular interactions. The formation of SAMs offers one of the most convenient ways to obtain ordered monolayers through chemisorption between the surface-active head group of a desired compound and a suitable substrate leading to the preparation of thermodynamically stable monolayers [74,75]. There are number of surface-active head groups, such as –SH, -CN, -COOH, -NH_2, silanes, and pyridine, which can be used for immobilization on selected metallic, like Au, Cu, Ag, Pd, Pt, Hg, and C, as well as semi conducting surfaces e.g. Si, GaAs, indium coated tin oxide etc [74, 76]. From the standpoint of electrochemistry, the most extensively studied class of SAMs is derived from the chemisorption of alkanethiols on gold [73].

The thiolate-on-gold SAM is usually prepared by adsorption of long chain alkanethiol molecules onto a clean gold surface. As shown in Figure 1.2.8, a stable, organized and densely packed alkanethiol monolayer is readily formed on the gold surface. The length of the alkanethiol chain provides the well-defined thickness of the monolayer. Also, the chain acts as a physical barrier and alerts electronic conductivity and local optical properties. The main axes of each molecule are tilted by an angle of approximately 30° from the normal to the structure. The sulphur atoms adopt a $(\sqrt{3}\times\sqrt{3})R30^{\circ}$ adlayer arrangement [73]. The main driving forces for the formation of this SAM are the thiolate-gold bonds and the lateral interactions among the aliphatic chains of neighbouring alkanethiol molecules. Adsorbed alkanethiol molecules lose their hydrogen atom from the thiol groups and form the new thiolate-gold bonds at Au-S interface. These new bonds are thermodynamically favourable and each bond has estimated to release 40-50 kcal/mol [77]. Moreover, although the lateral interactions are much weaker van der Waals forces, their cumulative magnitude is considerable for well-packed long chain alkanethiols monolayers. However, the detailed mechanism of the bond between thiolate and gold surface is still ambiguous [77,78]. In solution, it seems probable that the thiol hydrogen is lost in the form of water due to the presence of oxygen in the reaction medium [76].

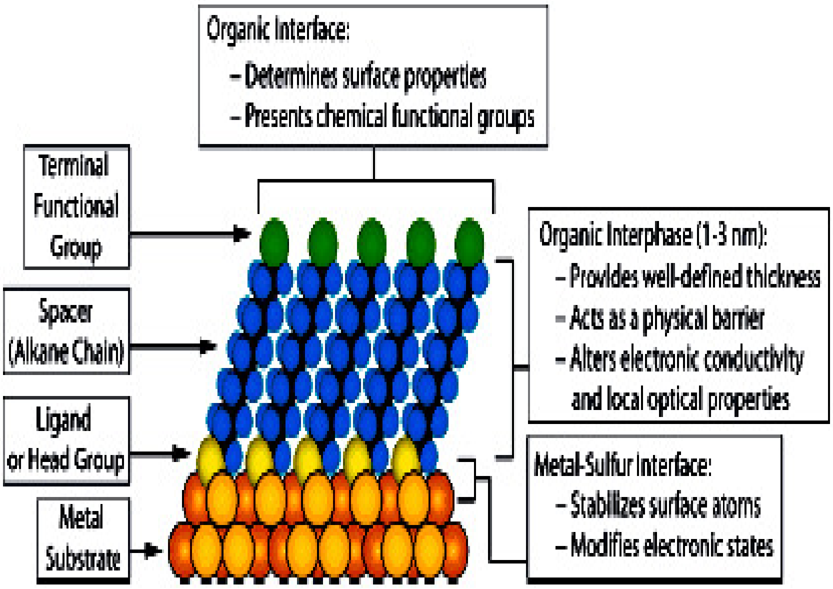

Figure 1.2.8. Schematic diagram of a thiolate-on-gold SAM. From ref [76]: J. C. Love, L. A. Estroff, J. K. Kriebel, R. G. Nuzzo, G. M. Whitesides. Chem Rev. 105 (2005) 1103.

1.2.5 Monolayers Incorporating Cyclodextrins

SAMs can be used to monitor binding ability at the interface, when functionalized with suitable receptor adsorbates. Therefore, a SAM of host molecules can act as a template, onto which guest molecules can be immobilized. Several supramolecular host molecules have been used to form an immobilized monolayer to bind guest molecules. These host molecules include crown ether by ammonium SAMs [79,80], His-tagged proteins by a Ni nirilotriacetic acid SAMs [81,82], and cyclodextrin complexation by adamantyl SAMs [83,84,85]. Among these SAM systems, immobilization of cyclodextrins on gold surfaces and the complexation behaviour of immobilized CDs have been shown to be able to form highly organized monolayers. These monolayers are suitable for the investigation of relations between the molecular structure and molecular-recognition properties of CDs. At the same time, the chemical structure of CD derivatives has a great effect on the molecular organization of the monolayers.

The first sample of monolayers incorporating cyclodextrins was introduced by Kaifer and co-workers [86]. They synthesized per-6-thio-β-cyclodetrins by converting all seven primary –OH groups of β-CD into –SH groups and these CDs were chemisorbed onto gold surfaces forming at least 6 S-Au bonds per β-CD. The surface coverage of CDs was about 64-75% of that expected for a hexagonal close-packed monolayer and revealed an imperfect monolayer, containing numerous defective sites or pinholes. This was attributed to the large cross-section area of the thiolated CDs and the rather poor lateral interactions among CD molecules. In order to 'patch' the holes or defective sites, pentanethiol was used as the second step procedure to form a mixed monolayer. Double layer capacitance measurements and a blocking efficiency were employed to characterize the CDs and mixed monolayers. Further, the binding constant of interfacial ferrocene complexation was determined as 3.9×10^4 M^{-1}, and the dynamic nature of the complexation process of ferrocene by the immobilized cyclodextrin was confirmed by competition experiments with *m*-toluic acid (mTA).

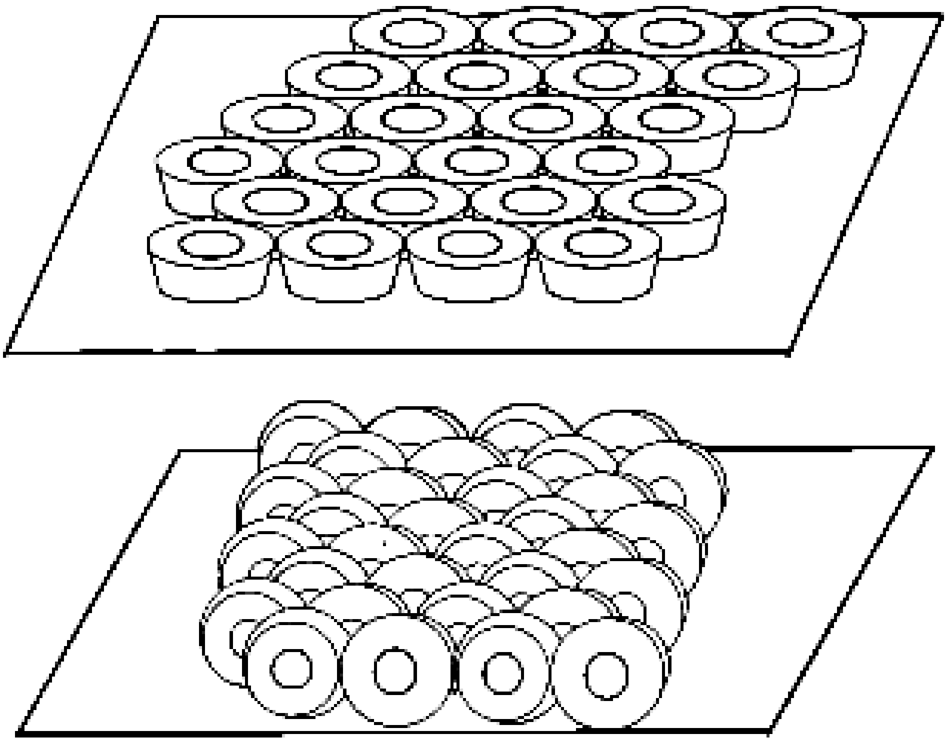

Figure 1.2.9. Two models for the arrangement of the CD tori monolayer: (top) hexagonal close-packed model and (bottom) brick packing model. From ref [87b]: M. Weisser, G. Nelles, P. Wohlfart, G. Wenz, S. Muttler-Neher. J. Phys. Chem. 100 (1996) 17893.

Mittler-Neher and co-workers [87] investigated the influence of the spacer length between the thiol group and the CD cavity of mono and multi thiolated CDs on the adsorption kinetics by using Fourier transform infrared (FTIR) spectroscopy, time-of-flight mass spectrometry, contact angle measurements, plasmon surface polariton (PSP) spectroscopy, and cyclic voltammetry. The adsorption kinetics can be described by a three-step process: a physical absorption process, a binding and orientation step, and an adlayer formation. Also, their work revealed the possible orientations of the CDs monolayer like hexagonal close-packed model and brick packed model (Figure 1.2.9).

Galla and co-workers have studied the complexation behaviour of the SAMs of mercaptopropane-N-mono-6-deoxy-β-cyclodextrin amide on gold surfaces and at the air-water interface [88] and demonstrated that the binding of guests can be reversed by adding excess CD in solution. Impedance spectroscopy revealed that the SAMs had a high surface coverage of more than 99% due to displacement caused by the flexible single-thiol spacer of the CD. X-ray photoelectron spectroscopy and time-of-flight secondary ion mass spectrometry clearly showed that the modified CD is chemisorbed on the gold surface by Au-S bonds.

Kitano et al included [89] the region- and stereo-selective complexation of chiral phenylazobenzoate compounds with the thiolated CD SAM on the gold electrode. The differences in association constants between ortho- and para-isomers and R- and S-enanitiomers of the ortho-isomer were determined using p-hydroquinone as a probe. Later, the use of thiolated CD SAMs as sensors for phtalic acid esters and bisphenols has been reported [90,91]. The effect of CD cavity orientation on the inclusion ability and the association constants for phtalic acid esters and bisphenols with the CD SAMs were elucidated.

Reinhoudt and co-workers reported the preparation of well-packed CD SAMs of dialkyl sulphide and alkanethiol ester [92,93]. These CD SAM adsorbates on gold were characterized by electrochemistry, wettability studies, X-ray photoelectron spectroscopy (XPS), time-of-flight secondary ion mass spectrometry (TOF-SIMS) and atomic force microscopy (AFM). AFM images indicated that the CD molecules with seven dialkyl sulphide moieties produced ordered layers. The association constant of the inclusion between the SAMs and 1-anilinonaphtalene-8-sulfonic acid was determined as 2×10^{6} M^{-1} using the Langmuir isotherm. These SAMs have also been applied in single molecule force spectroscopy measurements, where pull-off forces of individual host-guest complexes were quantified [94,95,96].

More recently, our group described the formation of di-6^{A},6^{B}-deoxy-6-(4-pyridylmethyl)amino-γ-cyclodextrin SAM on polycrystalline platinum electrodes [97]. The binding of these CD molecules with pyridine onto platinum electrodes has been characterized by using capacitance, blocking experiments, and surface-enhanced Raman spectroscopy (SERS).

The adsorption of these SAMs was a two-step process involving the chemisorption of CD molecules and a backfilling process with 1-nonanethiol to block defects. The most interesting aspect of this work was the observation of a reorientation of the CD molecules during the backfilling process (Figure 1.2.10). The backfilling process with 1-nonanethiol broke up the original orientation of CD cavities in monolayer, where the CD cavities faced each other and the electroactive guest, $[Co(biptpy)_2]^{2+}$ (cobalt bisdiphenylterpyridine), was blocked from entering into the cavity. Thus, backfilling forced the CD into an upright orientation whilst increasing the rigidity of the film and potentially disrupting any intermolecular interactions between the CDs making the CD host more amenable to inclusion with bulky solution-phase guests.

Finally, the Langmuir isotherm was used to determine the surface coverages and association constants for both reduced and oxidized forms of $[Co(biptpy)_2]^{2+}$ guest molecules. The surface saturation coverage for the oxidized guest form (1.03×10^{-11} mol cm^{-2}) was lower than that of the reduced form (1.49×10^{-11} mol cm^{-2}). This observation suggested that the trivalent form of the cobalt complex is expected to exit the cavity.

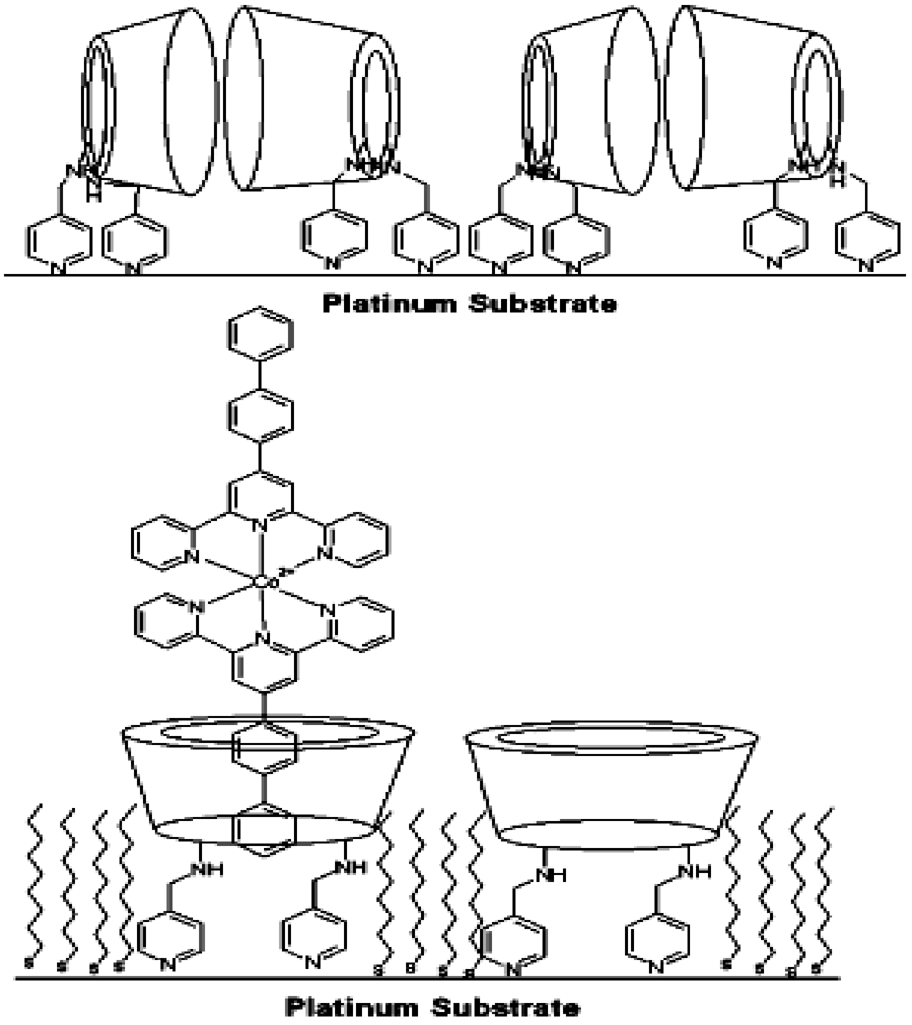

Figure 1.2.10. The possible orientation of the CD SAM on the platinum electrode before (top) and after (bottom) backfilling with 1-nonanethiol. From ref [97]: C. T. Mallon, R. J. Forster, A. McNally, E. Campagnoli, Z. Pikramenou, T. E. Keyes. Langmuir 23 (2007) 6997.

1.3 SURFACE PROTECTED GOLD NANOPARTICLES MULTILAYER

1.3.1 Surface Protected Gold Nanoparticles

Gold nanoparticles (AuNPs) possess fascinating properties such as their assembly of multiple types involving materials science, the behaviour of the individual particles, size-related electronic, magnetic and optical properties, and their applications to catalysis and biology [98]. However, in most of these applications, the AuNPs are surrounded by a self-assembled monolayer to form monolayer-protected gold nanoparticles. They are much more stable than bare AuNPs and do not aggregate in the solid state [99]. AuNPs protected by an electrochromic material monolayer or supramolecular host monolayer, which can form inclusion with electrochromic guest molecule, have the potential use as the electrochromic electrode in the display application of electrochromism.

The first sample of the stabilization of AuNPs using alkanethiols with different chain lengths was reported in 1993 by Mulvaney and Giersig [100]. However, Schiffrin and co-workers published the classical two-phase method for preparing AuNPs by thiols in 1994 [101]. This method has had a considerable impact on the overall field of AuNPs preparation, because it allowed the facile synthesis of thermally stable and air-stable AuNPs of reduced dispersity and controlled size for the first time. Figure 1.3.1 shows some particular thiol samples and the formation of AuNPs, which can be described by the following reactions (Equation 1.3.1 and 1.3.2). The thiols are added to organic-phase $AuCl^-$ (1:1) and strongly bind to gold to form Au clusters with core diameters in a range 1-3 nm due to the soft character of both Au and S, when $AuCl^-$ is reduced by $NaBH_4$ [101]. These reaction behaviours arise because larger thiol/gold mole ratios gives smaller average core sizes; fast reductant addition and cooled solutions produced smaller, more mono-disperse particles; and a higher abundance of small core sizes ($\leq$ 2 nm) is obtained by quenching the reaction immediately following reduction or by using sterically bulky ligands [99].

$$AuCl_4^-(toluene) + RSH \rightarrow (-Au^1SR-)_n(polymer) \qquad \textbf{(1.3.1)}$$

$$(-Au^{1}SR-)_{n} + BH_{4}^{-} \rightarrow Au_{x}(SR)_{y} \qquad \textbf{(1.3.2)}$$

Further, Schiffrin et al. extended the synthesis to *p*-mercaptophenol stabilized AuNPs in a single phase method [102], which allowed AuNPs to be stabilized by a wide range of functional thiol ligands. Murray and co-workers also reported the preparation of functionalized AuNPs in a 'place exchange' method by controlling the proportion of thiol ligands with various functional thiols, which can be used to form a multilayer [103] and this method can be described by the Equation below:

$$x(R^{'}SH) + (RS)_{m}MPC \rightarrow x(RSH) + (R^{'}S)_{x}(RS)_{m-x}MPC \qquad \textbf{(1.3.3)}$$

where *RS* alkanethiolate ligands stabilized AuNPs can be functionalized with *R'S* ligands; *x* and m are the numbers of *R'S* and *RS* alkanethiolate ligands, respectively. The rate and equilibrium stoichiometry (*x*) of the reaction can be controlled by factors such as the mole ratio of *R'SH* to *RS* ligands, their relative steric bulk, and *R* versus *R'* chain lengths [103b]. The dynamics and mechanism of place-exchange reaction show that exchange has a 1:1 stoichiometry and is an associative reaction. The reaction produces displaced ligand in solution as a thiol and does not involve the formation of disulfides or oxidized sulphur species. The time dependent rate of this reaction reflects a hierarchy of different core surface binding sites with associated susceptibility (vertices, edges > terraces) to place-exchange [103d].

The functional groups of *R'S* alkanethiolate ligands include Br, CN, Vinyl, Ferrocene, Ph, OH, CO_2H, CO_2CH_3, Anthraquinone et al [99]. As illustrated in Figure 1.3.2, Astruc and co-workers used this ligand substitution method to obtain functionalized AuNPs containing mixed dodecanethiol and amidoferrocenyl alkanethiol-type ligands with variation of the chain length, C_6 vs. C_{11}, and ring structure of the redox active ferrocenyl motif [104]. This mixed structure of AuNPs can be used as exo-receptors for the recognition of oxoanions by combining the effect of the topography of AuNPs and the supramolecular properties of the redox active termini.

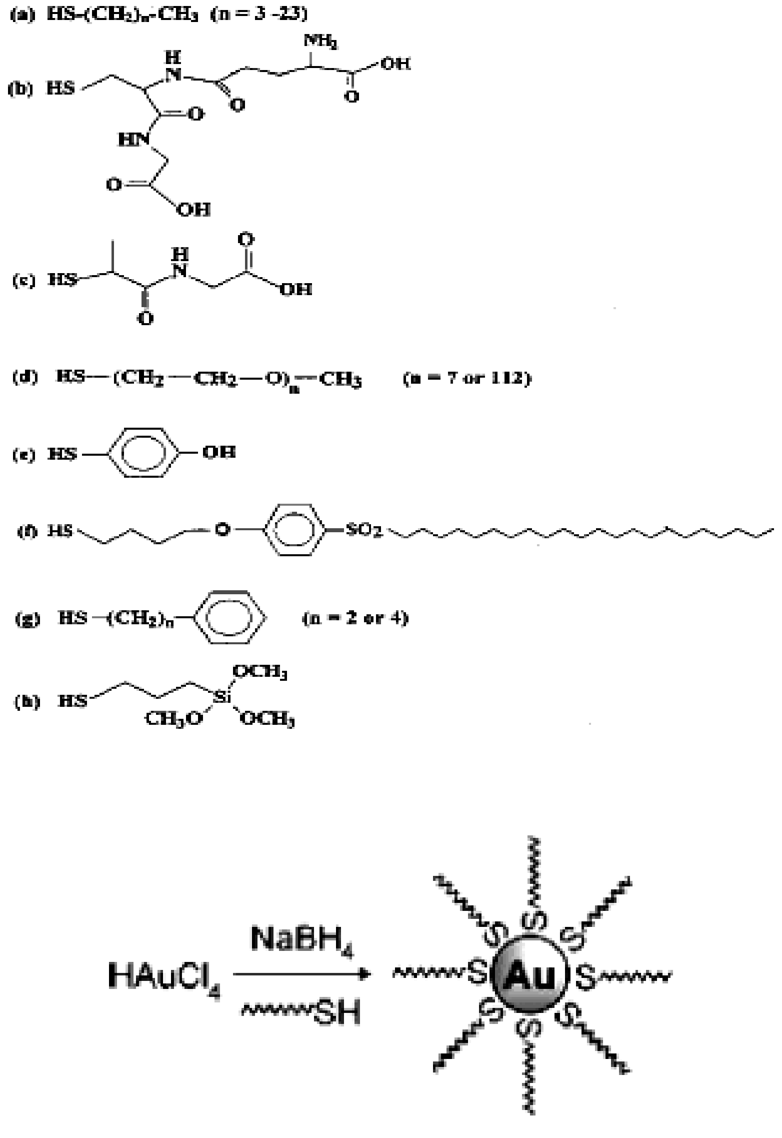

Figure 1.3.1. Examples of thiol ligands used to prepare AuNPs. From ref [99]:A. C. Templeton, W. P. Wuelfing, and R. W. Murray. Acc. Chem. Res. 33 (2000) 27. And formation of AuNPs with thiol ligands. From ref [105]: L. Sun, R. M. Crooks, V. Chechik. Chem. Commun. (2001) 359.

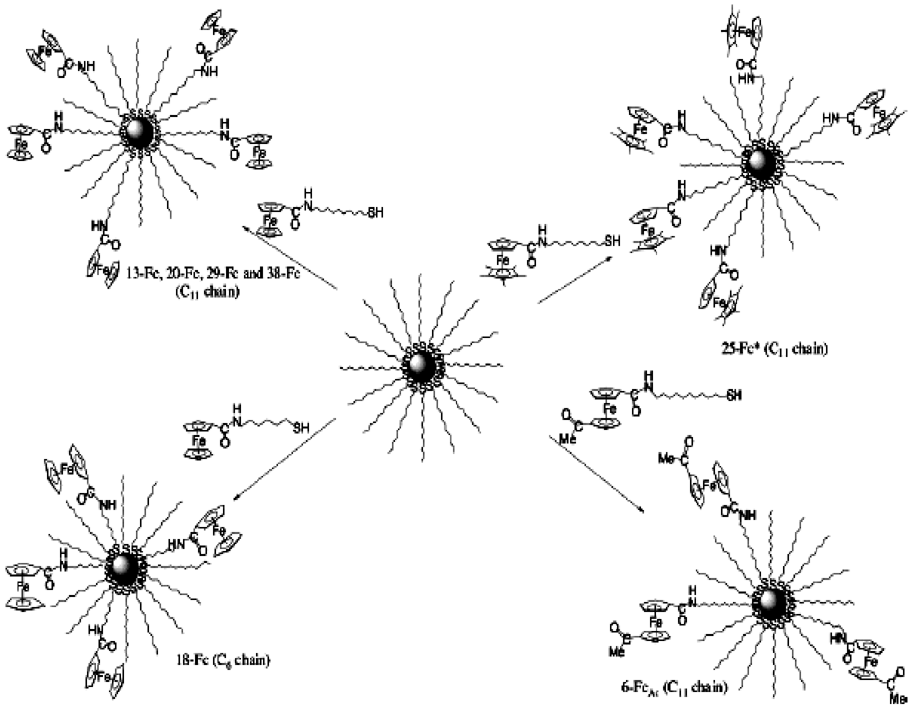

Figure 1.3.2. Examples of ligand exchange reactions for the syntheses of the AuNPs containing mixed dodecanethiol and amidoferrocenyl aldanethiol-type ligand. From ref [104]: A. Labande, J. Ruiz, D. Astruc. J. Am. Chem. Soc. 124 (2002) 1782.

1.3.2 Electrochemistry of AuNPs Multilayer Films

For some potential application for the AuNPs, such as chemical sensor development, AuNPs can form a monolayer or multilayer film on a electrode and it is very important to understand the dynamics of charge transport through such thin films by measuring the rate of charge transport [106]. Electrochemistry studies have been performed for some forms of AuNPs multilayer films, in which the nanoparticles in the multilayer films can be linked together by using carboxylate/metal ion/carboxylate linking, pyridine/metal ion/pyridine linking, and dithiol linking [107].

AuNPs multilayer films based on ligand/metal ion/ligand linking has been first described by Murray and co-workers [108]. They generated 1.6 nm diameter AuNPs with mixed hexanethiolate/mercaptohexanoic acid and built the multilayer films in a two-step dip and rinse cycle. As illustrated in Figure 1.3.3, carboxylic acid SAM on Au electrode was exposed to a metal ion solution and then to a solution of AuNPs. In the dip step, the AuNPs first attached to COOH- functionalized Au electrode by carboxylate/Zn^{2+} or Cu^{2+}/carboxylate. Further, the cycle step can be repeated to add more AuNPs to form the multilayer structure.

Murray and co-workers also reported the dynamics of electron self-exchange between nanoparticles in this kind of AuNPs multilayer film [109]. The electron self-exchange is measured as a diffusion-like electron-hopping process and the average electron diffusion coefficient is D_E=10±5 $\times 10^{-8}$ cm^2 s^{-1}. The rate of electron hopping between AuNPs, k_{HOP}, is about $2\pm1\times10^6$ s^{-1} and the average self-exchange rate constant, k_{EX}, is $2\pm1\times10^8$ M^{-1} s^{-1}. These rate constants depend on the length of the linking bridge between the Au cores. The flexibility of the linker chains allows considerable local mobility of the AuNPs multilayer structures and the operative electron tunnelling pathways involves the shorter, non-linker particle ligand. That the electrochemical reaction always occurs through a shorter tunnelling bridge in the multilayer can result in the faster electron transport rate.

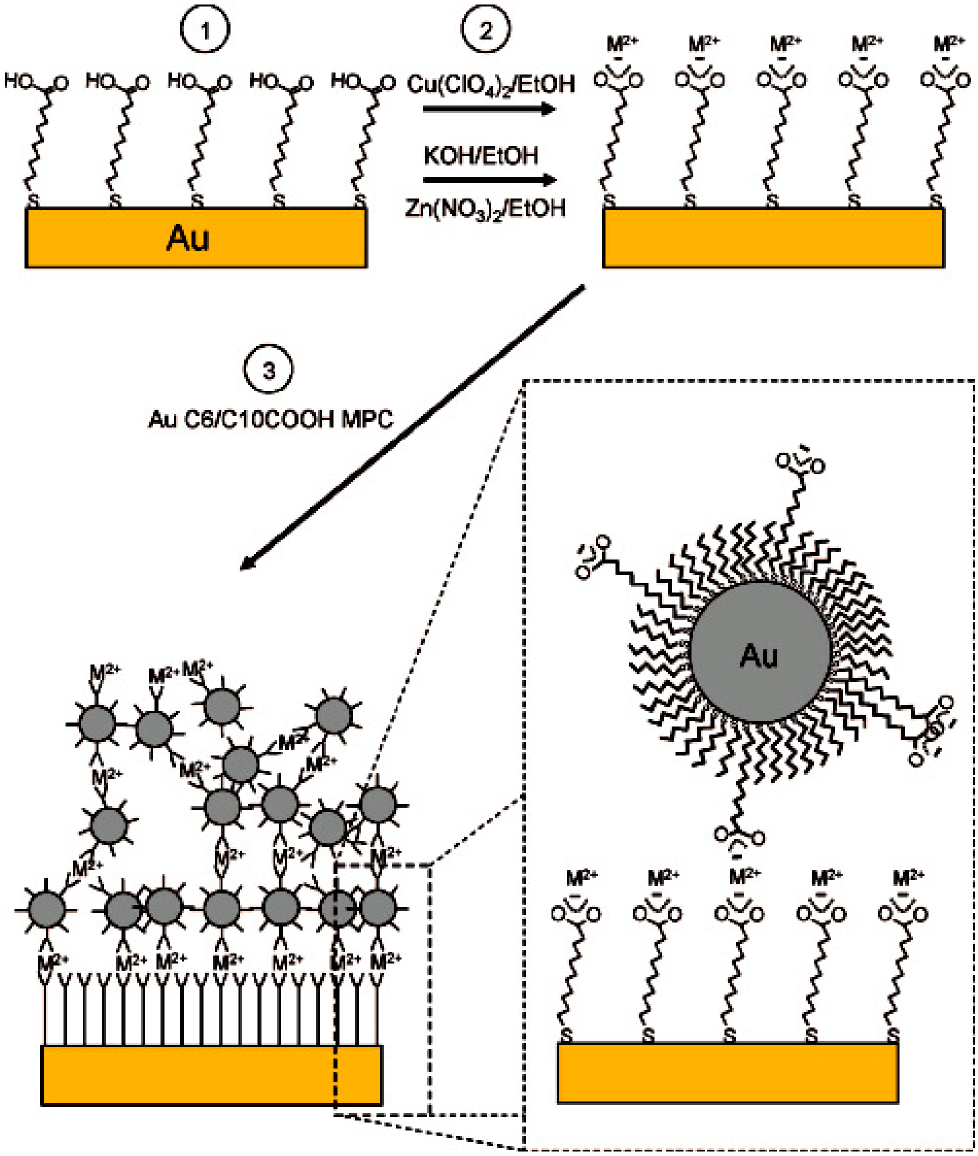

Figure 1.3.3. Formation of gold nanoparticle multilayer films based on ligand/metal ion/ligand linking. From ref [108]: F. P. Zamborini, J. F. Hicks, R. W. Murray. J. Am. Chem. Soc. 122 (2000) 4514.

Another kind of ligand/metal ion/ligand AuNPs multilayer was reported by Chen and co-worker [110], in which pyridine contained ligands replaced the carboxylic acid and the metal ion was Cu^{2+}. The thickness of the multilayer films was controlled by repetition of the alternate dipping cycles and deposition was monitored by quartz crystal microbalance (QCM). Electrochemistry studies of this AuNPs multilayer film revealed rectified quantized charging characters in aqueous solution in the presence of hydrophobic electrolyte anions and binding mechanism between the positively charged metal ion centres and hydrophobic electrolyte ions. Despite a long tunnelling distance between Au nanoparticle cores, this multilayer showed a fast electron transport rate because the metal ions centres may enhance the electron transfer kinetics of nanoparticle quantized charging.

Brennan et al. [106] described the rate of electron hopping between AuNPs in multilayer films linked together by α,ω-alkanedithiolates bridges and by carboxylate/Cu^{2+}/carboxylate bridges by contacting a solution of a redox species (decamethylferrocene, Cp*Fe). Controlling the electrode potential so that the film mediates oxidation of the redox probe can force control of the overall current onto the rate of electron hopping with the film, which was characterized as the apparent electron diffusion coefficient D_E. The electron diffusion coefficient can be translated into an apparent electron hopping rate k_{ET} by a cubic lattice model. The apparent hopping rates were in the 10^4-10^5 s^{-1} range and did not systematically respond to changes in the AUNP charge state, to changes in the dithiolate linker length, or to the differences between lengths of dithiolatd and carboxylate/Cu^{2+}/carboxylate linkers. These results suggest that the use of flexible linkers surrounded by shorter nonlinker ligands does not rigorously enforce distances or the lengths of tunnelling pathways between particle cores in these multilayer films.

Lev and co-workers also accessed the charge transport in self-assembled gold-dithiol films by conductivity measurement [111]. Conductivity studies demonstrated that the effective activation energy for conduction in gold-dithiol AuNPs films followed the electron-tunnelling mechanism and sharply increased with increasing the lengths of dithiol linkers from C_2 to C_8. A similar observation was obtained from the measurements of the electronic conductivities of other AuNPs films on an interdigitated electrode array (IDA) [112]. The conductivities and electron hopping rates of these dry films decrease and the activation energy barrier increases systematically with increasing alkanethiolate chain length. It emerged that the relevant parameter for analysis of the dependency of electron hopping rate on alkanethiolate ligand is the average separation between particle core edges.

1.3.3 Supramolecular AuNPs Network

AuNPs network has also been developed by combination with the supramolecular chemistry concepts [113]. An early example of this network was reported by Kaifer and co-workers [114]. They used fullerenes as non-covalent linkers to bridge γ-CD-capped gold nanoparticles via host-guest interaction to form a three dimensional multilayer network (Figure 1.3.4). The formation of this network was confirmed from transmission electron microscopy (TEM) and photon correlation spectroscopy (PCS). TEM images revealed an average diameter of 3.2 nm for γ-CD-capped gold nanoparticles and of about 300 nm for the C_{60} linked network. PCS results showed a typical network found in this sample, with a size consistent with the TEM data and indicated that the size of the C_{60} linked network could be obtained by adjustment of the temperature during the association process.

In addition, Reinhoudt and co-workers described the formation of large network aggregates composed of gold nanoparticles bearing surface-immobilized β-cyclodextrin hosts, whose assembly is driven by adamantyl-terminated guest molecules acting as non-covalent molecular linkers between the nanoparticles[115]. They probed the influence of multivalency and cooperativity on the assembly of network from β-CD-capped gold nanoparticles and adamantyl-terminated molecules.

However, much less is known about the dynamics of electron transfer through such multilayer films. In Chapter 5, we will report on the formation of CD-capped AuNPs multilayer via host-guest interaction and detail the electron transfer dynamics between particle cores.

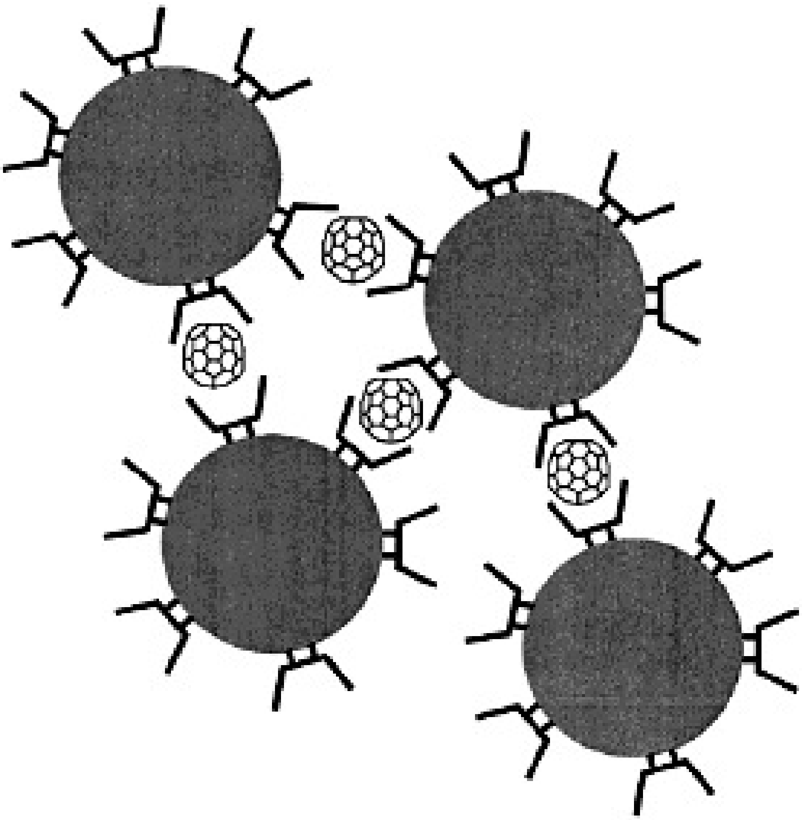

Figure 1.3.4. Fullerene-induced aggregation of γ-CD-capped gold nanoparticles. From ref [114]: J. Liu, J. Alvarez, W. Ong, and A. E. Kaifer. Nano. Lett. 1 (2001) 57.

1.4 CONCLUSIONS

In this review, the main objective was to understand the electrochromic materials and to study the potential formats of such materials on an electrode surface. Towards this, solid state film, supramolecular monolayer, and gold nanoparticles multilayer have been reported. In the former section of this chapter, electrochromic properties of electrochromism have been defined. The typical electrochromic materials, such as metal oxides, Prussian blue, viologens, conducting polymer, and metallopolymer, and their fundamentals have been also introduced and discussed.

The subsequent section had laid out the principle of supramolecular host-guest chemistry. The formation of interfacial supramolecular self-assembled monolayers has been emphasised by a number of literature and experimental observations. These monolayers provide well organized structures with good thermodynamic stability. In particular, self-assembled monolayer of cyclodextrin host molecules can be immobilized through complexation with suitable guest molecules to form highly organized monolayers. This format has potential use in the application of electrochromic devices when electrochromic materials are used as guest molecules.

Finally, the formation of gold nanoparticle multilayer has been described. The format of CD-capped AuNPs multilayer via host-guest interaction, where electrochromic materials can be used as guest molecules, may attract interest for electrochromic devices because the properties of electrical conductivity, plasmon enhanced optical absorption, and fast interfacial electron transfer offered by the gold nanoparticles may allow nano-crystalline electrochromism to have sharp contrast and fast switching rates, which are key elements in the application of an electrochromic device.

1.5 REFERENCES

[1] P. Bamfield, Chromic Phenomena: Technological Applications of Colour Chemistry, Royal Society of Chemistry, Cambridge, 2001.

[2] P. M. S. Monk, R. J. Mortimer, D. R. Rosseinsky. Electrochromism: Fundamentals and Applications, VCH, Weinheim, 1995.

[3] C. G. Granqvist. Handbook of Inorganic Electrochromic Materials, Elsevier, Amsterdam, 1995

[4] M. Green. Chem. Ind. (1996) 641.

[5] S. K. Deb. Appl. Opt. Suppl. 3 (1969) 192.

[6] M. Ristova, J. Velevska, M. Ristov. Sol. Energy Mater. Sol. Cells. 71 (2002) 219.

[7] L. D. Kadam, P. S. Patil, Sol. Energy Mater. Sol. Cell. 70 (2001) 15.

[8] P. S. Patil, S. B. Nikam, L. D. Kadam. Mater. Chem. Phys. 69 (2001) 77.

[9] P. M. S. Monk. J. Electroanal. Chem. 432 (1997) 175.

[10] K. Bange. Sol. Energy Mater. Sol. Cells 58 (1999) 1.

[11] D. R. Rosseinsky, R. J. Mortimer. Adv. Mater. 13 (2001) 783.

[12] K. J. Albert, N. S. Lewis, C. L. Schauer. G. A. Sotzing, S. E. Stitzel, T. P. Vaid, D. R. Walt. Chem. Rev. 100 (2000) 2595.

[13] D. T. McQuade, A. E. Pullen, T. M. Swager. Chem. Rev. 100 (2000) 2537.

[14] R. A. Colley, P. M. Budd, J. R. Owen, S. Balderson. Polym. Int. 49 (2000) 371.

[15] R. J. Mortimer, N. M. Rowley, Metal complexes as dyes for optical data storage and electrochromic materials in: Comprehensive Coordination Chemistry - II: J. A. McCleverty, T. J. Meyer, M. D. Ward (Eds.), From Biology to Nanotechnology 9.2, Elsevier, Oxford, 2004 pp. 581–619.

[16] A. A. Argun, P. H. Aubert, B. C. Thompson, J. R. Reynolds. Chem. Mater. 16 (2004) 4401.

[17] R. D. Overheim, D. L. Wagner. Light and Colour, Wiley, New York, 1982.

[18] M. D. Ward, J. A. McCleverty. J. Chem. Soc., Dalton Trans. (2002) 275.

[19] M. D. Ward. J. Solid State Electrochem. 9 (2005) 778.

[20] Z. C. Wu, Z. H. Chen, X. Du, J. M. Logan, J. Sippel, M. Nikolou, K. Kamaras, J. R. Reynolds, D. B. Tanner, A. F. Hebard, A. G. Rinzler. Science 305 (2004) 1273.

[21] R. D. Rauh. Eletrochim. Acta 44 (1999) 3165.

[22] J. Garcia-Canadas, A. P. Meacham, L. M. Peter, M. D. Ward. Angew. Chem. Int. Ed. 42 (2003) 3011.

[23] R. J. Mortimer. Chem. Soci. Rev. 26 (1997) 147.

[24] P. R. Somani, S. Radhakrishnan. Materials Chemisty and Physics 77 (2002) 117.

[25] A. A. Argun, Pierre-H. Aubert, B. Thompson, I. Schwendeman, C. L. Gaupp, J. Hwang, N. J. Pinto, D. B. Tanner, A. G. MacDiarmid, J. R. Reynolds. Chem. Mater. 16 (2004) 4401.

[26] R. J. Mortimer. Electrochim. Acta 44 (1999) 2971.

[27] R. J. Mortimer, A. L. Dyer, J. R. Reynolds. Displays. 27 (2006) 2.

[28] J. F. Rusling, R. J. Forster. J. Colloid and Interface Science. 262 (2003) 1.

[29] K. Kalyanasundaram. 'Photochemistry of Polypyridine and Porphyrin Complexes'; Academic Press,; London, 1992.

[30] D. M. Roundhill,; Photochemistry and Photophysics of Metal Complexes; Plenum: New York, 1994; p 165-215.

[31] V. Balzani, F. Scondola. Supramolecular Photochemistry; Ellis Horwood: Chichester, 1991.

[32] A. Juris, V. Balzani, F. Barigelletti, S. Campagna, P. Belser, A. Vonzelewsky. Coord. Chem. Rev. 84 (1988) 85.

[33] Y. Z. Hu, S. Tsukiji, S. Shinkai, S. Oishi, I. Hamachi. J. Am. Chem. Soc. 122 (2000) 241.

[34] H. Durr, S. Bossmann. Acc. Chem. Res. 34 (2001) 905.

[35] K. Kalyanasundaram. Coord. Chem. Rev. 46 (1982) 159.

[36] V. Balzani, A. Juris, M. Venturi. Chem. Rev. 96 (1996) 759.

[37] T. E. Keyes, D. Leane, R. J. Forster, C. G. Coates, J. J. McGarvey, M. N. Nieuwenhuyzen, E. Figgemeier, J. G. Vos. Inorg Chem. 41 (2002) 5721.

[38] I. Brady, D. Leane, H. P. Hughes, R. J. Forster, T. E. Keyes. J. Chem. Soc., Dalton Trans. (2004) 334.

[39] T. E. Keyes, B. Evrard, J. G. Vos, C. Brady, J. J. McGarvey, P. Jayaweera. J. Chem. Soc., Dalton Trans. (2004) 2341.

[40] T. E. Keyes, R. J. Forster, P. M. Jayaweera, J. G. Vos, J. J. McGarvey, Inorg. Chem. 22 (1998) 5925.

[41] T. E. Keyes, R. J. Forster, P. M. Jayaweera, J. G. Vos and J. J. McGarvey, J. Chem. Soc. Dalton Trans. (1997) 1627.

[42] J. P. Cronin, T. J. Gudgel, S. R. Kennedy, A. Agrawal, D. R. Uhlmann. Materials Research, 2 (1999) 1

[43] G. A. Niklasson, C. G. Granqvist, J. Mater. Chem. 17 (2007) 127.

[44] P. J. Cragg. A Practical Guide to Supramolecular Chemistry, John Wiley & Sons, Ltd, Chichester, 2005.

[45] J.-M. Lehn. Angew. Chem. Int. Ed. Engl. 27 (1988) 90.

[46] J.-M. Lehn. Proc. Natl. Acad. Sci. U. S. A. 99 (2002) 4763.

[47] J. L. Atwood, J. W. Steed. Encyclopaedia of Supramolecular Chemistry. Taylor & Francis Group. Boca Raton, 2004.

[48] D. J. Cram. Angew. Chem. Int. Ed. Engl. 25 (1986) 1039.

[49] J. W. Steed, J. L. Atwood. Supramolecular Chemistry, John Wiley & Sons, Ltd, Chichester, 2000.

[50] C. J. Pederson. J. Am. Chem. Soc. 89 (1967) 7017.

[51] Cation Binding by Macrocycles, Y. Inoue, G. W. Gokel. Eds., Marcel Dekker, New York, 1990 p 762.

[52] G. W. Gokel. Crown Ethers and Cryptands, The Royal Society of Chemistry, London, 1991 p 190.

[53] Comprehensive Supramolecular Chemistry, G. W. Gokel. Eds., Pergamon Press: Oxford, 1996 p 787.

[54] H. M. Colquhoun, J. F. Stoddart. J. Chem. Soc. Chem. Commun. (1981) 612.

[55] H. M. Colquhoun, J. F. Stoddart, D. J. Williams. J. Chem. Soc. Dalton. Trans, (1983) 607.

[56] H. M. Colquhoun, J. F. Stoddart, D. J. Williams. Angew. Chem. Int. Ed. Engl. 25 (1986) 487.

[57] A. C. R. Villiers. Acad. Sci. Paris. 112 (1891) 536.

[58] F. Schardinger, Z. Unters. Nahrungs-Genussmittel Gebrauchsgegenstande. 6 (1903) 865.

[59] W. Saenger, J. Jacob, K. Gessler, T. Steiner, D. Hoffman, H. Sanbe, K. Koizumi, S. M. Smith, T. Tahaka. Chem. Rev. 98 (1998) 1787.

[60] R. Villalonga, R. Cao, A. Fragoso. Chem. Rev. 107 (2007) 3088.

[61] P. R. Sundarajan, V. S. R. Rao. Carbohydr. Res. 13 (1970) 351.

[62] V. G. Murphy, B. Zaslow, A. D. French. Biopolymers. 14 (1975) 1487.

[63] S. Li, W. C. Purdy. Chem. Rev. 92 (1992) 1457.

[64] J. Szejtli. Chem. Rev. 98 (1998) 1743.

[65] M. V. Rekharsky, Y. Inoue. Chem. Rev. 98 (1998) 1875.

[66] G. Wenz. Angew. Chem. Int. Ed. Engl. 33 (1994) 803.

[67] A. E. Kaifer. Acc. Chem. Res. 32 (1999) 62.

[68] F. Hapiot, S. Tilloy, E. Monflier. Chem. Rev. 106 (2006) 767.

[69] T. Matsue, D. H. Evens, T. Osa, N. Kobayashi. J. Am. Chem. Soc. 107 (1985) 3411.

[70] (a) R. Isnin, C. Salam, A. E. Kaifer. J. Org. Chem. 56 (1991) 35. (b) R. Isnin, A. E. Kaifer. J. Am. Chem. Soc. 113 (1991) 8188. (c) L. A. Godinez, S. Patel, C. M. Criss, A. E. Kaifer. J. Phys. Chem. 99 (1995) 17449. (d) B. Gonzalez, I. Cuadrado, B. Alonso, C. M. Casado, M. Moran, A. E. Kaifer. Organometallics. 21 (2002) 3544.

[71] A. Mirzoian, A. E. Kaifer. Chem. Eur. J. 3 (1997) 1052.

[72] Y. Wang, S. Mendoza, A. E. Kaifer. Inorg. Chem. 37 (1998) 317.

[73] A. E. Kaifer, M. Gomez-Kaifer. Supramolecular Electrochemistry. Wiley-VCH. Weinheim. 1999 p.191.

[74] A. Ulman. Chem. Rev. 96 (1996) 1533.

[75] H. Kuhn, A. Ulman. In Thin Films; A. Ulman. Ed. Academic Press. New York. 1995, Vol, 20.

[76] J. C. Love, L. A. Estroff, J. K. Kriebel, R. G. Nuzzo, G. M. Whitesides. Chem Rev. 105 (2005) 1103.

[77] (a) L. H. Dubois, R. G. Nuzzo. Ann. Rev. Phys. Chem. 43 (1992) 437. (b) G. M. Whitesides, P. E. Laibinis. Langmuir 6 (1990) 87.

[78] (a) M. Hasan, D. Bethell, M. Brust. J. Am. Chem. Soc. 124 (2002) 1132. (b) W. Andreoni, A. Curioni, H. Gronbeck. Int. Quantum. Chem. 80 (2000) 598. (c) J-G. Lee, J. Lee, J. T. Yates. J. Am. Chem. Soc. 126 (2004) 440.

[79] F. Arias, L. A. Godinez, S. R. Wilson, A. E. Kaifer, L. Echegoyen. J. Am. Chem. Soc. 118 (1996) 6086.

[80] Y. Miura, S. Kimura, Y. Imanishi, J. Umemura. Langmuir 14 (1998) 2761.

[81] C. Dietrich, L. Schmitt, R. Tampe. Proc. Natl. Acad. Sci. U. S. A. 92 (1995) 9014.

[82] A. Thess, S. Hutschenreiter, M. Hofmann, R. Tampe, W. Baumeister, R. Guckenberger. J. Biol. Chem. 277 (2002) 36321.

[83] A. Fragoso, J. Caballero, E. Almirall, R. Villalonga, R. Cao. Langmuir 18 (2002) 5051.

[84] J. Huskens, M. A. Deij. D. N. Reinhoudt. Angew. Chem. Int. Ed. 41 (2002) 4467.

[85] T. Auletta, B. Dordi, A. Mulder, A. Sartori, S. Onclin, C. M. Bruinink, M. Peter, C. A. Nijhuis, H. Beijleveld, H. Schonherr, G. J. Vancso, A. Casnati, R. Ungaro, B. J. Ravoo, J. Huskens, D. N. Reinboudt. Angew. Chem. Int. Ed. 43 (2004) 369.

[86] M. T. Rojas, R. Koniger, J. F. Stoddart, A. E. Kaifer. J. Am. Chem. Soc. 117 (1995) 336.

[87] (a) G. Nelles, M. Weisser, R. Back, P. Wohlfart, G. Wenz, S. Muttler-Neher. J. Am. Chem. Soc. 118 (1996) 5039. (b) M. Weisser, G. Nelles, P. Wohlfart, G. Wenz, S. Muttler-Neher. J. Phys. Chem. 100 (1996) 17893. (c) M. Weisser, G. Nelles, G. Wenz, S. Muttler-Neher. Sens. Actuators. B 38 (1997) 58.

[88] (a) C. Henke, C. Steinem, A. Janshoff, G. Steffan, H. Luftmann, M. Sieber, H. J. Galla. Anal. Chem. 68 (1996) 3158. (b) A. Michalke, A. Janshoff, C. Steinem, C. Henke, M. Sieber, H. J. Galla. Anal. Chem. 71 (1999) 2528. (c) A. Janshoff, C. Steinem, A. Michalke, C. Henke, H. J. Galla. Sens. Actuators. B 70 (2000) 243.

[89] Y. Maeda, T. Fukuda, H. Yamamoto, H. Kitano. Langmuir 13 (1997) 4187.

[90] H. Kitano, Y. Taira, H. Yamamoto. Anal. Chem. 72 (2000) 2976.

[91] H. Endo, T. Nakaji-Hirabayashi, S. Morokoshi, M. Gemmei-Ide, H. Kitano. Langmuir 21 (2005) 1314.

[92] M. W. J. Beulen, J. Bugler, B. Lammerink, F. A. J. Geurts, E. Biemond, K. G. C. Van Leerdam, F. Van Veggel, J. F. J. Engbersen, D. N. Reinhoudt. Langmuir 14 (1998) 6424.

[93] M. W. J. Beulen, J. Bugler, M. R. De Jong, B. Lammerink, J. Huskens, H. Schonherr, G. J. Vancso, B. A. Boukamp, H. Wieder, A. Offenhauser, W. Knoll, F. Van Veggel, D. N. Reinhoudt. Chem-Eur. J. 6 (2000) 1176.

[94] H. Schonherr, M. W. J. Beulen, J. Bugler, J. Huskens, F. Van Veggel, D. N. Reinhoudt, G. J. Vancso. J. Am. Chem. Soc. 122 (2000) 4963.

[95] S. Zapotoczny, T. Auletta, M. R. De Jong, H. Schonherr, J. Huskens, F. Van Veggel, D. N. Reinhoudt, G. J. Vancso. Langmuir 18 (2002) 6988.

[96] T. Auletta, M. R. De Jong, A. Mulder, F. Van Veggel, J. Huskens, D. N. Reinhoudt, S. Zuo, S. Zapotoczny, H. Schonherr, G. J. Vancso, L. Kuipers. J. Am. Chem. Soc. 126 (2004) 1577.

[97] C. T. Mallon, R. J. Forster, A. McNally, E. Campagnoli, Z. Pikramenou, T. E. Keyes. Langmuir 23 (2007) 6997.

[98] M-C. Daniel, D. Astruc. Chem. Rev. 104 (2004) 293.

[99] A. C. Templeton, W. P. Wuelfing, R. W. Murray. Acc. Chem. Res. 33 (2000) 27.

[100] M. Giersig, P. Mulvaney. Langmuir 9 (1993) 3408.

[101] M. Brust, M. Walker, D. Bethell, D. J. Schiffrin, R. J. Whyman. J. Chem. Soc., Chem. Commun. (1994) 801.

[102] M. Brust, J. Fink, D. Bethell, D. J. Schiffrin, C. J. Keily. J. Chem. Soc., Chem. Commun. (1995) 1655.

[103] (a) M. J. Hostetler, S. J. Green, J. J. Stokes, R. W. Murray. J. Am. Chem. Soc. 118 (1996) 4212. (b) R.S. Ingram, M. J. Hostetler, R. W. Murray. J. Am. Chem. Soc. 119 (1997) 9175. (c) A. C. Templeton, M. J. Hostetler, C. T. Kraft, R. W. Murray. J. Am. Chem. Soc. 120 (1998) 1906. (d) M. J. Hostetler, A. C. Templeton, R. W. Muarry. Langmuir 15 (1999) 3782.

[104] A. Labande, J. Ruiz, D. Astruc. J. Am. Chem. Soc. 124 (2002) 1782.

[105] L. Sun, R. M. crooks, V. Chechik. J. Chem. Soc., Chem. Commun. (2001) 359.

[106] J. L. Brennan, M. R. Branham, J. F. Hicks, A. J. Osisek, R. L. Donkers, D. G. Georganopoulou, R. W. Murray. Anal. Chem. 76 (2004) 5611.

[107] R. W. Murray. Chem. Rev. 108 (2008) 2688.

[108] F. P. Zamborini, J. F. Hicks, R. W. Murray. J. Am. Chem. Soc. 122 (2000) 4514.

[109] J. F. Hicks, F. P. Zamborini, A. J. Osisek, R. W. Murray. J. Am. Chem. Soc. 123 (2001) 7048.

[110] S. Chen, R. Pei, T. Zhao, D. J. Dyer. J. Phys. Chem. B 106 (2002) 1903.

[111] N. Fishelson, I. shkrob, O. Lev, J. Gun, A. D. Modestov. Langmuir 17 (2001) 403.

[112] (a) W. P. Wuelfing, S. J. Green, J. J. Pietron, D. E. Cliffel, R. W. Murray. J. Am. Chem. Soc. 122 (2002) 11465. (b) W. P. Wuelfing, R. W. Murray. J. Phys. Chem. B 106 (2002) 3139.

[113] A. B. Descalzo, R. M-Manez, F. Sancenon, K. Hoffmann, K. Rurack. Angew. Chem. Int. Ed. 45 (2006) 5924.

[114] J. Liu, J. Alvarez, W. Ong, A. E. Kaifer. Nano. Lett. 1 (2001) 57.

[115] O. Crespo-Biel, B. Dordi, D. N. Reinhoudt, J. Huskens. J. Am. Chem. Soc. 127 (2005) 7594.

CHAPTER 2

Synthesis and Characterisation of Novel Three Colour Electrochromic Metallopolymer Based on a Ruthenium Phenolate Complex Bound to Poly(4-vinyl)Pyridine

2.1 INTRODUCTION

Electrochromism generates different colours by switching between reduction state (gain of electrons) and oxidation state (loss of electrons), on passage of electrical current after application of an appropriate electrode potential [1,2,3]. The colour change can be between a transparent (‘bleached’) state and a coloured state, between two coloured states, or more than two colour states. Interest in electrochromic materials from both academia and industry has continued for several decades because of their fundamental spectroelectrochemical properties and their commercial applications [1]. As a class of electrochromic materials, metallopolymers incorporating transition metal coordination complexes are potentially useful because of their intense coloration and redox reactivity [2,3]. Chromophoric properties typically arise from low-energy metal-to-ligand charge transfer (MLCT), intervalence CT, intraligand excitation and related visible region electronic transitions, because these transitions involve valence electrons, the chromophoric characteristics of metallopolymers are altered or eliminated upon oxidation or reduction of the complexes [1,4,5,6]. Also, metallopolymers have been widely used to check chemically modified electrodes [7,8,9], which play important roles in the preparation of chemical sensors [10] because of their highly localized electrochemical activity.

In particular, Ruthenium- O^- coordinated quinoid ligands containing complexes and their metallopolymers are of interest because the phenolate moieties are noninnocent and show possess strong charge-transfer transitions in the visible and NIR spectral regions [11,12,13]. As strong σ donors, phenolate bonds are capable of increasing the electron density at the metal site of Ru (II) complexes. This increased electron density reduces the oxidation potential of the metal centre which is attractive for low-power/voltage applications and extends the visible absorbance range of the material by making ILCT transitions possible [11].

Here, metallopolymer was produced by coordinating $[Ru(bpy)_2]^{2+}$ to the conjugated polymer backbones, where bpy is 2,2 bipyridyl. The conjugated polymers used as backbones are of interest due to their non-linear optical behaviour, electronic conductivity and exceptional mechanical properties [14,15]. Two polymer backbones containing the phenol ligands, poly([1,7-dihydrobenzo bismidazol-2,6-diyl]-2,5-[1,4-

digydroxyphenylene]) and poly([1,7-digydrobenzo bismidazol-2,6-diyl]-2,5-[bydroxyphenylene]) (Chart 2.1), have been successfully synthesized by modifying a literature method developed for polymer without the phenol groups [16]. This method for the synthesis of polymer backbones is based on the procedure for synthesizing benzobisazole fragment (Scheme 2.1), using a condensation polymerisation reaction between tetraminobenzene tetrahydrochloride (TBA 4HCl)) and (di)hydroxyterephthalic acid in polyphosphoric acid (PPA) and P_2O_5 to remove water released by condensation reaction.

One of the major barriers of functionalising these polymer backbones with Ru polypyridyl complexes is their insolubility in common organic solvents. The insolubility of these polymers is due to their rigid-rod structures rather than to their high molecular weight since even low molecular weight structural analogues or model compounds are equally insoluble [17]. However, they are soluble in strong concentrated acid, such as methanesulfonic acid (MSA), trifluoroacetic acid (TFA), and formic acid to form liquid-crystalline solution or in nitromethane/$AlCl_3$ mixture to form the highly polarized polymer/Lewis acid complex [18]. The disadvantages of using these strong acidic solvents or solvent systems include their highly corrosive nature, the difficulty in volatility and the strong protonation of the polymer [17,18]. This final feature is a significant issue since protonation can block the formation of the Ru-phenolate bound.

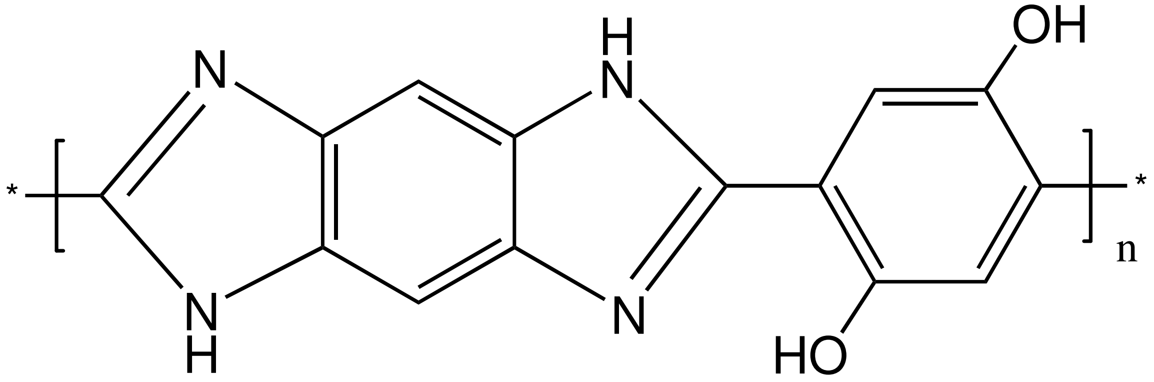

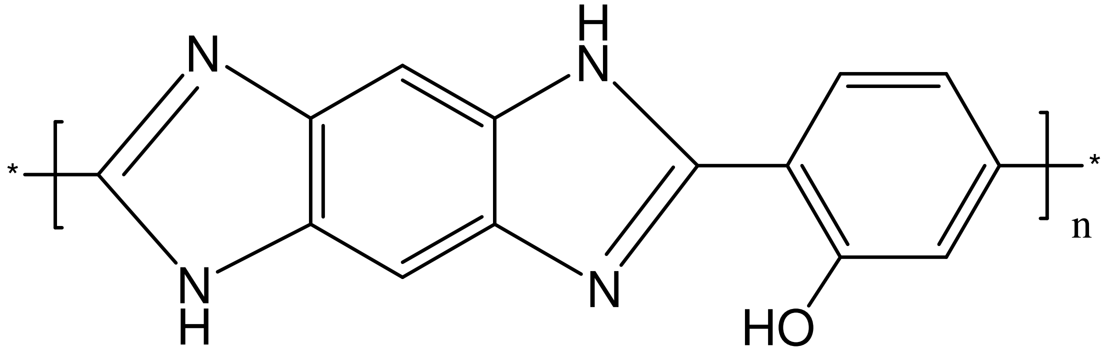

Chart 2.1. Structures of the conjugated polymer backbones, poly([1,7-dihydrobenzo bismidazol-2,6-diyl]-2,5-[1,4-digydroxyphenylene]) and poly([1,7-digydrobenzo bismidazol-2,6-diyl]-2,5-[bydroxyphenylene]).

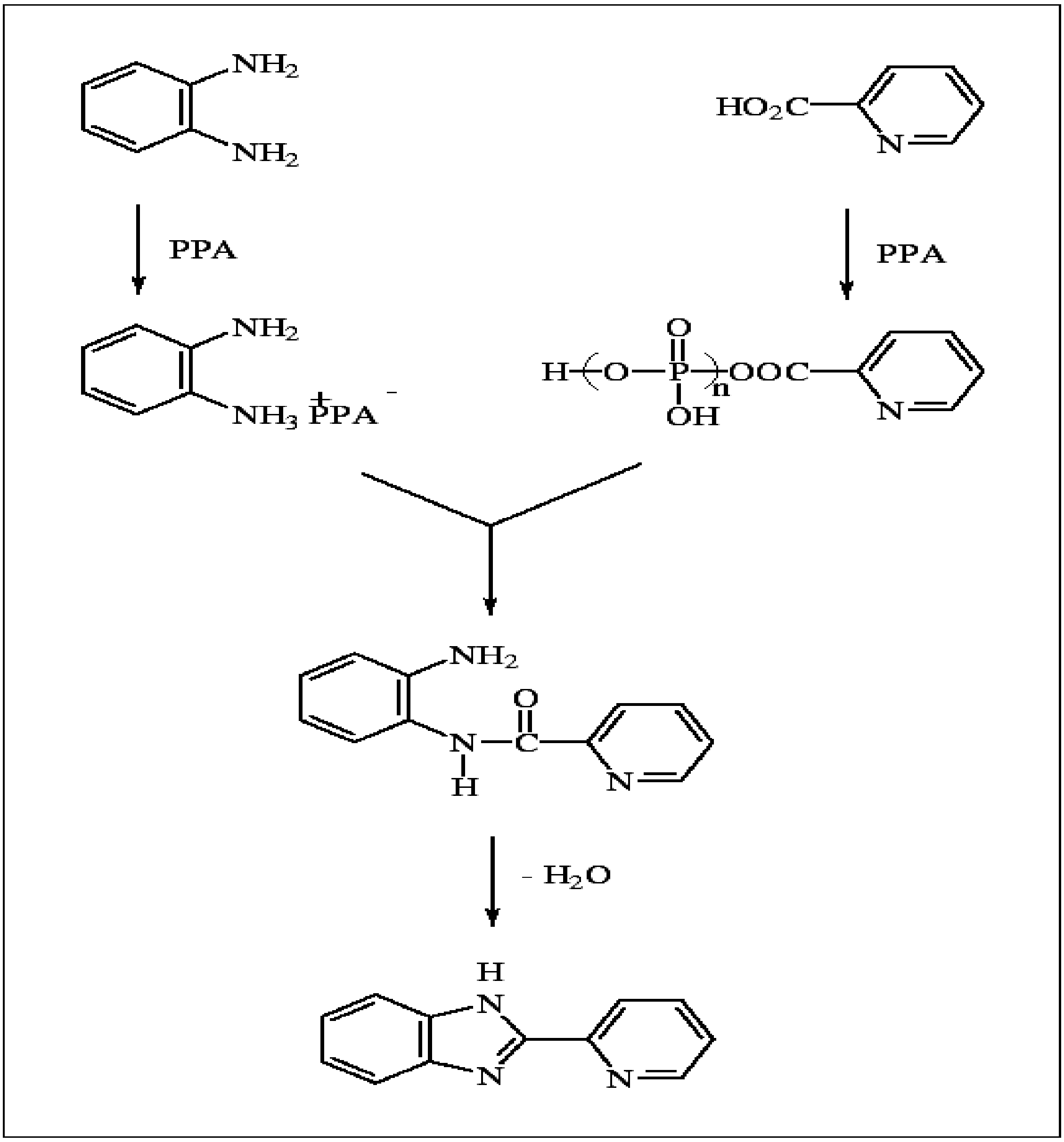

Scheme 2.1. The formation of benzobisazole fragment. From ref [16]: C. G. Cameron, T. J. Pittman, P. G. Pickup. J. Phys. Chem. B 105 (2001) 8838.

In contrast to conjugated polymers, which display significant conductivity over a relatively wide potential range, redox polymers are characterized by the presence of specific spatially and electrostatically isolated electrochemically active sites. Electroactivity in the redox polymer is highly localized with respect to voltage. A redox polymer consists of a redox active transition metal based pendant group, which is covalently bound to a polymer backbone.

In this chapter, a novel metallopolymer, [Ru(terpy)(box)PVP$_{20}$]PF$_6$, is reported that incorporates a Ru metal centre that is O, N coordinated to a phenolate donor ligand, terpy is $2,2^{\prime}:6^{\prime},2^{\prime\prime}$-terpyridine, box is 2-(2-hydroxyphenyl)benzoxazole, and PVP is poly(4-vinylpyridine) in which one in every twenty of the monomer units is labelled with the Ru(terpy)(box). The structures of the complex and metallopolymer are shown in Chart 2.2 and 2.3. Metallopolymers based on pre-formed redox polymer backbones offer the advantage of synthetic flexibility [19] and ease of characterisation. Moreover, by controlling the ruthenium loading the extent of interaction between the centres can be systematically varied so as to tune the optical and electrochromic properties [10,20]. The metallopolymer exhibits a range of charge transfer transitions that generate electrochromic responses in the visible and NIR regions. The combination of colour changes, i.e., one that can be read visually and another that requires instrumentation, is particularly attractive for diverse applications ranging from security to monitoring packaging integrity in foods and pharmaceuticals. Detailed spectroscopic and electrochemical characterisation of these materials, are presented and resonance Raman spectroscopy is exploited to identify the nature of the optical transitions.

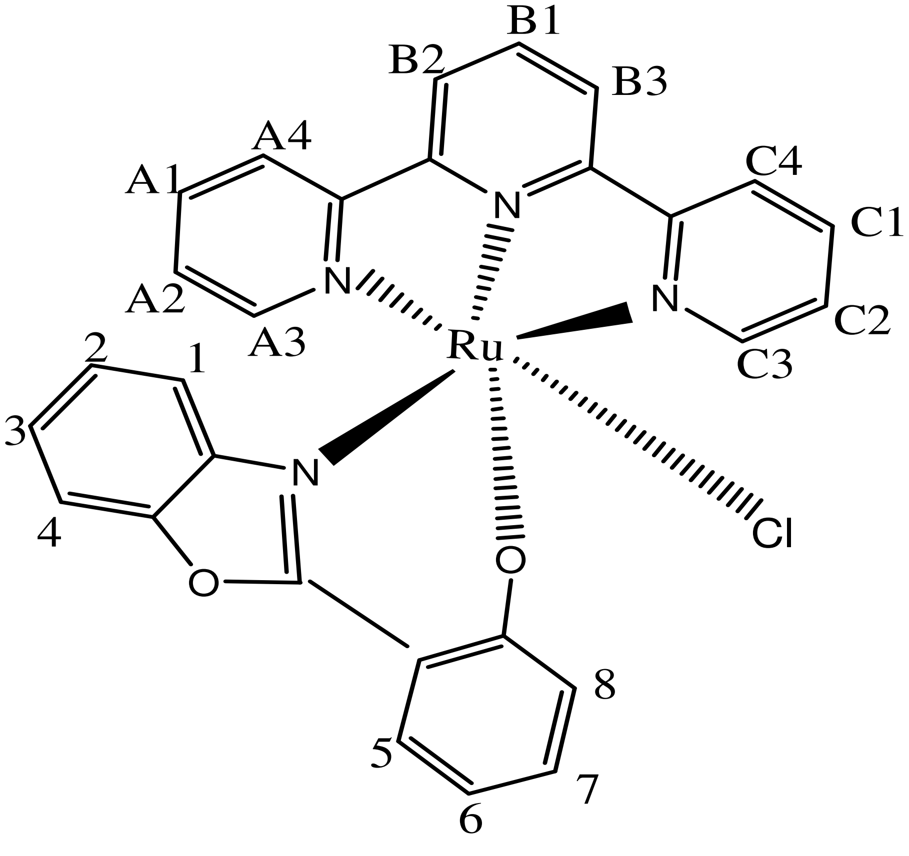

Chart 2.2. Structure of the monomeric [Ru(terpy)(box)Cl] complex illustrating the numbering scheme for ^{1}H NMR.

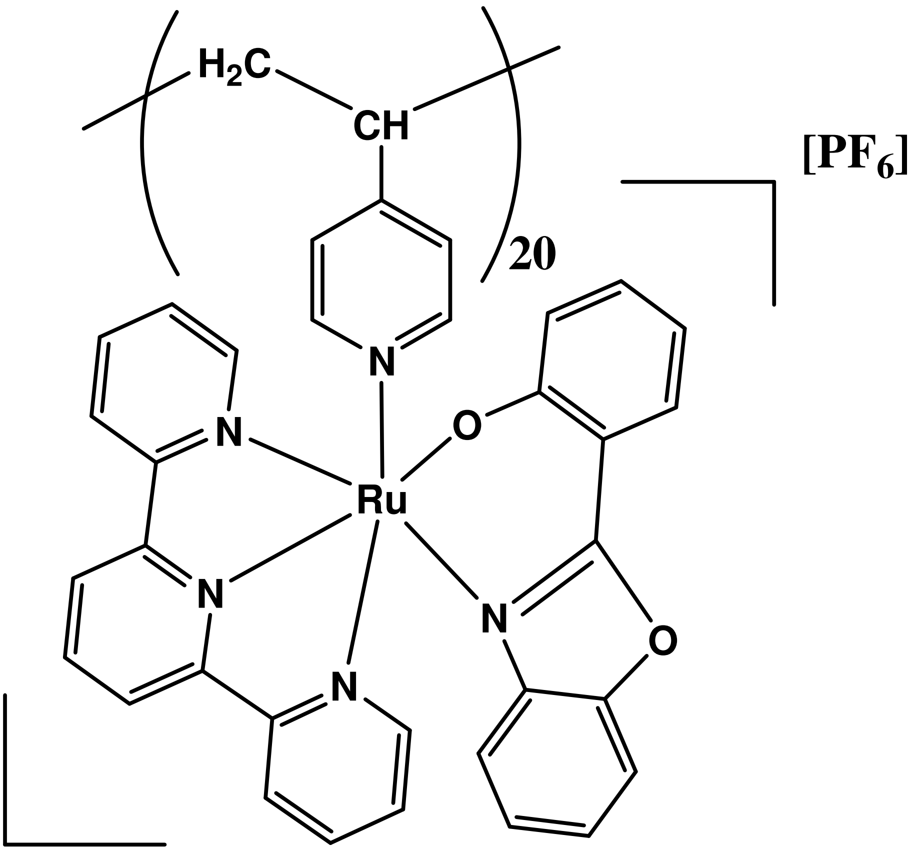

Chart 2.3. Structure of [Ru(terpy)(box)PVP$_{20}$][PF$_6$] metallopolymer.

2.2 EXPERIMENTAL

2.2.1 Materials and Methods.

All reagents used in synthesis were analytical grade. For absorption and emission spectroscopy, DMF used as solvent was spectroscopic grade. For solution phase electrochemistry, anhydrous DMF was used as the solvent. Water was purified using a Milli-Qplus 185 Millipore system. Chemicals purchased from Aldrich were used as received.

2.2.1.1 Synthesis of [Ru(terpy)Cl_3].

The preparation of this material is based on the literature procedure [21,22]. Terpyridine (1.17 g, 5 mmol) and $RuCl_3•3H_2O$ (1.31 g, 5 mmol) were added to 500 ml absolute ethanol and the solution was heated at reflux for 3 h with stirring. After this time the mixture was cooled to room temperature, the brown precipitate was filtered, washed with ethanol and ether, and air-dried (yield 1.64 g, 76%).

2.2.1.2 Synthesis of [Ru(terpy)(box)Cl].

A quantity (0.1324g, 0.3mmol) of Ru(terpy)Cl_3 was dissolved in ethanol/water (3:1 v/v, 30ml) containing triethylamine (15%, v/v), and 0.0693g of LiCl by warming. This solution was deoxygenated with argon and heated to reflux. A solution of the box ligand (0.0640g, 0.3mmol) in ethanol/water (3:1 v/v, 30ml) (15% TEA) was added slowly over 20min. The mixture was heated under reflux in an argon environment for 4 h. After which time, the mixture was reduced to half volume and allowed to stand for a few hours. Then the mixture was filtered and the brown red solid collected. The product was recrystallized twice from ethanol (Yield 36.20%).

Anal. Calcd for [Ru(terpy)(box)Cl], $RuC_{28}H_{19}N_4O_2Cl$: C, 57.93; H, 3.28; N, 9.66. Found: C, 57.38; H, 3.47; N, 9.26.

^{1}H NMR (400 MHz, DMSO-d) numbering scheme shown in Chart 2.3: H^{B2}, H^{B3}, 8.64-8.66 (d, 2H); H^{A3}, H^{A4}, H^{C3}, H^{C4}, 8.54-8.59 (m, 4H); H^{A2}, H^{C2}, 7.94-7.96 (m, 2H); H^{B1}, 7.86-7.92 (m, 1H); H^8, 7.73-7.75 (d, 1H); H^{A1}, H^{C1}, 7.60-7.63 (m, 2H); H^1, H^6, 7.37-7.43 (m, 2H); H^5, 7.26-7.28 (d, 1H); H^2 6.97-7.01 (m, 1H); H^3 6.71-6.77 (m, 1H); H^7 6.48-6,52 (m, 1H); H^4 5.44-5.46 (d, 1H).

ES MS m/z (calc): 580 (580, [M]), 545 (545, $[M\text{-}Cl]^+$).

2.2.1.3 Synthesis of [Ru(terpy)(box)PVP_{20}][PF_6].

[Ru(terpy)(box)Cl] complex (0.3mmol) and poly(4-vinylpyridine) (PVP) (6 mmol monomer) were heated in ethanol under reflux for 5 days. Then the solution was reduced in to 1/3 volume. 10ml of saturated aqueous NH_4PF_6 were added to the solution, and the resulting dark red solid were collected by filtration.

2.2.2 Instrumentation.

2.2.2.1 Nuclear Magnetic Resonance (NMR) Spectroscopy.

^{1}H-NMR and COSY spectra were obtained using a 400 MHz Bruker NMR instrument. Deuteriated d_8-dimethylsulfoxide (d_8-DMSO) used as solvents was supplied from Sigma-Aldrich.

2.2.2.2 Mass Spectroscopy.

Mass spectra were obtained by using a Bruker LC/MS Esquire Series mass spectrometer. Spectra were collected by constant infusion of the analyte dissolved in ethanol.

2.2.2.3 Elemental Analysis.

Elemental analysis for carbon, hydrogen and nitrogen was performed at University College Dublin (UCD) microanalytical laboratories.

2.2.2.4 Absorption Spectroscopy.

UV/Vis spectra were carried out on a Shimadzu UV-3100 spectrophotometer in a 1 cm quartz cuvette.

2.2.2.5 Emission Spectroscopy.

Emission spectra were obtained by a Cary Eclipse luminescence spectrometer at room temperature or a Perkin Elmer LS50 luminescence spectrometer at 77 K.

2.2.2.6 Solution Phase Electrochemistry.

Cyclic voltammetry (CV) was carried out using a CH instruments Model 660a electrochemical workstation for solution phase. In these experiments, a traditional 3-electrodes cell was used. A 3mm glassy carbon electrode was used as the working electrode with a platinum macroelectrode acting as counter electrode. The reference electrode used in these measurements was an Ag/Ag^+ non-aqueous electrode and purchased from CH instrument. This reference electrode consists of a Teflon cap with a Ag wire, a glass tubing, and a porous glass tip sealed to the glass tubing with Teflon heat shrinkable tubing. The glass tubing is filled with 10 mM $AgNO_3$ and 0.1 M $TBAFB_4$ (tetraethylammonlum tetrafluoroborate) in ACN. All electrolyte solutions were deoxygenated for at least 15 min using N_2. During the experiments, a blanket of N_2 gas was kept over the electrolyte solution. Glassy carbon working electrodes were polished successively with 1.0, 0.3, and 0.05 μm alumina powder and sonicated in distilled water for 5 min and rinsed with acetone after each step.

2.2.2.7 Spectroelectrochemistry.

Spectroelectrochemistry was carried out in a spectroelectrochemical cell (1 mm), using a platinum gauze as working electrode, an Ag/AgCl non-aqueous quasi-reference electrode and a platinum wire as auxiliary electrode. The electrolyte used was 0.1 M $TBAFB_4$ (tetraethylammonlum tetrafluoroborate) in DMF and the UV/Visible/NIR spectra were recorded using the Shimadzu 3100 UV/NIR spectrometer. The working electrode was held at the required potential for 2 min before the first scan. During the spectral scan, a CH instrument Model 660a electrochemical workstation was used as the potentiostat.

2.2.2.8 Raman Spectroscopy.

Raman spectroscopy was obtained on a Dilor. Jobinyvon. Spex Labram. Argon ion laser was used as source for excitation at 488 nm. Helium-Neon laser was used for excitation at 632.8 nm. As well as, a Ti-sapphire laser pumped by an Argon ion laser was available for excitation at 785 nm. A backscattering geometry was used to collect scattered light by using an air cooled CCD array by one of two interchangeable gratings, 1800 lines/mm, which was used for 488 nm and 632.8 nm excitation with a spectral resolution of 1.5 cm^{-1} per pixel, or 600 lines/mm, which was employed for 785 nm excitation. Before use, the wavenumber axis of the Raman was calibrated with the silicon line at 521 cm^{-1}.

2.3 RESULTS AND DISCUSSION

2.3.1 Synthesis and Structural Characterisation

The complex, [Ru(terpy)(box)Cl], was synthesized according to standard techniques. In order to deprotonate the phenolate site to permit coordination of O, N-bound Ru complexes, it is essential to conduct the synthesis in a high pH environment. Triethylamine was used as both a reducing agent and to adjust the pH, e.g. it reduced Ru (III) to Ru (II) and achieved a pH of approximately 12.

The complex is diamagnetic under ambient conditions and sharp well-defined ^{1}H NMR resonances are observed and shown in Figure 2.1. A singlet peak was observed at 11.23 ppm for the phenolate site in free box ligand. However, this singlet peak was not present in the Ru complex. It suggests that the deprotonated hydroxyl remains in the complex. As shown in Figure 2.2, a complete assignment of NMR resonance is achieved for the complex using a combination of COSY 45 techniques, in which centre spectrum shows cross peaks with the signals of both of its neighbours. Coordination of the $[Ru(terpy)]^{2+}$ unit shifts the resonances observed for the free box ligand. For the coordinated site, the doublet H^8, adjacent to the coordinated phenolate O^- observed at 8.06 ppm in free box ligand shifts upfield by 0.32 to 7.74 ppm on coordination. The H^1, adjacent to the coordinated nitrogen in the box ligand, shifts by -0.44 ppm to 7.43 ppm. Also structural characterisation of the complex was conducted using elemental analysis and mass spectrometry. The molecular weight obtained from mass spectrometry is indistinguishable from the anticipated value. The mass spectrum also showed isotopic pattern expected for a Ru complex. This also suggests that the phenolate site in the box ligand was deprotonated and coordinated with $[Ru(terpy)]^{2+}$ unit to form the new complex.

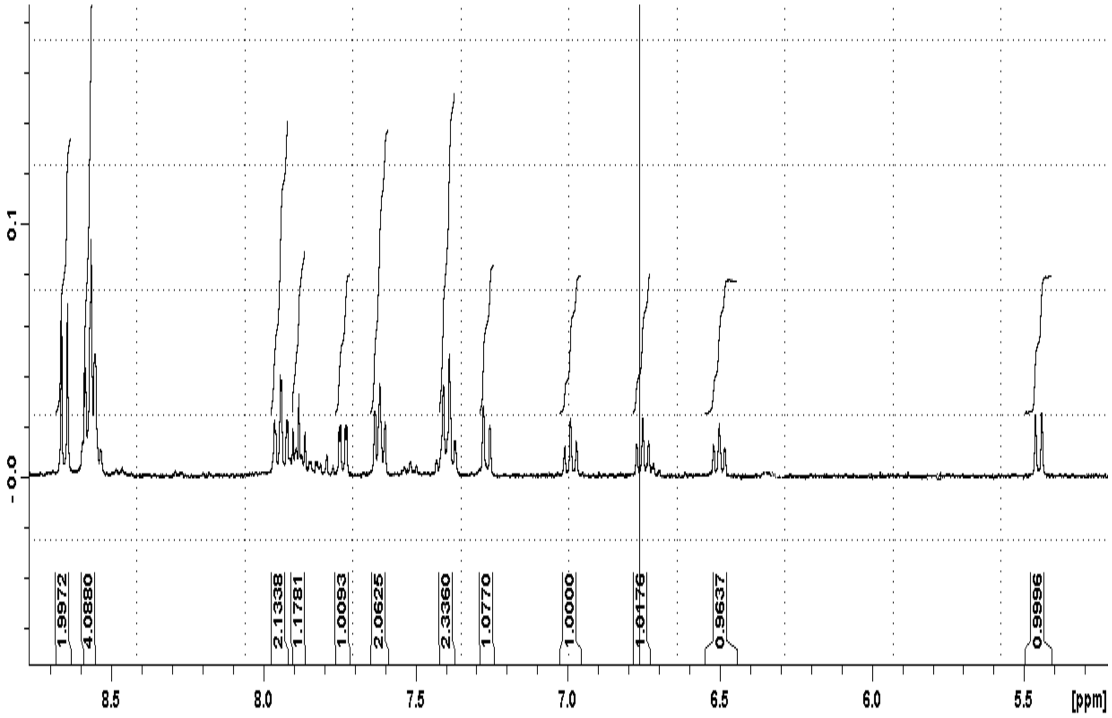

Figure 2.1. ^{1}H NMR spectrum of [Ru(terpy)(box)Cl] complex in d_6-DMSO.

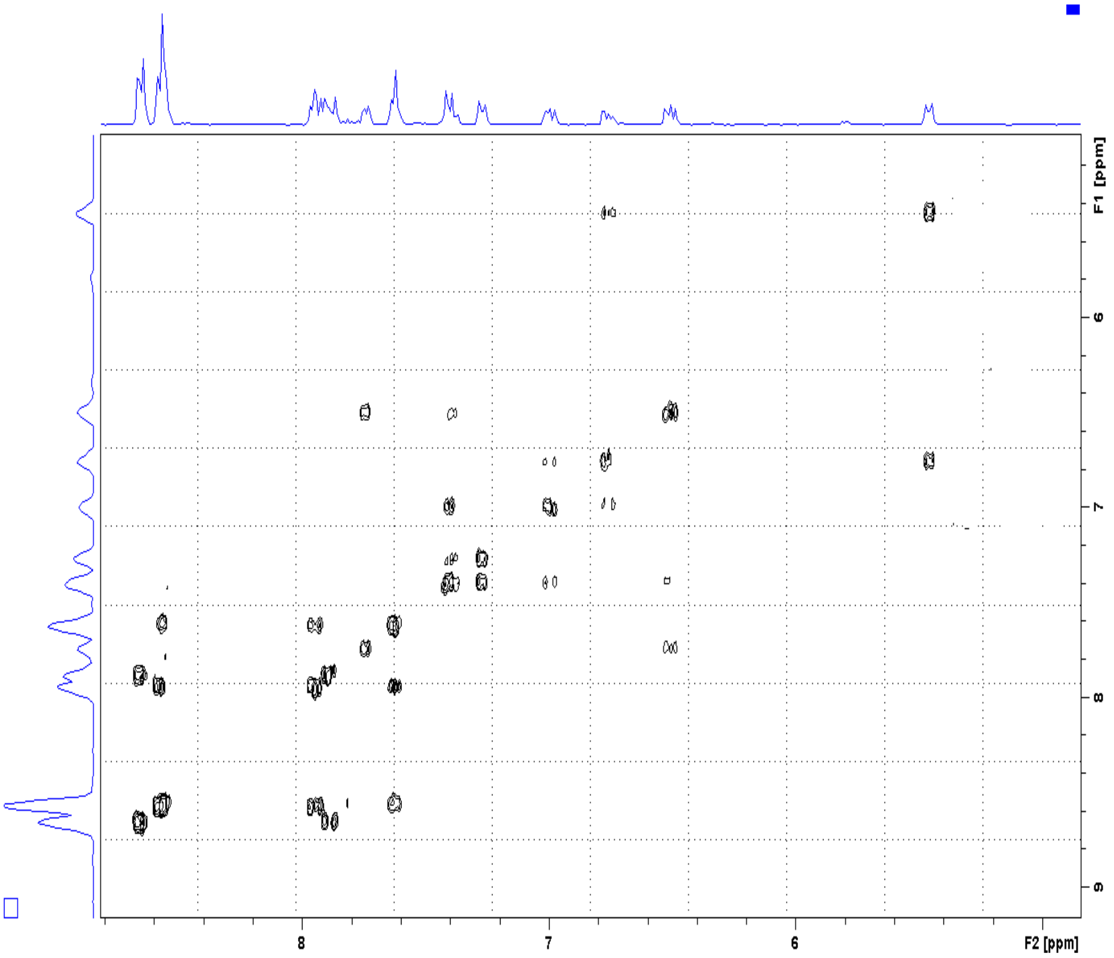

Figure 2.2. COSY 45^{o} ^{1}H NMR spectrum of [Ru(terpy)(box)Cl] complex in d_6-DMSO.

2.3.2 Absorption and Emission Spectroscopy

Electronic spectroscopy is useful for characterizing ruthenium complexes and ruthenium-containing polymers due to the rich spectroscopy of such materials. The electronic transition of metal-to-ligand charge-transfer bands (MLCT) observed in the visible region is determined by the energy of metal $d_{(t_{2g})}$ orbital and modified by the σ-donor ability of the ligand, while the excited state responsible for the emission is typically derived from the lowest metal-to-ligand based triplet excited state (^{3}MLCT). The visible absorption and the low temperature emission data are shown for monomer and polymer in Table 1.

[Ru(terpy)(box)Cl] exhibits a λ_{max} absorbance around 518 nm, and a shoulder centred around 588 nm. This main feature is ascribed to a metal to ligand charge transfer (MLCT) Ru (t_{2g}) to terpy (π^*) transition and the shoulder is associated with an interligand charge-transfer transition (ILCT) π (box) to π^* (terpy). This behaviour has been reported previously in hydroquinone and box ligand bound Ru(bpy) complexes [11,12,13]. The analogous features in the [Ru(terpy)(box)PVP_{20}][PF_6] are observed around 480 nm for MLCT and a shoulder evident around 550 nm for ILCT.

For [Ru(terpy)(box)Cl] complex and [Ru(terpy)(box)$PVP_{20}]^-$ metallopolymer, since minor changes in the ligand field around the metal does not affect the energy of the π^* orbitals of terpy acceptor ligand and box ligand, the wavelength of the MLCT is determined by the energy of the metal $d(t_{2g})$ orbitals, which is modified by the σ-donor ability of Cl^- ligand and pyridine ligand in PVP. The MLCT absorption wavelength shifts to higher energy, when the σ-donor ability of the ligand decreases. Compared to Cl^- ligand, the pyridine ligand in PVP has weaker σ-donor ability. This causes the MLCT in [Ru(terpy)(box)$PVP_{20}]^-$ metallopolymer to shift to shorter wavelength around 480 nm. For the ILCT transition, the wavelength has shifted to the blue for the same reason. Successful synthesis of the metallopolymer will be supported and confirmed by the resonance-Raman and electrochemical data in the following sections.

Luminescence was not detected in solution at room temperature for the Ru complex and metallopolymer. This agrees with observations from other terpy based Ru complexes because of their short ^{3}CT excited state lifetime due to efficient, thermally activated decay via a proximal ^{3}d-d state [23,24]. Luminescence was only observed at 77 K.

Table 2.1. Absorption and emission data of Ru-complex and Ru-containing polymer. The solvent in each case is DMF.

	Transition	Absorption wavelength	Emission wavelength (77 K)
[Ru(terpy)(box)Cl]	MLCT ILCT	518 nm, 588 nm	603 nm
[Ru(terpy)(box)PVP$_{20}$][PF$_6$]	MLCT ILCT	480 nm, 550 nm	613 nm

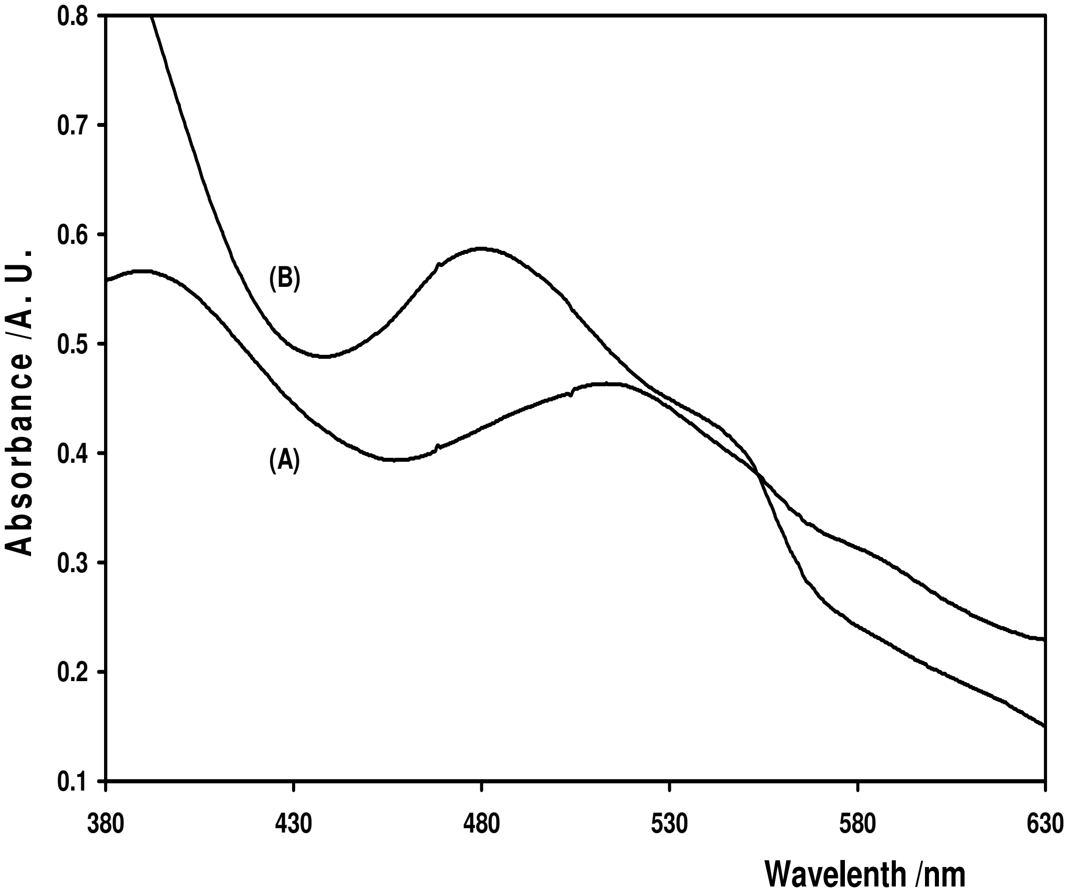

Figure 2.3. UV-vis absorption spectra of (A) 0.1 mM of [Ru(terpy)(box)Cl] complex and (B) 0.1 mM of Ru-containing PVP polymer in DMF.

2.3.3 Solution Phase Electrochemistry

Table 2 summarizes the electrochemical data from the model monomer and metallopolymer obtained in DMF containing 0.1 M $TBAFB_4$ (tetraethylammonlum tetrafluoroborate) on a 3 mm glassy carbon electrode at scan rate of 0.5 V/s. All potentials are versus Ag/AgCl reference electrode. Two oxidation processes are observed for [Ru(terpy)(box)Cl] complex, a reversible one-electron oxidation at around –0.101V and an irreversible one-electron oxidation at 0.743V. Two reversible one-electron reductions are obtained at –2.00 and –2.41V versus Ag/AgCl and are assigned to the reduction of the terpyridine moieties. As previously reported [11,12,13], in Ru-phenolate complexes, the first reversible oxidation process is attributed to the $Ru^{3+/2+}$ couple and the low oxidation potential is due to the strong σ donor ability of phenolate and chloride bonds, which increase the electron density at the metal site of Ru (II) complexes. The second irreversible process is associated with the phenolate oxidation on the basis of comparison with the electrochemistry of the free box ligand. The irreversible process is attributed to the decomposition of the electron poor Ru (III) – O (phenoxy) bond [11] and exhibits a tendency to adsorb onto the electrode surface.

Also, the $[Ru(terpy)(box)PVP_{20}][PF_6]$ metallopolymer exhibits similar oxidation processes to the complex. One reversible oxidation is obtained at 0.121 V and one irreversible oxidation is observed at 0.781 V. Based on the spectroelectrochemistry study in the following section, when the applied potential is held beyond the first oxidation, the main feature of Ru ($d\pi$) – terpy (π^*) MLCT transition around 480 nm is lost. This suggests that the first oxidation is Ru metal based. As shown in Figure 2.4, the oxidation potential of Ru couple in $[Ru(terpy)(box)PVP_{20}][PF_6]$ metallopolymer shifts in a positive potential direction. By comparison with ligand bound to Ru centre, this indicates that the redox potential shift of the Ru couple is dependent on the σ-donor properties of the coordinated ligands. The σ-donor ability of the pyridine ligand in PVP polymer backbone is much weaker than Cl^-. Coordination between metal site and pyridine decreases the energy of the Ru (t_{2g}) orbital and results in forcing the metal centre oxidation to higher potential.

Table 2.2. Solution phase electrochemistry data of Ru complex and Ru-containing metallopolymer in DMF containing 0.1 M $TBAFB_4$ at scan rate of 0.5 V/s.

	$E_{1/2}{}^{red}{}_{terpy}$	$E_{1/2}{}^{ox}{}_{Ru}{}^{+2/+3}$	$E^{ox}{}_{O^-}$
[Ru(terpy)(box)Cl]	-2.00V, -2.41V	-0.101V	0.743V
[Ru(terpy)(box)PVP_{20}][PF_6]	-1.70V, -2.10V	0.121V	0.781V

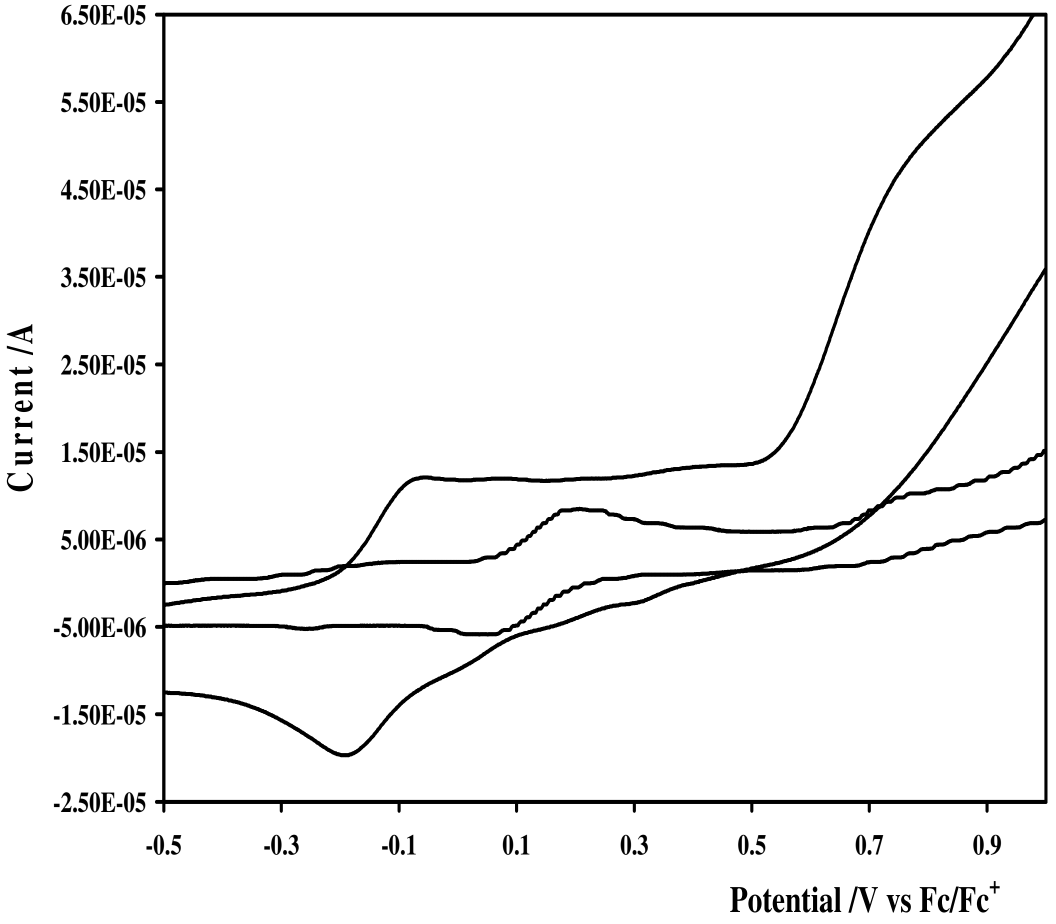

Figure 2.4. Cyclic voltammetry of (a) 0.1 mM of [Ru(terpy)(box)Cl] complex and (b) 0.1 mM of [Ru(terpy)(box)PVP$_{20}$][PF$_6$] metallopolymer conducted at scan rate of 0.5 V/s in DMF containing 0.1 M TBAFB$_4$ (tetraethylammonlum tetrafluoroborate) on a 3 mm glassy carbon electrode, potentials are versus non-aqueous Ag/AgCl reference electrode.

2.3.4 Spectroelectrochemistry

In systems with electrochemically active ligands, it is important to establish if the redox processes are metal or ligand based. In order to identify the electrochemical and optical changes, spectroelectrochemistry was carried out on the metallopolymer.

Figure 2.5 shows the changes in the absorbance spectrum of a solution of $[Ru(terpy)(box)PVP_{20}]PF_6$ following oxidation at +0.500 V. The spectrum of the reduced metallopolymer extends to over 1000 nm. As the metallopolymer is oxidised at 0.5 V vs. Ag/AgCl, which is beyond the first oxidation, the main feature of Ru (dπ) – terpy (π*) MLCT transition around 480 nm is gradually lost and the colour switches from wine red to light green (Figure 2.6). Also as shown in Figure 2.6, a red orange colour is also observed for mixed redox composition. This observation strongly suggests that the first reversible oxidation is Ru metal centre based. When Ru (II) is oxidized to Ru (III), a broad new feature grows in centred at 760 nm, which is considered to be an LMCT transition between phenolate and Ru(III) (dπ*). This transition arises because it becomes more facile to oxidise phenolate site in the oxidized metallopolymer than terpyridine. Significantly, this redox induced colour switching is fully reversible over several hundred cycles. As the potential is returned to 0 V, the original UV/vis spectrum of the reduced metallopolymer was is recovered gradually.

However, as shown in Figure 2.7, the LMCT transition is lost after oxidation at 1.5 V, which is beyond the most positive oxidation at 0.781V. It suggests that the most anodic oxidation is phenolate based and the phenolate is involved in the LMCT transition. The irreversibility of this process is most likely due to cleavage of the electron deficient Ru(III) – O(phenoxy) bond [11]. Application of 1.5 V does not result in any visible colour changes because the LMCT lies in the NIR region. However, this combination of a reversible colour change in the visible region and a second irreversible change that cannot be discerned by eye is useful for many practical applications.

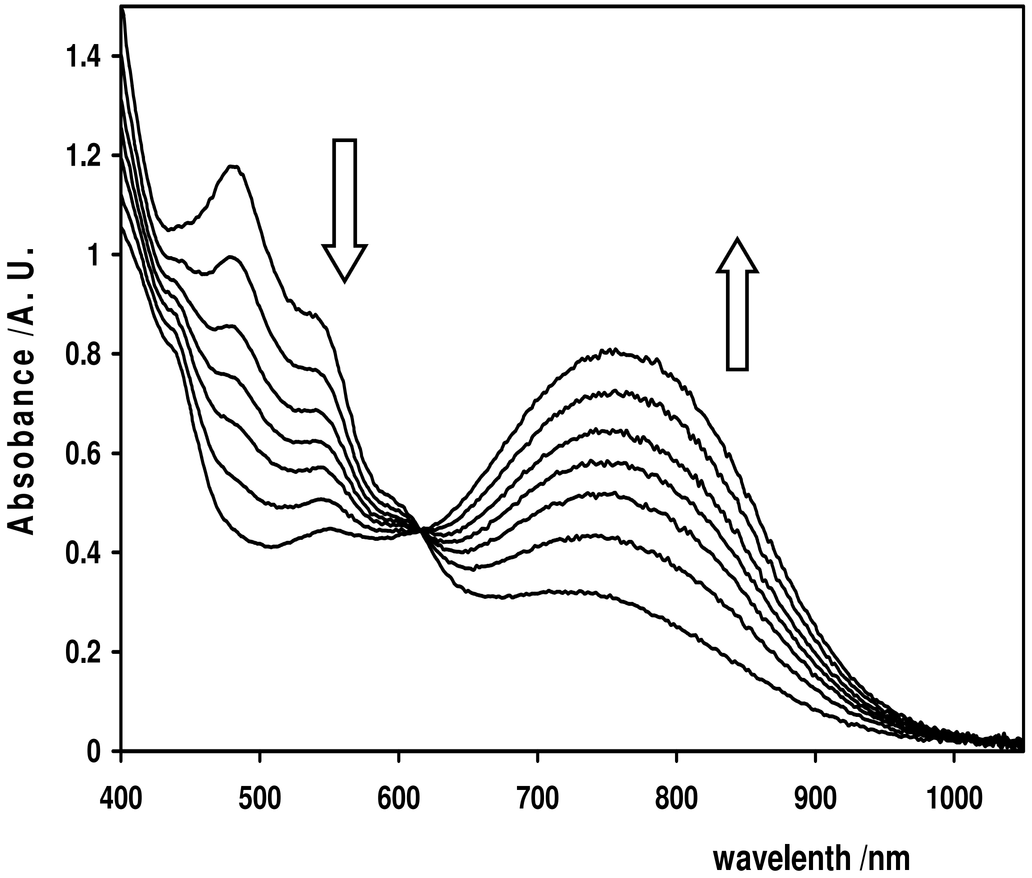

Figure 2.5. Time dependent changes in the visible and near infra-red region of the spectrum of 0.1 mM of [Ru(terpy)(box)PVP$_{20}$][PF$_6$] in DMF containing 0.1 M TBAFB$_4$ as supporting electrolyte following application of +0.500 V. Spectra were recorded at 2 min intervals.

Figure 2.6. Electrochromic properties of [Ru(terpy)(box)PVP_{20}][PF_6] when a potential +0.500 V is applied; from left to right: wine red (reduced state), red orange (mixed redox composition), and light green (metal oxidation).

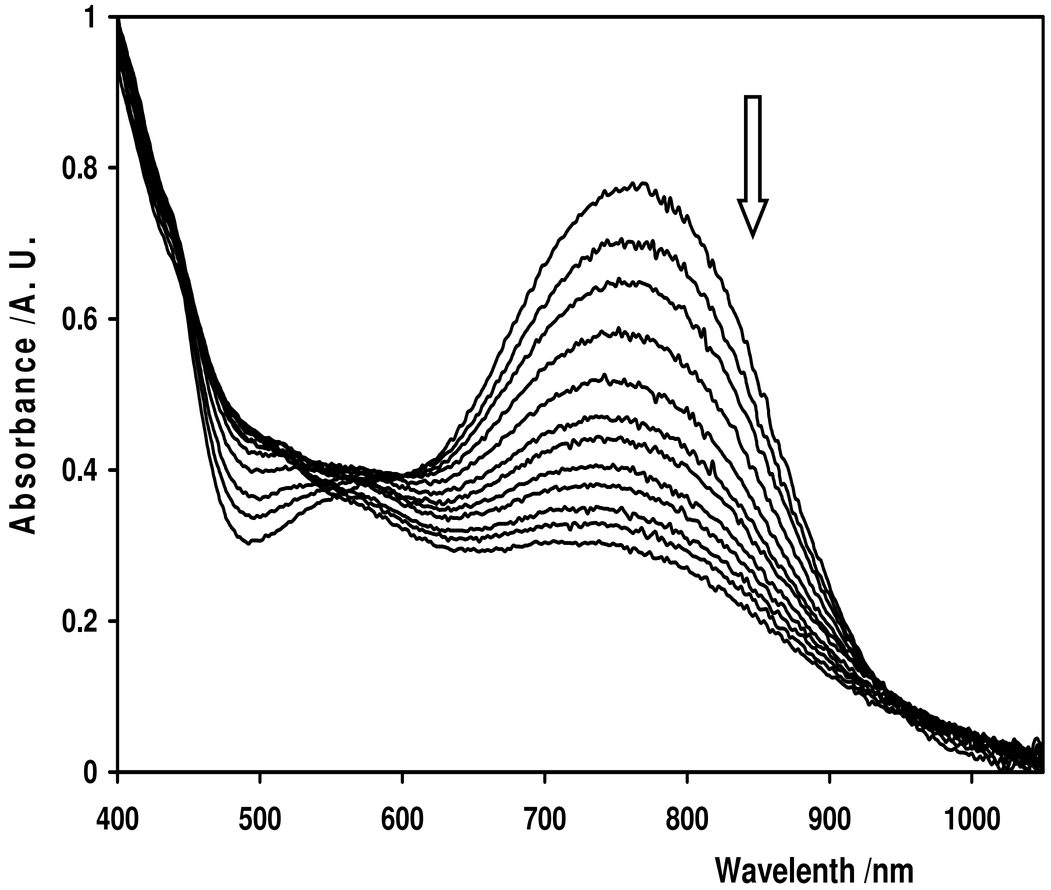

Figure 2.7. Time dependent changes in the near infra-red region of the spectrum of 0.1 mM of [Ru(terpy)(box)PVP_{20}][PF_6] dissolved in DMF containing 0.1 M $TBAFB_4$ as supporting electrolyte following application of +1.500 V. Spectra were recorded at 2 min. intervals.

2.3.5 Raman Spectroscopy

Raman spectroscopy is a very useful technique for investigating the optical transitions in ruthenium-polypyridyl complexes. To better understand the absorption features of the metallopolymer, and further substantiate the spectroelectrochemical data presented above, thin films of [Ru(terpy)(box)PVP_{20}][PF_6] were coated on a glassy carbon electrode and Raman experiments are carried out using excitation at 488 nm, 632.8 nm, and 785 nm.

Figure 2.8 shows the Raman spectra for [Ru(terpy)(box)PVP_{20}][PF_6] excited at 488 nm, which was used to investigate the MLCT absorption at around 480 nm. The features at 1601, 1541, 1484, 1328, 1251, 1187, 1165, 1021, 726, and 673 cm^{-1} are all characteristic of terpyridyl unit vibration [25] in a Ru (dπ) – terpy (π^*) MLCT transition and these features are similar to those bounds for bipyridyl units. In the low frequency end of the spectrum, a Ru-N stretching vibration is also observed at 385 cm^{-1} [26]. The feature at 1430 cm^{-1} is thought to arise from the box ligand because it is not observed in the Raman spectrum for Ru-terpy complexes in the absence of box ligand.

Excitation at 632.8 nm is post-resonant with the low-energy ILCT absorbance shoulder at around 550 nm. This excited wavelength was chosen to avoid the tail of the MLCT transition at 480 nm. As shown in Figure 2.9, although the contribution from the MLCT is minimal, some terpy-based vibration features at 1600, 1333, 1250, 1163, and 1025 cm^{-1} are still evident. The feature at 1431 cm^{-1} associated with quinoid ligand is present. In the low energy region, the feature at 677 cm^{-1} and new features at 652, 563, and 481 cm^{-1} are apparent. The former, obscured by the terpy feature at 673 cm^{-1} excited at 488 nm, is attributed to the box ligand and the latter features are associated with Ru-O and box [11]. The intensity of the Ru-N feature at 384 cm^{-1} is significantly reduced suggesting that the longer wavelength absorbance is associated with an inter/intra ligand charge-transfer transition involving the phenolate and terpyridyl units. Such behaviour has been reported previously in hydroquinone bound Ru(bpy) units [11,27].

Figure 2.10 shows the Raman spectrum excited at 785 nm. As described previously, oxidation of the Ru centre generates a new band around 760 nm, which is due to phenolate-to-$Ru_{(III)}$, LMCT, transition. The excitation at 785 nm is resonant with this feature. The terpy bands associated with the MLCT transition shown in Figure 2.7 are completely lost under these conditions. However, bands associated with the box ligand still remain. The bands at 1596, 1312, 1140, 1012, and 856 cm^{-1} are attributed to the box ligand C-C and ring stretch modes. The bands at 676, 650, and 561 cm^{-1} are attributed to Ru-O bridge coupled modes. Also, these three bands are comparable to those observed for resonance Raman of the ILCT. The band at 465 cm^{-1} is attributed to Ru-O (box) and the band at 380 cm^{-1} is attributed to Ru(III)-N. The shift of the latter band from 385 cm^{-1} for Ru(II) to 380 cm^{-1} for Ru(III) is consistent with oxidation of the metal. All features observed using 785 nm excitation indicate that the metal is participating in the electronic transition. No terpy-based vibration evidence was found in this transition. Therefore, it strongly indicates that the transition at 760 nm is attributed to phenolate (π) to $Ru_{(III)}$ ($d\pi$).

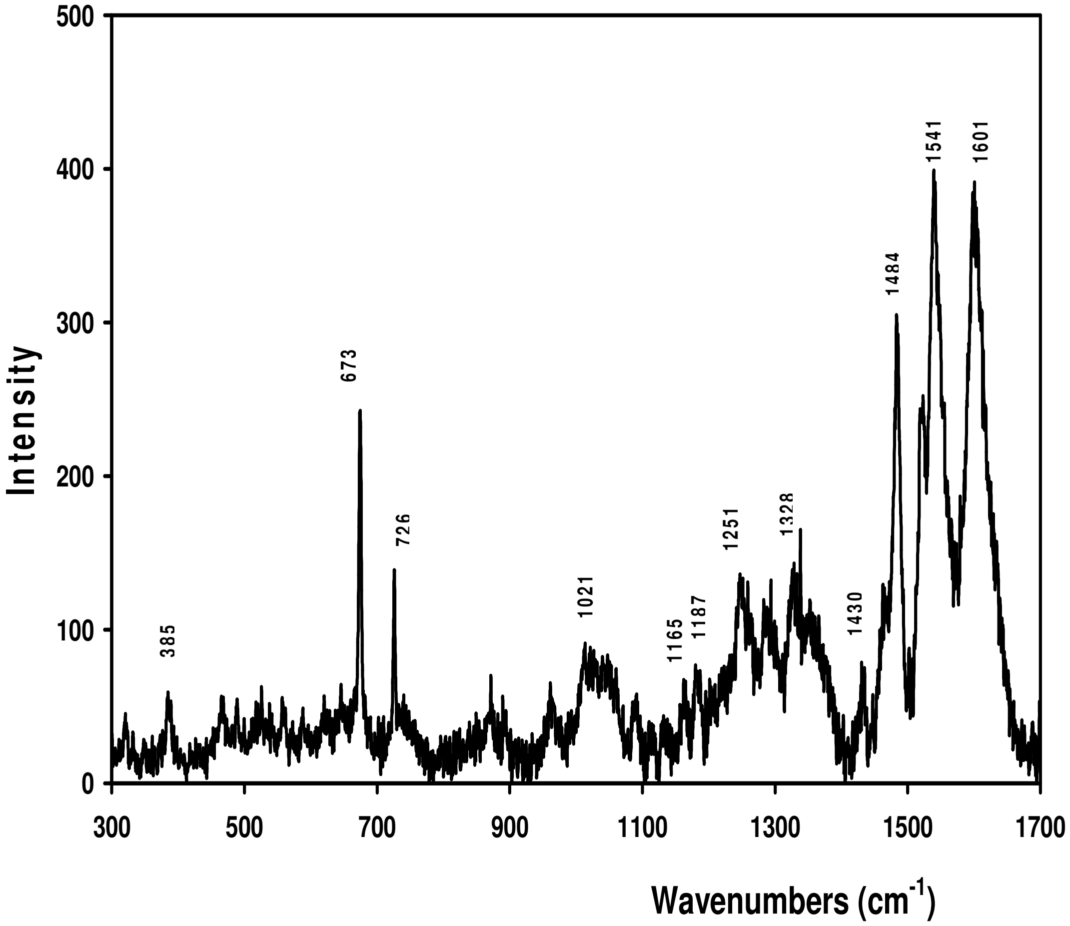

Figure 2.8. Resonance Raman spectra of dry [Ru(terpy)(box)PVP$_{20}$][PF$_6$] metallopolymer film coated on 3 mm glassy carbon electrode excited at 488 nm.

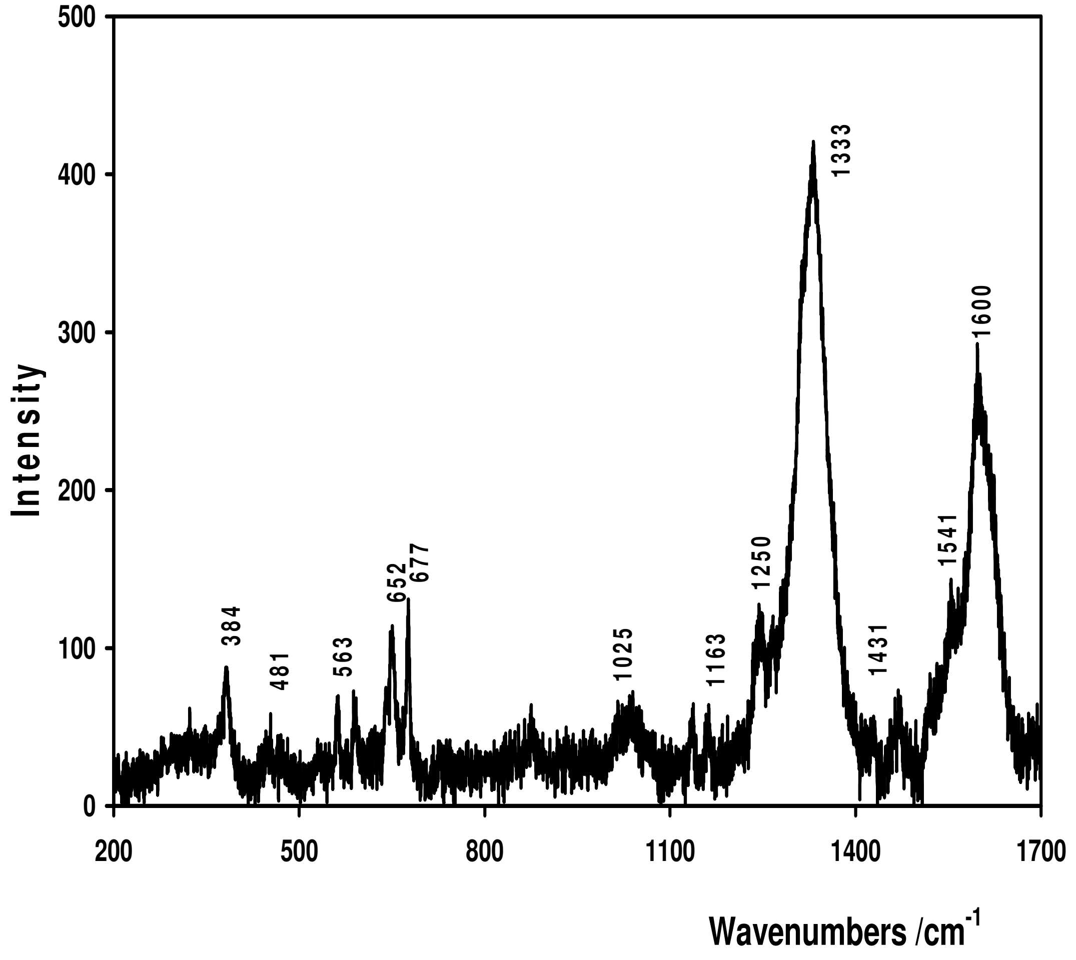

Figure 2.9. Resonance Raman spectra of dry [Ru(terpy)(box)PVP$_{20}$][PF$_6$] metallopolymer film coated on 3 mm glassy carbon electrode excited at 632.8 nm.

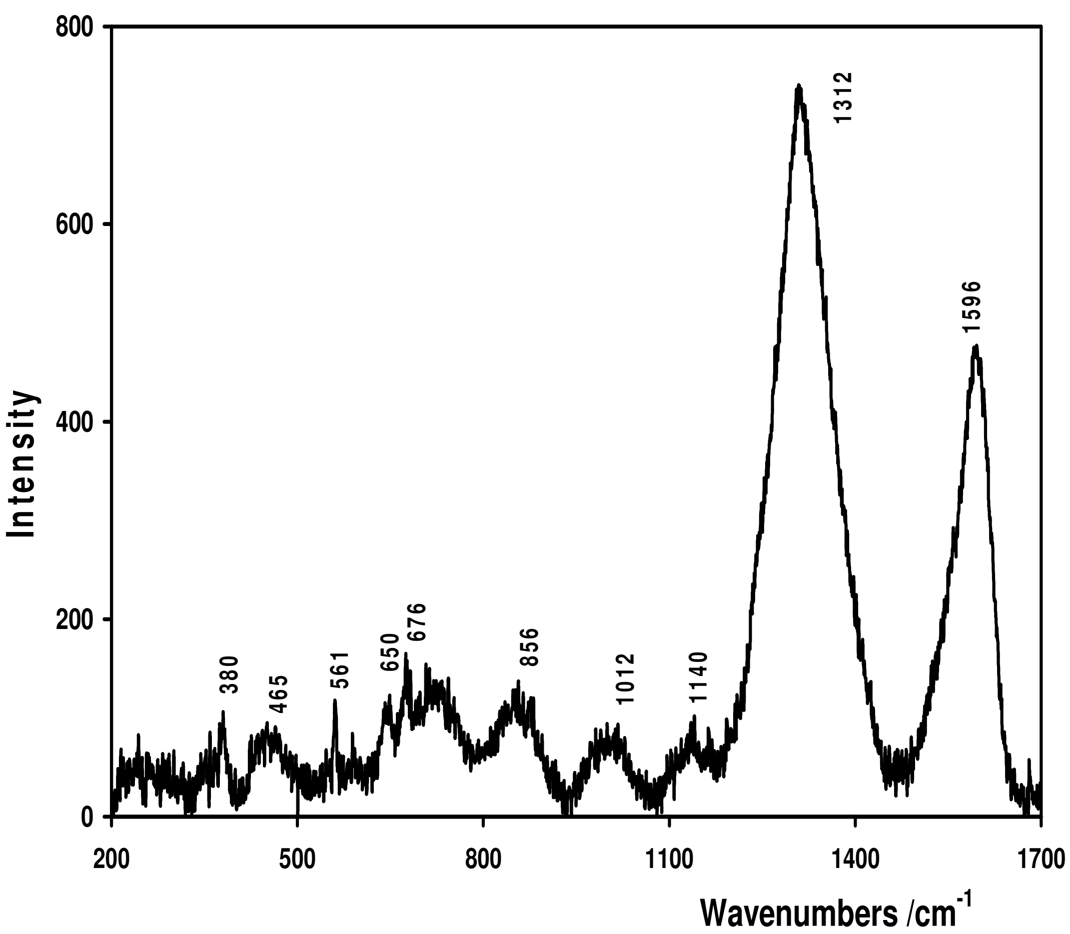

Figure 2.10. Potential controlled Raman spectroscopy of the metallopolymer, [Ru(terpy)(box)PVP_{20}][PF_6], coated on 3 mm glassy carbon electrode excited at 785 nm. The potential was kept at 0.6 V vs Ag/AgCl, and the electrolyte was 0.1 M $LiClO_4$ aqueous solution. Raman experiment was carried out, when the colour of the metallopolymer was fully changed from dark red to light green.

2.4 CONCLUSIONS

The synthesis and characterization of a new electrochromic metallopolymer, $[Ru(terpy)(box)PVP_{20}][PF_6]$, which contains $Ru\text{-}O^-$ coordinated quinoid ligands has been reported in this chapter. Spectroelectrochemistry and resonance Raman studies indicate that the first reversible redox process is Ru centre based and this redox process results in a new low energy ligand (box)-to-metal (Ru_{III}) charge transfer transition. The rich electrochromic behaviour rises from the oxidation processes of the metallopolymer both in solution and within thin films. For example, oxidation at +0.5 V switches the colour from wine red to green while oxidation at potentials above +1.0 V produces a change in the NIR region of the spectrum. The combination of the electrochromic properties is particularly attractive for diverse applications ranging from security to monitoring packaging integrity in foods and pharmaceuticals.

2.5 REFERENCES

[1] R. J. Mortimer. Chem Soci Rev., 26 (1997) 147.

[2] R. J. Mortimer, N. M. Rowley, Metal complexes as dyes for optical data storage and electrochromic materials in: J. A. McCleverty, T. J. Meyer, M. D. Ward (Eds.), Comprehensive Coordination Chemistry - II: From Biology to Nanotechnology 9.2, Elsevier, Oxford, 2004 pp. 581–619.

[3] A. Juris, V. Balzani, F. Barigelletti, S. Campagna, P. Belser, A. V. Zelewsky. Coord. Chem. Rev., 84 (1988) 85.

[4] R. J. Mortimer, A. L. Dyer, J. R. Reynolds. Displays, 27 (2006) 2.

[5] P. M. S. Monk, R. J. Mortimer, D. R. Rosseinsky. Electrochromism and Electrochromic Devices. Cambridge University Press, New York, 2007 p 254.

[6] F. S. Han, M. Higuchi, D. G. Kurth. J. Am. Chem. Soc., 130 (2008) 2073.

[7] R. W. Murray. Electroanal. Chem., 13 (1984) 191.

[8] M. Kaneko, D. Wöhrle. Adv. Polym. Sci., 84 (1988) 141.

[9] H. D. Abruña. Coord. Chem. Rev., 86 (1988) 135.

[10] J. F. Rusling, R. J. Forster. J. Colloid and Interface Science. 262 (2003) 1.

[11] T. E. Keyes, D. Leane, R. J. Forster, C. G. Coates, J. J. McGarvey, M. N. Nieuwenhuyzen, E. Figgemeier, J. G. Vos. Inorg Chem., 41 (2002) 5721.

[12] I. Brady, D. Leane, H. P. Hughes, R. J. Forster, T. E. Keyes. J. Chem. Soc., Dalton Trans., (2004) 334.

[13] T. E. Keyes, B. Evrard, J. G. Vos, C. Brady, J. J. McGarvey, P. Jayaweera. J. Chem. Soc., Dalton Trans., (2004) 2341.

[14] J. A. Osaheni, S. A. Jenekhe. Chem. Mater. 4 (1992) 1282.

[15] M. F. Robert, S. A. Jenekhe. Chem. Mater. 6 (1994) 135.

[16] C. G. Cameron, T. J. Pittman, P. G. Pickup. J. Phys. Chem. B 105 (2001) 8838.

[17] S. A. Jenekhe, P. O. Johnson. Macromolecules, 23 (1990) 4419.

[18] S. A. Jenekhe, P. O. Johnson, A. K. Agrawal.Macromolecules, 22 (1989) 3216.

[19] A. P. Clarke, J. G. Vos. Trends in Electrochem., 1 (1992) 167

[20] J. M. Calvert, R. H. Schmehl, B. P. Sullivan, J. S. Facci, T. J. Meyer, R. W. Murray. Inorg. Chem., 22 (1983) 2151

[21] P. A. Adcock, F. R. Keene, R. S. Smythe, M. R. Snow. Inorg. Chem., 23 (1984) 2336.

[22] B. P. Sullivan, J. M. Calvert, T. J. Meyer. Inorg. Chem., 19 (1980) 1404.

[23] C. R. Hecker, A. K. Cushurst, D. R. McMillin. Inorg. Chem. 30 (1991) 538.

[24] J. Sauvage, J. Collin, J. Chambron, S. Gullerez, C. Coudret. Chem. Rev. 94 (1994) 993.

[25] S. Schneider, G. Brehm, C. J. Prenzel, J. Raman Spectroscopy. 27 (1996) 163.

[26] T. C. Strekas, H. D. Gafiney, S. A. Tysoe, R. P. Thumel, F. Lefoulon. Inorg. Chem., 28 (1989) 2964.

[27] T. E. Keyes, P. M. Jayaweera, J. J. McGarvey, J. G. Vos. J. Chem. Soc., Dalton Trans., (1997) 1627.

CHAPTER 3

Redox Induced Switching Dynamics of the $[Ru(terpy)(box)PVP_{20}][PF_6]$ Metallopolymer Film

3.1 INTRODUCTION

There is currently significant interest in electrochromic metallopolymers incorporating transition metal coordination complexes because of the opportunity to couple electrochemical and optical processes leading to significant potential applications [1,2,3]. For the practical application in display devices the switching rate is equally important [4]. Factors such as ion and electron ion through the films as well as the rate of heterogeneous charge transport can affect this switching rate.

In the previous chapter, preliminary data were reported on the colour changes that occur within a novel metallopolymer, $[Ru(terpy)(box)PVP_{20}]PF_6$, incorporating a Ru metal centre that is O, N coordinated to a phenolate donor ligand, terpy is $2,2':6',2''$-terpyridine, box is 2-(2-hydroxyphenyl)benzoxazole, and PVP is poly(4-vinylpyridine) in which one in every twenty of the monomer units is labelled with the ruthenium complex (Chart 3.1). This material exhibits a range of charge transfer transitions in the visible and NIR regions that can be controlled by applying a potential to oxidise either the ruthenium or phenolate ligand.

In this chapter, investigations using cyclic voltammetry that probe the nature of the electrochemical properties of thin films of the metallopolymer are reported in aqueous electrolyte. Moreover, the rate of charge transport has been measured as a function of electrolyte concentration and identity. In this way, insights into the nature of the rate determining process for charge transport through the layer has been obtained. The significance of these findings for the design of intensely coloured, fast switching electrochromic films is discussed.

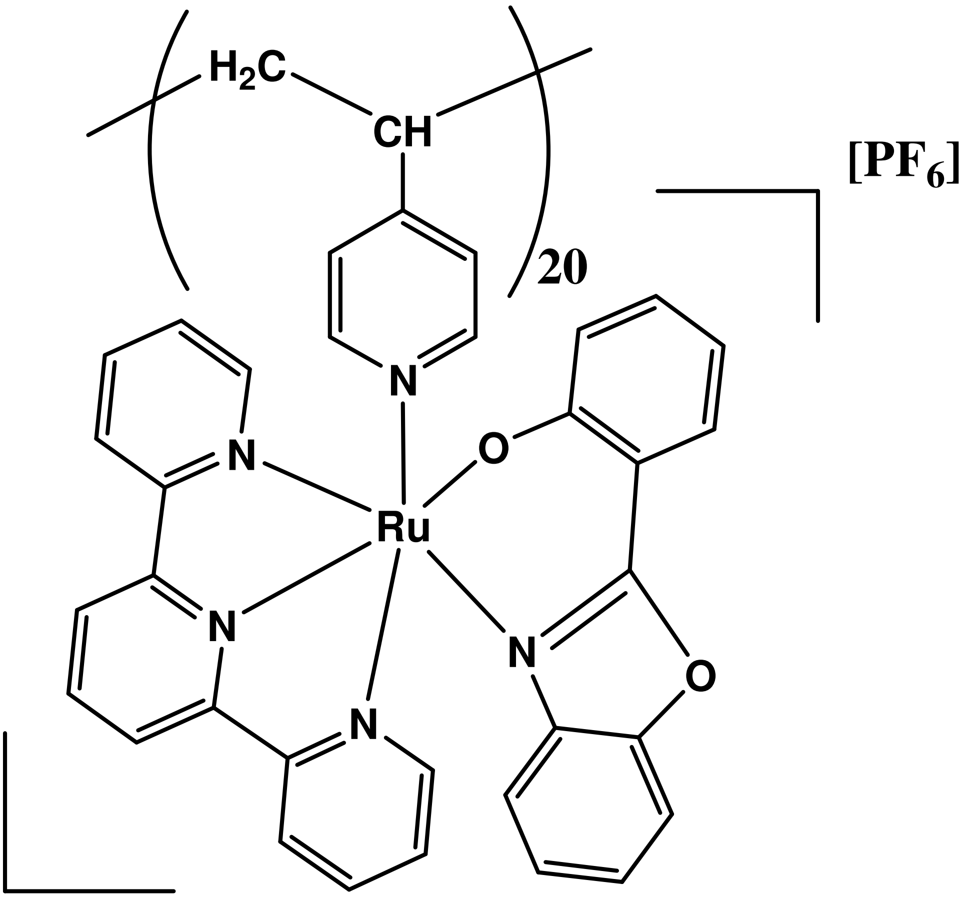

Chart 3.1. Structure of [Ru(terpy)(box)PVP$_{20}$][PF$_6$] metallopolymer.

3.2 EXPERIMENTAL

3.2.1 Materials.

The metallopolymer was synthesized as described in Chapter 2. Water was purified using a Milli-Qplus 185 Millipore installation. Electrolyte chemicals were purchased from Aldrich and used as received.

3.2.2 Instrumentation and Apparatus

Electrochemistry was performed in conventional three-electrode cells using an Ag/AgCl aqueous electrode (CH instrument) as reference. This electrode consists of a Teflon cap with a AgCl coated Ag wire, a glass tubing, and a porous glass tip sealed to the glass tubing with Teflon heat shrinkable tubing and filled with 3 M KCl aqueous solution. Cyclic voltammetry (CV) was carried out using a CH instruments Model 660a electrochemical workstation. All electrolyte solutions were deoxygenated for at least 15 min using N_2 gas before use and maintained under a nitrogen blanket during measurement. Glassy carbon working electrodes were polished successively with 1.0, 0.3, and 0.05 μm alumina powder and modified by evaporating the required volume of a 1 % metallopolymer solution in ACN/MeOH (1:1) followed by air-drying.

The maximum concentration of ruthenium centres within the metallopolymer film was estimated from the density of the dry metallopolymer as measured by flotation in non-swelling solvents, i.e., 0.1 ml of petroleum ether and 1 ml of chloroform. This gave a value of fixed site concentration of 0.5 M.

Both experimental and theoretical works have demonstrated the advantages of interdigitated electrode arrays for few reasons. First, as long as the microelectrode in the array do not interact with each other, a stead-state current is monitored at long times. Second, Arrays of microelectrodes exhibit higher signal-to-noise ratios than macroelectrodes having an equivalent surface area. Lower current detection limits can be achieved that are important for electrochemical detectors in measuring small quantities of materials. Chart 3.2 shows two designs of interdigitated electrode arrays.

In general, two-point IDAs are usually used for the measurement of electron conduction in the absence of macroscopic ion motion. Four-point system combines IDA electrode with reference electrode and counter electrode together and can be used as chemical sensors or biosensors by measuring small quantities of materials and electrolyte sample solution.

For metallopolymer conductivity measurement, a CH instruments Model 760b electrochemical workstation was employed. Two-point platinum interdigitated electrode arrays, IDAs, were purchased from Abtech Scientific. Inc. The IDA electrodes had 50 digit pairs, a digit width and inter-digit gap width of 15 μm, a digit height of 180 nm. Metallopolymer films were prepared by evaporating the required volume of a 1 % metallopolymer solution in ACN/MeOH (1:1) on the IDA fingers and gaps between fingers. In order to cover the IDA fingers and gaps completely, the metallopolymer solution were drop-cast on the IDA electrodes several times to form a thick metallopolymer film. The thickness can be determined from the surface coverage of metallopolymer film with about 400 nm, which is higher than the height of the IDA digit of 180 nm.

Scanning electron microscopy (SEM) was performed using a Hitachi S-3000N system to probe the physical characteristics of the deposits and to determine if voltammetric cycling results in any morphological changes in the deposit. In SEM investigations, films were formed on 3 mm radius carbon disks. To probe the effect of redox cycling, the modified disks were electrochemically cycled and the films were then washed in electrolyte free Milli-Q water and dried in a vacuum desiccator for several hours.

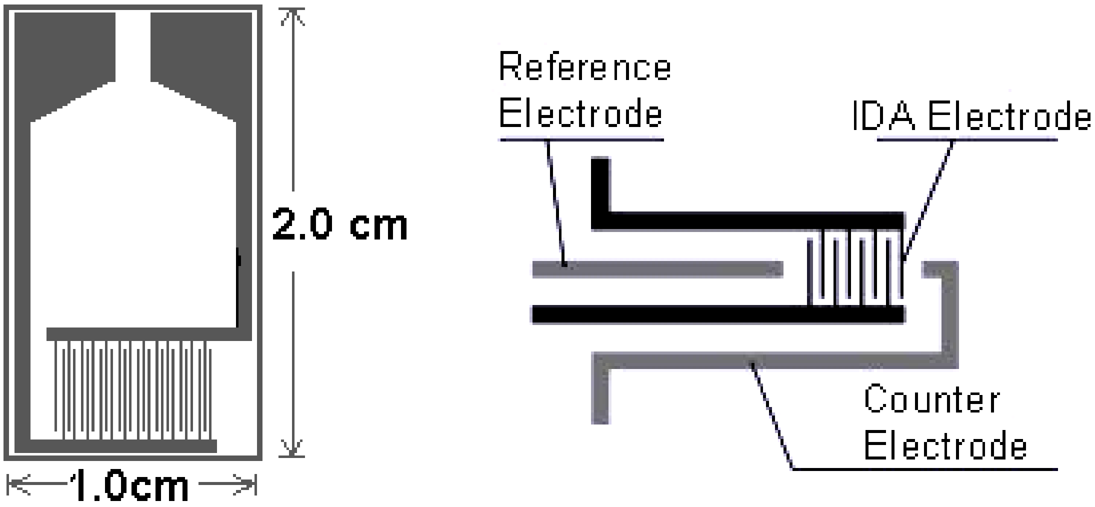

Chart 3.2. Designs of 2-point (left) and 4-point (right) interdigitated electrode arrays (IDAs)

3.3 RESULTS AND DISCUSSION

3.3.1 “Break In” Phenomena

Figure 3.1 shows the initial voltammetric response of a [Ru(terpy)(box)PVP$_{20}$][PF$_6$] metallopolymer film on a 3mm glassy carbon electrode when it is first cycled in 0.1 M LiClO$_4$ aqueous solution. The response changes remarkably little during these initial scans. The changes of the anodic peak current and the cathodic peak current are approximately 5 and 2%, respectively. The oxidation and reduction peak potentials remain constant at 458±4 mV and 370±4 mV, respectively. Significantly, after approximately 20 scans, the response no longer changes and the response observed is similar to an ideal reversible redox reaction that is controlled by semi-infinite diffusion. When the metallopolymer film is repeatedly cycled over 1000 scans, it remains stable for at least 1.5 hr. These observations indicate that the redox process is reversible and that metallopolymer film adheres strongly to the electrode surface.

The overall charge on the metal centre is increased from 2+ to 3+ for oxidation and counteranions must be incorporated into the film from the connecting electrolyte solution to maintain electroneutrality. Therefore, the minor changes in peak currents observed when the film is first cycled may be linked to transport of charge compensating perchlorate ions into the metallopolymer film. However, changes in the film structure driven by differences in solubility of the oxidized and reduced forms may also contribute to the observed behaviour [5,6]. These changes can be revealed using scanning electron microscopy [7,8].

Figure 3.2(A) shows the SEM image prior to voltammetric cycling. The film is not uniform across the surface of the electrode and exists as a rather rough, amorphous coating. The amorphous particles are of order of 50 μm in diameter. After cycling, as shown in Figure 3.2(B), the SEM images reveal that the repetitive cycling reduces both the absolute size of the individual particles within the film and range of particle size, but voltammetric cycling does not significantly affect the structure of the film. This result is consistent with the observation in Figure 3.1, where there is no loss from voltammetry and the metallopolymer deposit film is stable to electrochemical cycling.

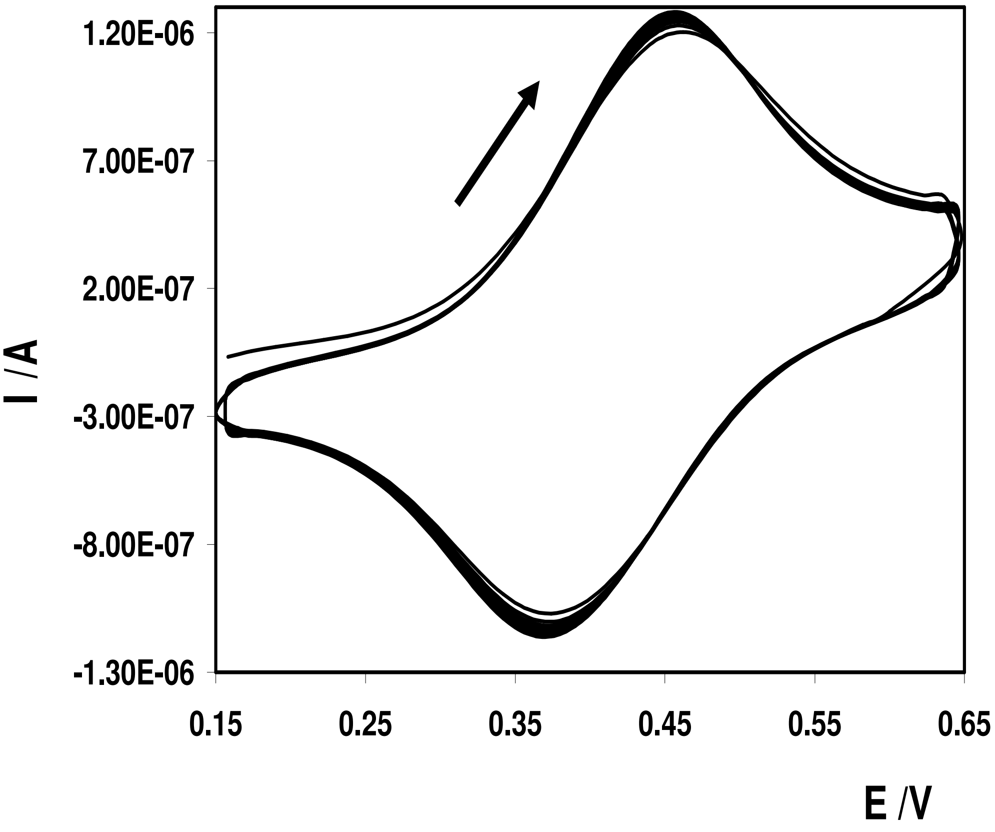

Figure 3.1. First 30 voltammetric cycles for a solid state [Ru(terpy)(box)PVP_{20}][PF_6] metallopolymer film coated on 3 mm glassy carbon electrode in 0.1 M aqueous $LiClO_4$ electrolyte. The scan rate is 0.1 V s^{-1}.

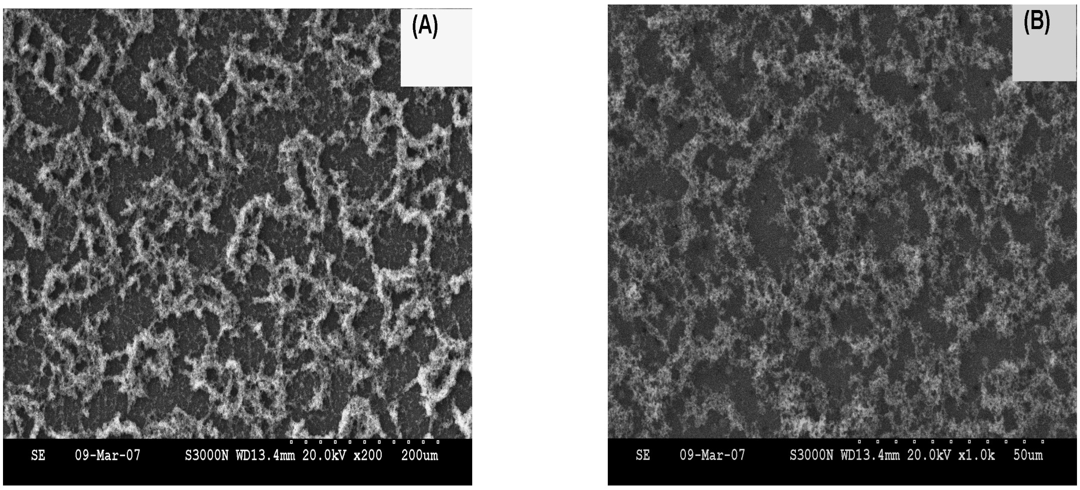

Figure 3.2. SEM images of a [Ru(terpy)(box)PVP$_{20}$][PF$_6$] metallopolymer film drop cast on a 3 mm glassy carbon electrode: (A) as deposited, before voltammetric cycling; (B) is after 100 voltammetric cycles between 0.10 V and 0.75 V in 0.1 M LiClO$_4$ at a scan rate of 0.1 V s^{-1}.

3.3.2 General Electrochemical Properties

Figure 3.3 illustrates the slow sweep voltammetric response for a thin layer of the metallopolymer, $[Ru(terpy)(box)PVP_{20}][PF_6]$, coated on 3mm glassy carbon electrode recorded from 20 to 100 mVs^{-1},where the supporting electrolyte is aqueous 0.1 M $LiClO_4$. The formal potential, E°′, for the $Ru^{2+/3+}$ couple is 0.380V. This formal potential is significantly more positive than that found in solution where E°′ is 0.121 V indicating differences in the solvation shell or extents of ion pairing within the film compared to solution. The peak shape of the metallopolymer film is independent of scan rate up to 100 mV/s, and as shown in Figure 3.4, the peak height scales linearly with increasing scan rate, rather than the $\upsilon^{1/2}$ dependence observed for higher scan rate over 100 mV/s.

Where there are no lateral interactions between surface-confined redox centres and a rapid equilibrium is established with the electrode, a zero peak-to-peak separation, ΔE_p, and a full width at half-maximum (FWHM) of 90.6 mV are expected for a one-electron transfer [9].

$$FWHM = 3.53\frac{RT}{nF} = \frac{90.6}{n}mV \ (25°C) \tag{3.1}$$

For the scan rate between 20 mV/s and 100 mV/s, the ΔE_p value is 92±5 mV, and the fwhm is 160±8 mV. The observation that the peaks are broader than theoretically expected for an ideal Nernstian system may suggest that there are weak destabilizing interactions between the metal centres [10]. The ΔE_p is independent of scan rate, indicating that slow heterogeneous electron transfer is not responsible for the observed behaviour. Ohmic effects are not responsible for this behaviour ether, as the increased currents at higher scan rate would be expected to increase the ΔE_p value. Similar non-idealities in related systems have been interpreted in terms of Feldberg's unusual quasi-reversibility model [11]. Also, the potential range for the distinct colour changes of an electrochromic material can be determined by the values of ΔE_p and FWHM associated with the formal potential of the material. The suitable electrochromic potential results in shorter switching time. As reported in Chapter 2, the potential at 0.6 V was used as the electrochromic potential of the metallopolymer for the potential controlled Raman spectroscopy. A reasonable switching time was obtained at this potential within 15 min, which was shorter than the time observed at 0.45 V (over 20 min).

The charge, Q, as determined by integrating background corrected cyclic voltammograms is obtained at slow scan rate. It can be used to determine the surface coverage, Γ, of electroactive redox centres using Equation 3.2:

$$\Gamma = \frac{Q}{nFA} \qquad \textbf{(3.2)}$$

where *F* is Faraday's constant and *A* is the area of the electrode surface. The surface coverage in Figure 3.3 is 4.9×10^{-10} mol cm^{-2}.

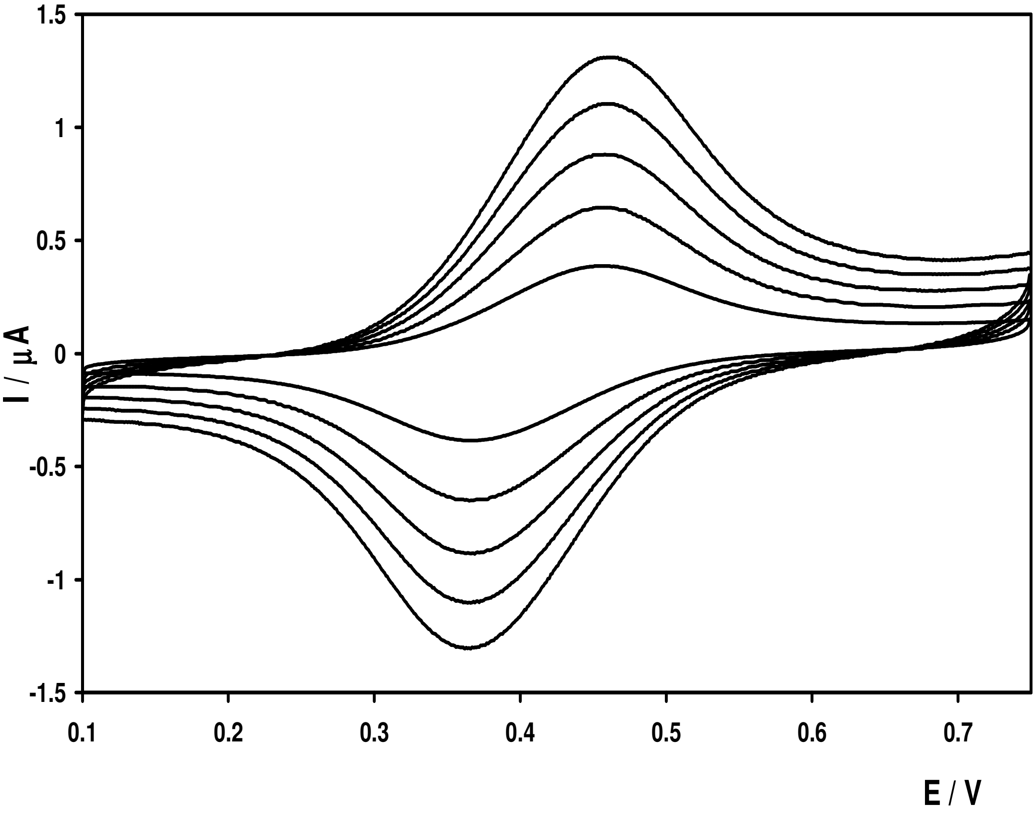

Figure 3.3. Cyclic voltammograms for a [Ru(terpy)(box)PVP$_{20}$][PF$_6$] metallopolymer film coated on 3 mm glassy carbon electrode in 0.1 M aqueous LiClO$_4$ electrolyte. Scan rates are (from bottom to top) 20, 40, 60, 80, and 100 mV/s. The surface coverage is 4.9×10^{-10} mol cm^{-2}.

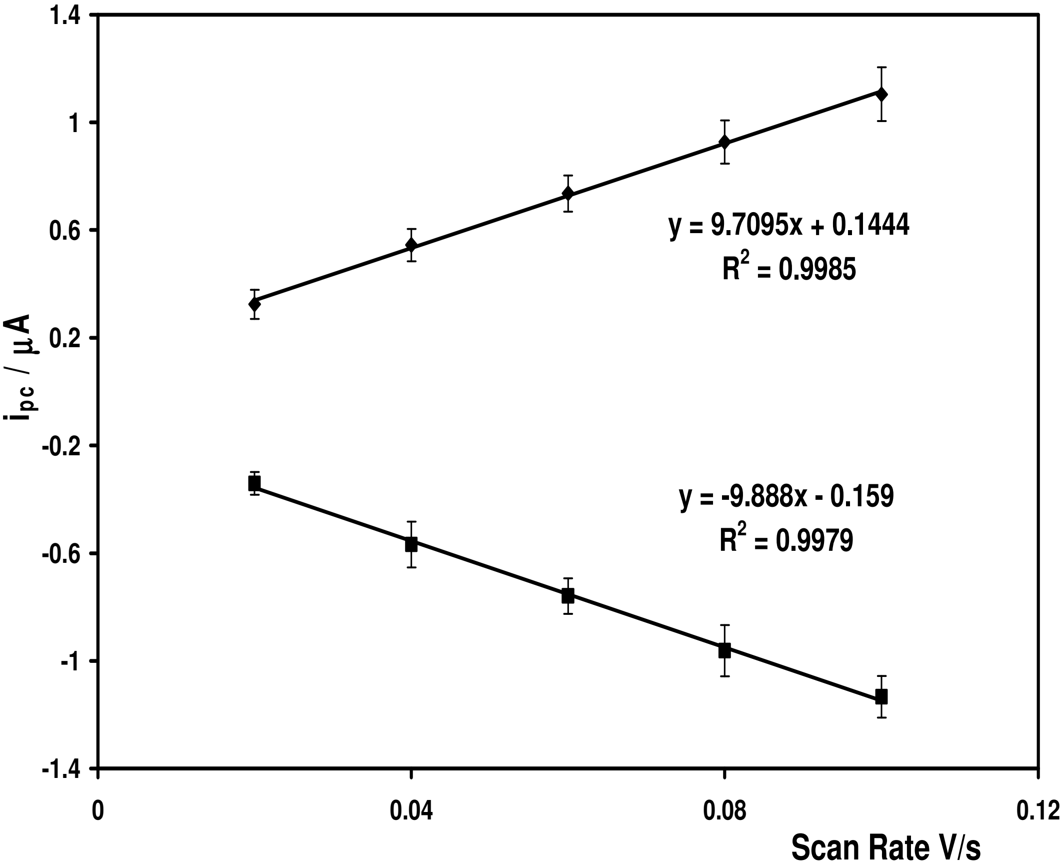

Figure 3.4. The plot of peak current Vs. scan rate for the [Ru(terpy)(box)PVP$_{20}$][PF$_6$] metallopolymer film coated on 3 mm glassy carbon electrode in 0.1 M aqueous LiClO$_4$ electrolyte. Scan rates are 20, 40, 60, 80, and 100 mV/s. The numbers of repetitive measurement (n=5).

3.3.3 Ion Pairing Effects.

An important objective when developing electrochromic films is to minimize the voltage required to change the optical response. The formal potential of an immobilized electroactive group is sensitive to both the solvation shell of the redox centre and to the extent of ion-pairing [12,13,14]. It is therefore a sensitive probe of the local microenvironment within the metallopolymer film. Shifts in formal potential with changes in electrolyte concentration reflect differences in the relative stability between the two redox states, and can be used to probe ionic interactions. Therefore, it ought to be possible to change the formal potential by changing the identity and concentration of the charge compensating counterion in solution [15].

The effect of electrolyte concentration on the formal potential of the Ru centres redox reaction has been examined for 0.1 M ≤ [$LiClO_4$] ≤ 1.0 M. Cyclic voltammetry is used to determine the formal potential, at a scan rate of less than 0.5 V/s to avoid any influence from interfacial charge transfer kinetics. As shown in Figure 3.5, $E^{o\prime}$ shifts in a negative potential direction with increasing $LiClO_4$ concentration indicating that the metal centre is easier to be oxidized when the supply electrolyte concentration is higher. This response is consistent with ion-pairing between the electrolyte anions and the metal redox centres. This situation is summarized in the following Nernstian reaction,

$$[Ru(terpy)(box)PVP_{20}]^{+}(X^{-})_{\zeta} - e^{-} + \rho(X^{-}) \leftrightarrow [Ru(terpy)(box)PVP_{20}]^{2+}(X^{-})_{\zeta+\rho} \qquad \textbf{(3.3)}$$

where both redox forms participate in the ion-paring equilibrium.

Figure 3.5 illustrates a plot of the formal potential for the $Ru^{2+/3+}$ couple within a [Ru(terpy)(box)PVP_{20}][PF_6] metallopolymer film versus the logarithm of the [$LiClO_4$] concentration. The slope observed for the metallopolymer film is 52±3 mV, which is close to the theoretical (59/*p*) mV/decade, where *p* is the difference in the number of anions pairing with the oxidized and reduced forms of the metal centre. It indicates that a single extra anion becomes bound to the metal centre in the oxidized state [16].

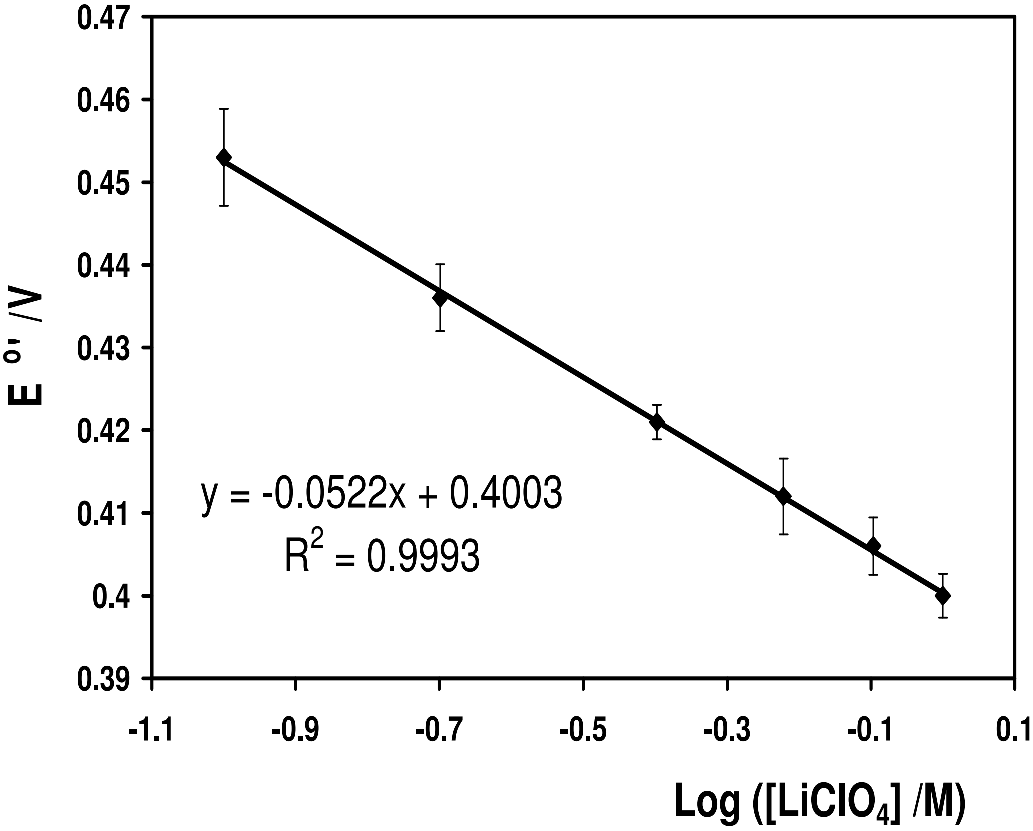

Figure 3.5. Dependence of the formal potential for the $Ru^{2+/3+}$ couple within a $[Ru(terpy)(box)PVP_{20}][PF_6]$ metallopolymer film on the $\log[LiClO_4]$ as supporting electrolyte. The numbers of repetitive measurement (n=5).

3.3.4 Homogeneous Charge Transport Rate of Metallopolymer Film

The well defined metal based oxidation processes for [Ru(terpy)(box)PVP$_{20}$][PF$_6$] metallopolymer film allow the dynamics of charge transport to be investigated. The rate of charge transport through the metallopolymer layer can be quantified by measuring the charge transfer diffusion coefficient, for metallopolymer layer, using cyclic voltammetry [17,18]. For cyclic voltammetry, the experimental timescale and hence the fraction of the electrolysed film can be easily controlled through the scan rate. At faster scan rates, only a small fraction of the total amount of material immobilised is electrolysed and the depletion zone remains well within the deposit. Under these conditions, linear diffusion predominates and, in common with solution phase reactants, the peak current varies as $\upsilon^{1/2}$ [19].

Figure 3.6 illustrates the voltammetric responses for the metallopolymer film coated on 3 mm glassy carbon electrode in 0.1 M aqueous LiClO$_4$ at scan rates between 100 and 2000 mV/s. For this range of scan rates, ΔE_p value for the metal centre is about 97 mV, which is larger than the 57 mV expected for a reversible redox reaction involving the transfer of a single electron, but it is independent of scan rate up to at least 2000 mV/s. The consistent ΔE_p value indicates that the rate of heterogeneous electron transfer across the electrode/film interface or ohmic effects is not responsible for this behaviour.

As shown in the Figure 3.7, the voltammetric peak current increases linearly with $\upsilon^{1/2}$ indicating that the response is controlled by semi-infinite linear diffusion [20]. The peak current, i_p, can be expressed in terms of the Randles-Sevcik equation:

$$i_p = 2.69 \times 10^5 n^{3/2} A D_{CT}{}^{1/2} C_{eff} \nu^{1/2} \tag{3.4}$$

where n is the number of electrons transferred, A is the area of the working electrode, D_{CT} is the homogeneous charge transport diffusion coefficient, and C_{eff} is the effective fixed site concentration of the redox centre. The equation allows the metallopolymer film $D_{CT}{}^{1/2}C_{eff}$ to be determined from the slope of the plot of i_p Vs $\upsilon^{1/2}$. Further, the D_{CT} values have been determined using a maximum concentration of Ru redox centre of 0.5 M. The values of D_{CT} for the oxidation and reduction processes of Ru centre are $(3.7\pm0.1)\times10^{-13}$ cm^2 s^{-1} and $(3.8\pm0.2)\times10^{-13}$ cm^2 s^{-1}.

Based on a maximum fixed site concentration of 0.5 M, the minimum film thickness of the metallopolymer, δ, is approximately 102 nm where the surface coverage is 5.1×10^{-9} mol cm^{-2}. Under semi-infinite linear diffusion condition and using the homogeneous charge transport diffusion coefficient in conjunction with Equation below, it would take approximately 90 s to fully oxidize the metallopolymer film and regenerate the Ru^{3+} mediating centres. There is only about 5% of the metallopolymer film thickness (5.4 nm) electrolysed at scan rate of 100 mV/s.

$$t = \frac{\delta^2}{\pi D_{ct}} \tag{3.5}$$

However, in the previous section SEM images of metallopolymer film showed that the metallopolymer film was not uniform across the surface of the electrode and existed as a rather rough, amorphous coating. This observation may cause that the switching time would be longer than 90 s to fully oxidize the metallopolymer film because the film thickness somewhere on the electrode surface is higher than the average of 100 nm. In order to observe shorter switching time and uniform colouration, spin coating can be used to apply uniform thin metallopolymer films to flat electrode surface for practical electrochromic applications. In short, an excess amount of a metallopolymer solution can be placed on the electrode surface, which is then rotated at high speed in order to spread the fluid by centrifugal force. Also, it is perhaps important to note that for practical electrochromic applications longer switching times may be observed because of the typically greater resistance of optically transparent electrodes and the need to use larger surface areas that may introduce greater ohmic drop.

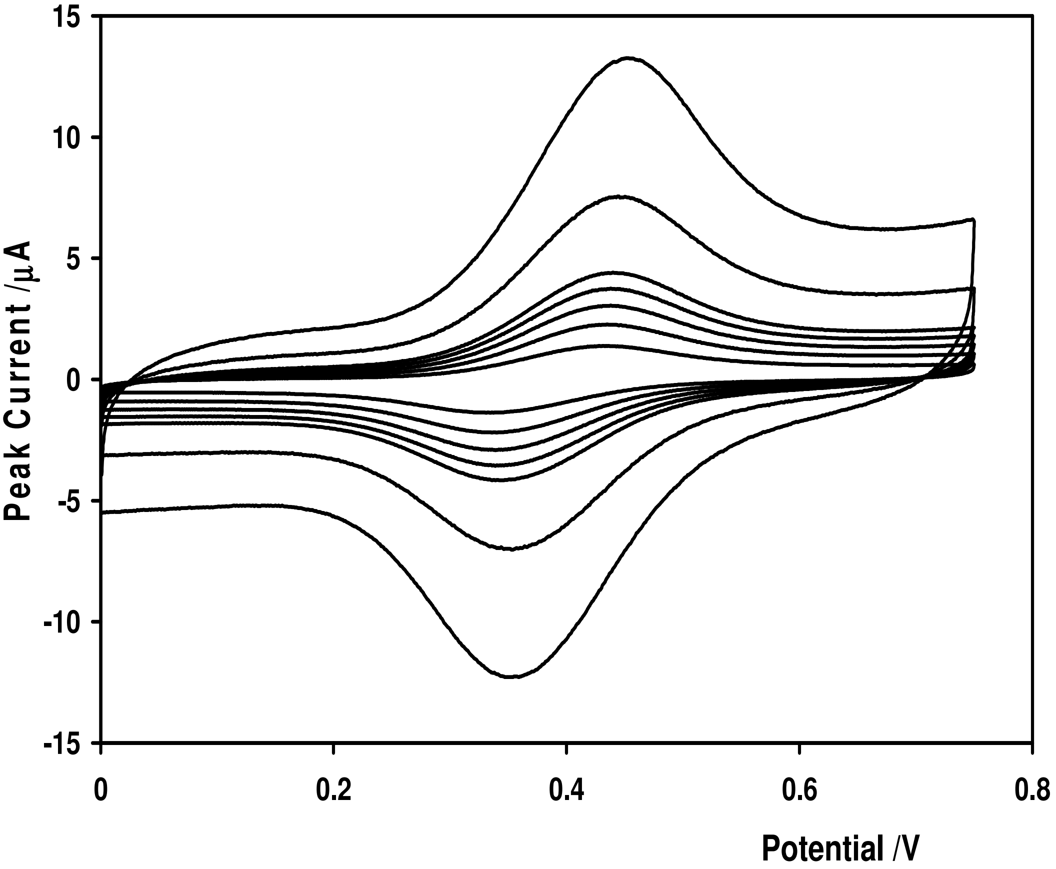

Figure 3.6. Scan rate dependence of the voltammetric response of metallopolymer film on 3 mm glassy carbon electrode in 0.1 M $LiClO_4$. $\Gamma = 5.1\times10^{-9}$ mol cm^{-2}. υ =2000, 1000, 500, 400, 300, 200, and 100 mV/s (from top to bottom).

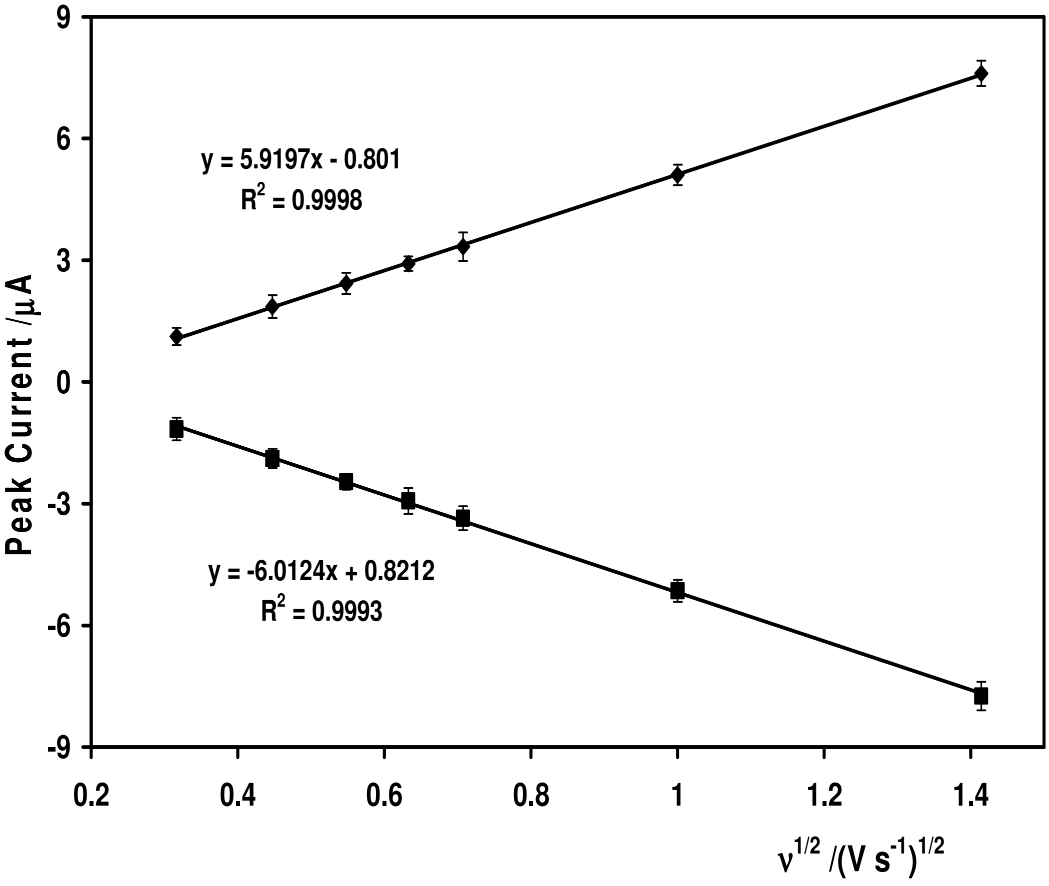

Figure 3.7. A plot of i_p vs. $\upsilon^{1/2}$ is obtained for the metallopolymer film on 3 mm glassy carbon electrode in 0.1 M $LiClO_4$. The scan rates are from 0.1 to 2.0 V/s. The numbers of repetitive measurement (n=5).

3.3.5 Effect of Electrolyte Concentration on D_{CT}

There are a number of processes that contribute to homogeneous charge transport through films of this kind, including electron hopping, counterion diffusion/migration or the movement of polymer chains or segments to bring adjacent redox centres sufficiently close to allow electron transfer to occur [21]. When charge-compensating counterions are freely available within the structure, electron hopping or the rate of segmental polymer chain motion is rate limiting and D_{CT} is expected to depend only weakly on the electrolyte concentration.

Figure 3.8 shows that D_{CT} decreases somewhat as the concentration of the supporting electrolyte increases. For anodic process, D_{CT} decreases from 3.5×10^{-13} cm^2 s^{-1} to 2.7×10^{-13} cm^2 s^{-1} as the $LiClO_4$ concentration increases from 0.1 M to 1.0 M. Taking into account the associated error bars, the overall change in D_{CT} observed is not significant and indicates that D_{CT} is at best very weakly dependent on the perchlorate concentration. This observation suggests that counterion availability is not rate-determining and the overall rate of charge transport through the metallopolymer film is limited by electron hopping or segmental chain motion prior to electron transfer.

The relatively low loading of ruthenium centres, 1 in 20 monomer units, makes the intersite separation large, of the order of 40 Å. This large distance means that movement of the polymer chain segments rather that the actual electron transfer itself, is likely to represent the rate determining step. This conclusion is consistent with the fact that the D_{CT} measured here is at least two orders of magnitude lower that those found for electron hopping in related systems [22]. The small decrease in D_{CT} most likely reflects a change in the film structure. For example, perchlorate is known to dehydrate PVP based polymer films making the layer more compact at higher electrolyte concentrations [22]. Additional insight into the nature of the rate determining step can be obtained by changing the charge to volume ratio of the charge compensating counterion.

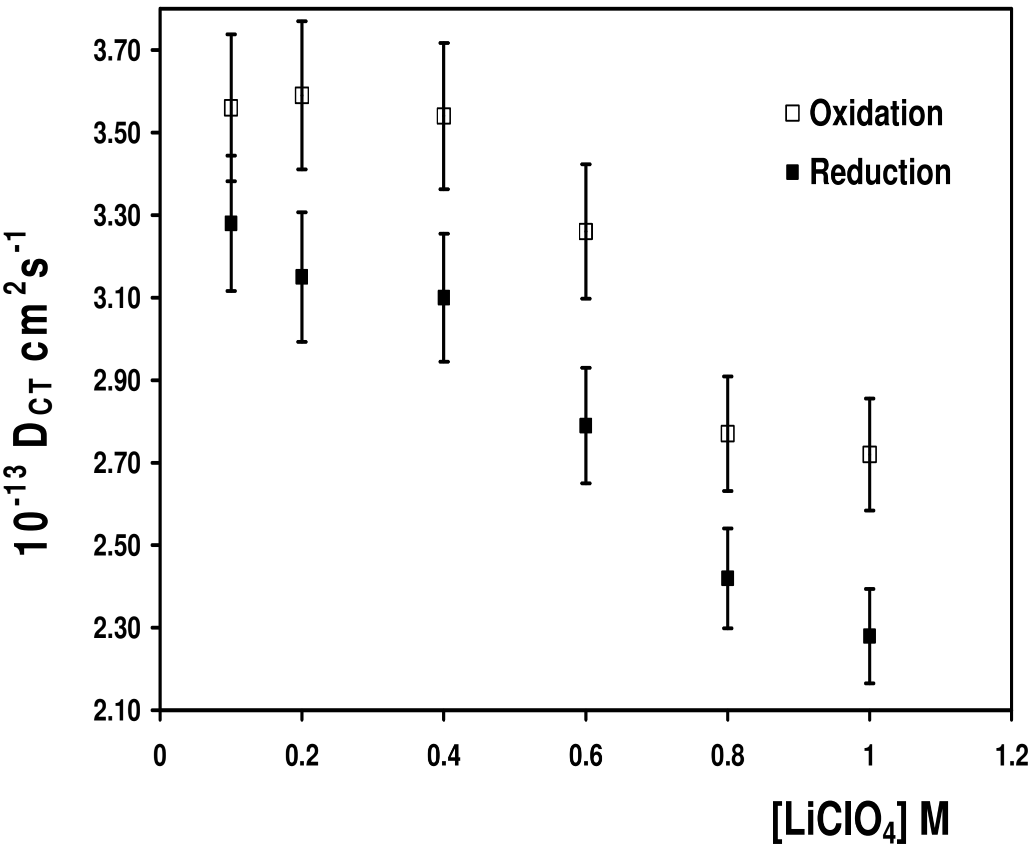

Figure 3.8. Dependence of D_{CT} on the concentration of aqueous $LiClO_4$ as supporting electrolyte for a $[Ru(terpy)(box)PVP_{20}][PF_6]$ metallopolymer film. The numbers of repetitive measurement (n=5).

3.3.6 Effect of Anion Identity

There may be substantial effects on charge transfer from changing the identity of the anion. In aqueous electrolyte solution, ions and water form hydrated ions. Because of the same ionic radii of cations, the size of hydrated anions can influence the change of the voltammetric behaviour.

Table 3.1 contains D_{CT} values measured in 0.1 M electrolytes where the anion is perchlorate, nitrate, chloride or sulphate. Significantly, D_{CT} changes by less than a factor of four across this range of anions despite the significant differences in stokes radii suggesting that the ion size does not dramatically affect the rate of charge transport. However, perchlorate has the smallest stokes radius [23], which is related to the hydrated radius and exhibits the fastest charge transport rate. Compared to other anions, ClO_4^- anion is more hydrophobic thus increasing its permeation rate and ease of movement within the film [24]. These effects result in a more negative oxidation potential value of Ru redox centre. Big shifts toward more positive potential are observed in the formal potential, $E°'$, when changing the electrolyte from relatively hydrophobic ClO_4^- to the relatively hydrophilic SO_4^{2-}. For these anions, the Gibbs free energy for transfer of the anion from the aqueous to the solid phase is likely to be large making the film dynamically more difficult to be oxidised when in contact with media containing strongly hydrated anions such as SO_4^{2-}.

There is also a kinetic effect with lower D_{CT} values being observed for the larger ions, e.g., SO_4^{2-}. The smallest ClO_4^- anion is relatively more mobile and possesses a stronger ability to permeate and move through the film as a counterion in the process of an electrode reaction, causing smaller peak-peak separation value observed. Behaviour of this kind has previously been observed for the solid-state voltammetry [25,26] of compounds such as TCNQ and is relate to the energy barrier for insertion and expulsion of counterions. In general, a strong ability of ClO_4^- to permeate and move through the film is a key reason to cause a more negative oxidation potential, and a smaller peak separation value.

For NO_3^- and Cl^-, they have similar ionic radius. Their formal potential, $E°'$, and D_{CT} values are similar. But for their stokes radius, mobility of larger size hydrated Cl^-

anion is less than NO_3^- anion. It results in a more positive potential and a bigger peak-peak separation.

Table 3.1. Charge transfer properties of the metallopolymer film coated on 3 mm glassy carbon electrode in 0.1 M of various aqueous supporting electrolytes. The model and stokes radius as well as the Gibbs free energies are from Ref. [23]. Potentials are versus aqueous Ag/AgCl reference electrode and obtained using cyclic voltammetry at 100 mV s^{-1}. The numbers of repetitive measurement (n=5).

	Model radius	**Strokes radius**	**Gibbs free energies kJ mol^{-1}**	E^{o}**' mV**	**Peak separation mV**	**10^{-13} D_{CT} Oxidation cm^2 s^{-1}**	**10^{-13} D_{CT} reduction cm^2 s^{-1}**
ClO_4^-	1.4	2.6	-1270	401±4	97±5	3.6±0.1	3.3±0.2
NO_3^-	2.0	3.3	-1362	474±4	111±6	2.8±0.2	2.1±0.2
Cl^-	2.0	3.9	-1403.5	498±6	127±3	2.4±0.3	1.7±0.2
SO_4^{2-}	3.1	5.3	-3202	519±5	144±4	1.0±0.3	0.7±0.3

3.3.7 Electrical Conductivity.

To address the issue of whether electron hopping or segmental polymer chain motion prior to electron transfer are rate limiting, the electronic conductivity has been determined using interdigitated array electrodes (IDAs) coated with the metallopolymer. As originally demonstrated by Wrighton and co-workers [27,28,29], the film conductivity is obtained from the slope $\partial i / \partial E$.

Figure 3.9 shows that the current varies linearly with potential between –0.2 V and +0.2 V and the slopes can be used in conjunction with Equation 3.6 below to determine the conductivity, σ, where (d_G / A_{total}) is the Zaretsky cell constant. The constant of the IDAs used in this experiment is 0.04 cm^{-1}.

$$\sigma = d_G \partial i / A_{total} \partial E \qquad \textbf{(3.6)}$$

The change of film conductivity has been measured in the presence of dry N_2 and an ACN/MeOH (1:1) solvent vapour bath at room temperature and pressure. The slopes of the best fit line to the data in Figure 3.9 yield conductivities of $1.2\times10^{-10}\ \Omega^{-1}\ cm^{-1}$ for the film exposed to dry N_2 and $2.8\times10^{-10}\ \Omega^{-1}\ cm^{-1}$ for the film exposed to ACN/MeOH (1:1) vapour. Thus, exposure to solvent increases the conductivity of the film by a factor of approximately two perhaps reflecting plasticization of the layer.

When electron hopping represents the overall charge transport rate through the metallopolymer film, the Dahms-Ruff equation [30,31] can be used to calculate the electron self-exchange rate constant, k_{SE}, from the D_{CT} according to Equation 3.7:

$$D_{CT} = D_{phys} + \frac{1}{6} k_{SE} \delta^2 C \qquad \textbf{(3.7)}$$

where C is the concentration of Ru redox centres within the film, δ is the intersite separation between adjacent Ru redox centres, and D_{phys} describes physical diffusion in the absence of electron hopping. In this situation, D_{phys} is assumed to be zero, because the Ru centres are bound to the polymer chains. Therefore, Equation 3.7 reduces to:

$$D_{CT} = \frac{1}{6} k_{SE} \delta^2 C \qquad \textbf{(3.8)}$$

For a hypothetical cubic lattice model [32,33] applied to electron transport in redox polymers, the electron self-exchange rate constant, k_{SE}, also can be described by Equation 3.9,

$$k_{SE} = \frac{6RT\sigma}{10^{-3} F^2 \delta^2 [Ru]^{2+} [Ru]^{3+}} \qquad \textbf{(3.9)}$$

where k_{SE} is the electron self-exchange rate constant, R is the gas constant, σ is the conductivity at temperature T *(K)*, F is the Faraday constant, and δ is the intersite separation between adjacent Ru redox centres. As reported previously [32,33], the conductivity of redox polymer film is maximized at the formal potential of polymer, where the concentration ratio of mixed valencies polymer is one. Therefore, for the metallopolymer film the rate should maximize at the concentration ratio as $[Ru]^{2+}/[Ru]^{3+}=1$. When we combine Equation 3.8 and 3.9, and make the concentration ratio as $[Ru]^{2+}/[Ru]^{3+}=1$, D_{CT} is given by Equation 3.10:

$$D_{CT} = \frac{4RT\sigma}{10^{-3} F^2 C} \qquad \textbf{(3.10)}$$

For the dry film, the D_{CT} obtained is 2.5×10^{-13} cm^2 s^{-1} while the value obtained for the solvent equilibrated film is 5.8×10^{-13} cm^2 s^{-1}. Significantly, both of these values are consistent with those obtained using cyclic voltammetry for the films in contact with aqueous electrolyte. Therefore, these IDA measurements confirm that the movement of charge compensating counterions does not represent the rate determining step for homogeneous charge transport through these films. The fact that charge transport proceeds more rapidly when the films are exposed to acetonitrile/methanol vapour, coupled to the relatively large separation of the redox centres (of the order of 40 Å) suggests that segmental polymer chain motion limits D_{CT}.

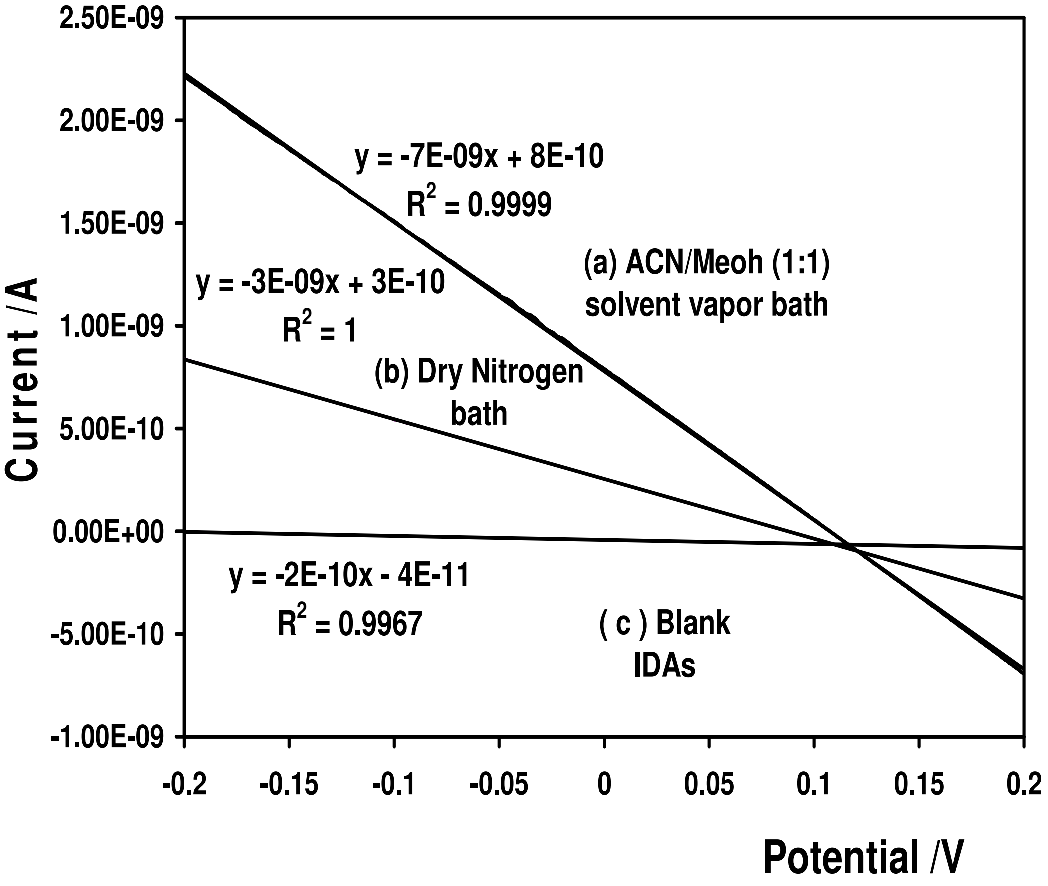

Figure 3.9. Dependence of the current on the applied potential for blank IDAs in contact with air and IDAs modified with [Ru(terpy)(box)PVP$_{20}$][PF$_6$] metallopolymer films equilibrated with dry N_2 and ACN/MeOH (1:1) vapour. In each case, one of the IDA combs was maintained at 0 V while the other was scanned at 50 mV/s.

3.4 CONCLUSIONS

A new electrochromic metallopolymer containing Ru-O$^-$ coordinated quinoid ligands has been synthesized and characterized. The metallopolymer exhibits rich electrochromic behaviour both in solution and within thin films. The electrochromic switching rate, D_{CT}, associated with oxidizing or reducing the ruthenium centres is of the order of 10^{-13} cm^2 s^{-1} and it would take approximately 90 s to fully oxidize the metallopolymer film and regenerate the Ru^{3+} mediating centres. The switching rate varies by less than 25% on going from 0.1 to 1.0 M aqueous $LiClO_4$ as supporting electrolyte and changes by approximately a factor of three between sulphate (slowest) and perchlorate (fastest) based electrolytes. Investigations using thin films on IDA electrodes where ion movement does not contribute to the observed response yield D_{CT} values that are consistent with those obtained using cyclic voltammetry. Taken together, these data indicate that the redox switching rate is controlled by the segmental polymer chain movement necessary to bring adjacent ruthenium centres sufficiently close to allow electron hopping to occur.

3.5 REFERENCES

[1] R. J. Mortimer. Chem Soci Rev. 26 (1997) 147.

[2] R. J. Mortimer, N. M. Rowley, Metal complexes as dyes for optical data storage and electrochromic materials in: J. A. McCleverty, T. J. Meyer, M. D. Ward (Eds.), Comprehensive Coordination Chemistry - II: From Biology to Nanotechnology 9.2, Elsevier, Oxford, 2004 pp. 581–619.

[3] A. Juris, V. Balzani, F. Barigelletti, S. Campagna, P. Belser, A. V. Zelewsky. Coord. Chem. Rev. 84 (1988) 85.

[4] A. A. Argun, P. H. Aubert, B. C. Thompson, J. R. Reynolds. Chem. Mater. 16 (2004) 4401.

[5] D. A. Walsh, T. E. Keyes, R. J. Forster. J. Electroanal. Chem. 538 (2002) 75.

[6] R. J. Forster, T. E. Keyes, A. M. Bond. J. Phys. Chem. B 104 (2000) 6389.

[7] R. J. Forster, T. E. Keyes. Phys. Chem. Chem. Phys. 3 (2001) 1336.

[8] L. Keane, C. Hogan, R. J. Forster. Langmuir 18 (2002) 4826.

[9] (a) E. J. Laviron. J. Electroanal. Chem. 52 (1974) 395. (b) A. P. Brown, F. C. Anson. Anal. Chem. 49 (1977) 1589.

[10] J. Hjelm, R. W. Handel, A. Hagfeldt, E. C. Constable, C. E. Housecroft, R. J. Foster. J. Phys. Chem. B 107 (2003) 10431.

[11] S.W. Feldberg and I. Rubinstein, J. Electroanal. Chem. 240 (1988) 1.

[12] S. E. Creager, G. K. Rowe. Anal. Chim. Acta. 246 (1991) 233.

[13] G. K. Rowe, S. E. Creager. Languir 7 (1991) 2307.

[14] T. Nagamura, K. Sakai. J. Chem. Soc. Faraday Trans. 84 (1988) 3529.

[15] T. Nagamura, K. Sakai. Chem. Phys. Leter. 141 (1987) 553.

[16] D. A. Buttry. Langmuir 6 (1990) 1319.

[17] A. M. Bond, F. J. Marken. Electroanal. Chem. 372 (1994) 125.

[18] P. J. Kuleszea, L. R. Faulkner. J. Am. Chem. Soc. 115 (1993) 11878.

[19] R. M. Wightman, D. O.Wipf. Electroanalytical Chemistry, A. J. Bard., Ed.; Marcel Dekker: New York, 1989, Vol. 15.

[20] A. J. Bard, L. R. Faulkner. Electrochemical Methods: Fundamentals and Applications; 2 Ed.; Wiley: New York, 2001.

[21] R. J. Forster and J. G. Vos in Comprehensive Analytical Chemistry, Ed. G. Svehla, Elsevier, Amsterdam, 1992, vol. XXVII, p. 465.

[22] R. J. Forster, A. J. Kelly, J. G. Vos. J. Electroanal. Chem. 270 (1989) 365.

[23] Y. Marcus. Ion Properties; Marcel Dekker: New York, 1997.

[24] S. M. Oh, L. R. Faulkner. J. Am. Chem. Soc. 111 (1989) 5613.

[25] A. M. Bond, S. Fletcher, F. Marken, S. J. Shaw, P. G. Syons. J Chem. Soc., Faradsy Trans. 92 (1996) 3925.

[26] A. M. Bond, S. Fletcher, P. G. Symons. Analyst. 123 (1998) 1891.

[27] E. W. Paul, A. J. Ricco, M. S. Wrighton. J. Phys. Chem. 89 (1985) 1441.

[28] J. W. Thackeray, H. S. White, M. S. Wrighton. J. Phys. Chem. 89 (1985) 5133.

[29] D. Ofer, R. M. Crooks, M. S. Wrighton. J. Am. Chem. Soc. 112 (1990) 7869.

[30] H. Dahms. J Phys. Chem. 72 (1968) 362.

[31] I. Ruff, V. J. Friedrich, K. Demeter, K. Csillag. J. Phys. Chem. 75 (1971) 3303.

[32] R. H. Terrill, J. E. Hutchinson, R. W. Murray. J. Phys. Chem. B 101 (1997) 1535.

[33] W. P. Wuelfing, S. J. Green, J. J. Pietron, D. E. Cliffel, R. W. Murray. J. Am. Chem. Soc. 122 (2000) 11465.

CHAPTER 4

Host-Guest Inclusion between [Os(CAIPA)$_2$Cl$_2$] and A Surface Immobilized β-CD-(4-py)$_2$ Backfilled Monolayer

4.1 INTRODUCTION

Molecular recognition via noncovalent interaction in host-guest chemistry has attracted interest for chemical sensing and biochemistry [1,2]. Cyclodextrins are cyclic oligosaccharides with a hydrophobic internal cavity and have become the most widely used host molecules to include a guest molecule by hydrophobic forces [3,4]. In particular, self-assembled cyclodextrins on gold or platinum surfaces can form an organized interfacial structure through a large number of weak interactions [5] and provides unique opportunities to increase fundamental understanding of self-organization, structure-property relationships, and interfacial phenomena [6]. Moreover, the inclusion behaviour between suitable guest molecules and immobilized CD host molecules is also available for the investigation of relationships between the molecular structure and molecular-recognition properties of CDs.

In this chapter, the two-step preparation of a backfilled di-6^A,6^D-deoxy-6-(4-pyridylmethyl)amino-β-cyclodextrin monolayer binding with pyridine on polycrystalline platinum electrodes is reported. The formation of this backfilled monolayer was demonstrated by measuring the changes of capacitance and blocking behaviour of the platinum electrode. Also, the effect of inclusion between electroactive guest molecules and the immobilized CD monolayer on the capacitance and blocking ability of the modified electrodes has been investigated.

4.2 EXPERIMENTAL

4.2.1 Materials.

β-CD-(4-py)$_2$ and [Os(CAIPA)$_2$Cl$_2$] were obtained as gifts from Reena Marthi within our group, where β-CD-(4-py)$_2$ is di-6^A,6^D-deoxy-6-(4-pyridylmethyl)amino-β-cyclodextrin, and CAIPA is 2-(4-carboxyphenyl)imidazo[4,5-f][1,10]-phenanthroline-1-adamantylamine. The structure of β-CD-(4-py)$_2$ and Os complex are shown in the Chart 4.1 and 4.2. Other chemicals were purchased from Sigma-Aldrich and used as received. Moreover, water was purified using a Milli-Qplus 185 Millipore installation.

4.2.2 Instrumentation and Methods

Electrochemistry was performed in conventional three-electrode cells using an Ag/AgCl electrode filled with 3 M KCl (aq) (CH instrument) as reference. Cyclic voltammetry (CV) and impedance measurements were carried out using a CH instruments Model 660a electrochemical workstation. Capacitance-potential traces were constructed using an excitation signal of 5 mV at a frequency of 518 Hz and capacitance-time profiles were obtained at potentials of 0.3 V. All electrolyte solutions were deoxygenated for at least 15 min using N$_2$ gas before use and maintained under a nitrogen blanket during measurement.

Raman spectroscopy was conducted on a Dilor. Jobinyvon. Spex Labram. Excitation at 514 nm was accomplished using an Argon ion laser. A backscattering geometry was used to collect scattered light by using an air cooled CCD array by interchangeable gratings, 1800 lines/mm. Before use, the wavenumber axis of the Raman was calibrated with the silicon line at 521 cm^{-1}.

3 mm diameter macro-platinum working electrodes were polished successively with 1.0, 0.3, and 0.05 μm alumina powders on polishing pads and sonicated in Milli-Q water for 15 mins to remove any absorbed alumina powders from the surface after each accomplished polishing. Then, these electrodes were further electrochemical cleaned in 0.5 M H$_2$SO$_4$ (Figure 4.1). A salt bridge filled with 0.5 M H$_2$SO$_4$ was used

to separate the reference electrode from the electrolyte solution to prevent the working electrolyte solution being contaminated by chloride ions. Platinum working electrodes were first scanned between -0.25 and 1.45 V at a scan rate of 0.1 V/s for 10 cycles and then between -0.2 and 1.35 V until a stable voltammetric response was obtained. Finally, the electrodes were hold at 0.3 V for 30 s to remove absorbed hydrogen from the electrode surfaces. The microscopic area of the platinum electrode surface can be obtained from the charges passed under the platinum oxide reduction peak in 0.5 M H_2SO_4, taking the charge per cm^2 as 420 μC for platinum [7].

The formation of CD monolayer on the platinum electrode surface is based on the reported methods developed in our group previously [8]. Monolayers of β-CD-$(4\text{-py})_2$ were self-assembled onto the surface of the platinum electrodes by immersing the electrodes in the solutions containing 100 μM β-CD-$(4\text{-py})_2$ at room temperature overnight. Backfilling the layers was obtained by further immersing the β-CD-$(4\text{-py})_2$ layers in a solution containing 2 mM 1-admantylamine and 0.2 mM 1-nonanethiol in ethanol for at least 40 h. Monolayer containing Os complexes as guests backfilled with 1-admantylamine were formed by immersing the backfilled CD layer in 0.1 mM Os complex in H_2O/ACN (9:1). Both treated and untreated monolayers of β-CD-$(4\text{-py})_2$ were rinsed with Milli-Q water before use.

Aqueous $[Os(CAIPA)_2Cl_2]$ solutions in the concentration range from 2 – 45 μM were prepared in H_2O/ACN (9:1) containing 0.1 M $LiClO_4$ as supporting electrolyte by dissolving the Os complex first in pure acetonitrile and followed by addition of water.

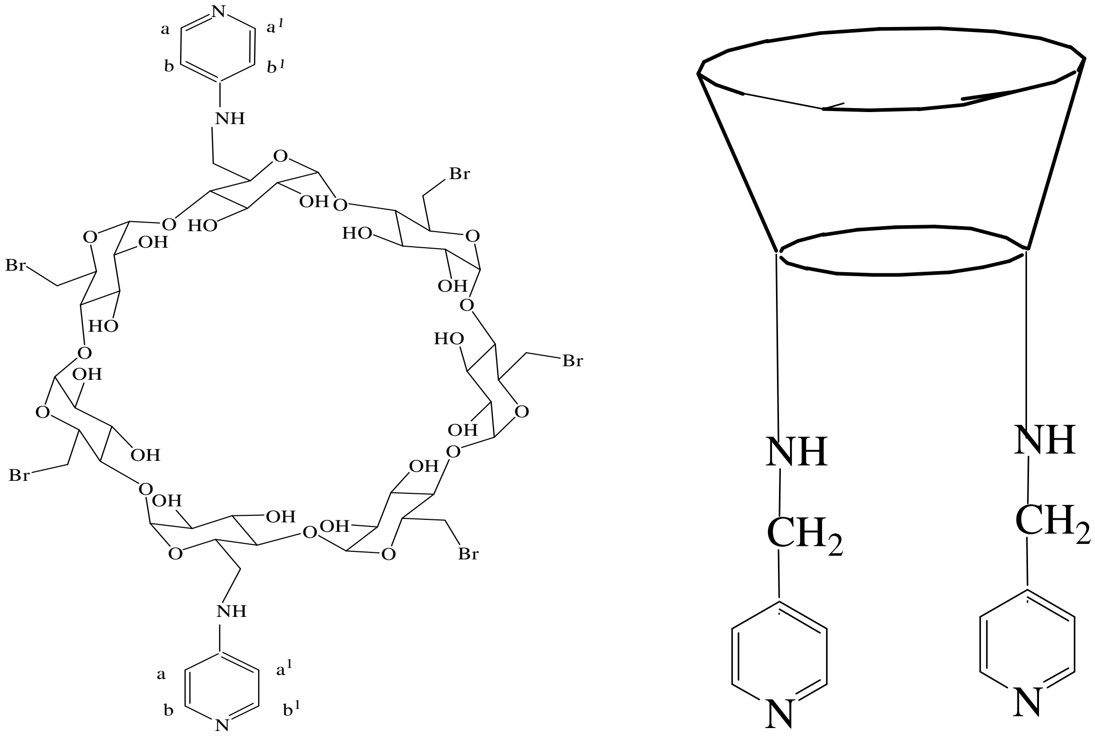

Chart 4.1. The structure of β-CD-(4-py)$_2$.

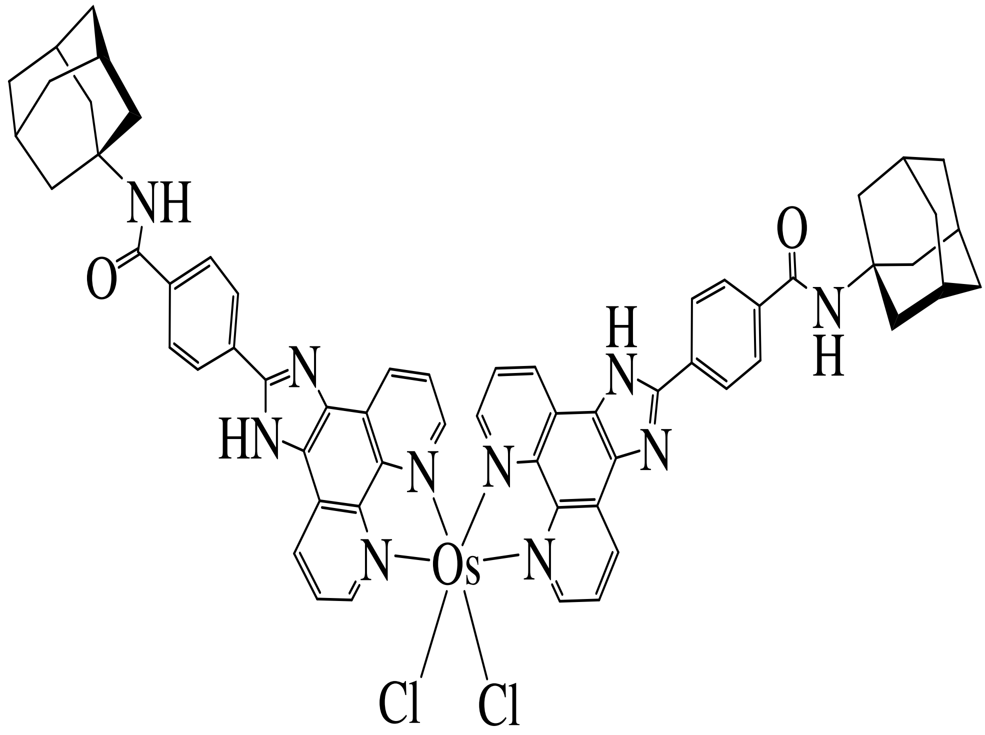

Chart 4.2. The structure of [Os(CAIPA)$_2$Cl$_2$], where CAIPA is 2-(4-carboxyphenyl)imidazo[4,5-f][1,10]-phenanthroline-1-adamantylamine.

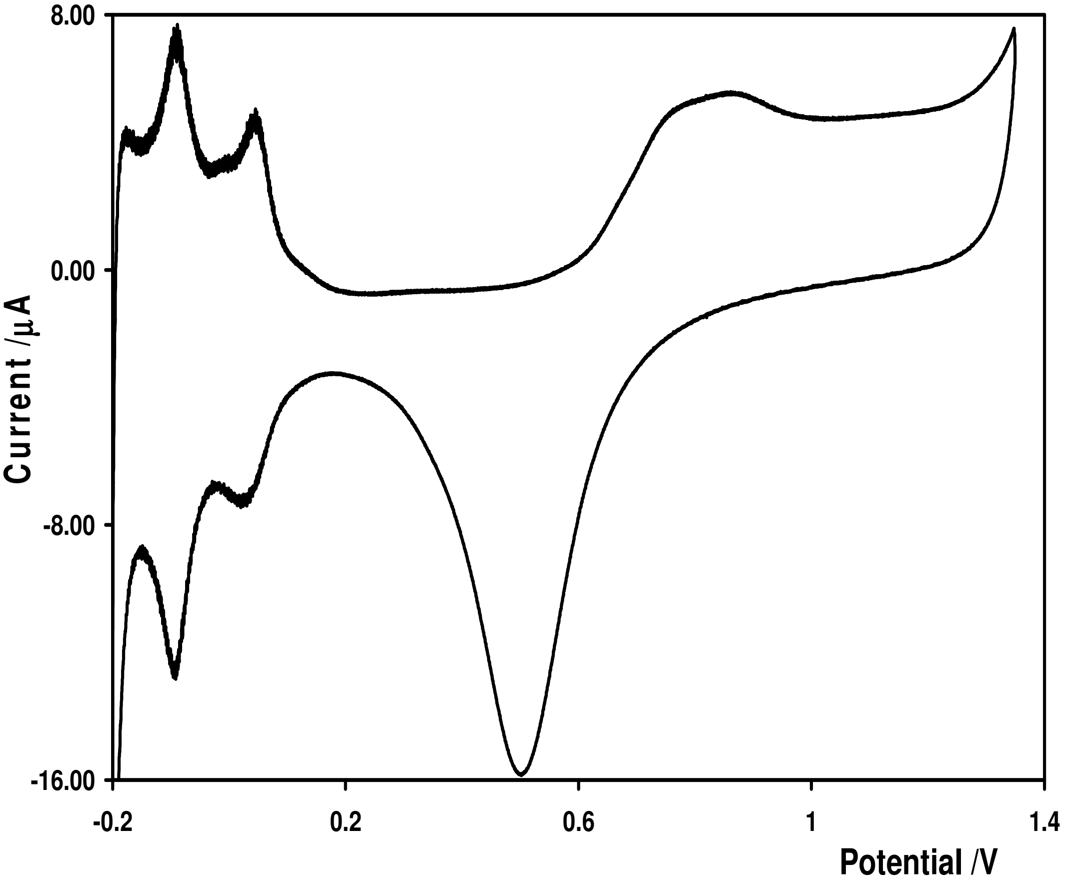

Figure 4.1. Voltammetric response for electrochemical cleaning of a 3 mm diameter platinum electrode in 0.5 M H_2SO_4 at scan rate of 0.1 V/s. The redox potentials of the platinum electrode are around 0.8 V and 0.5 V for oxidation and reduction processes, respectively.

4.3 RESULTS AND DISCUSSION

4.3.1 Capacitance Properties of the Backfilled Monolayer

Capacitance is due to the build-up of electrolyte counterions at the electrode surface, which generates an electrochemical double layer between an electrode and the electrolyte solution. When a redox-inactive monolayer forms on the electrode surface, it pushes the compact electrolyte counterions layer away from the electrode surface, consequently decreasing the interfacial capacitance. Thus, capacitance is the important factor to be used to monitor the successful formation of a monolayer.

Figure 4.2 shows capacitance-potential profiles for platinum electrodes before and after each one of processes of the monolayer modification in 0.1 M $LiClO_4$. The electrode capacitances measured over the range from 0 V to 0.5 V are reduced after a cleaned Pt electrode exposed to 100 μM β-CD-(4-py)$_2$ solution overnight. It suggests that the CDs are adsorbed and form a self-assembled monolayer on the electrode surface. Subsequent treatment with 1-nonanethiol results in a further substantial drop in capacitance, which are somewhat independent of the potential and exhibit an average value of 3.2 μF/cm^2. This observation indicates that a more compact and pinhole free layer is formed as the backfilling process with 1-nonanethiol seals the active sites of the Pt electrode surface between adjacent CDs and prevents the counterions permeation through the backfilled monolayer to the electrode surface.

Figure 4.2 also illustrates that capacitance properties of alkanethiol layer formed at the electrochemically cleaned Pt electrode surface after 40 h exposing the electrode to the backfilling solution containing 0.2 mM 1-nonanethiol in ethanol. The alkanethiol layer exhibits an average capacitance value of 0.9 μF/cm^2, which is much lower than that obtained from the backfilled CD layer. This suggests that the self-assembled pyridine bound CD molecules are not replaced by the alkanethiol molecules from the Pt electrode surface. This observation is consistent with previous report in our research group [8], where the capacitance properties of the backfilled γ-CD-(4-py)$_2$ monolayer has been investigated.

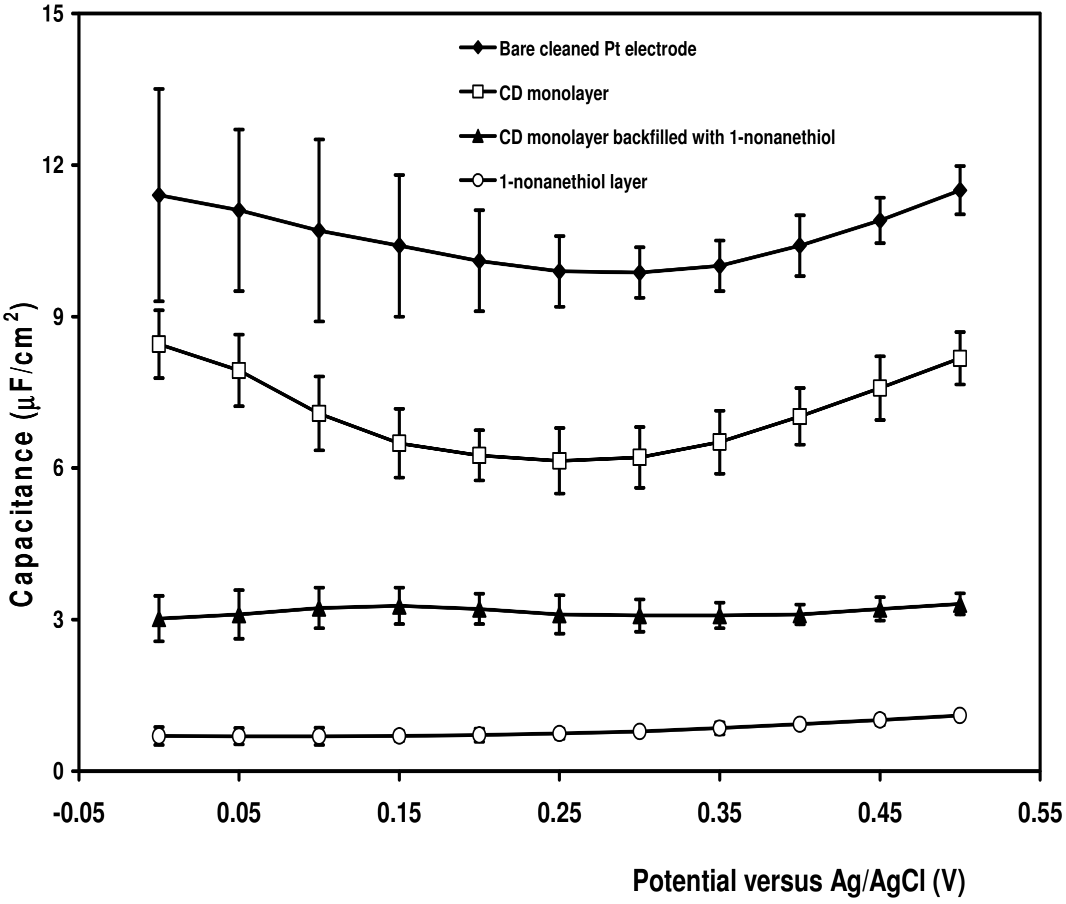

Figure 4.2. Capacitance measurements from AC impedance for bare Pt electrode, and β-CD-(4-py)$_2$ monolayer, backfilled CD layer, 1-nonanethiol layer modified Pt electrodes in 0.1 M LiClO$_4$. The numbers of repetitive measurement (n=5).

4.3.2 Blocking Behaviour of the Backfilled Monolayer

A self-assembled monolayer at an electrode surface acts as a barrier between the electrode surface and electroactive species in the solution. The blocking effect is heavily influenced by defects or pinholes, at which electron transfer electron transfer reactions between electroactive species and electrode surface may take place with considerably less hindrance [9]. Ferrocyanide is used as the water-soluble electroactive specie, due to its well defined electrochemistry and reversible electron kinetics [10,11,12]. Moreover, the voltammetry of ferrocyanide is very sensitive to the nature of the electrode surface [13,14] and is sensitive to ion-pairing effects. It results in the changes in the peak to peak separation, ΔE_p, values and redox peak currents for the surface modified electrodes. In this section, the blocking behaviours of the monolayers of β-CD-(4-py)$_2$, backfilled CDs and pure alkanethiol using 1 mM $[Fe(CN)_6]^{4-}$ in 0.1 M $LiClO_4$ as the water-soluble probe were investgated.

Figure 4.3 shows voltammetric response on (A) bare Pt electrode, (B) β-CD-(4-py)$_2$ monolayer, (C) β-CD-(4-py)$_2$ monolayer backfilled with 1-nonanethiol, and (D) 1-nonanethiol layer. As expected, the voltammetric response on bare Pt electrode is close to ideally reversible (ΔE_p = 57 mV) with a ΔE_p of 72 mV. However, Figure 4.3 (B) and Table 4.1 show that β-CD-(4-py)$_2$ monolayer increases the ΔE_p value from 72 mV to 163 mV and reduces the peak current by 40-60% compared to the bare Pt electrode. These differences are due to the presence of the β-CD-(4-py)$_2$ monolayer, since ferrocyanide does not transfer through the CD cavity because of its relative size [15]. However, ferrocyanide can permeate through defects remaining between the CD cavities. Furthermore, as shown in Figure 4.3 (C) and Table 4.1, the backfilled CD monolayer exhibits much greater blocking behaviour than the CD monolayer presumably due to defects being blocked by adsorbed alkanethiols. This observation indicates that the backfilled monolayer is relatively defect free compared to the CD layer. Finally, Figure 4.3 (D) illustrates that the signal of peak current totally disappears when a hydrophobic alkanethiol layer is formed on cleaned Pt electrode. This behaviour suggests that the alkanethiol layer is defect free and ferrocyanide can not permeate through the layer to the electrode surface. Also, the difference between Figure 4.3 (C) and (D) further confirms that the surface bound CD layer is not lost during the backfilling step.

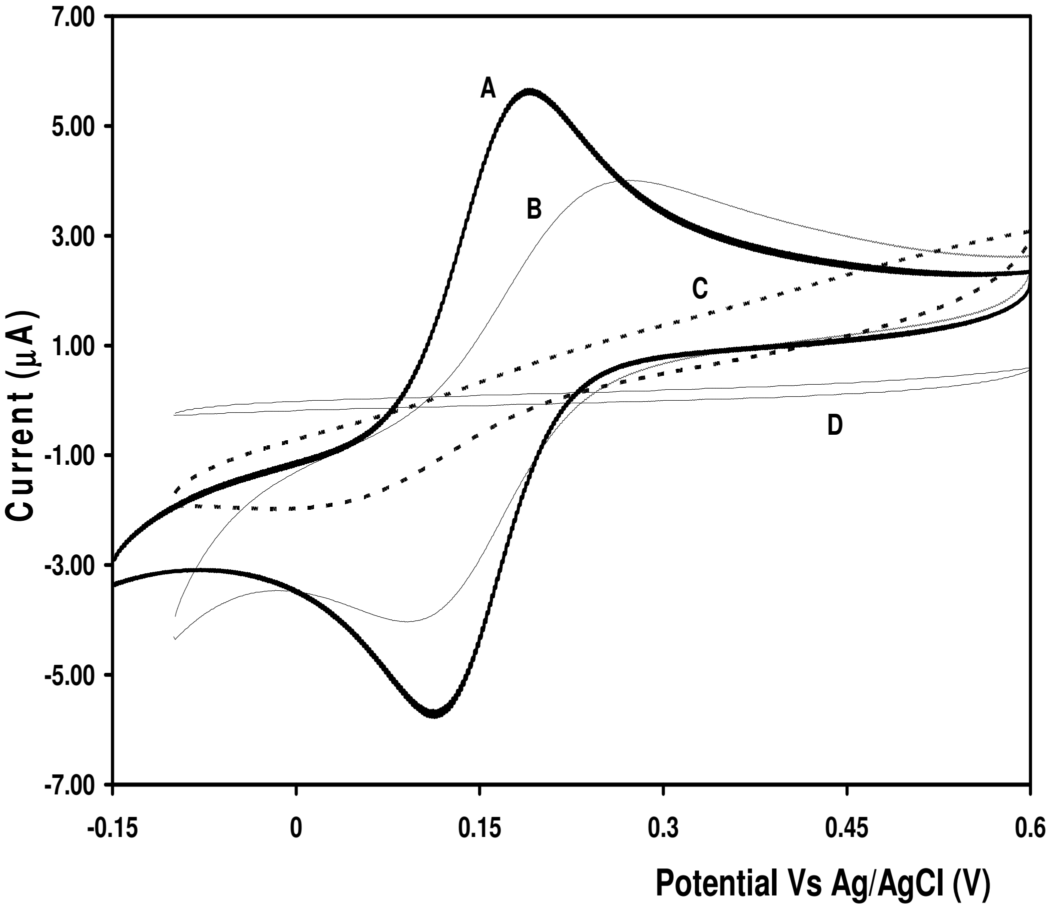

Figure 4.3. Voltammetric response of (A) bare Pt electrode, and platinum electrode modified with (B) β-CD-(4-py)$_2$ monolayer, (C) β-CD-(4-py)$_2$ monolayer backfilled with 1-nonanethiol, and (D) 1-nonanethiol layer. The electrolyte is aqueous 1 mM $[Fe(CN)_6]^{4-}$ at 0.1 M $LiClO_4$. In all cases, scan rate is 0.1 V s^{-1}.

Table 4.1. Peak-to-peak separations and current ratios for the different modifications at electrochemically cleaned Pt electrode surface in 0.1 M $LiClO_4$ containing 1 mM $[Fe(CN)_6]^{4-}$ at a scan rate of 0.1 V s^{-1}. The numbers of repetitive measurement (n=5).

Pt electrode modification	ΔE_p ***(mV)***	I_{ox} / I_{bare}	I_{red} / I_{bare}
Bare	72±4	1	1
CD monolayer	163±5	0.6±0.04	0.4±0.06
Backfilled CD monolayer	N/A	N/A	0.16±0.03
Alkanethiol layer	N/A	N/A	N/A

4.3.3 Effect of Host-Guest Inclusion on Capacitance of Backfilled Monolayer

The backfilling process forces the CD monolayer into an upright orientation while making the CD host more amenable to inclusion with bulky solution-phase guests [8]. When immersed in the Os complex solution, the backfilled CD monolayer stimulates binding of adamantyl group ends of [Os(CAIPA)$_2$Cl$_2$] to the β-CD cavities through the host-guest molecular interaction, as the adamantyl group has a high-affinity for inclusion in CD. Figure 4.4 illustrates [Os(CAIPA)$_2$Cl$_2$] included in the CD cavity of the backfilled layer. Osmium complexes were used as guests because of their low redox potential at around -0.1 V. Their binding properties with the backfilled monolayer are reported in the following sections.

Surprisingly, binding of the metal complex raises the capacitance of the backfilled layer. For example, as shown in Figure 4.5, the capacitance of the backfilled monolayer was monitored for 10 min and a very stable baseline was obtained at approximately 3.15 μF/cm^2, which is similar to that obtained in the previous section. However, injection of Os complex results in an increase of capacitance of the backfilled monolayer to about 3.85 μF/cm^2 after 30 min. Over a longer monitoring time scale (Figure 4.6), the capacitance gradually increases over a range of potential from 0 to 0.5 V when the backfilled monolayer was exposed to the Os complex solution for 5 min, 1h, 20h and 46h. After immersing for 46 h, the capacitance is stable at around 4.43 μF/cm^2.

Compared to the capacitance of bare Pt electrode and CD monolayer modified Pt electrodes, this increase in capacitance is very weak. It indicates that neither the CD layer nor the thiol molecules are lost or exchanged during the process because loss of backfilled layer would increase the electrochemically active sites of the electrode surface, thus increasing the capacitance significantly. Rather, these observations are probably attributable to the electrostatic properties of the Os guest complexes. A charged redox-active layer is formed when Os complexes are included into the CD cavities. It is likely to increase the capacitance of the modified electrode due to the additional ions and solvent [16,17,18].

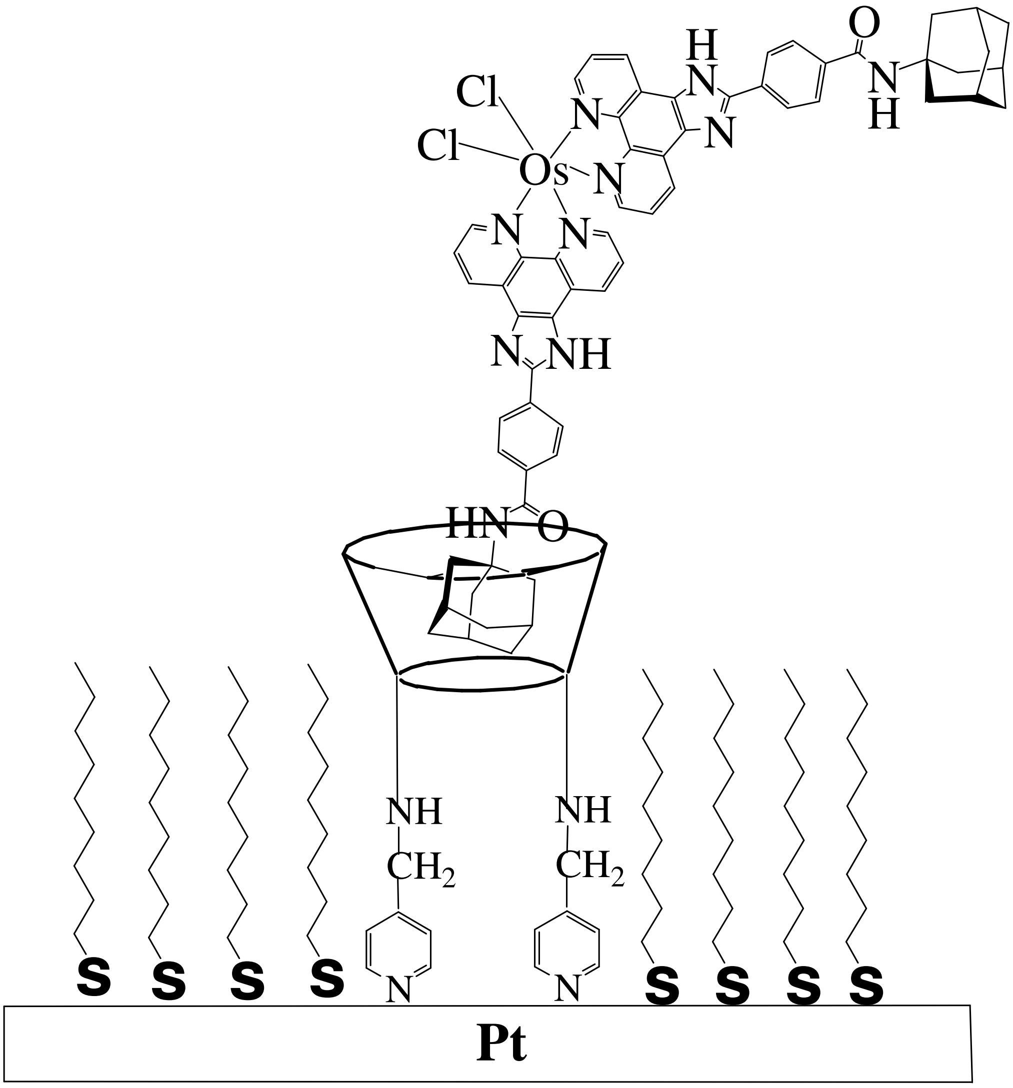

Figure 4.4. The possible binding of [Os(CAIPA)$_2$Cl$_2$] to the CD cavity of the backfilled layer.

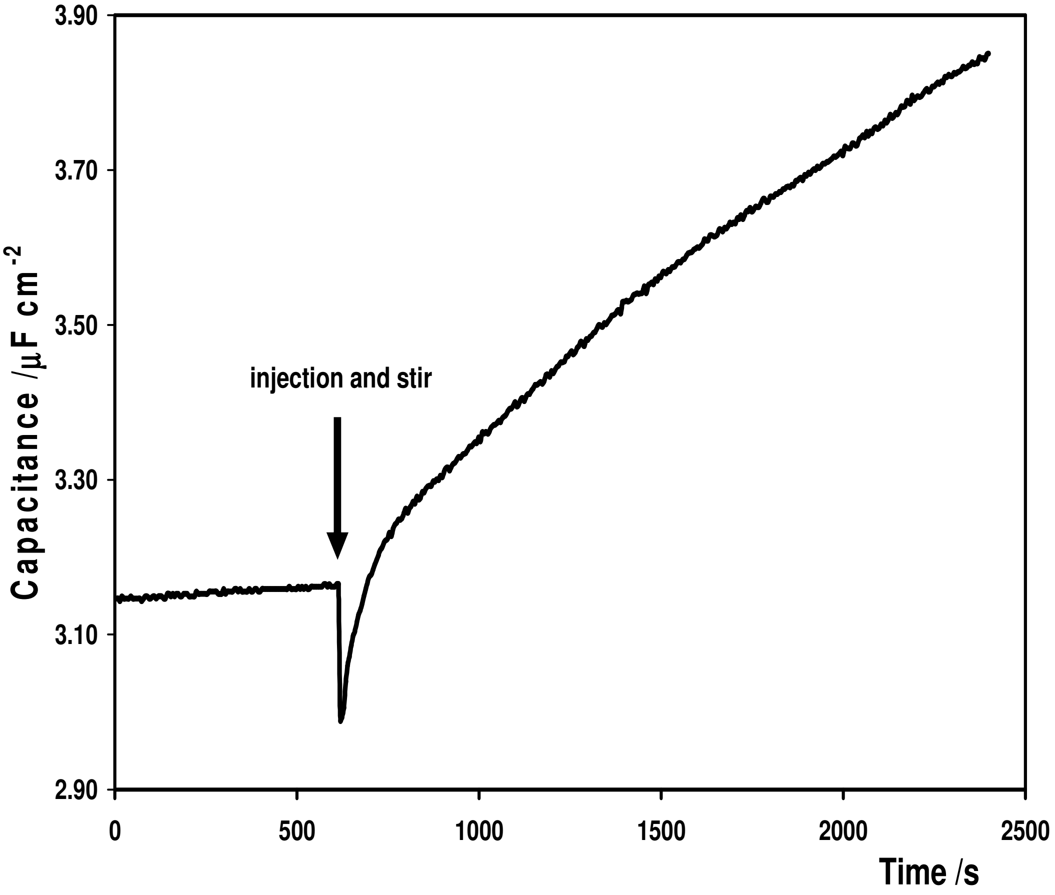

Figure 4.5. Capacitance-time profiles of the backfilled monolayer obtained at potentials of 0.3 V in 0.1 M $LiClO_4$. 100 μl of 0.02 M Os complex solution was injected at 10 min and capacitance was monitored for 30 min.

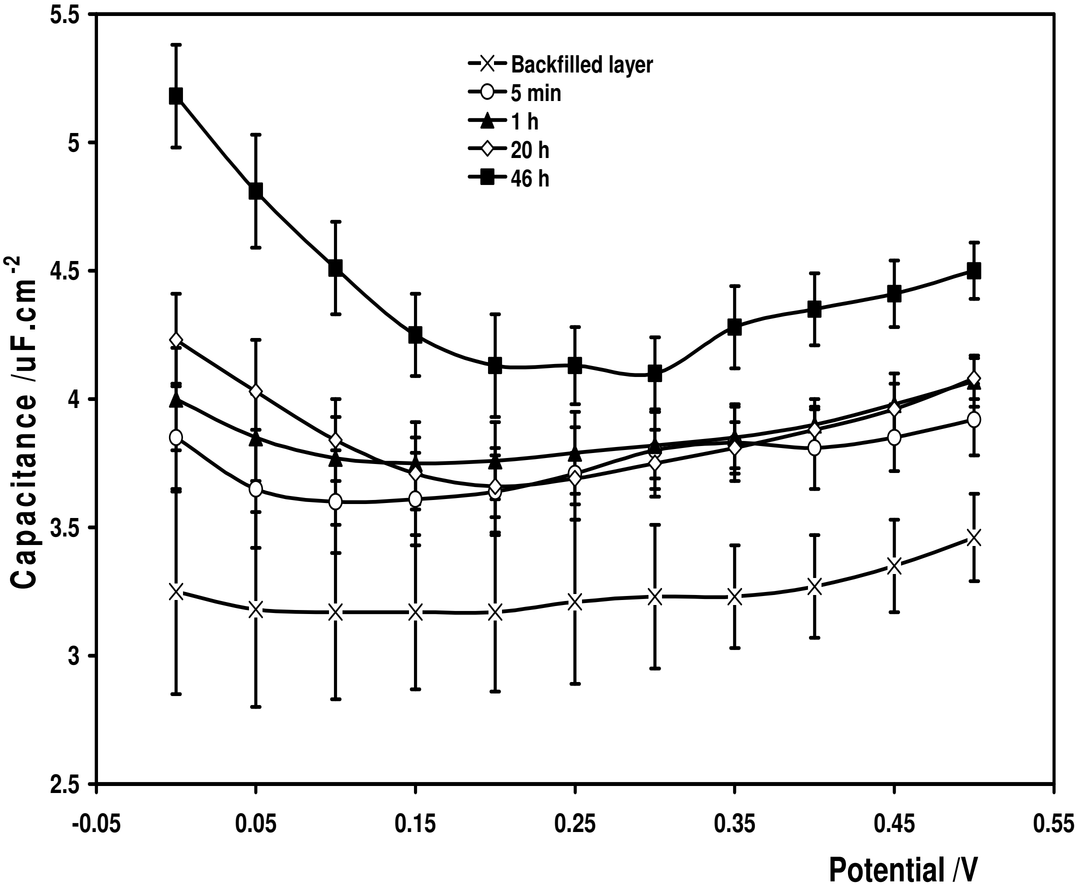

Figure 4.6. Capacitance of the backfilled monolayer and after 5 min, 1 h, 20 h, 46 h immersed in $[Os(CAIPA)_2Cl_2]$ solution in 0.1 M $LiClO_4$. The numbers of repetitive measurement (n=5).

4.3.4 Effect of Host-Guest Inclusion on Electron Transport of Backfilled Monolayer

The previous section indicates that the backfilling process creates a relatively defect free CD monolayer on the Pt electrode and this monolayer is responsible for the electrode passivation. However, as shown in Figure 4.7, the reversibility of the CD backfilled monolayer modified Pt electrode is restored as the Os complex becomes included into the CD cavities. This observation suggests that the Os complexes provide the necessary conduction pathways to promote the electron transfer from electrode surface to the $[Fe(CN)_6]^{4-}$ redox probes, probably due to the electrostatic interaction between the positively charged Os^{2+} redox active centre and the negatively charged redox probe[19,20]. The redox process of Os complex are not observed in Figure 4.7, because the concentration of Os complex is significantly low compared to the bulk concentration of $[Fe(CN)_6]^{4-}$ redox probes. After being further seeded with Os complexes on a longer time scale, the modified electrodes exhibit more reversible and enhanced behaviour of the peak current. Table 4.2 shows that the ΔE_p value decreases from 143 mV, when the backfilled layer is exposed to Os complex solution for 10 s, to 85 mV, after the layer immersed in Os guest solution for 46 h. This suggests that the electron transfer process that is blocked with the backfilled CD monolayer is restored upon association of the Os complexes into the CD cavities. Taken together, the reversibility of the Os/backfilled CD/Pt electrode is remarkably improved to the similar level as that of bare Pt electrode as the electrochemical active sites of this modified electrode are increased when more Os guest molecules are induced into the CD cavities.

The electrode reaction is controlled by the electron-transfer kinetics. As a function of scan rate, the electron transfer rate constant of the electrode reactions can be associated with the peak potential separation, ΔE_p, using the kinetic parameter, ψ, and Equations 4.1 and 4.2 [21]:

$$\psi = \frac{k^o}{\left(D_0 \pi \frac{nF}{RT} \upsilon \right)^{1/2}} \qquad \textbf{(4.1)}$$

where D_0 is the standard diffusion coefficient and υ is scan rate.

$$\Delta E_p = f(\psi) \qquad \textbf{(4.2)}$$

At the bare Pt electrode the current for the $[Fe(CN)_6]^{4-}$ redox probe depends on linearly on $\upsilon^{1/2}$. Under these conditions, the Randles-Sevcik equation allows the diffusion coefficient, D_o, value to be determined as 2.1×10^{-6} cm^2 s^{-1}. In Table 4.2, the rate constants of different modified electrodes are calculated at a scan rate of 0.1 V s^{-1}. At this scan rate, defects in the backfilled CD monolayer can result in overlapping linear diffusion layers. The effect of ohmic drop is minimal and is less than a few mV. The rate constant of the backfilled layer exposed to Os guest solution increases with increasing occupancy of Os^{2+}. This indicates that the electrochemical activity of the modified electrode has been increased by the inclusion of Os complex into the CD cavity as the kinetics of the electrode reaction appear faster than the electron transfer rate of the CD backfilled monolayer. The fraction of the total active area will manifest itself as an apparent kinetic limitation [22]. Equation 4.3 shows that the fraction of the total active area ($1-\theta$) can be associated with the standard electron rate of bare electrode (k^o) and the apparent rate constant (k_{app}) [23].

$$k_{app} = k^o(1-\theta) \qquad \textbf{(4.3)}$$

The inclusion of Os complex into the CD cavity results in an increase of electrochemical active sites of Os centres compared to the CD backfilled monolayer. Therefore, this increases the fraction of the total active area.

Further, resonance Raman was conducted to confirm the binding of the $[Os(CAIPA)_2Cl_2]$ to the CD backfilled monolayer using excitation at 514 nm. This excitation wavelength is close to resonance with the absorption features of the $[Os(CAIPA)_2Cl_2]$ complex at 410 and 500 nm. Spectra recorded for the backfilled layer alone contained no information as the surface enhancement due to the very limited SERs ability of platinum at this wavelength and no resonance excitation occurs. However, some features, such as 1600, 1556, 1483, 1443, 1321, and 1039 cm^{-1} are observed and attributed to the CAIPA unit vibration [24,25,26]. This observation indicates the presence of $[Os(CAIPA)_2Cl_2]$ because of the host-guest inclusion with CD cavities in the backfilled layer.

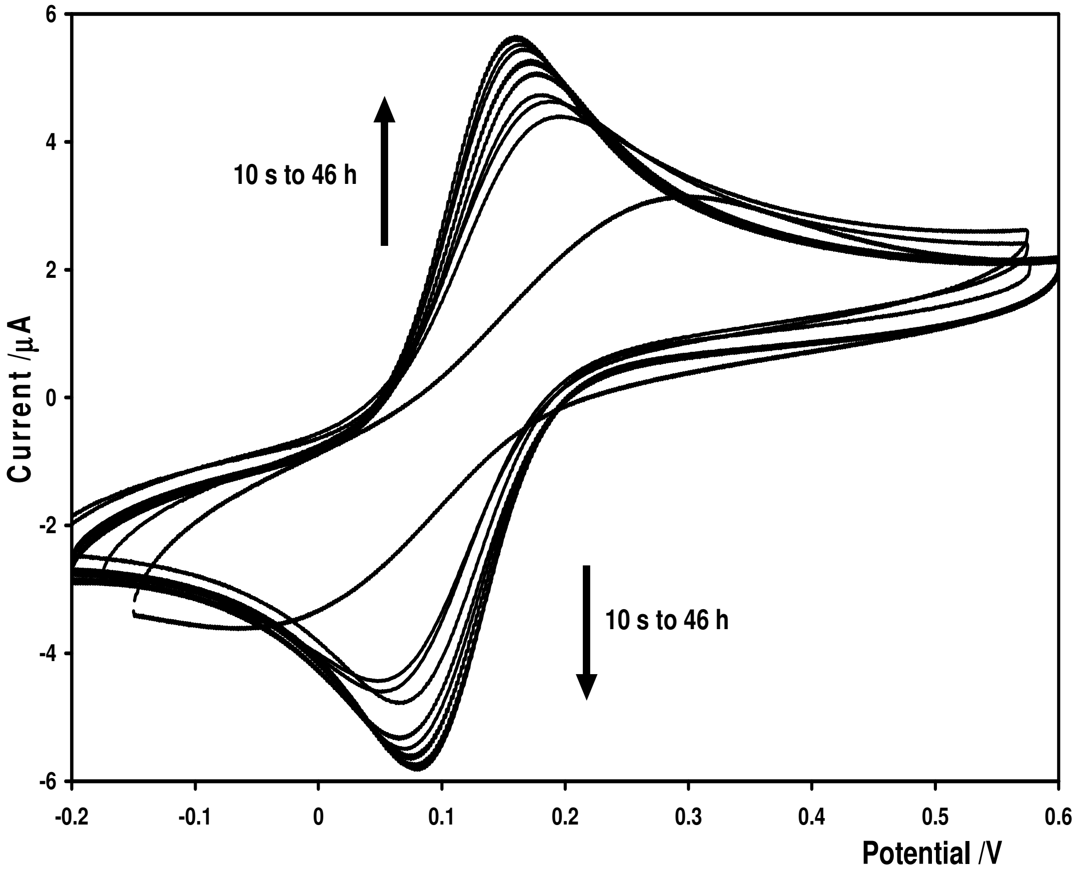

Figure 4.7. From top to bottom, voltammetric response of a CD backfilled monolayer modified Pt electrode after exposed to 0.1 M Os guest solution for 46 h, 20 h, 1 h, 30 min, 5 min, 1 min, 30 s, 10 s, and 0 s (the backfilled CD monolayer layer). 1 mM $[Fe(CN)_6]^{4-}$ is used as the water-soluble electroactive species and the supporting electrolyte is 0.1 M $LiClO_4$ aqueous solution. In all cases, the scan rate is 0.1 V s^{-1}.

Table 4.2. Rate of electron transport related to *ΔE_p* and the fraction of total active area for backfilled CD monolayer and the layer after exposed to 0.1 M Os guest solution for 10 s , 30 s, 1 min, 5 min, 30 min, 1 h, 20 h, and 46 h in 1 mM $[Fe(CN)_6]^{4-}$ in 0.1 M $LiClO_4$ at a scan rate of 0.1 V s^{-1}.

	***ΔE_p* (mV)**	***Ψ* ref[21]**	***k* (cm.s^{-1})**	***1-θ***
Bare Pt electrode	72	2.01	1.0×10^{-2}	-
Backfilled CD monolayer	278	0.1	5.1×10^{-4}	5.1%
10 s	143	0.238	1.2×10^{-3}	12%
30 s	135	0.269	1.4×10^{-3}	14%
1 min	120	0.356	1.8×10^{-3}	18%
5 min	112	0.417	2.1×10^{-3}	21%
30 min	101	0.568	2.9×10^{-3}	29%
1 h	96	0.653	3.3×10^{-3}	33%
20 h	89	0.77	3.9×10^{-3}	39%
46 h	85	0.92	4.7×10^{-3}	47%

4.3.5 Binding Ability Between [Os(CAIPA)$_2$Cl$_2$] and Backfilled CD Monolayer

Figure 4.8 shows the voltammetric responses for bare Pt electrode and a backfilled β-CD-(4-py)$_2$ monolayer modified Pt electrode in 10 μM [Os(CAIPA)$_2$Cl$_2$] in H$_2$O/ACN (9:1) containing 0.1 M LiClO$_4$ electrolyte at the scan rate of 30 V s^{-1}. No significantly detectable Os$^{2+/3+}$ couple response is reserved for the bare Pt electrode, due to the low bulk concentration of [Os(CAIPA)$_2$Cl$_2$]. However, voltammetric response of the backfilled CD monolayer modified Pt electrode shows the reversible Os$^{2+/3+}$ couple at -0.096 V with the ΔE_p about 49 mV. The ΔE_p is higher than that expected for an ideal surface confined signal, but this value is significantly lower than that expected for a solution phase species (57 mV). This observation indicates that the response for the Os$^{2+/3+}$ couple is surface confined.

Also, Figure 4.9 illustrates the scan rate dependent cyclic voltammetry of the backfilled CD monolayer modified platinum electrode over a range of scan rates between 30 to 200 V s^{-1} in the same conditions. For this range of scan rates, the response of a surface confined signal for the Os$^{2+/3+}$ couple is consistent at -0.096 V and the peak current scales linearly with scan rate (Figure 4.10).

Fast scan rates ($\geq$ 30 V s^{-1}) are employed to investigate the interaction between [Os(CAIPA)$_2$Cl$_2$] and the surface attached cyclodextrins as fast scan rates minimise the contribution from the solution phase [Os(CAIPA)$_2$Cl$_2$] redox species to the overall current response. Under these conditions, the surface coverage of surface confined Os$^{2+/3+}$ couple can be determined by integrating the oxidation and reduction peaks, based on the real surface area of the electrochemically cleaned platinum electrode.

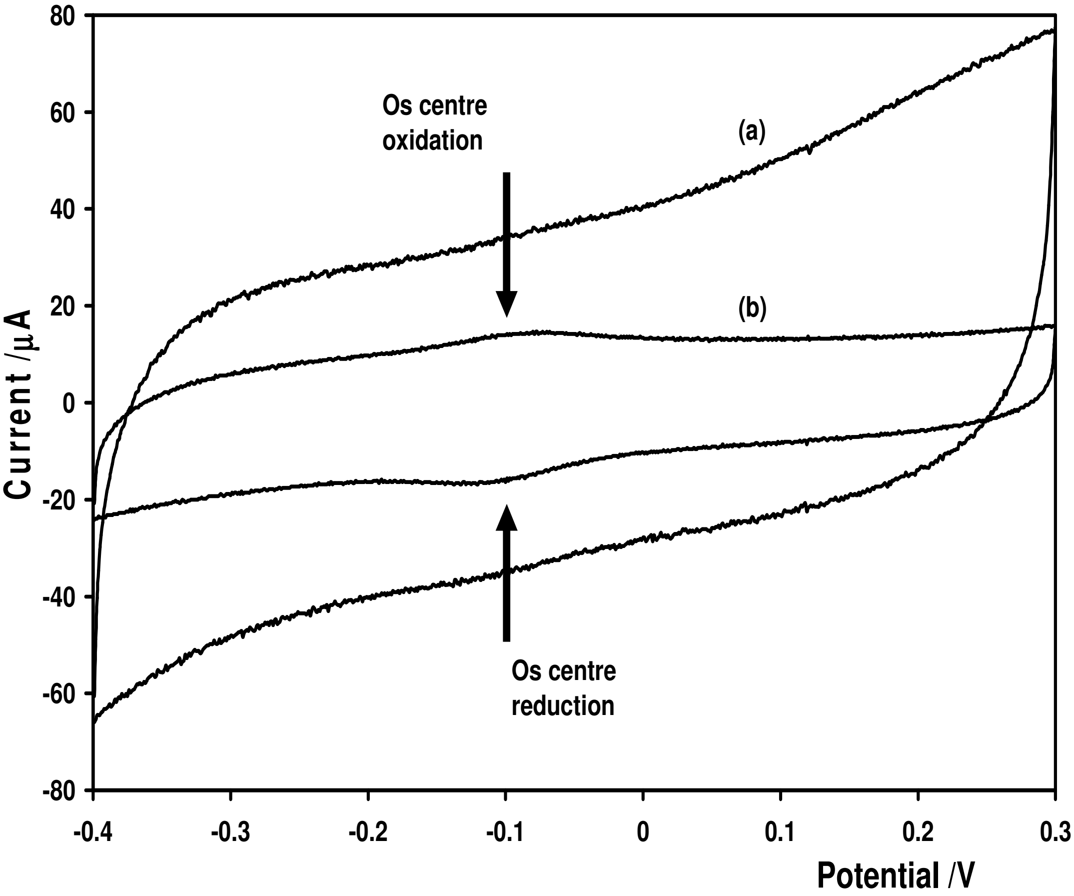

Figure 4.8. Voltammetric responses of (a) bare Pt electrode and (b) backfilled CD monolayer modified Pt electrode in 10 μM [Os(CAIPA)$_2$Cl$_2$] in H$_2$O/ACN (9:1) containing 0.1 M LiClO$_4$ electrolyte. Scan rates are 30 V s^{-1} in both cases. For the backfilled CD monolayer modified Pt electrode, the surface coverage from the anodic charge is 3.8×10^{-12} mol cm^{-2}.

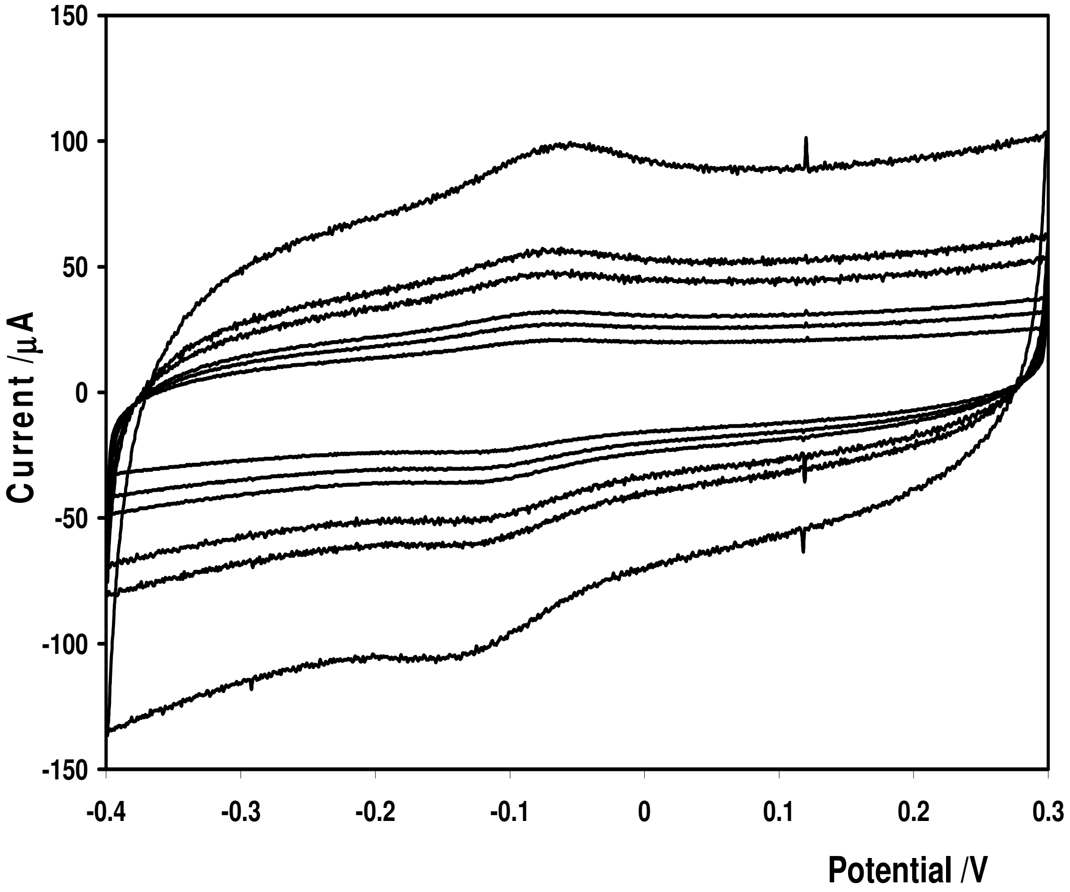

Figure 4.9. Cyclic voltammograms of backfilled CD monolayer modified Pt electrode in 10 μM [Os(CAIPA)$_2$Cl$_2$] in H_2O/ACN (9:1) containing 0.1 M $LiClO_4$ electrolyte. Scan rates are (from top to bottom) 200, 100, 80, 50, 40, and 30 V s^{-1}.

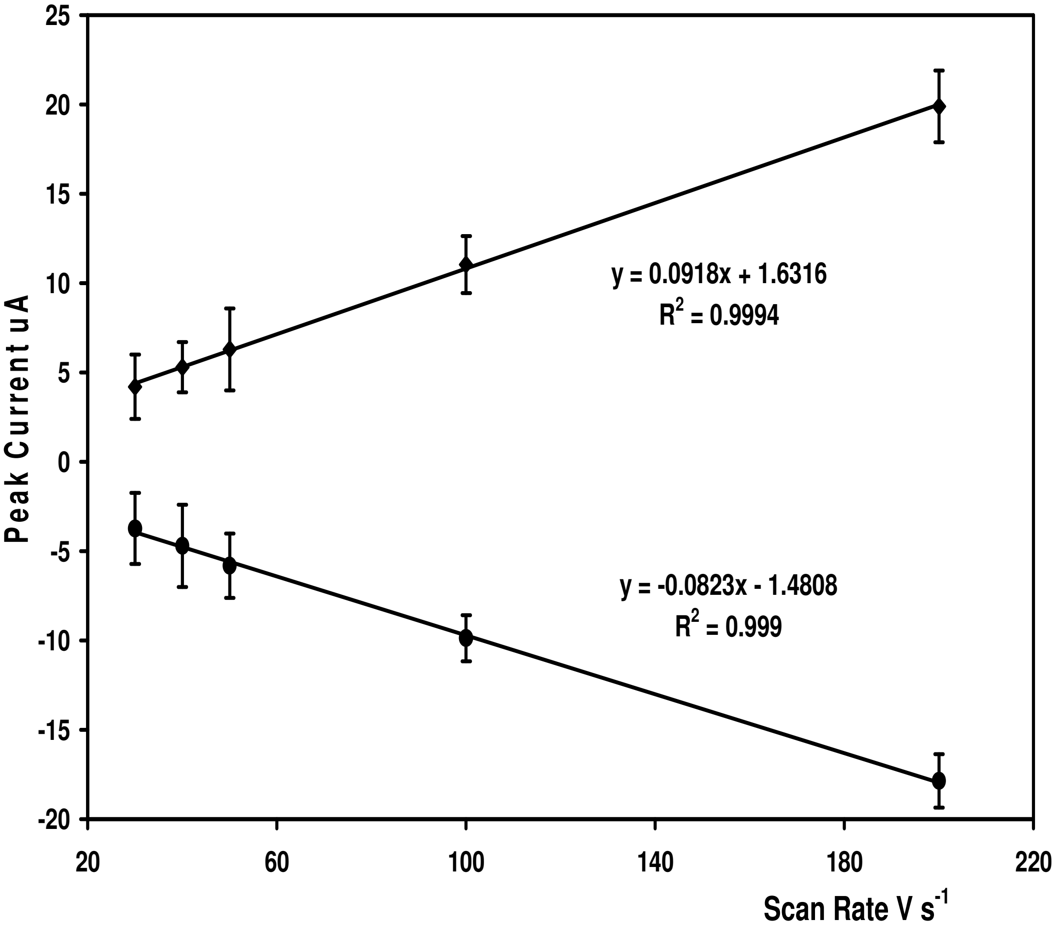

Figure 4.10. A plot of peak current Vs. scan rate for backfilled CD monolayer modified Pt electrode in 10 μM [Os(CAIPA)$_2$Cl$_2$] in H$_2$O/ACN (9:1) containing 0.1 M LiClO$_4$ electrolyte. Scan rates are 200, 100, 80, 50, 40, and 30 V s^{-1}. The numbers of repetitive measurement (n=5).

In order to better understand the binding ability between [Os(CAIPA)$_2$Cl$_2$] and backfilled CD monolayer, a Langmuir adsorption isotherm is used to determine the association constant (K_A) [8,10,27]. The dependence of the surface coverage on the concentration of [Os(CAIPA)$_2$Cl$_2$] in the solution has been investigated. The surface coverage for both Os^{2+} and Os^{3+} species follow Equation 4.4, which is derived from the Langmuir isotherm as shown in Figure 4.11, and saturate ion is expected at high [Os(CAIPA)$_2$Cl$_2$] concentration. However, a high concentration of Os complex solution can not be obtained because of the low solubility of the Os complex. The linear form of Equation 4.4 can be derived as Equation 4.5, which allows the maximum surface coverage and association constant for both Os^{2+} and Os^{3+} species to be determined from the slope and the intercept of the plot of C/Γ versus C in Figure 4.12. The Langmuir Equation is:

$$\frac{\Gamma}{\Gamma_{\max} - \Gamma} = \beta C \tag{4.4}$$

$$\frac{C}{\Gamma} = \frac{C}{\Gamma_{\max}} + \frac{1}{\beta \Gamma_{\max}} \tag{4.5}$$

where C is the bulk concentration of Os complex solution, Γ is the surface coverage, Γ_{max} is the maximum surface coverage, and β is the association constant for the guest-CD interaction, K_A. Also, the free adsorption energy can be obtained from the association constant using Equation 4.6,

$$\Delta G_{ads} = -RT \ln \beta \tag{4.6}$$

where R is the gas constant and T is the temperature in K. The values of the maximum surface coverage, association constant, and the free adsorption energy for the Os$^{2+/3+}$ couple are presented in Table 4.3.

The maximum surface coverage expected from linear best fit for the Os oxidation and reduction forms are 9.3±0.5×10^{-12} and 7.9±0.3×10^{-12} mol cm^{2-}, respectively. These values are about 10% of the theoretical surface coverage 8.9×10^{-11} mol cm^{2-}, where a close-packed β-CD-(4-py)$_2$ monolayer forms on the electrode surface and each cavity was filled by [Os(CAIPA)$_2$Cl$_2$]. Also, they are relatively lower than those reported previously for guest-CD inclusion monolayer [8,10,28]. This is probably because the CD coverage on the electrode surface is below saturation, i.e. the CDs are not in close contact or a fraction of the CDs still face each other thus preventing osmium binding, even after backfilling with alkanethiol. As shown in Table 4.3, [Os(CAIPA)$_2$Cl$_2$] to β-CD interfacial interaction leads to a high association constant and a strong bonding, which are consistent with the observation of solution phase inclusion between [Os(CAIPA)$_2$Cl$_2$] and β-CD obtained in our research group, where the association constant is determined as 2×10^4 M^{-1} in H_2O/Ethnol mixture (80:20) by using titration method. Also, the behaviours of this immobilized system are similar as those of a CD-adamantane interaction for solution phase [29] or for the immobilized CDs on gold nanoparticle surface (2.31×10^4 M^{-1} and -28.4 KJ mol^{-1}) [30]. This observation may suggest that the interfacial binding between [Os(CAIPA)$_2$Cl$_2$] to β-CD is independent on the solution and the mobility of host molecules. The slight difference in the association constant is probably because the changes in the CD orientation can impact on the thermodynamics of host-guest association. Presence of the interfacial electric field or difference in the ionic strength of the electrolyte solution can also influence the association constant [8].

Also as shown in Table 4.3, the maximum surface coverage of the oxidized form of Os complex is significantly lower than that of the reduced form of Os complex. This observation is because the trivalent form is expected to exit the cavity as it is absent in the bulk concentration. The free oxidized form guests would be released from the CD cavities to the bulk concentration due to relatively weak binding between the oxidized form and CD cavities. Therefore, it would cause a decrease of association concentration and result in a lower association constant and surface coverage for the oxidized form.

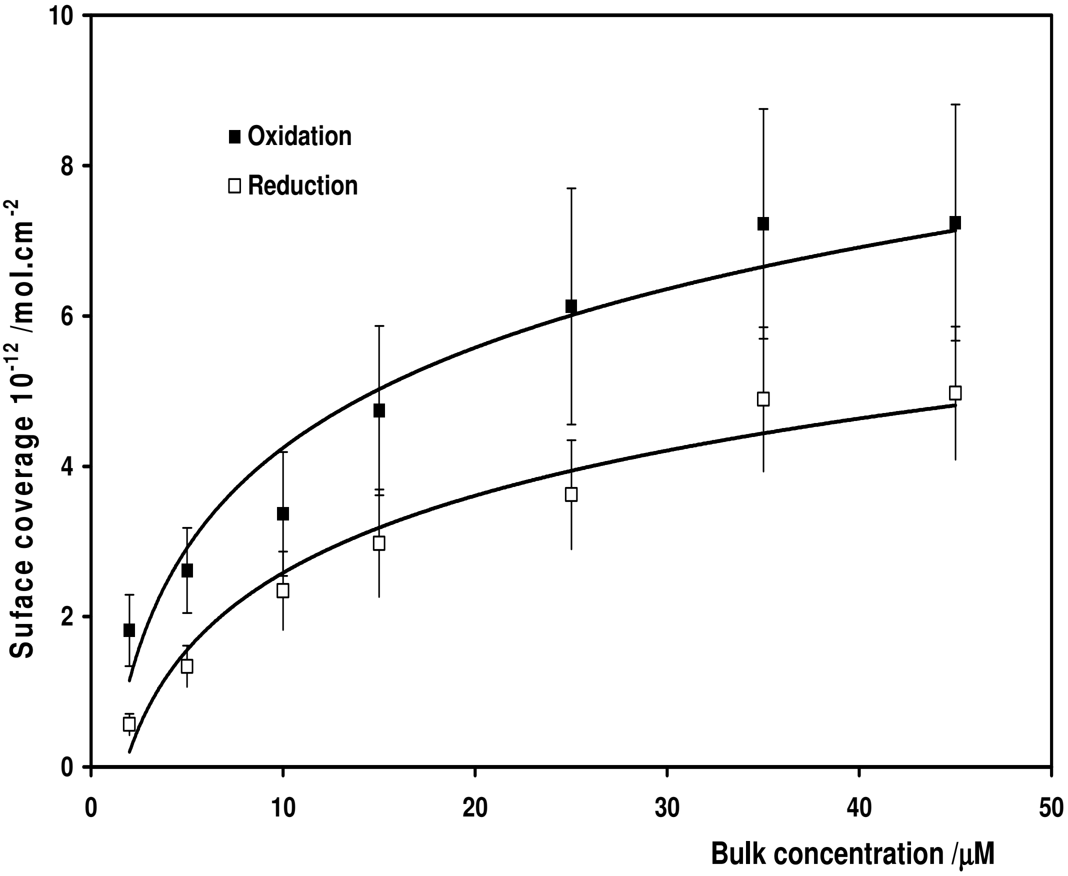

Figure 4.11. Langmuir isotherm for the surface coverage of $Os^{2+/3+}$ couple as a function of the Os complex concentration at scan rate of 30 V s^{-1} in 0.1 M $LiClO_4$ electrolyte. The numbers of repetitive measurement (n=5).

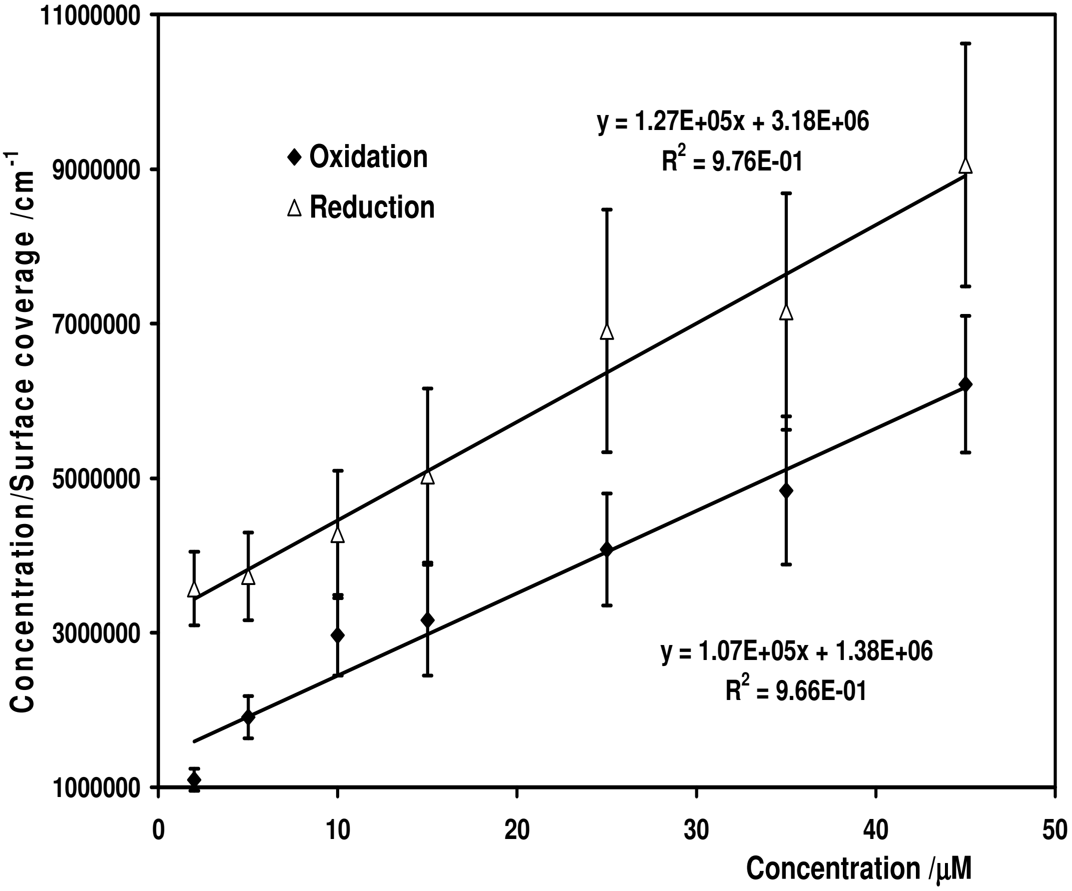

Figure 4.12. The linear relation of Langmuir isotherm at scan rate of 30 V s^{-1} in 0.1 M $LiClO_4$ electrolyte. The numbers of repetitive measurement (n=5).

Table 4.3. Maximum surface coverage (Γ_{max}), association constant (K_A), and free energy of adsorption (ΔG_{ads}) for both reduced and oxidized forms of $[Os(CAIPA)_2Cl_2]$-CD inclusion.

Complex	Γ_{max} **(mol cm^{-2})**	$K_A=\beta$ **(M^{-1})**	$\Delta G^{\#}_{ads}$ **(kJ mol^{-1})**
Os^{2+}	$(9.34\pm0.48)\times10^{-12}$	$(7.76\pm0.79)\times10^{4}$	$-(27.42\pm0.25)$
Os^{3+}	$(7.87\pm0.31)\times10^{-12}$	$(4.00\pm0.40)\times10^{4}$	$-(25.82\pm0.40)$

4.4 CONCLUSIONS

The two-step preparation of the backfilled di-6^A,6^D-deoxy-6-(4-pyridylmethyl)amino-β-cyclodextrin monolayer binding with pyridine on polycrystalline platinum electrodes has been described. The formation of this backfilled monolayer was demonstrated by measuring the changes of capacitance and blocking behaviour of the platinum electrode. The electrode capacitances were significantly reduced after the CD self-assembled monolayer backfilled with 1-nonanethiol to block the defects in the films. Also, this defect free layer at the electrode surface can act as a barrier between the electrode surface and electroactive species, such as ferrocyanide in the solution causing higher blocking ability of the modified electrodes. However, the host-guest inclusion between the immobilized CD monolayer and $[Os(CAIPA)_2Cl_2]$ complex can increase the electroactivity of the modified electrodes and result in higher capacitance and less blocking behaviour due to the electrochemical redox centre of osmium in the complex. Further, the binding ability of the inclusion was investigated by fitting the Langmuir isotherm. Experimental data indicated that the association constant between adamantyl end group of the Os complex and CD monolayer is of the order of 10^4 M^{-1}, which was consistent with that in a CD-adamantane interaction.

4.5 REFERENCES

[1] Maria. T. Rojas, Rainer Koniger, J. F. Stoddart, and A. E. Kaifer. J. Am. Chem. Soc. 117 (1995) 336.

[2] T. E. Creighton. Proteins: Structures and Molecular Properties. Freeman, New York, 1984. Chapter 4.

[3] S. Li, W.C. Purdy. Chem. Rev. 92 (1992) 1457.

[4] W. Saenger. Angew. Chem. Int. Ed. 19 (1980) 344.

[5] A. E. Kaifer, M. Gomez-Kaifer. Supramolecular Electrochemistry. Wiley-VCH. Weinheim. 1999 p.191.

[6] A. Ulman. Chem. Rev. 96 (1996) 1533.

[7] S. Trasatti, O. A. Petrii. Pure Appl. Chem. 63 (1991) 711.

[8] C. T. Mallon, R. J. Forster, A. McNally, E. Campagnoli, Z. Pikramenou, T. E. Keyes. Langmuir, 23 (2007) 6997.

[9] A. E. Kaifer, M. Gomez-Kaifer. Supramolecular Electrochemistry, Wiley: New York, 1999.

[10] Maria. T. Rojas, Rainer Koniger, J. F. Stoddart, and A. E. Kaifer. J. Am. Chem. Soc. 117 (1995) 336.

[11] G. Nelles, M.Weisser, R. Back, P.Wohlfart, G.Wenz, and S. Mettler-Neher. J. Am. Chem. Soc, 118 (1996) 5039.

[12] Y. Maeda, T. Fukuda, H. Yamamoto, and H. Kitano. Langmuir, 13 (1997) 4815.

[13] T. J. Davies, R. R. Moore, C. E. Banks, R. G. Compton. J. Electroanal. Chem. 574 (2004) 123.

[14] T. J. Davies, C. E. Banks, R. G. Compton. J. Solid State Electrochem. 9 (2005) 797.

[15] P. He, J. Ye, Y. Fang, T. Osa. Electroanalysis 9 (1997) 68.

[16] M. J. Weaver. Langmuir 14 (1998) 3932.

[17] H. O. Finklea, in: A. J. Bard, I. Rubinstein (Eds.), Electroanalytical Chemistry, vol. 19, Marcel Dekker, New York, 1996, p. 109.

[18] H. O. Finklea, in: R. A. Meyers (Eds.), Encyclopedia of Analytical Chemistry: Applications, Theory and Instrumentations, vol. 11, Wiley, Chichester, 2000, p. 10090.

[19] K. I. Ozoemena, T. Nyokong, D. Nkosi, I. Chambrier, M. J. Cook. Electrochim. Acta. 52 (2007) 4132.

[20] D. Nkosi, K. I. Ozoemena. Electrochim. Acta. 53 (2008) 2782.

[21] R. S. Nicholson. Anal. Chem. 37 (1965) 1351.

[22] C. Amatore, J. M. Saveant, D. Tessier. J. Electroanal. Chem. 147 (1983) 39.

[23] E. Sabatani, I. Rubinstein. J. Phys. Chem. 91 (1987) 6663.

[24] Y. Pellegrin, R. J. Foster, T. E. Keyes. Inorg. Chim. Acta. 361 (2008) 2683.

[25] B. Abraham, C. V. Sastri, B. G. Maiya, S. Umapathy. J. Raman. Spectrosc. 35 (2004) 13.

[26] R. J. H. Clarke, P. C. Turtle, D. P. Strommen, B. Streusand, J. Kincaid, R. Nakamoto. Inorg. Chem. (1977) 84.

[27] Y. Meada, T. Fukuda, H. Yamamoto, H. Kitano. Langmiur 13 (1997) 4187.

[28] Y. Wang, A. E. Kaifer. J. Phys. Chem. B 102 (1998) 9922.

[29] M. V. Rekharsky, Y. Inoue. Chem. Rev. 98 (1998) 1875.

[30] O. Crespo-Biel, A. Jukovic, M. Karlsson, D. N. Reinhoudt and J. Huskens. Israel Journal of Chemistry. 45 (2005) 353.

CHAPTER 5

Preparation and Charge Transfer Dynamics of Three-Dimensional Gold Nanoparticles Multilayer Film via Host-Guest Interaction with Redox Labels

5.1 INTRODUCTION

Monolayer-protected gold nanoparticles or monolayer-protected gold clusters are nanometre-scale gold particles surrounded by a self-assembled monolayer shell. These gold nanoparticles are stable and do no aggregate, therefore enabling a wide range of measurements [1]. There is significant interest in nanoparticles and composites materials because of their unique electronic, magnetic, and optical properties [2] and potential applications in catalysis and chemical sensor development [3,4,5]. In many of these applications, the nanoparticles are formed as a monolayer or multilayer film on a substrate and it is very important to understand the dynamics of charge transport through thin films on experimentally addressable surfaces by measuring the rate of charge transport [6].

To build the superstructures of monolayer-protected gold nanoparticles, the nanoparticles in the multilayer films are linked together by using carboxylate/metal ion/carboxylate linking, pyridine/metal ion/pyridine linking, and dithiol linking [7]. Also, the electrochemical properties of these multilayer films have been investigated [6,8,9,10]. Alternatively, multilayers can be developed by combining nanomaterials, which can be used as solid supports, and supramolecular concepts [11], and the network of these materials may provide three-dimensional arrangements by molecular recognition interactions between hybrid materials and some functional molecules. As reported previously by Kaifer and co-workers [12,13], gold colloidal particles can be capped with molecular receptors, cyclodextrins, which can build the multilayer network via host-guest interactions. In additional, Reinhoudt and co-workers created more complex three-dimensional structures of cyclodextrin capped gold nanoparticles by layer-by-layer techniques by using the strong cyclodextrin-adamantane host-guest interactions as the supramolecular driving force [14].

Despite these innovations in film assembly, much less is known about the dynamics of electron transfer through these films. In this contribution, we report on the formation of three dimensional gold nanoparticles multilayer via cyclodextrin-adamantane host–guest interaction, where the guest linker is $[Os(CAIPA)_3](ClO_4)_2$ complex, CAIPA is 2-(4-carboxyphenyl)imidazo[4,5-f][1,10]-phenanthroline-1-adamantylamine (Chart 5.1 and 5.2). Detailed spectroscopic and microscopic characterisations of the AuNPs multilayer are presented and resonance Raman spectroscopy is used to probe the nature of the optical transitions of this multilayer. Moreover, the Os complex link bridge is also used as a redox label to measure the rate of diffusion-like charge transport through AuNPs multilayer films deposited on glassy carbon electrodes using cyclic voltammetry. In this way, insights into the nature of nanoparticle to nanoparticle electron transfer dynamics have been obtained.

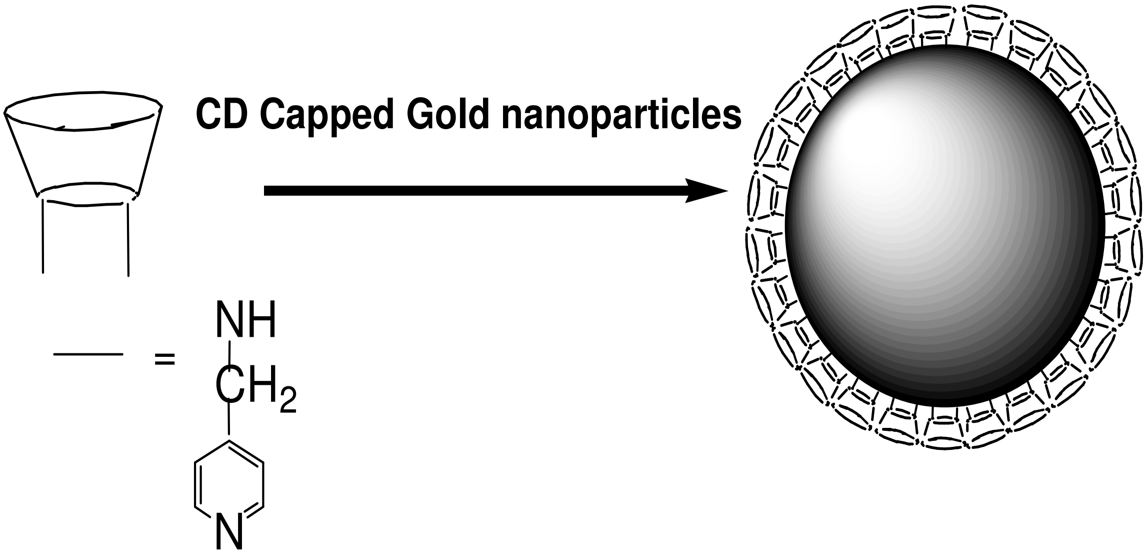

Chart 5.1. Chemical Structure of β-CD-(4-py)$_2$ and Formation of β-CD-(4-py)$_2$ Capped AuNPs.

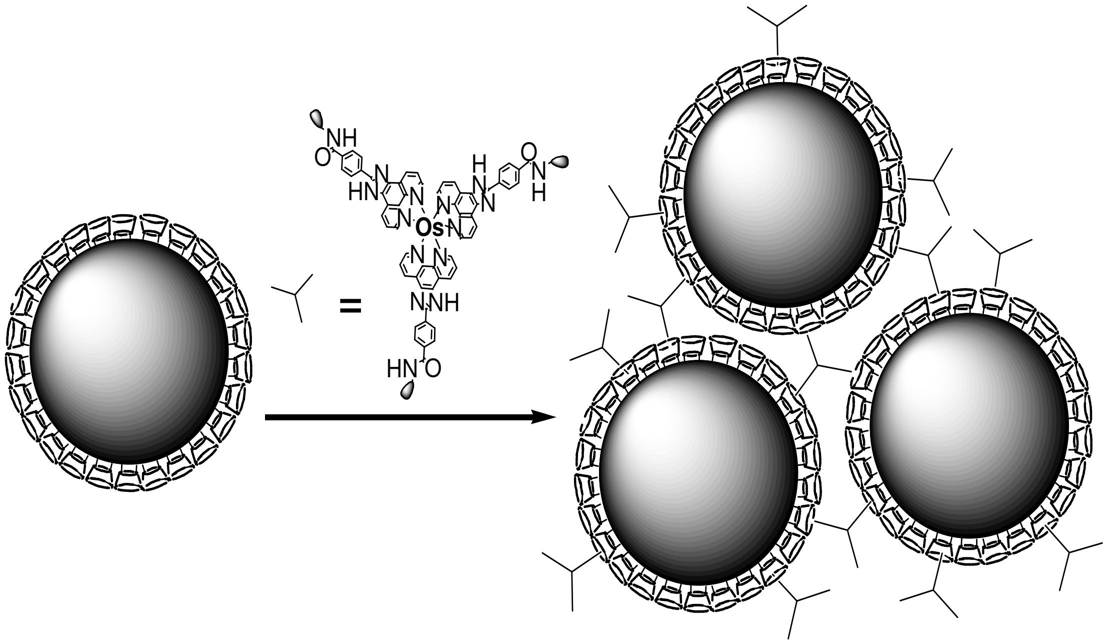

Chart 5.2. Schematic of the Preparation of the Host-Guest Inclusion Induced Aggregation Network of β-CD-(4-py)$_2$ Capped AuNPs.

5.2 EXPERIMENTAL

5.2.1 Materials.

All reagents were analytical grade. A colloidal solution of 100 nm gold nanoparticles (AuNPs) with concentration of 5.6×10^{-9} particles per ml was purchased from BB (British Biocell) International and used as received. β-CD-(4-py)$_2$ and [Os(CAIPA)$_3$](ClO$_4$)$_2$ were obtained as gifts from Reena Marthi within our group, where β-CD-(4-py)$_2$ is di-6^A,6^D-deoxy-6-(4-pyridylmethyl)amino-β-cyclodextrin.

5.2.2 Preparation of β-CD-(4-py)$_2$ Capped AuNPs and the [Os(CAIPA)$_3$](ClO$_4$)$_2$ Linked β-CD-(4-py)$_2$-Capped AuNPs Multilayer.

As shown in Chart 1, β-CD-(4-py)$_2$ capped AuNPs were prepared by mixing 2 ml of 100 nm AuNPs colloidal solution with 5 ml of 0.1 mM β-CD-(4-py)$_2$ aqueous solution then the mixture was left standing overnight at room temperature in dark. Further, the surface modified AuNPs was mixed with 5 ml of 0.1 mM [Os(CAIPA)$_3$](ClO$_4$)$_2$ solution (90% H_2O, 5% MeOH, 5% ACN) for overnight, where Os complex was dissolved in ACN&MeOH mixture first and this solution was made up to 5 ml by adding the required volume of water. After each individual step, the AuNPs were collected by centrifugation, washed with Milli-Q water, and then characterized by using UV/Visible spectroscopy.

5.2.3 Instrumentation.

UV/Vis spectra were carried out on a Shimadzu UV-3100 spectrophotometer.

Scanning electron microscopy (SEM) was performed using a Hitachi S-3000N system operated at the applied voltage on the cathode of 20 kV. The required volume of sample solutions were dropped on silicon wafers, which were pre-cleaned by rinsing with acetone and ethanol, and followed by air-drying. Transmission electron microscopy (TEM) was conducted using a JEOL JEM-2011 electron microscopy operated at an accelerating voltage of 200 kV with a LaB6 filament. Images were recorded using a Gatan DualVision 600t CCD camera attached to the microscopy.

Samples for imaging were deposited onto a 400 mesh copper grid with a carbon film (Agar Scientific), and the liquid was allowed to dry in air at room temperature. The concentration of samples for both unmodified and modified AuNPs is similar.

Raman spectroscopy was obtained on a Dilor. Jobinyvon. Spex Labram. Argon ion and Helium-Neon lasers were available sources for excitation at 458 nm, 514 nm and 632.8 nm, respectively. A backscattering geometry was used to collect scattered light by using an air cooled CCD array by interchangeable gratings, 1800 lines/mm. Before use, the wavenumber axis of the Raman was calibrated with the silicon line at 521 cm^{-1}.

Electrochemistry was performed in conventional three-electrode cells using an Ag/AgCl electrode filled with 3 M KCl (aq) (CH instrument) as reference. Cyclic voltammetry (CV) was carried out using a CH instruments Model 660a electrochemical workstation. All electrolyte solutions were deoxygenated for at least 15 min using N_2 gas before use and maintained under a nitrogen blanket during measurement. Glassy carbon electrodes were used as working electrodes in this experiment due to the surface stability at high potential in both neutral and acidic electrolytes. The working electrodes were polished successively with 1.0, 0.3, and 0.05 μm alumina powder before use, then modified by evaporating the required volume of a 1 % $[Os(CAIPA)_3](ClO_4)_2$ solution in ACN/MeOH (1:1), an aqueous solution of naked AuNPs or an aqueous solution of aggregated AuNPs followed by air-drying.

The maximum concentration of osmium centres within the osmium complex film was determined as 0.71 M by flotation in non-swelling solvents, i.e., petroleum ether and dichloromethane. The maximum concentration of Os redox centres within AuNPs multilayer was obtained from the layer of the inclusion between osmium guest and CD host on each particle surface as 0.57 M, where a close-packed monolayer of β-CD-(4-py)$_2$ was expected to form on the gold nanoparticle surface and every cavity was filled by $[Os(CAIPA)_3]^{2+/3+}$.

For conductivity measurement, a CH instruments Model 760b electrochemical workstation was employed. Platinum interdigitated electrode arrays, IDAs, were purchased from Abtech Scientific. Inc. Films were prepared by evaporating the required volume of sample solutions on the IDA fingers and gaps between fingers. In order to cover the IDA fingers and gaps completely, the sample solutions were drop-cast on the IDA electrodes several times.

5.3 RESULTS AND DISCUSSION

5.3.1 Absorption Spectroscopy.

The aggregation process of AuNPs was monitored by using absorption spectroscopy as aggregation leads to a red-shift of the plasmon absorption band [15]. As shown in Figure 5.1(A), the surface plasmon resonance (SPR) absorption of 100 nm diameter AuNPs is at 565 nm. This wavelength agrees with previous reports on similar size AuNPs as the absorption red shifts with increasing AuNPs size [16]. The absorption spectra of the β-CD-(4-py)$_2$ capped AuNPs is shown in Figure 5.1(B). Compared with unmodified AuNPs, the SPR absorption of the β-CD-(4-py)$_2$ capped AuNPs remains unchanged. Modification of the AuNPs with β-CD-(4-py)$_2$ results in the appearance of a second broad plasmon absorption centred around 740 nm, which may be due to longitudinal mode. Figure 5.1(C) shows that the metal-to-ligand charge-transfer bands (MLCT) of $[Os(CAIPA)_3](ClO_4)_2$ are observed in the visible region at 453 and 503 nm, respectively.

As the adamantyl group is a high-affinity guest for inclusion with CD, the osmium complex acts as a bridge to link the individual β-CD-(4-py)$_2$ capped gold nanoparticle together by the host-guest molecular interaction between β-CDs and adamantyl group ends of osmium complex. As shown in Figure 5.1(D), the features of both osmium complex and AuNPs remain. Inclusion between β-CD and adamantyl does not affect the wavelength of the MLCT as the adamantyl pendant is relatively remote from the osmium centre [17]. However, the aggregation due to this inclusion results in a red-shift of the SPR absorption of AuNPs approximately 5 nm.

The peak details of each spectrum in Figure 5.1 could be obtained by software simulation. Based on Beer-Lambert law, the concentration of Os complex and AuNPs within the aggregates after centrifuging to remove unbound Os complex were estimated as 4.3×10^{-3} mM and 8.5×10^{8} particles/ml, when the effect on extinction coefficient due to aggregation was ignored and where the original concentration of pure Os complex and AuNPs solutions were 0.1 mM and 2.4×10^{9} particles/ml, respectively. The ratio of osmium centres to AuNPs in Figure 5.1(D) can be obtained as about 3×10^{6} per particle, where the numbers of Os complex molecules and AuNPs were calculated by using the concentrations of these two components within aggregation. This ratio is 2 orders of magnitude higher than the theoretical number of 17500, which was obtained as expected if a close-packed monolayer of β-CD-(4-py)$_2$ was formed on the gold nanoparticle surface and every cavity was filled by $[Os(CAIPA)_3]^{2+/3+}$. The number of CD molecules contained in the close-packed monolayer was estimated by using ratio between surface area of a 100 nm diameter gold nanoparticle and footprint surface area of a β-CD molecule with a external diameter of 15.3 Å. There appear to be at least two possibilities to account of the discrepancy of the ratio of osmium centres to AuNPs observed here. First, it might be the decreased intensity of the SPR absorption due to aggregation [18,19] and second, it might be attributed to the slow precipitation of large aggregated AuNPs, which would result in attenuation of the SPR absorption [12]. Both possibilities above would result in the decrease of extinction coefficient of gold plasmon absorption.

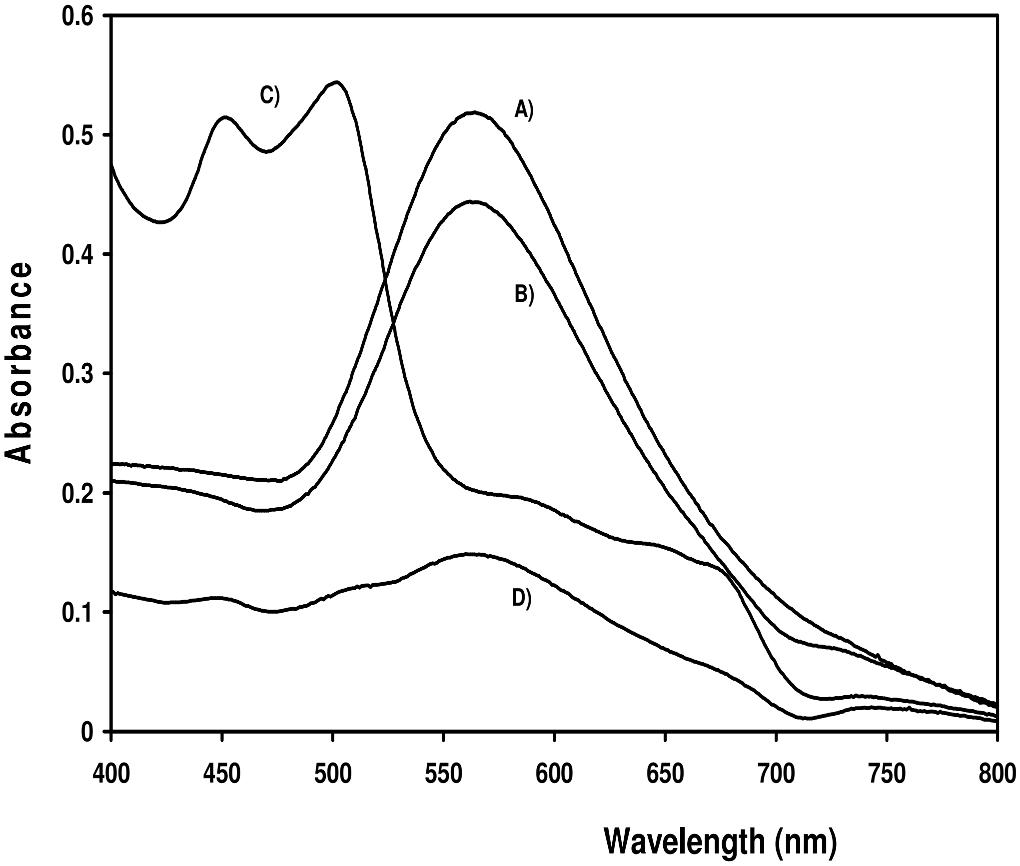

Figure 5.1. Absorption spectra of 100 nm AuNPs aqueous solution: (A) Unmodified, (B) CD modified, (D) Aggregated, and (C) 0.1 mM $[Os(CAIPA)_3](ClO_4)_2$ in MeOH/ACN (1:1).

5.3.2 SEM and TEM.

SEM and TEM measurements were used to directly visualise the formation of the gold nanoparticle networks. SEM images (Figure 5.2 B and C) show that β-CD-(4-py)$_2$ capped AuNPs are randomly dispersed and show relatively little aggregation. These images are similar to the image of the original AuNPs (Figure 5.2 A). It suggests that the first modification step with β-CD-(4-py)$_2$ did not result in a large change. Further, TEM image of β-CD-(4-py)$_2$ capped AuNPs (Figure 5.2 E) reveals that the inter-particle distance is about 3 nm for the close packed particles and confirmed that the particles are discrete and not fused. However, both SEM and TEM images (Figure 5.2 D and F) show a typical large non-uniform aggregation as expected for linkages formed between [Os(CAIPA)$_3$](ClO$_4$)$_2$ linkers and β-CD-(4-py)$_2$-capped AuNPs by the host-guest inclusion. The structure of larger aggregation can be clearly seen that a close-packed three-dimension lattice of the AuNPs is formed.

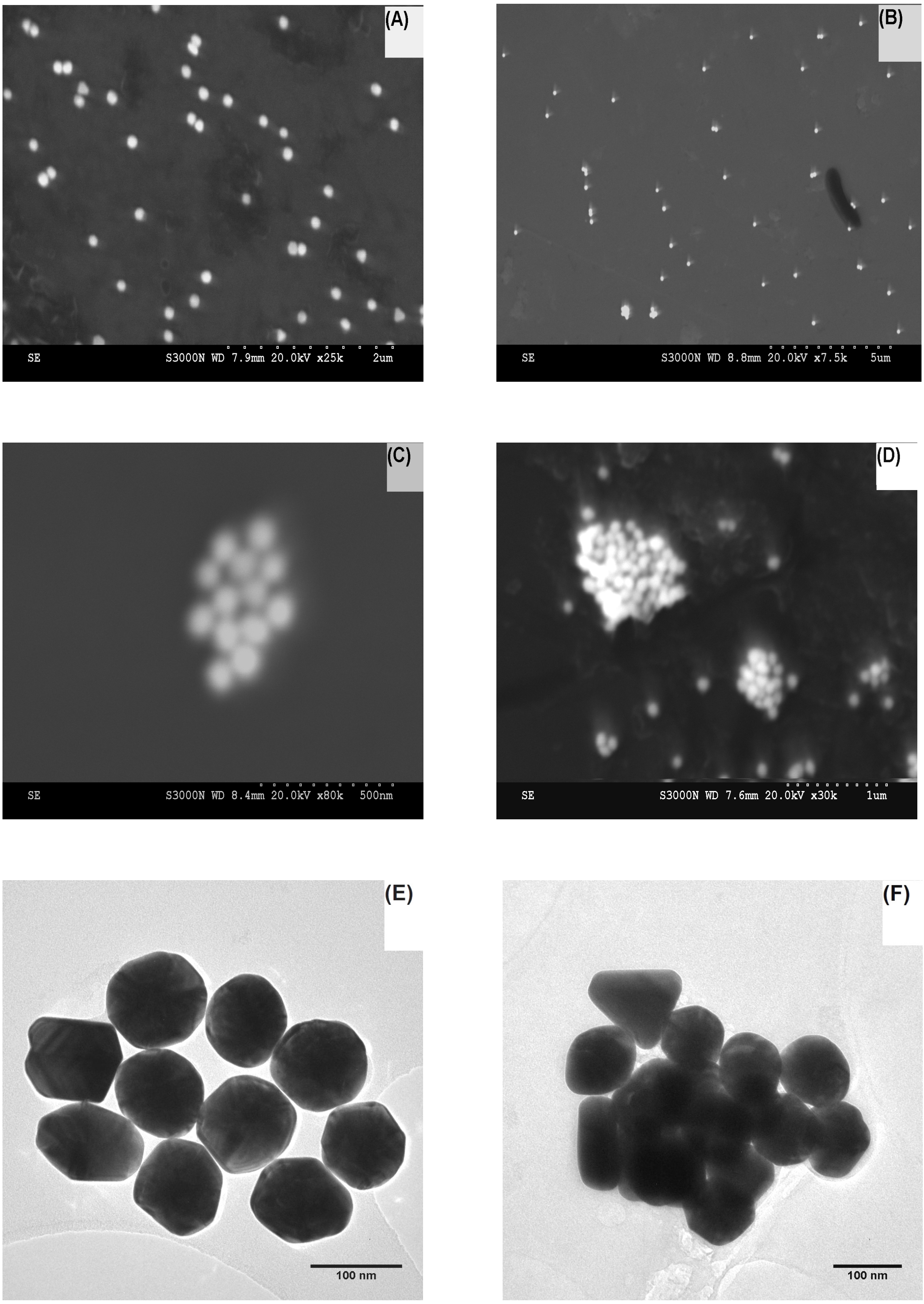

Figure 5.2. SEM images obtained from original AuNPs (A), β-CD-(4-py)$_2$ capped AuNPs (B, C), and the AuNPs multilayer network (D). Also TEM images for β-CD-(4-py)$_2$ capped AuNPs and the AuNPs multilayer network are shown as (E) and (F).

5.3.3 Raman Spectroscopy.

To better understand the surface enhancement of the $[Os(CAIPA)_3](ClO_4)_2$ linked β-CD-$(4\text{-}py)_2$-capped AuNPs, thin films of these AuNPs were coated on a glassy carbon electrode and conducted Raman experiments at 458 nm, 514 nm and 632.8 nm. As a comparison, Raman experiments of solid deposits of $[Os(CAIPA)_3](ClO_4)_2$ were also carried out at the same conditions.

Figure 5.3 shows the Raman spectrum for solid $[Os(CAIPA)_3](ClO_4)_2$ excited at 458 nm, which is resonant with the MLCT absorption of this complex. The features at 1616, 1566, 1503, 1457, 1422, 1368, 1313, 1251, 1195, 1145, 1079, 1048, 733, and 443 cm^{-1} are all characteristic of CAIPA unit vibration [17,20,21] in the MLCT transition. The same features are obtained in aggregated β-CD-$(4\text{-}py)_2$ capped AuNPs indicating that $[Os(CAIPA)_3](ClO_4)_2$ is present in the aggregated β-CD-$(4\text{-}py)_2$ capped AuNPs film.

The excitation at 514 nm was chosen to be resonant with both the MLCT of the osmium complex and the plasmon absorption of AuNPs. As shown in Figure 5.4, the spectrum of osmium complex film remains unchanged with the maximum intensity of 2800. For the aggregated AuNPs film, the spectrum is considerably more complex at this excitation wavelength. The intensity of the CAIPA features is effectively surface enhanced due to its proximity to the AuNPs surface by the host-guest inclusion. This observation agrees with the previous work in our group on β-CD-(py) layers, which were prepared on electrochemically roughened Au to give spectra with much higher intensity [22]. All of the features present at 458 nm remain at 514 nm for the aggregated AuNPs film. But in addition, the enhanced intensity is accompanied by new features at 776, 617, 536, 495, 468 cm^{-1} attributed to CAIPA unit vibration [21] and 354 cm^{-1} associated with the Os-N stretch [17].

Figure 5.5 shows the Raman spectrum excited at 632.8 nm. The CAIPA bands associated with the MLCT transition shown in Figure 5.3 are completely lost under these conditions for the osmium complex film. However, some of these bands are still evident in the spectrum of aggregated AuNPs film due to the surface enhancement by AuNPs. Also, β-CD-$(4\text{-}py)_2$ capped on the surface of AuNPs using pyridine as anchors is dominated by pyridine bands at 1288 and 1024 cm^{-1}, respectively [23]. These two pyridine bands were not evident in the spectra of aggregated AuNPs at 458 and 514 nm due to the overlay of the CAIPA bands below 1800 cm^{-1}. Similar observations are obtained for β-CD bands, which are overlaid by a large number of bands attributed to overtones and combination bands of CAIPA around 3000 cm^{-1} [21].

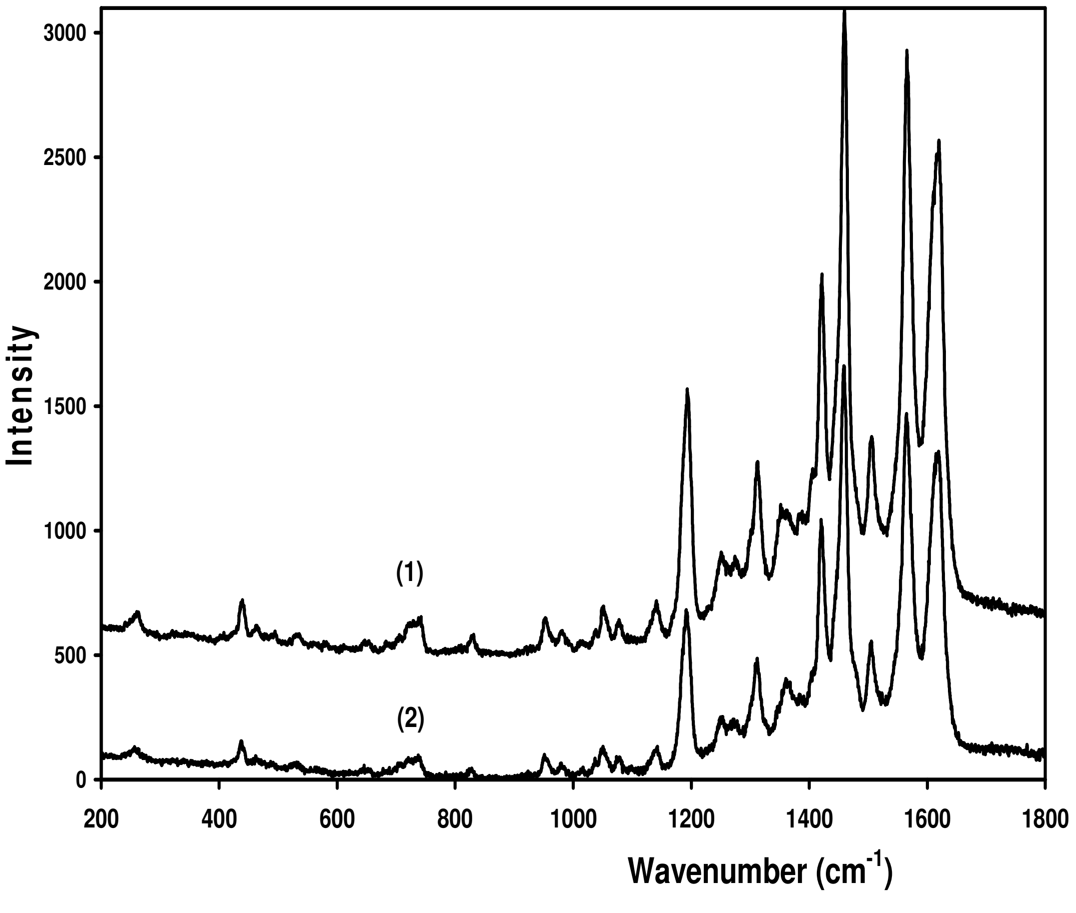

Figure 5.3. Resonance Raman spectra of a dry $[Os(CAIPA)_3](ClO_4)_2$ film (1) and $[Os(CAIPA)_3](ClO_4)_2$ linked β-CD-(4-py)$_2$-capped AuNPs film (2) formed on a 3 mm glassy carbon electrode excited at 458 nm.

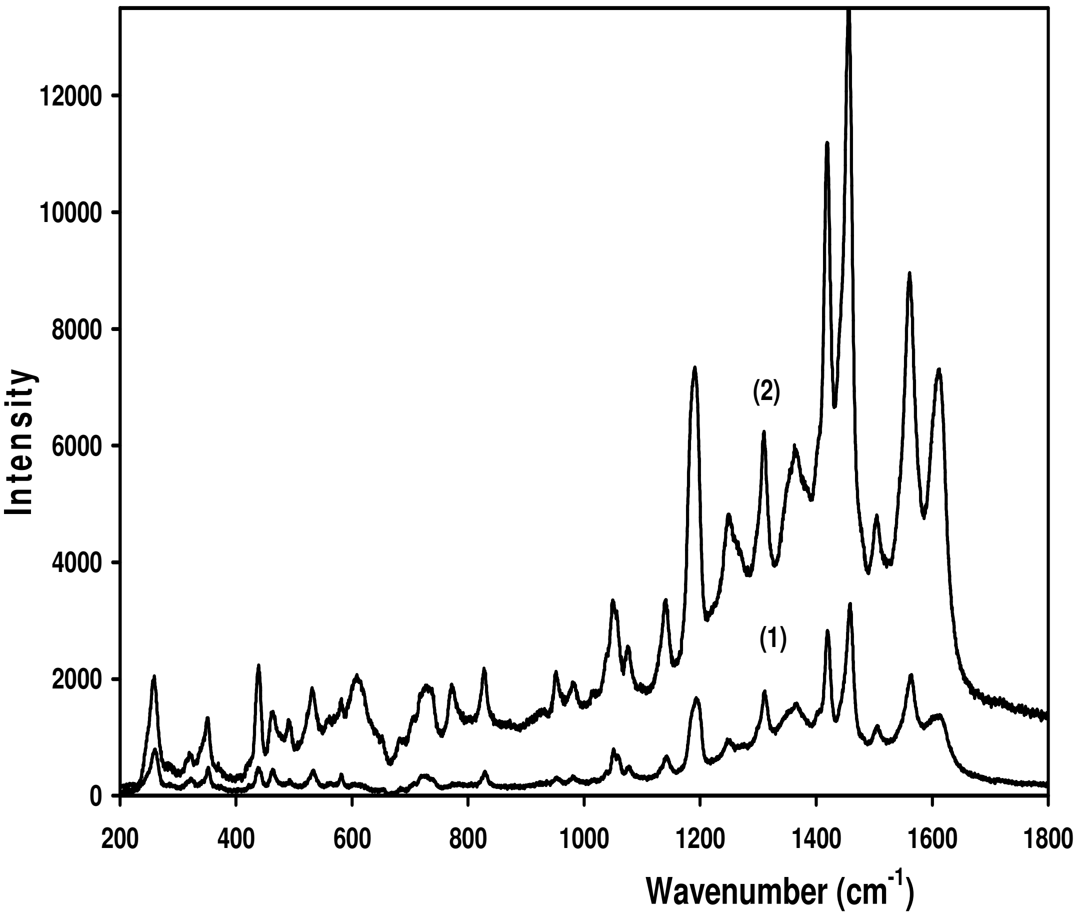

Figure 5.4. Resonance Raman spectra of a dry $[Os(CAIPA)_3](ClO_4)_2$ film (1) and $[Os(CAIPA)_3](ClO_4)_2$ linked β-CD-(4-py)$_2$-capped AuNPs film (2) formed on a 3 mm glassy carbon electrode excited at 514 nm.

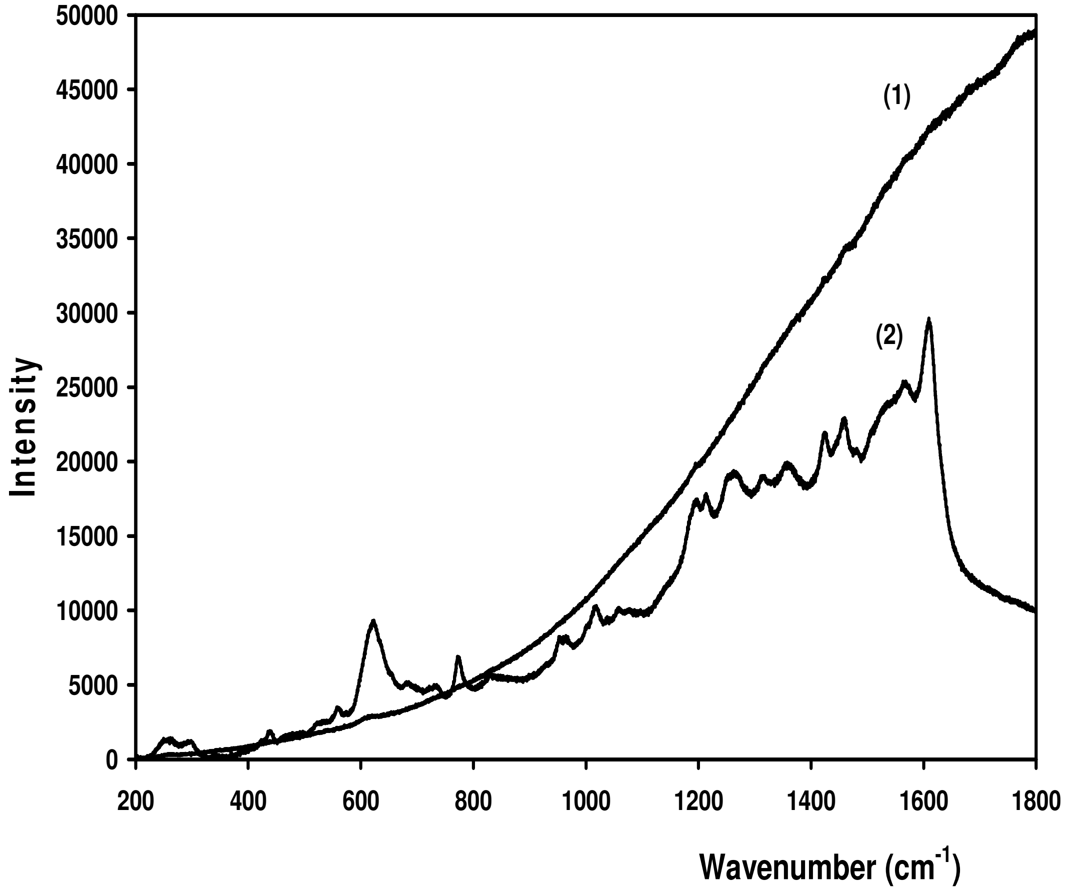

Figure 5.5. Resonance Raman spectra of a dry $[Os(CAIPA)_3](ClO_4)_2$ film (1) and $[Os(CAIPA)_3](ClO_4)_2$ linked β-CD-(4-py)$_2$-capped AuNPs film (2) formed on a 3 mm glassy carbon electrode excited at 632.8 nm.

5.3.4 Electrochemical properties and Electron Transfer Dynamics of AuNPs Multilayer in Neutral Electrolyte.

In order to investigate the electron-transfer dynamics in the films of the AuNPs multilayer, cyclic voltammetry was used to probe the electroactive osmium complex linkers. In our previous reports, the CAIPA ligand is capable of undergoing a protonation or a deprotonation reaction depending on the pH of the contacting solution [17,24]. Protonation of $[Os(CAIPA)_3](ClO_4)_2$ dissolved in DMF/H_2O (4:1) containing 0.1 M $LiClO_4$ causes an increase in the overall charge on the complex and results in a positive shift in the oxidation potential of the Os^{2+} metal centre from 443 mV in 0.1 M $LiClO_4$ DMF electrolyte solution to 581 mV (Figure 5.6), indicating that the oxidation becomes thermodynamically more difficult.

As a control, voltammograms of a solid state deposit of the osmium complex film on a 3mm glassy carbon electrode were monitored in 0.1 M $LiClO_4$ aqueous electrolyte. As illustrated in Figure 5.7, the formal potential, $E°'$, for the $Os^{2+/3+}$ couple is 631 mV. This value is significantly more positive than that found for the complexes dissolved in DMF/H_2O (4:1) containing 0.1 M $LiClO_4$ where $E°'$ is 581 mV suggesting that there are significant differences in the solvation shell or a relatively high Gibbs energy barrier for ion transport within the immobile solid film compared to solution. As shown in Figure 5.8, the peak shape is independent of scan rate up to 200 mV s^{-1} and the response is consistent with a surface confined signal for Os centre as the peak height scales linearly with increasing scan rate and plots of log peak current versus log scan rate have slopes of 1. The peak to peak separation (ΔE_p) is 26±3 mV and the full width at half-maximum (FWHM) is 184±6 mV. The non-zero ΔE_p value exceeds that expected for a reversible redox reaction under finite diffusion control, but is significantly lower than that expected for a solution phase species, 57 mV. The observation that the peaks are broader than theoretically expected for an ideal Nernstian system indicates that there are repulsive interactions between adjacent adsorbates.

The rate of charge transport through the osmium complexes films can be quantified by measuring the homogeneous charge transfer diffusion coefficient, D_{CT}. In fast scan cyclic voltammetry only a small fraction of the total amount of material immobilised is electrolysed and the depletion zone remains well within the film. Under these conditions, linear diffusion predominates and the peak current varies as $\upsilon^{1/2}$. Figure 5.9 illustrates the voltammetric responses for the osmium complex film at scan rates between 200 and 500 mV s^{-1}. For this range of scan rates, ΔE_p value for the metal centre increases from 51 mV to 117 mV. Even at the relatively higher scan rates, the ohmic drop is less than a few mV suggesting that the rate of heterogeneous electron transfer across the electrode/film interface is responsible for this change in ΔE_p. Consistent with semi-infinite linear diffusion control, Figure 5.10 shows that the voltammetric peak current increases linearly with $\upsilon^{1/2}$. The peak current, i_p, can be expressed in terms of the Randles-Sevcik equation,

$$i_p = 2.69 \times 10^5 n^{3/2} A D_{CT}{}^{1/2} C_{eff} v^{1/2} \qquad \textbf{(5.1)}$$

where n is the number of electrons transferred, A is the area of the working electrode, D_{CT} is the homogeneous charge transport diffusion coefficient, and C_{eff} is the effective fixed site concentration of the redox centre, which has been measured as 0.71 M. This equation allows the D_{CT} value of the Osmium film to be determined from the slope of the plot of i_p vs. $\upsilon^{1/2}$. The D_{CT} is estimated for the oxidation and reduction processes as $(2.2\pm0.2)\times10^{-10}$ cm^2 s^{-1} and $(2.4\pm0.1)\times10^{-10}$ cm^2 s^{-1}, respectively. Comparing the diffusion coefficient for solid films, the AuNPs multilayers can reveal differences between the two systems, e.g. the effective electron transfer distance.

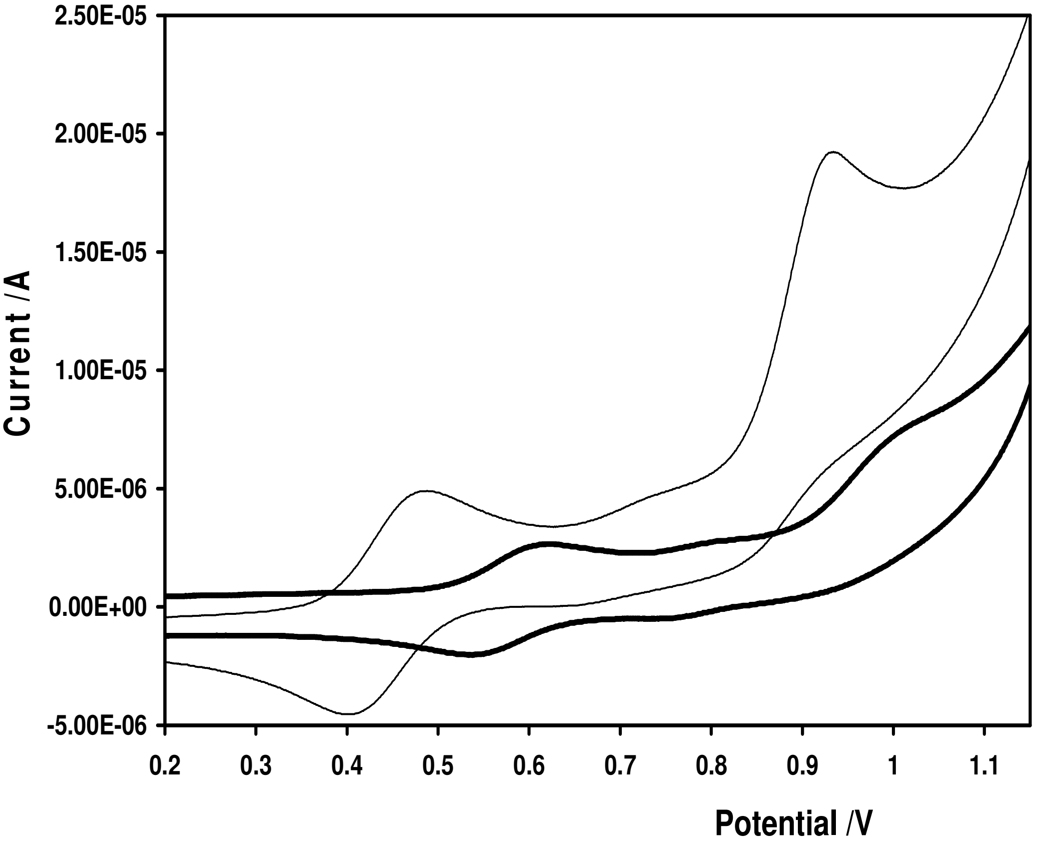

Figure 5.6. CV of solution phase electrochemistry: (thin line) $[Os(CAIPA)_3](ClO_4)_2$ dissolved in DMF containing 0.1 M $LiClO_4$, and (thick line) $[Os(CAIPA)_3](ClO_4)_2$ dissolved in DMF/H_2O (4:1) containing 0.1 M $LiClO_4$.

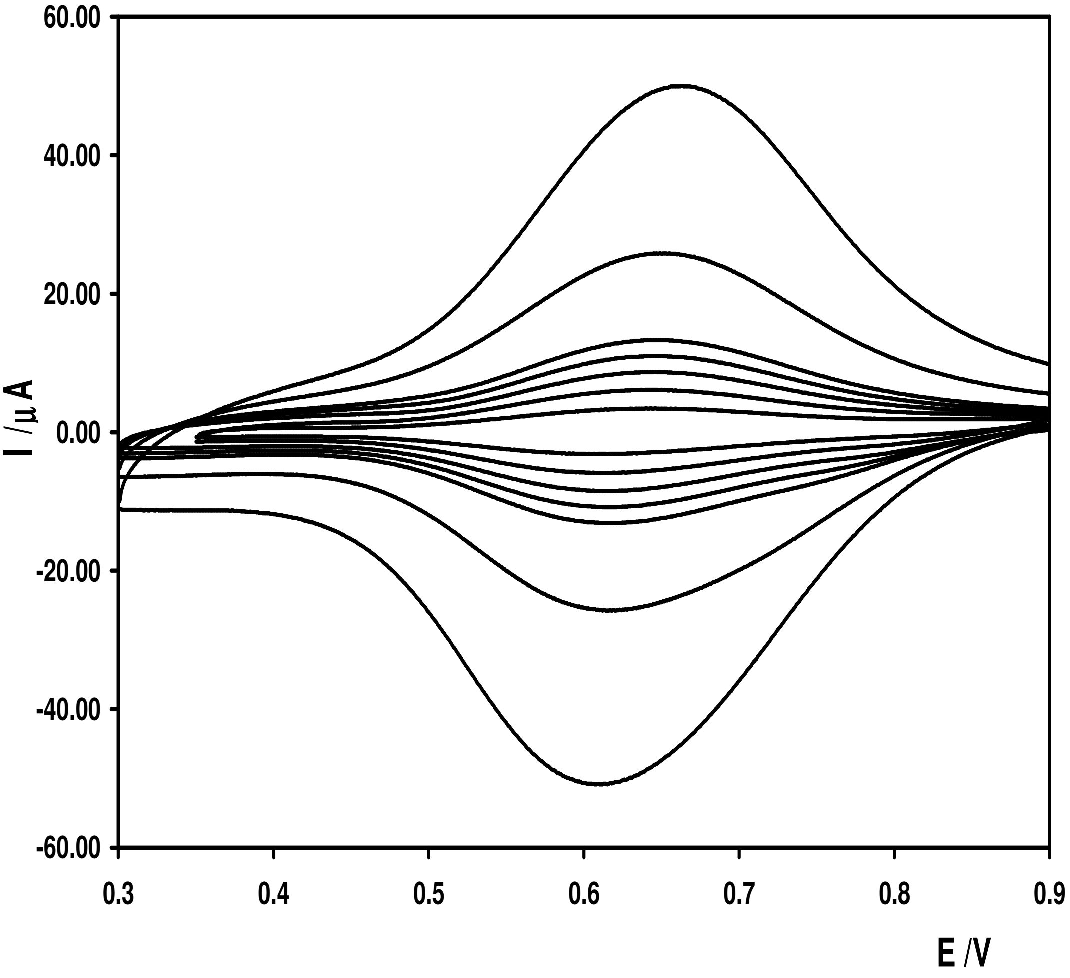

Figure 5.7. Cyclic voltammograms for a [Os(CAIPA)$_3$](ClO$_4$)$_2$ film coated on 3 mm glassy carbon electrode in 0.1 M aqueous LiClO$_4$ electrolyte. Scan rates are (from bottom to top) 10, 20, 30, 40, 50, 100 and 200 mVs^{-1}. $\Gamma = 8.0\times10^{-9}$ mol cm^{-2}.

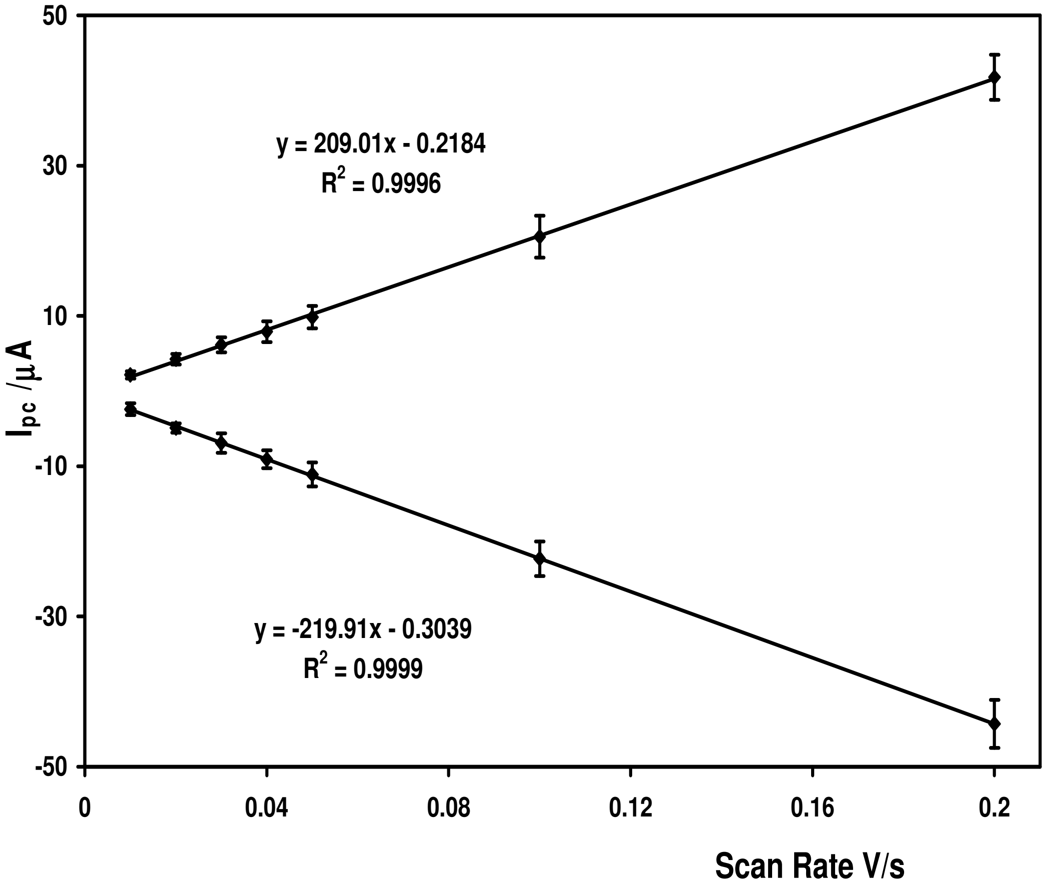

Figure 5.8. A plot of peak current vs. scan rate for a $[Os(CAIPA)_3](ClO_4)_2$ film coated on 3 mm glassy carbon electrode in 0.1 M aqueous $LiClO_4$ electrolyte. Scan rates are 10, 20, 30, 40, 50, 100 and 200 mVs^{-1}. The numbers of repetitive measurement (n=5).

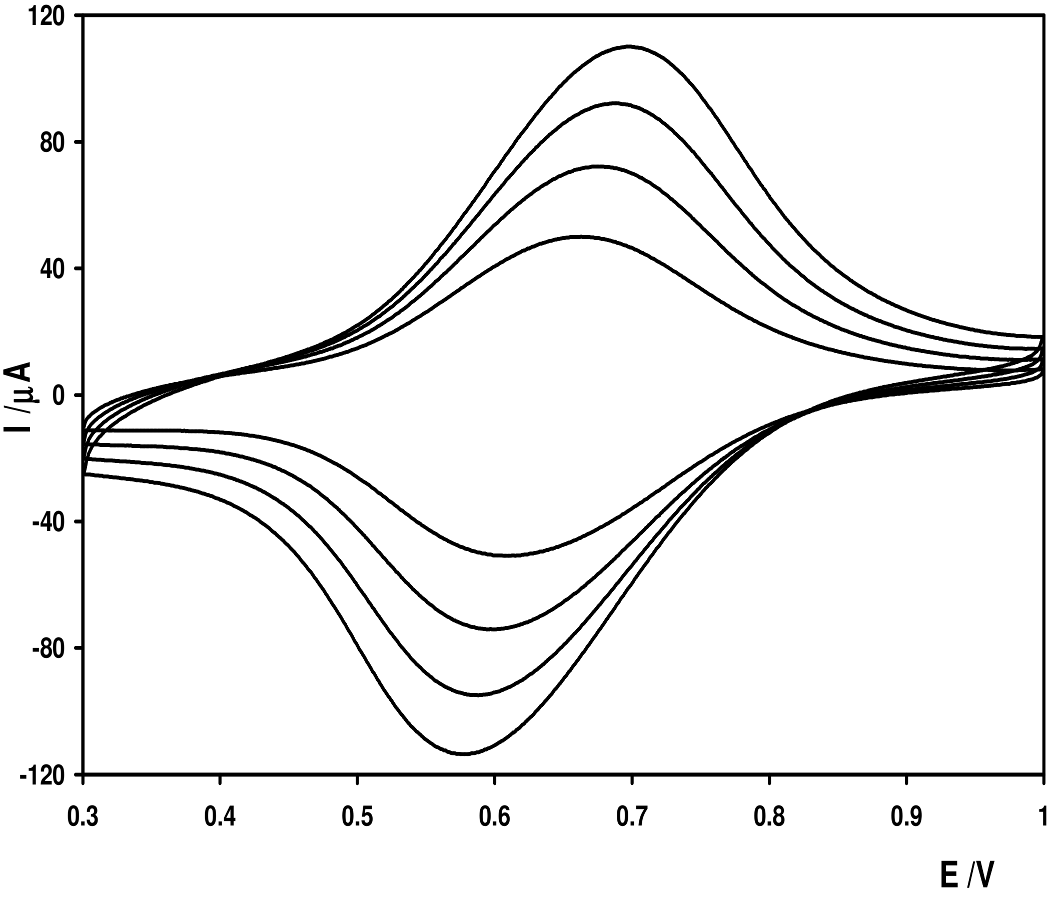

Figure 5.9. Scan rate dependence of the voltammetric response of $[Os(CAIPA)_3](ClO_4)_2$ film on 3 mm glassy carbon electrode in 0.1 M $LiClO_4$. υ =500, 400, 300, and 200 mV/s (from top to bottom). $\Gamma = 8.0\times10^{-9}$ mol cm^{-2}.

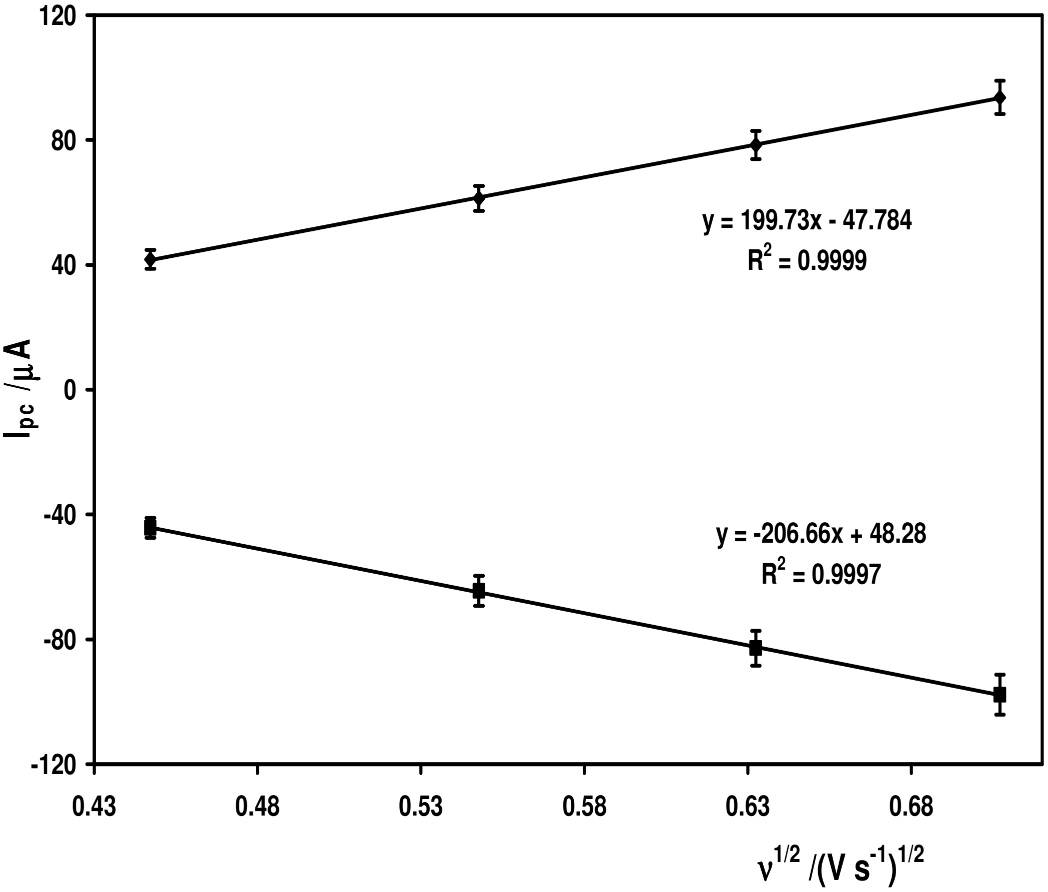

Figure 5.10. A plot of i_p vs. $\upsilon^{1/2}$ for a $[Os(CAIPA)_3](ClO_4)_2$ film on 3 mm glassy carbon electrode in 0.1 M $LiClO_4$. υ =500, 400, 300, and 200 mV/s. The numbers of repetitive measurement (n=5).

Figure 5.11 shows that the cyclic voltammetry of the AuNPs multilayer coated on 3 mm glassy carbon electrode in 0.1 M aqueous $LiClO_4$ at scan rates between 10 and 100 mV/s. For this range of scan rates, $E^{\circ\prime}$ is 620 mV and does not depend on the scan rate. As shown Figure 5.12, the peak current scales linearly with scan rates. The ΔE_p is 43±6 mV and FWHM is 173±10 mV, which are higher than that expected for an ideal surface confined signal, but the ΔE_p is lower than that expected for a solution phase species. Unlike the compact $[Os(CAIPA)_3](ClO_4)_2$ film on the glassy carbon electrode, the voltammetric peaks of Os redox centres in the AuNPs multilayer became much sharper and the formal potential shifted in a negative potential direction. This observation might reflect the spatial distribution of osmium linkers in the multilayer. Due to host-guest inclusion with the CD monolayer on the gold nanoparticle surface, osmium linkers are well-organized and immobilized in the CD cavities. This suggests that the spatial location of osmium linkers were changed due to host-guest inclusion [25,26] compared to Os film. This structure of osmium linkers in the multilayer may facilitate penetration for electrolyte ion for charge compensation with a relatively low Gibbs energy barrier and result in a low formal potential for osmium linkers. Compared to osmium film, the surface coverage value of osmium linkers, which can be obtained from the measurement of the charge by integrating background corrected cyclic voltammograms of Os oxidation peak and the surface area of the 3 mm diameter glassy carbon electrode, in the multilayer is much smaller. It indicates that the content of Os complexes in the AuNPs multilayer is less than that contained in the complex film. But surprisingly, the redox current of Os complexes in the multilayer is higher than that in the solid deposits at scan rates between 10 and 30 mV/s. This observation suggests that the AuNPs would improve electron transfer, which could result in the increase in the redox current [27].

Cyclic voltammetry of the AuNPs multilayer has been undertaken under semi-infinite linear diffusion conditions to measure the rate of homogeneous charge transport through the multilayer. Figure 5.13 shows the voltammetric responses at scan rates between 100 and 500 mV/s under this condition. At this range of scan rates, the ΔE_p increases with increasing scan rate from 57 mV to 136 mV. However, the total cell resistance was measured as 316 Ω, leading an ohmic drop of approximately 11 mV, which is negligible as compared with the observed ΔE_p value of 136 mV. It suggests that heterogeneous electron transfer is responsible for this behaviour rather than the ohmic drop. Also as shown in Figure 5.14, the voltammetric peak current increases linearly with $\upsilon^{1/2}$. It allows the D_{CT} values to be determined by using Equation 5.1. Using this approach and measured Os complex concentration of 0.57 M yields D_{CT} values of $(6.1\pm0.6)\times10^{-11}$ cm^2 s^{-1} and $(6.5\pm0.4)\times10^{-11}$ cm^2 s^{-1} for oxidation and reduction of the redox labels in the AuNPs multilayer, respectively.

The rate determining step could be limited ether by electron hopping between the sites or by the counterion diffusion necessary to maintain electroneutrality [28]. Compared to the solid deposit, the structure of multilayer may facilitate transfer of the electrolyte anion from the aqueous electrolyte phase to the AuNPs multilayer meaning that the Gibbs free energy of multilayer is relatively small. This should lead a faster rate of homogeneous charge transport through the AuNPs multilayer. However, the rate through the multilayer is slower than the rate through solid deposit. It suggests that the rate is limited by electron hopping between adjacent Os decorated AuNPs Os-Au core-Os through the whole multilayer network. And the decrease of the electron transport is probably because of the long chain of the linker bridge, which would slow the electron hopping rate [9].

When electron hopping represents the overall charge transport rate through the metallopolymer film, the Dahms-Ruff equation [29,30] can be used to calculate the electron self-exchange rate constant, k_{SE}, from the D_{CT} according to Equation 5.2:

$$D_{CT} = D_{phys} + \frac{1}{6} k_{SE} \delta^2 C \qquad \textbf{(5.2)}$$

where C is the local concentration of redox centres within Os/CD monolayer on each particle, δ is the intersite separation between adjacent redox centres, and D_{phys} describes physical diffusion in the absence of electron hopping. In this situation, D_{phys} is assumed to be zero, because the Os complexes are linked to the AuNPs surface and immobilised within the multilayer. The intersite separation is estimated as 104.1 nm, which is based on summation of the gold nanoparticle core diameter (101 nm) and two extended chain distances between Au core edge and Os redox label centre (2×15.5 Å). Using these values, Equation 5.2 yields the electron self-exchange rate constant of 5.9 M^{-1} s^{-1}.

This rate constant is much lower than those found in other osmium bipyridyl complex film of 10^4 to 10^6 M^{-1} s^{-1} [31,32]. There appear to be two possibilities to account of the small rate constant observed here. First, the homogeneous charge transport diffusion coefficient obtained in the multilayer is approximately one or two order magnitude lower than those observed in the solid deposits [31,32]. Second, the intersite separation of Os centres is extremely large in the multilayer because of the large core diameter of gold nanoparticle. Compared to the linking chain of Os complex, AuNPs are not barriers for electron transfer. The intersite separation of Os centres in the multilayer can be reduced to 3.1 nm. This separation is still relatively large, however, the rate constant resulted from this value can be obtained as 6.7×10^3 M^{-1} s^{-1}, which is reasonable for the electron self-exchange through the Os linkers.

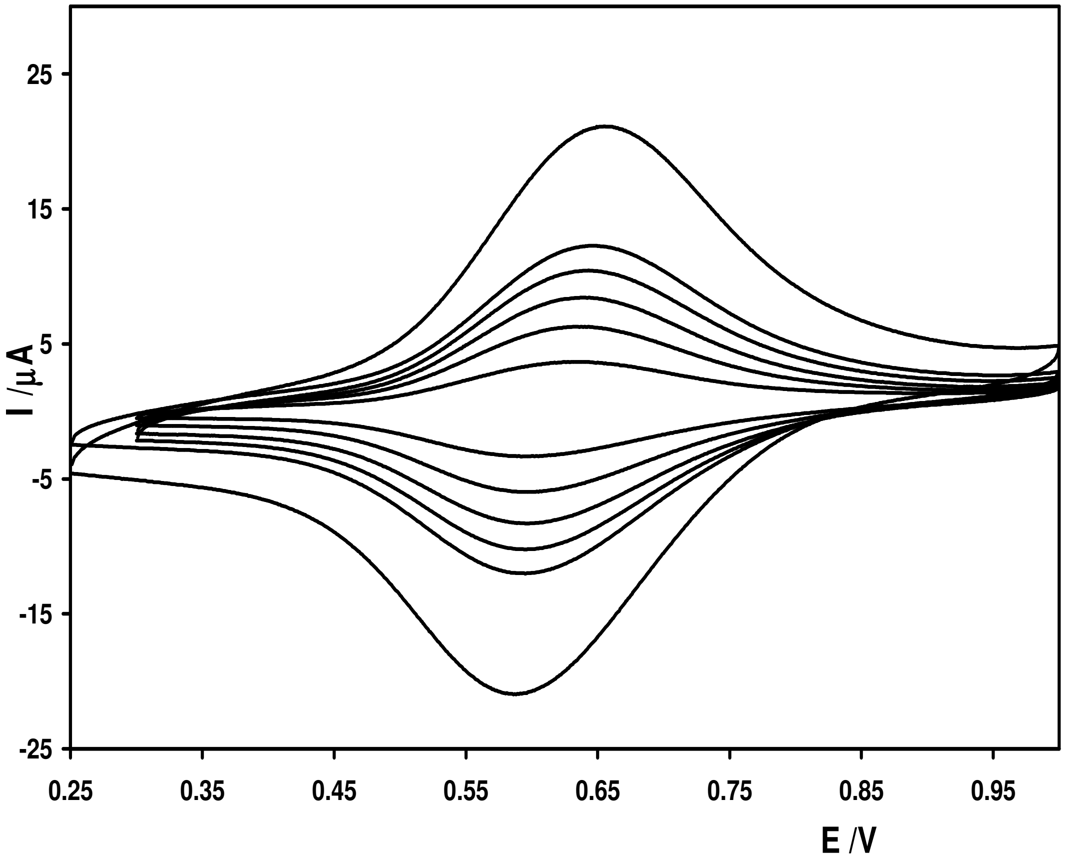

Figure 5.11. Voltammetric response of the AuNPs multilayer coated on 3 mm glassy carbon electrode in 0.1 M aqueous $LiClO_4$ at scan rates between 10 and 100 mV/s (from bottom to top). $\Gamma = 1.1\times10^{-9}$ mol cm^{-2}.

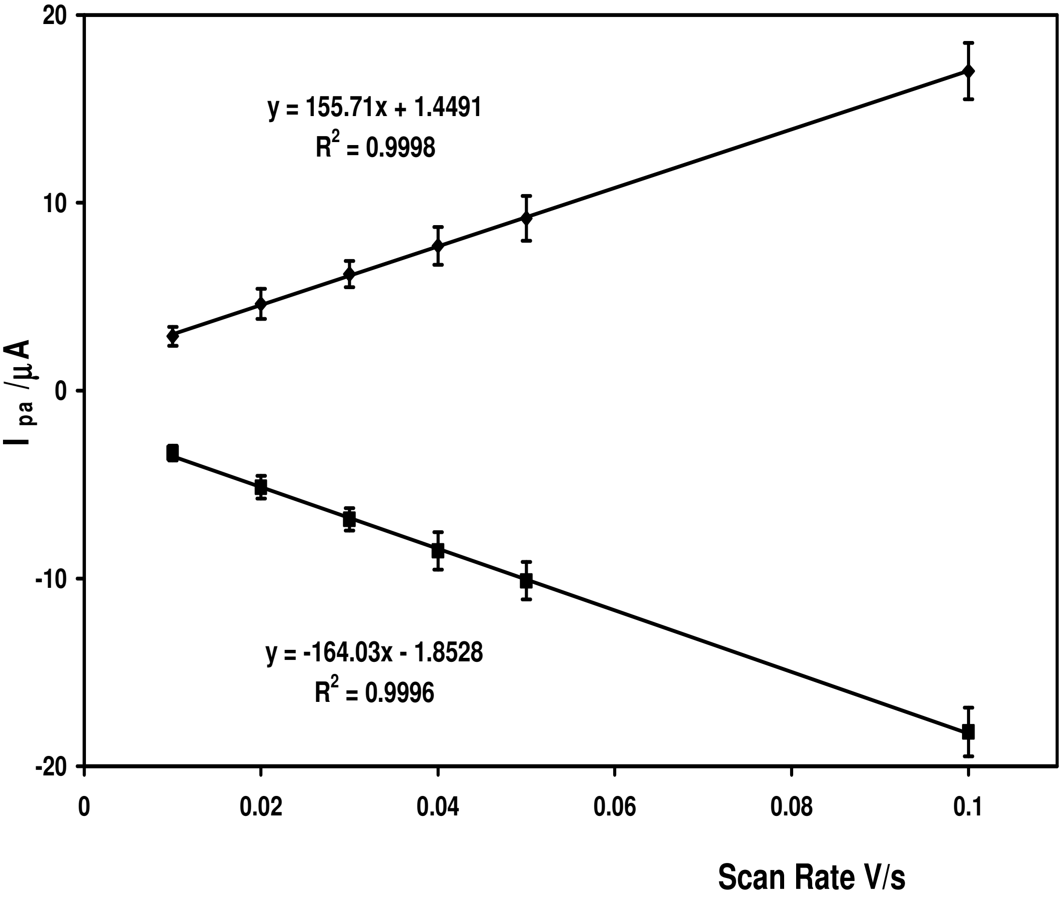

Figure 5.12. The plot of scan rate dependence of peak current for the AuNPs multilayer coated on 3 mm glassy carbon electrode in 0.1 M aqueous $LiClO_4$ at scan rates between 10 and 100 mV/s. The numbers of repetitive measurement (n=5).

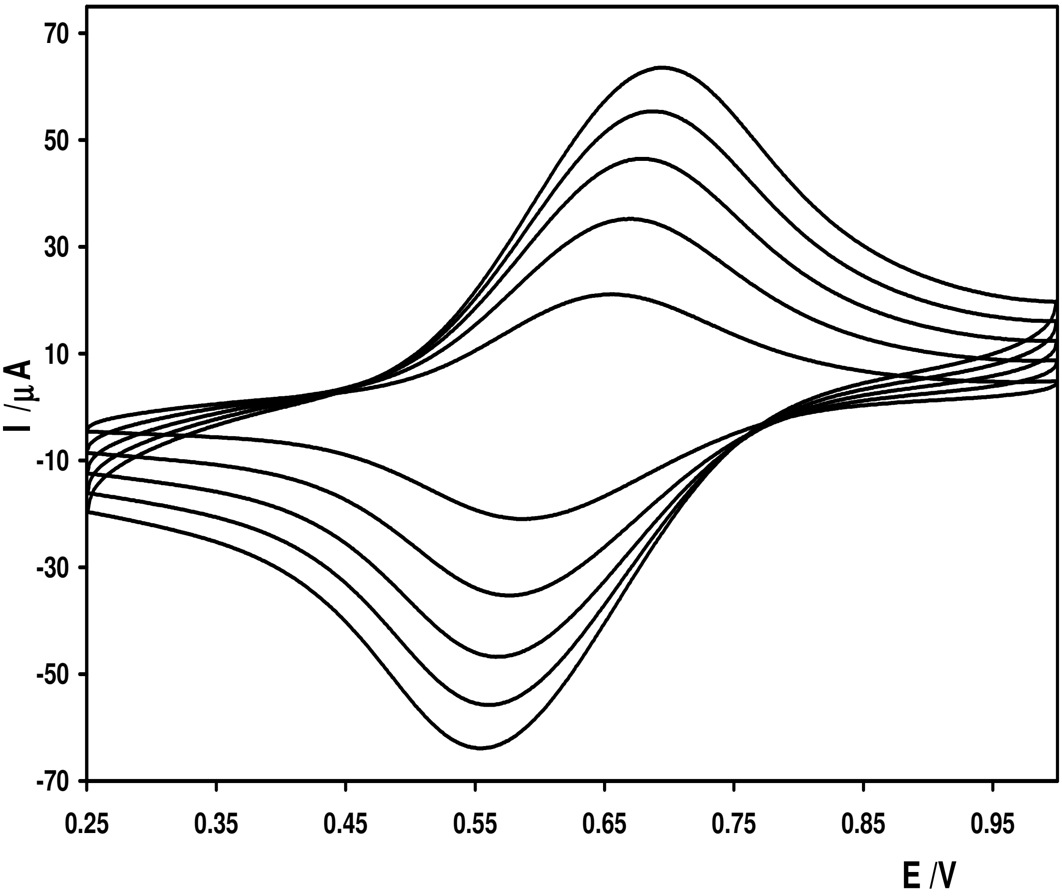

Figure 5.13. Scan rate dependence of the voltammetric response of AuNPs multilayer on 3 mm glassy carbon electrode in 0.1 M $LiClO_4$. υ =500, 400, 300, 200 and 100 mV/s (from top to bottom). $\Gamma = 1.1\times10^{-9}$ mol cm^{-2}.

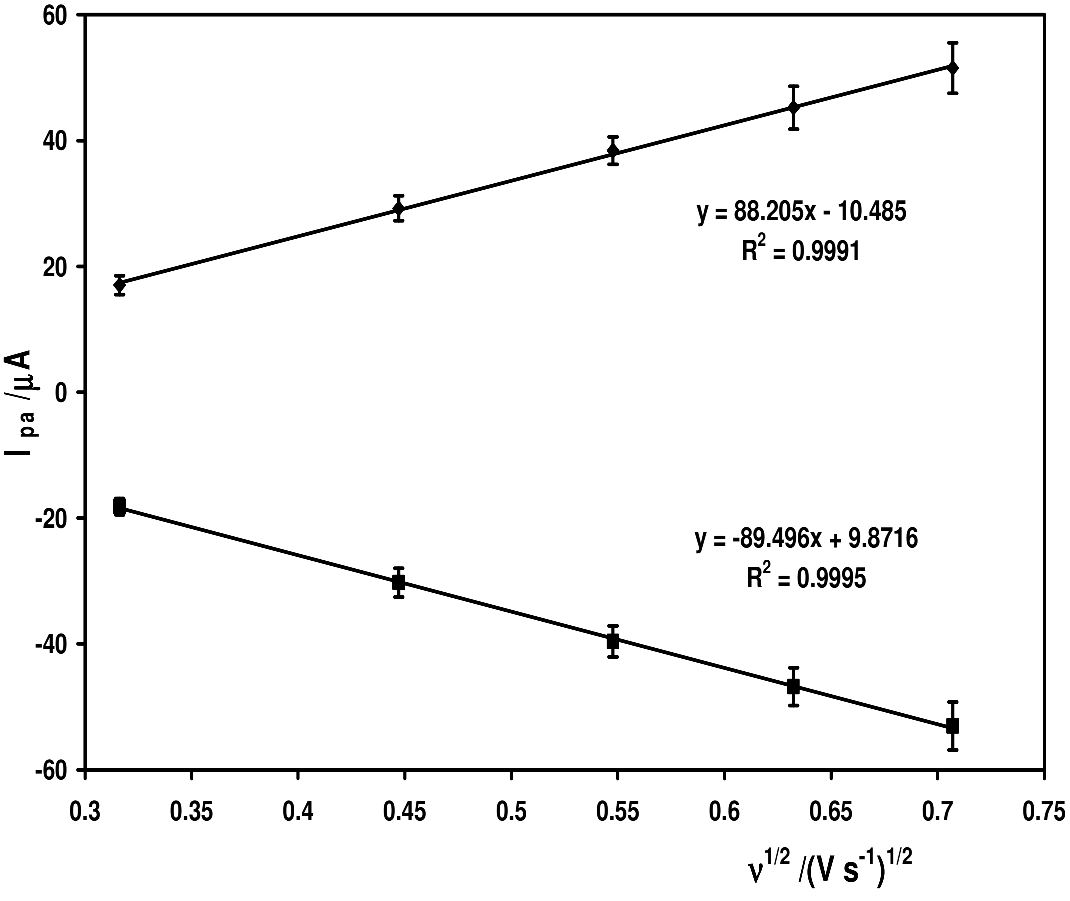

Figure 5.14. Plot of i_p vs. $\upsilon^{1/2}$ for the AuNPs multilayer on 3 mm glassy carbon electrode in 0.1 M $LiClO_4$. υ =500, 400, 300, 200 and 100 mV/s. The numbers of repetitive measurement (n=5).

5.3.5 Electrical Conductivity of AuNPs Multilayer.

To address the issue of whether electron hopping is rate limiting, the electronic conductivity of AuNPs multilayer has been determined using interdigitated array electrodes (IDAs) coated with the metallopolymer. As originally demonstrated by Wrighton and co-workers [33,34,35], the film conductivity is obtained from the slope $\partial i / \partial E$.

Figure 5.15 shows that the current varies linearly with potential between –0.05 V and +0.05 V and the slopes can be used in conjunction with Equation 5.3 below to determine the conductivity, σ, where (d_G / A_{total}) is the Zaretsky cell constant. The constant of the IDAs used in this experiment is 0.04 cm^{-1}.

$$\sigma = d_G \partial i / A_{total} \partial E \qquad \textbf{(5.3)}$$

The slopes of the best fit line to the data present in Figure 5.17 yield conductivities of 3.3×10^{-7} Ω^{-1} cm^{-1} for the Os complex film and 6.9×10^{-9} Ω^{-1} cm^{-1} for the AuNPs multilayer. The conductivity of blank IDAs was measured as 1.2×10^{-11} Ω^{-1} cm^{-1} for comparison. All measurements were carried out in contact with dry air at room temperature.

The relationship between the rate of electron transport D_{CT} and the conductivity can be described by the Equation 5.4 [36]:

$$D_{CT} = \frac{4RT\sigma}{10^{-3}F^2C} \qquad \textbf{(5.4)}$$

For Os complex film, the D_{CT} obtained is 4.8×10^{-10} cm^2 s^{-1} while the value obtained for the AuNPs multilayer is 1.3×10^{-11} cm^2 s^{-1}. Significantly, both of these values are consistent with those obtained using cyclic voltammetry for the films in contact with aqueous electrolyte. Therefore, these IDA measurements confirm that the movement of charge compensating counterions does not represent the rate determining step for homogeneous charge transport through these films. The solid-state electron hopping conductivity of the AuNPs multilayer is affected by the chain length of linker bridge and the activation-barrier energy of the electron transfer at the linker bridge [37,38]. This fact suggests that the rate charge transport of the AuNPs multilayer proceeds more slowly, as coupled to the relatively long chain of the linker bridge between Au cores. This longer pathway results in the larger activation-barrier energy, which would decrease the rate of electron transfer.

For a hypothetical cubic lattice model [37,39], the electron self-exchange rate constant, k_{SE}, also can be calculated as Equation 5.5,

$$k_{SE} = \frac{6RT\sigma}{10^{-3} F^2 \delta^2 [Os]^{2+} [Os]^{3+}} \qquad \textbf{(5.5)}$$

where k_{SE} is the electron self-exchange rate constant, R is the gas constant, σ is the conductivity at temperature T *(K)*, F is the Faraday constant, δ is the intersite separation between adjacent redox centres, and the ratio should maximize at $[Os]^{2+}$ / $[Os]^{3+}$ = 1. The electron self-exchange rate constant for AuNPs multilayer is determined as 1.2 M^{-1} s^{-1} using Equation 5.5. This value is comparable with that obtained from the D_{CT} in solution indicating that the rate constant is not affected by the counterion motion. This small value of rate constant can arise due to two reasons. First, in the multilayer the rate of electron transport and conductivity through the Os complex linkers are small. Second, the intersite separation between two redox label centres is big because large size gold nanoparticles are used. If the intersite separation is taken from the extended chain length of Os linker of 3.1 nm and the core diameter of gold nanoparticle is ignored as AuNPs should not be barriers for electron transport, the rate constant can be observed as 1.4×10^3 M^{-1} s^{-1}, which agrees to the rate constant of multilayer obtained using cyclic voltammetry.

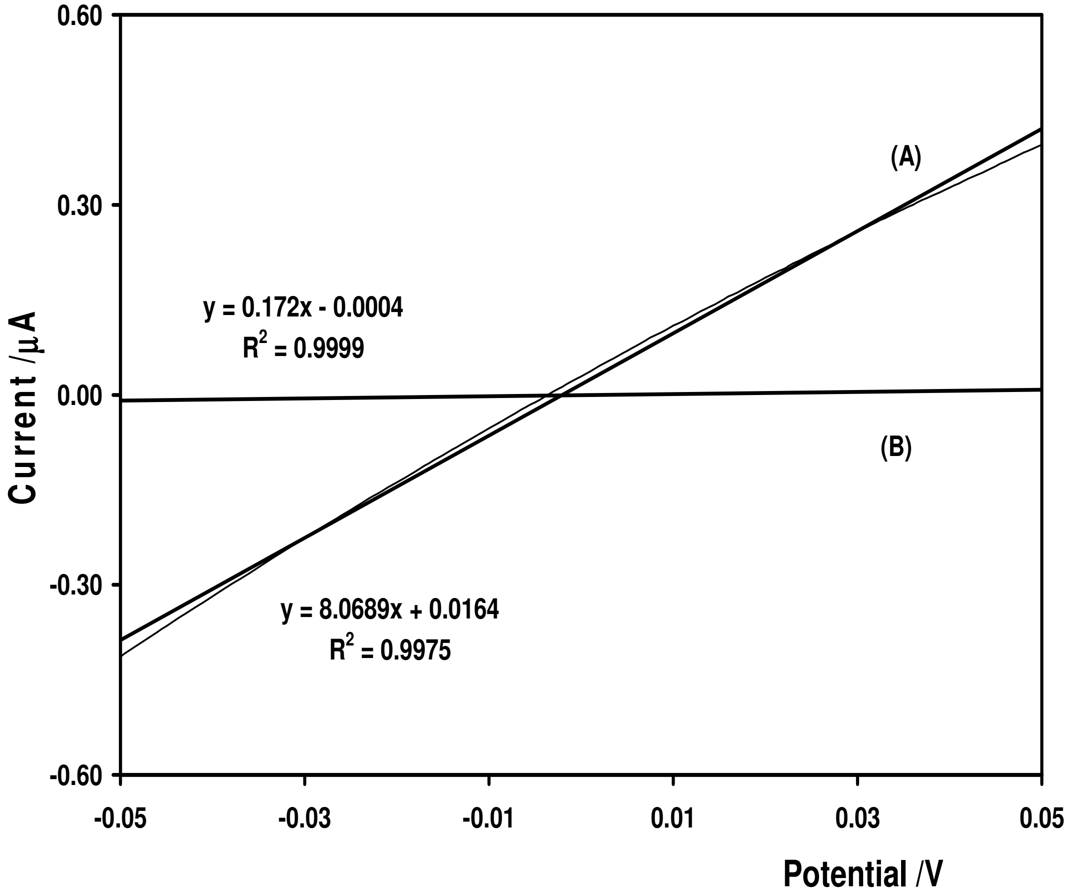

Figure 5.15. Dependence of the current on the applied potential for IDAs modified with Os complex film (A) and AuNPs multilayer (B) in contact with air. In each case, the IDAs electrode was scanned at 100 mV s^{-1}.

5.3.6 Electrochemical Properties of the AuNPs Multilayer in Acidic Electrolyte.

The total surface areas of AuNPs can be determined using cyclic voltammetry in H_2SO_4 [40]. Figure 5.16 shows the CV responses of the unmodified AuNPs film, which is formed on 3mm glassy carbon electrode and cycled between 0.5 V and 1.6 V in 0.5 M H_2SO_4. The broad oxidation wave between 1.1 V and 1.6 V is associated with the formation of gold oxide and the reduction peak around 0.94 V is ascribed to removal of the gold oxides. The charges obtained from the integration of the reduction peak can be used to calculate the total surface areas of AuNPs using the reported value of 390±10 $\mu C/cm^2$ for clean polycrystalline gold [40].

Figure 5.17 illustrates the initial voltammetric response of $[Os(CAIPA)_3](ClO_4)_2$ linked β-CD-(4-py)$_2$-capped AuNPs film in the same condition as the CV response obtained from the unmodified AuNPs film. This figure reveals that are significant differences in the behaviour observed at neutral and acidic electrolyte environment. In acidic electrolyte, the oxidation and reduction potentials of Os centres are 0.89 V and 0.84 V, respectively. For the first scan, in contrast to the redox potentials found in neutral electrolyte, these two potentials of $Os^{+2/+3}$ couple shifts in a positive direction because of the protonation of CAIPA ligands at low pH. The oxidation and reduction potentials of AuNPs remain unchanged at 0.148 V and 0.94 V for the first scan, respectively. But the integrated area under the reduction peak, indicating the active area of AuNPs surface, is remarkably decreased compared to the integrated area for the unmodified AuNPs film (Figure 5.16). This may be due to the surface area available for oxide formation on AuNPs was reduced by coverage with the $[Os(CAIPA)_3]^{+2}$ linked β-CDs monolayer [41,42].

The ratio of osmium centres to each gold nanoparticle in the AuNPs multilayer can be estimated by integrating the areas under the osmium oxidation peak and reduction peak of AuNPs in the first CV cycle to calculate the charge consumed by each process. The number of moles of Os complex molecules within the multilayer can be calculated from the charge of Os oxidation peak. The number of AuNPs is determined from the gold oxide reduction peak. The ratio of Os centres to AuNPs is obtained as 2.98×10^6 per gold nanoparticle, which is much higher than the theoretical calculation (10^4) because of the loss of electroactive surface area of AuNPs.

However, this ratio is in close agreement with that observed by the electronic spectroscopy method. This may suggest that the degree of effect of modification and aggregation of AuNPs is similar in both methods.

In addition, the formal potential, $E^{o\prime}$, of the osmium centres shifts in a positive potential direction and the peak current for both AuNPs oxidation and reduction are decreased upon repeated cycling in Figure 5.17. The former feature results from the reduced electron-donating ability of the protonated ligand or higher overall positive charge on the protonated complex. This similar observation has been reported on similar complexes undergoing protonation reaction in low pH electrolyte [43,44]. The latter feature is more likely that kinetics of gold oxide reduction are slower than oxidation [45].

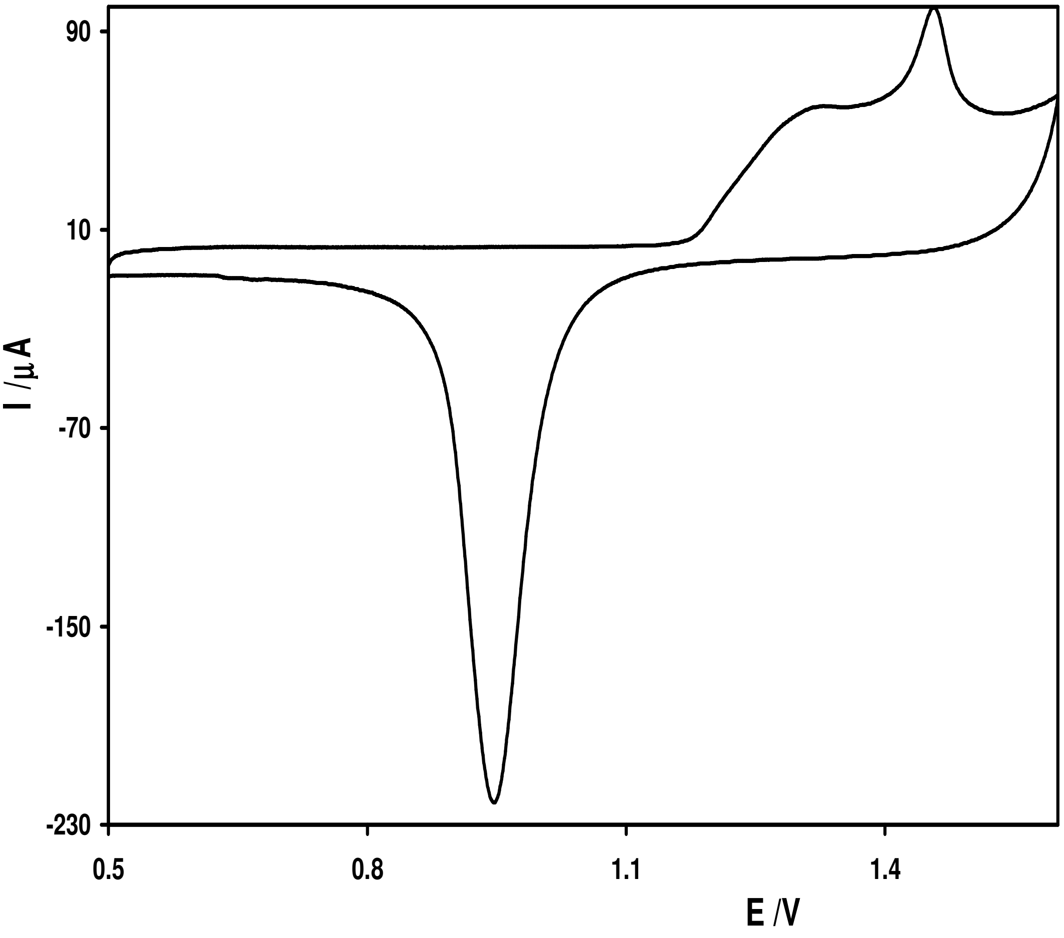

Figure 5.16. The cyclic voltammetry of the unmodified AuNPs film formed on 3mm glassy carbon electrode and cycled between 0.5 V and 1.6 V in 0.5 M H_2SO_4 at 100 mV/s.

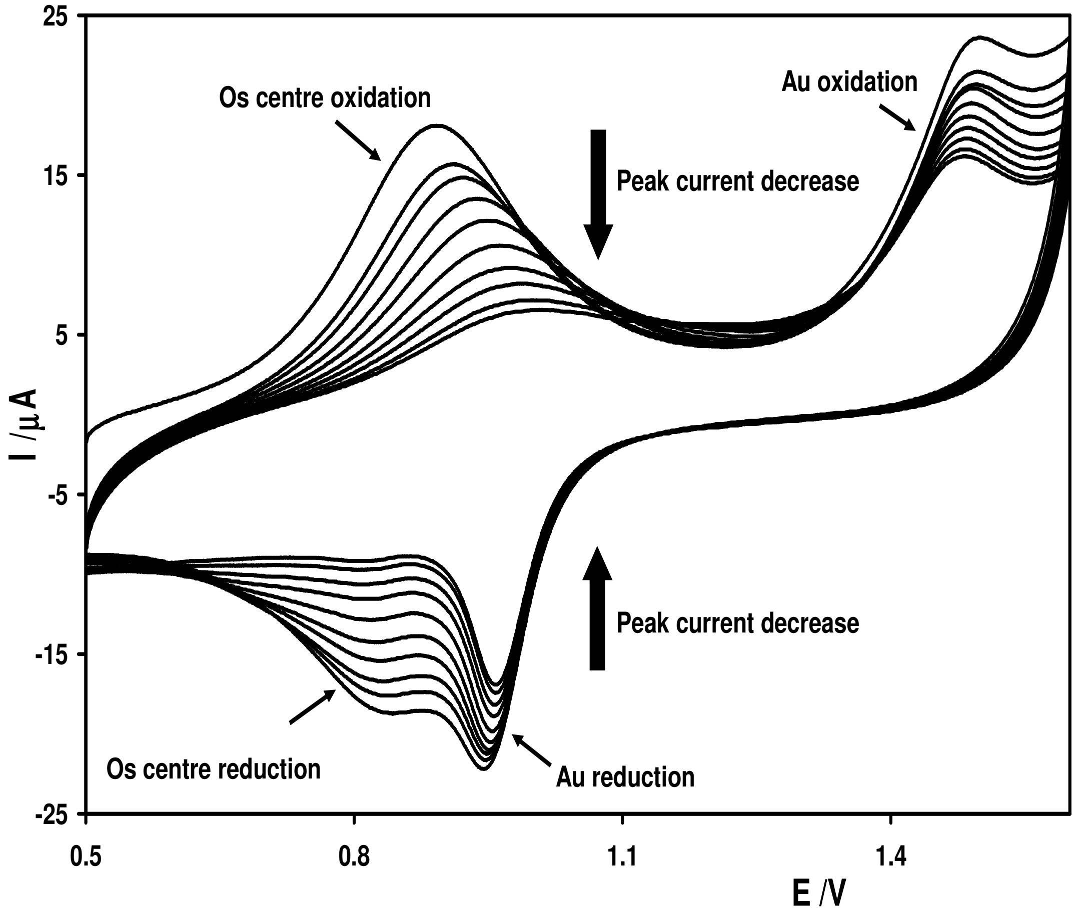

Figure 5.17. Effect of repeated scanning at 100 mV/s on the voltammetric response of AuNPs multilayer formed on 3mm glassy carbon electrode and cycled between 0.5 V and 1.6 V in 0.5 M H_2SO_4.

5.4 CONCLUSIONS

A new three dimensional gold nanoparticles multilayer assembled via cyclodextrin-adamantane host –guest interaction with Os metal centres as redox labels has been formed and characterized. The general electrochemical properties and the diffusion-like electron transport dynamics of this AuNPs multilayer have been investigated using cyclic voltammetry. The homogeneous charge transport diffusion coefficient, D_{CT}, associated with oxidizing or reducing the osmium redox labels is of the order of 10^{-11} cm^2 s^{-1} and limited by electron hopping. These values are apparent smaller than those observed in the $[Os(CAIPA)_3](ClO_4)_2$ complex film under the same conditions, because electron transfer distance is large. Also, analysis of the D_{CT} value according to the Dahms-Ruff equation yields a self-exchange rate constant of 5.9 M^{-1} s^{-1} for AuNPs multilayer. Further investigations using thin films of the multilayer and Os complex on IDA electrodes where ion movement does not contribute to the observed response yield D_{CT} and rate constant values that are consistent with those obtained using cyclic voltammetry. Taken together, these data indicate that the rate of electron transport is controlled by the electron hopping and affected by the length of electron transfer pathway.

5.5 REFERENCES

[1] A. C. Templeton, W. P. Wuelfing, R. W. Murray. Acc. Chem. Res. 33 (2000) 27.

[2] M-C. Daniel, D. Astruc. Chem. Rev. 104 (2004) 293.

[3] Y. W. C. Cao, R. C. Jin, C. A. Mirkin, Science. 297 (2002) 1536.

[4] J. Liu, Y. Lu. J. Am. Chem. Soc. 125 (2003) 6642.

[5] T. F. Jaramillo, S. H. Baeck, B. R. Cuenya, E. W. McFarland. J. Am. Chem. Soc. 125 (2003) 7148.

[6] (a) R. Shenhar, V. M. Rotello. Acc. Chem. Res. 36 (2003) 549. (b) M. Brust, C. Kiely. J. Colloids Surf. A. 202 (2002) 175. (c). J. L. Brennan, M. R. Branham, J. F. Hicks, A. J. Osisek, R. L. Donkers, D. G. Georganopoulou, R. W. Murray. Anal. Chem. 76 (2004) 5611.

[7] R. W. Murray. Chem. Rev. 108 (2008) 2688.

[8] F. P. Zamborini, J. F. Hicks, R. W. Murray. J. Am. Chem. Soc. 122 (2000) 4514.

[9] J. F. Hicks, F. P. Zamborini, A. J. Osisek, R. W. Murray. J. Am. Chem. Soc. 123 (2001) 7048.

[10] S. Chen, R. Pei, T. Zhao, D. Dyer. J. Phys. Chem. B 106 (2002) 1903.

[11] A. B. Descalzo, R. M-Manez, F. Sancenon, K. Hoffmann, K. Rurack. Angew. Chem. Int. Ed. 45 (2006) 5924.

[12] J. Liu, S. Mendoza, E. Roman, M. J. Lynn, R. Xu, A. E. Kaifer. J. Am. Chem. Soc. 121 (1999) 4304.

[13] J. Liu, J. Alvarez, W. Ong, A. E. Kaifer. Nano. Lett. 1 (2001) 57.

[14] O. Crespo-Biel, B. Dordi, D. N. Reinhoudt, J. Huskens. J. Am. Chem. Soc. 127 (2005) 7594.

[15] M. D. Malinsky, K. L. Kelly, G. C. Schatz, R. P. Van Duyne. J. Am. Chem. Soc. 123 (2001) 1471.

[16] (a) S. Link, M. A. El-Sayed. J. Phys. Chem. B 103 (1999) 4212. (b) S. Link, M. A. El-Sayed. Int. Rev. Phys. Chem. 19 (2000) 409. (c) P. K. Jain, K. S. Lee, I. H. El-Sayed and M. A. El-Sayed. J. Phys. Chem. B 110 (2006) 7238.

[17] Y. Pellegrin, R. J. Foster, T. E. Keyes. Inorg. Chim. Acta. 361 (2008) 2683.

[18] O. Crespo-Biel, A. Jukovic, M. Karlsson, D. N. Reinhoudt and J. Huskens. Israel Journal of Chemistry. 45 (2005) 353.

[19] Z. Liu, M. Jiang. J. Mater. Chem. 17 (2007) 4249.

[20] B. Abraham, C. V. Sastri, B. G. Maiya, S. Umapathy. J. Raman. Spectrosc. 35 (2004) 13.

[21] R. J. H. Clarke, P. C. Turtle, D. P. Strommen, B. Streusand, J. Kincaid, R. Nakamoto. Inorg. Chem. (1977) 84.

[22] A. Mcnally. Ph.D Thesis, Dublin Institute of Technology. (2005).

[23] W-B. Cai. J. Chem. Soc., Faraday Trans. 94 (1998) 3127.

[24] R. J. Forster, Y. Pellegrin, T. E. Keyes. Electrochem. Commun. 9 (2007) 1899.

[25] B. Kazakeviciene, G. Valincius, G. Niaura, Z. Talaikyte, M.Kazemekaite, V. Razumas, D. Plausinaitis, A. Teiserskiene, V. Lisauskas. Langmuir 23 (2007) 4965.

[26] Y. Tu, H. Chen. Anal. Biochem. 299 (2001) 71.

[27] F. Zuo, C. Luo, Z. Zheng, X. Ding, Y. Peng. Electroanalysis 20 (2008) 894.

[28] R. J. Forster and J. G. Vos in Comprehensive Analytical Chemistry, Ed. G. Svehla, Elsevier, Amsterdam, 1992, vol. XXVII, p. 465.

[29] H. Dahms. J Phys. Chem., 72 (1968) 362.

[30] I. Ruff, V. J. Friedrich, K. Demeter, K. Csillag. J. Phys. Chem., 75 (1971) 3303.

[31] L. Keane, C. Hogan, R. J. Forster. Langmuir. 18 (2002) 4826.

[32] D. A. Walsh, T. E. Keyes, R. J. Forster. J. Electroanal. Chem. 75 (2002) 538.

[33] E. W. Paul, A. J. Ricco, M. S. Wrighton. J. Phys. Chem. 89 (1985) 1441.

[34] J. W. Thackeray, H. S. White, M. S. Wrighton. J. Phys. Chem. 89 (1985) 5133.

[35] D. Ofer, R. M. Crooks, M. S. Wrighton. J. Am. Chem. Soc. 112 (1990) 7869.

[36] Q. Zeng, A. McNally, T. E. Keyes, R. J. Forster. Electrochim. Acta. 53 (2008) 7033.

[37] W. P. Wuelfing, S. J. Green, J. J. Pietron, D. E. Cliffel, R. W. Murray. J. Am. Chem. Soc. 122 (2000) 11465.

[38] W. P. Wuelfing, R. W. Murray. J. Phys. Chem. B 106 (2002) 3139.

[39] R. H. Terrill, J. E. Hutchinson, R. W. Murray. J. Phys. Chem. B, 101 (1997) 1535.

[40] R. Woods in Electroanalytical Chemistry, A. J. Bard (Ed), Marcel Dekker, New York, 1976, vol. 9, p. 1.

[41] J. Shi, Y-Q. Hu, Y-X. Hua. Electroanalysis 20 (2008) 1483.

[42] E. Sabatani, I. Rubinstein. J. Phys. Chem 91 (1987) 6663.

[43] R. J. Forster, T. E. Keyes, A. M. Bond. J. Phys. Chem. B 104 (2000) 6389.

[44] R. J. Forster, T. E. Keyes. Phys. Chem. Chem. Phys. 3 (2001) 1336.

[45] N. Zhao, Y. Wei, N. Sun, Q. Chen, J. Bai, L. Zhou, Y. Qin, M. Li, L. Qi. Langmuir. 24 (2008) 991.

CHAPTER 6

Effect of Addition of Nanoparticles on Charge Transport in the [Ru(terpy)(box)PVP$_{20}$][PF$_6$] Metallopolymer Film

6.1 INTRODUCTION

The mixing of polymers and nanoparticles is opening up new pathways for engineering flexible composites that exhibit useful electrical, optical, or mechanical properties [1]. The successful combination of the characteristics of parent polymer and nanoparticles into one material can facilitate increasing efficiency of the given properties [2,3]. The enhanced properties of nanocomposites can be used in certain applications, such as batteries [4], photovoltaic and display devices [5], and environmentally-responsive sensors [6].

Our group [7] has reported on the preparation of dispersed nanoparticle-metallopolymer composites in which the gold nanoparticle is loaded within an $[Os(bpy)_2PVP_{10}Cl]^+$ polymer by binding of free pyridine moieties and gold nanoparticle, bpy is 2,2′-bipyridyl and PVP is poly(4-vinylpyridine). The combination of both gold nanoparticles and ruthenium redox centres leads to unique redox and electrical conductivity effects. In particular, the composites provide enhanced conductivity in the dry state and the rate of charge transport in thin films of the composites has been found to depend on the loading of gold nanoparticles when in contact with aqueous electrolyte.

For the practical application of electrochromic materials in display devices the switching rate is important [8]. In Chapter 2 and 3, the structure of the metallopolymer, $[Ru(terpy)(box)PVP_{20}]PF_6$, where terpy is 2,2':6',2''-terpyridine and box is 2-(2-hydroxyphenyl)benzoxazole, in which one in every twenty of the PVP monomer units is labelled with the ruthenium complex was reported. Also, the rate of charge transport of the metallopolymer thin films in aqueous electrolyte was described. The charge transport diffusion coefficient, D_{CT}, associated with oxidizing or reducing the ruthenium centres is of the order of 10^{-13} cm^2 s^{-1} and it would take approximately 90 s to fully oxidize the metallopolymer film and regenerate the Ru^{3+} mediating centres. Compared to other PVP contained metallopolymers [9,10], this switching rate is relatively slow due to the low loading of ruthenium centres and associated large electron transfer distance.

In this chapter, investigations using cyclic voltammetry into the effect of incorporating gold nanoparticles into the [Ru(terpy)(box)PVP$_{20}$][PF$_6$] metallopolymer by binding to the free PVP pyridine moieties on the efficiency of charge transport is reported. The improvement of the charge transport efficiency within nanocomposites is found compared to the pure metallopolymer. Further, this improvement is confirmed by the dry state conductivity measurement for the nanocomposite films. Significantly, this finding has potential use in some fast switching electrochromic applications.

6.2 EXPERIMENTAL

6.2.1 Materials.

The preparation of the [Ru(terpy)(box)PVP$_{20}$]PF$_6$ metallopolymer has been described in Chapter 2. A colloidal solution of 100 nm gold nanoparticles (AuNPs) with concentration of 2.68 μM was purchased from BB (British Biocell) International and concentrated to 50 μM by centrifugation. Water was purified using a Milli-Qplus 185 Millipore installation. The electrolyte chemical of LiClO$_4$ with the purity of 99%was purchased from Aldrich and used as received.

6.2.2 Instrumentation and Apparatus

Electrochemistry was performed in conventional three-electrode cells using an Ag/AgCl electrode filled with 3 M KCl (aq) (CH instrument) as reference. Cyclic voltammetry (CV) was carried out using a CH instruments Model 660a electrochemical workstation. All electrolyte solutions were deoxygenated for at least 15 min using N$_2$ gas before use and maintained under a nitrogen blanket during measurement. Glassy carbon working electrodes were utilised as substrates for depositing nanocomposite films and were polished successively with 1.0, 0.3, and 0.05 μm alumina powder prior to use. After each polishing step, the electrodes were sonicated in Milli-Q water to remove the alumina powder. Nanocomposite films were prepared by evaporating a 20 μl drop of a series of mixtures of 1 % (fixed at 3 mM) metallopolymer and 100 nm gold colloidal solutions (5, 10, 15, 20, and 25 μM) to give mole ratio of AuNPs/Ru centres as 1/600, 1/300, 1/200, 1/150, and 1/120, onto clean electrodes and following by air-drying.

For measuring the nanocomposite conductivity, a CH instruments Model 760b electrochemical workstation was employed. Platinum interdigitated electrode arrays, IDAs, were purchased from Abtech Scientific. Inc. Nanocomposite films were formed by depositing a series of nanocomposites solutions onto the IDA fingers and gaps between fingers. In order to cover the IDA fingers and gaps completely, the nanocomposite solutions were drop-cast on the IDA electrodes several times.

6.3 RESULTS AND DISCUSSION

6.3.1 General Electrochemical Properties

Figure 6.1 shows the voltammetric response for a thin film of the nanocomposite by depositing mixed solution with the AuNPs/metallopolymer mole ratio of 1/120 onto 3mm glassy carbon electrode recorded between 0.1 and 0.5 V s^{-1}, where the supporting electrolyte is aqueous 0.1 M $LiClO_4$. The formal potential associated with the $Ru^{2+/3+}$ couple is at approximately 0.4 V, which is indistinguishable to that of the Ru centres in the metallopolymer films described in Chapter 3.

For scan rates between 0.1 and 0.5 V s^{-1}, the nanocomposite film displays identical characteristics as metallopolymer film with the ΔE_p value of 98±6 mV, and the fwhm of 162±5 mV under the semi-infinite diffusion conditions. The ΔE_p is independent of scan rates, indicating that slow heterogeneous electron transfer is not responsible for the observed behaviour. Ohmic effects are not responsible for this behaviour ether, as the increased currents at higher scan rate would be expected to increase the ΔE_p value. Also, for this range of scan rate, the ratio of the anodic to cathodic peak currents is unity, suggesting that the electron transfer reaction is reversible.

The surface coverage can be determined by integrating the area under the $Ru^{2+/3+}$ redox peaks at slow scan rate. The surface coverage for all nanocomposite films is similar. In all cases, the average surface coverage is $1.5\pm0.2\times10^{-8}$ mol cm^{-2}.

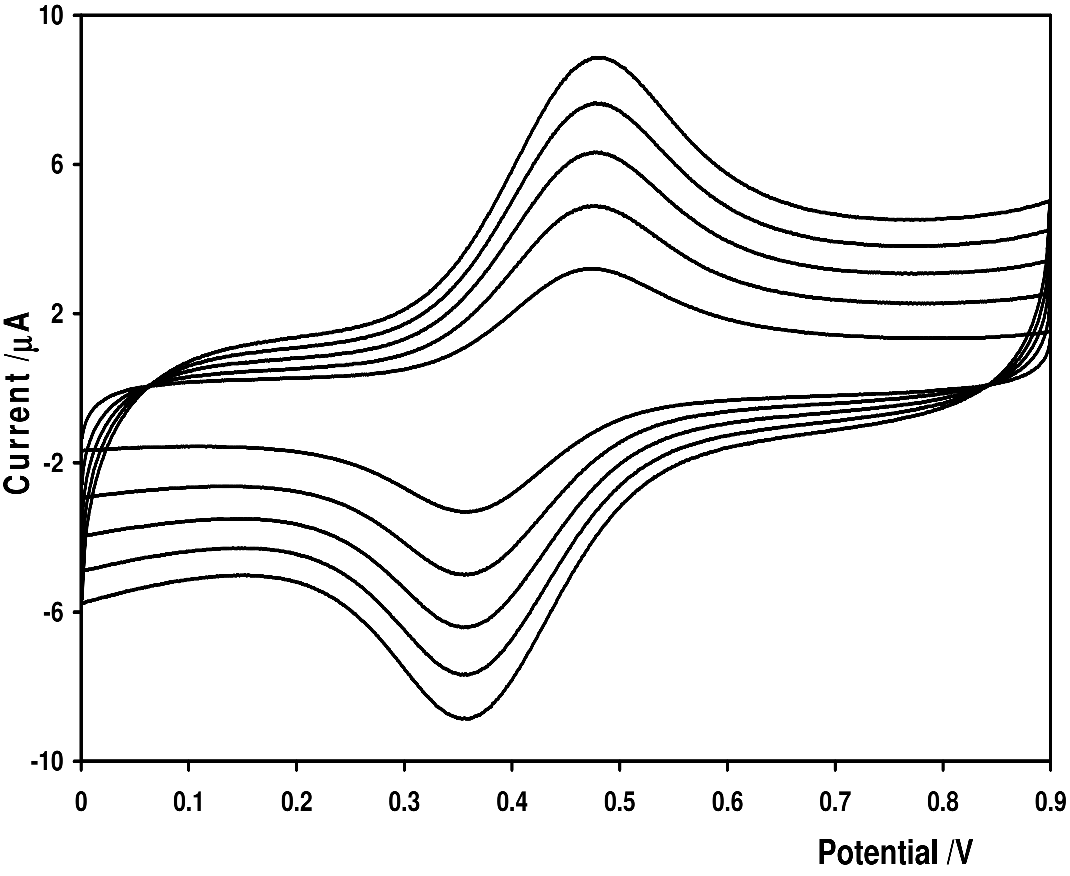

Figure 6.1. Scan rate dependence of the voltammetric response of nanocomposite film (the mole ratio of AuNPs/metallopolymer=1/120) on 3 mm glassy carbon electrode in 0.1 M $LiClO_4$. Surface coverage (Γ) is $1.5 \pm 0.2 \times 10^{-8}$ mol cm^{-2}. υ =0.5, 0.4, 0.3, 0.2, and 0.1 V s^{-1} (from top to bottom).

6.3.2 Charge Transport in Nanocomposite Films

The dynamics of charge transport in the nanocomposite films can be determined using cyclic voltammetry [11,12]. As shown in Figure 6.2, the voltammetric peak current increases linearly with $\upsilon^{1/2}$, which is consistent with the response being controlled by semi-infinite linear diffusion [13]. The peak current, i_p, can be expressed in terms of the Randles-Sevcik equation:

$$i_p = 2.69 \times 10^5 n^{3/2} A D_{CT}{}^{1/2} C_{eff} v^{1/2} \quad \textbf{(6.1)}$$

where n is the number of electrons transferred, A is the area of the working electrode, D_{CT} is the homogeneous charge transport diffusion coefficient, and C_{eff} is the effective fixed site concentration of the redox centre. The equation allows the nanocomposite films $D_{CT}{}^{1/2}C_{eff}$ to be determined from the slopes of the plot of i_p Vs $\upsilon^{1/2}$. The D_{CT} values have been determined using a max concentration of Ru redox centre of 0.5 M described in Chapter 3.

In Table 6.1, the slope of the straight line fit to each plot of i_p Vs $\upsilon^{1/2}$ is clearly shown to increase with increasing AuNPs content in the nanocomposite film. This result allows the D_{CT} value of each nanocomposite film to be determined and the change of the D_{CT} values agrees with the observation of the slopes of the nanocomposite films. Compared to pure metallopolymer film, the D_{CT} values of the nanocomposite films are higher by a factor of approximately two. It indicates that the presence of AuNPs in the metallopolymer film improves the efficiency of the charge transport. However, this increase of the D_{CT} value is much lower than that obtained in other metallopolymer-AuNPs nanocomposite system, in which the D_{CT} value is about an order of magnitude larger for the nanocomposite containing the highest AuNPs mole fraction, 0.85, than that found for the pure metallopolymer [7]. The minor increase of the D_{CT} value in this nanocomposite probably arises because of the low concentration of AuNPs loading. The concentration of the commercial gold nanoparticles is low (2.68 μM) and it is difficult to obtain the high concentration as the metallopolymer to make the high mole ratio between AuNPs and metallopolymer in the nanocomposite solution. This difficulty causes that there is no significant increase of the D_{CT} value observed in this nanocomposite film.

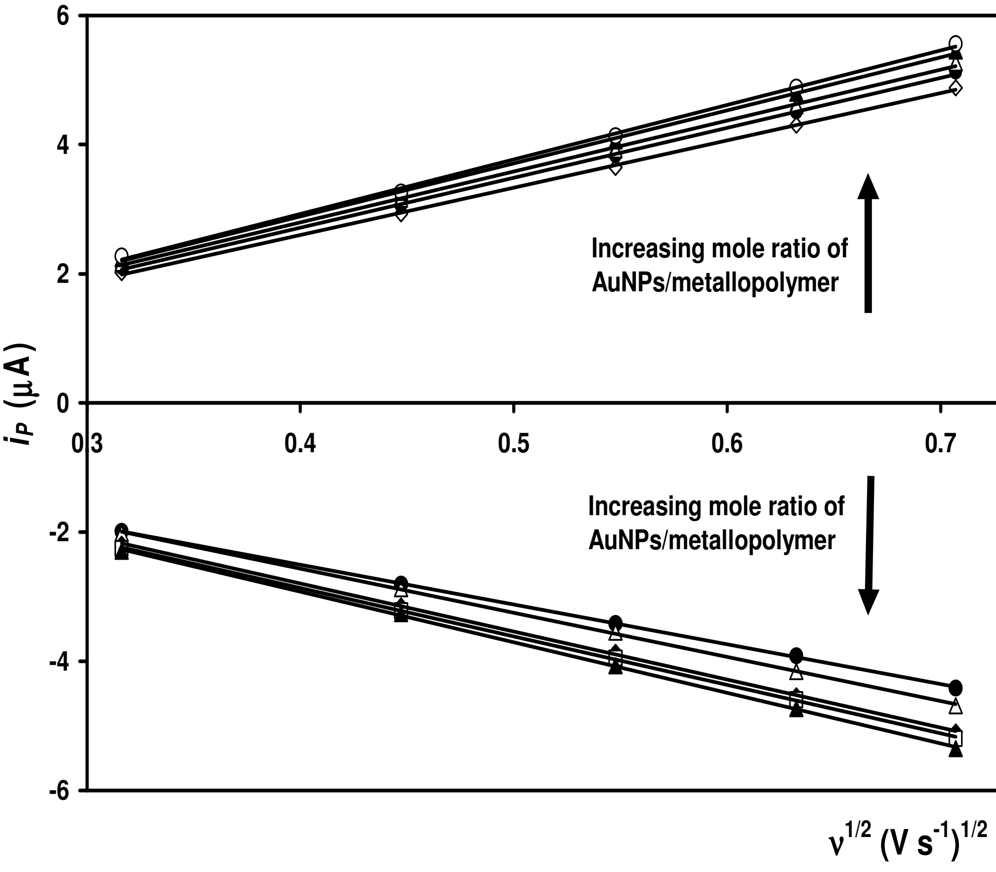

Figure 6.2. Plots of i_p vs. $\upsilon^{1/2}$ are obtained for the nanocomposite films on 3 mm glassy carbon electrode in 0.1 M $LiClO_4$. In both cases, the range of scan rates is from 0.1 to 0.5 V s^{-1} and the mole ration of AuNPs/metallopolymer increases from 1/600 to 1/120.

Table 6.1. Charge transfer properties of nanocomposite films with the different mole ratio of AuNPs/metallopolymer on 3 mm glassy carbon electrodes in 0.1 M $LiClO_4$.

The mole ratio of AuNPs/metallopolymer	**10^{-6} Slope of oxidation linear equation /A (V s^{-1})$^{-1/2}$**	**10^{-6} Slope of reduction linear equation /A (V s^{-1})$^{-1/2}$**	**10^{-13} D_{CT} oxidation /cm^2 s^{-1}**	**10^{-13} D_{CT} reduction /cm^2 s^{-1}**
0	-	-	3.6±0.1	3.3±0.2
1/600	7.3	6.2	5.7±0.4	4.0±0.2
1/300	7.7	6.8	6.4±0.1	5.0±0.3
1/200	7.9	7.4	6.6±0.2	5.9±0.1
1/150	8.2	7.5	7.2±0.2	6.0±0.2
1/120	8.5	7.8	7.6±0.3	6.5±0.1

6.3.3 Electrical Conductivity

The electronic conductivity has been determined using interdigitated array electrodes (IDAs) coated with the nanocomposite. As originally demonstrated by Wrighton and co-workers [14,15,16], the film conductivity is obtained from the slope $\partial i / \partial E$.

Figure 6.3 shows that the current varies linearly with potential between –0.2 V and +0.2 V and the slopes can be used in conjunction with Equation 6.2 below to determine the conductivity, σ, where (d_G / A_{total}) is the Zaretsky cell constant. The constant of the IDAs used in this experiment is 0.04 cm^{-1}.

$$\sigma = d_G \partial i / A_{total} \partial E \qquad \textbf{(6.2)}$$

The conductivities of the nanocomposite films have been measured in the presence of dry air at room temperature and pressure from the slopes of the best fit line to the data. The relationship between charge transport and conductivity of a nanocomposite film for a hypothetical cubic lattice model can be described in the Equation 6.3 [17]:

$$D_{CT} = \frac{4RT\sigma}{10^{-3} F^2 C} \qquad \textbf{(6.3)}$$

The presence of the gold nanoparticles enhances both the conductivity and D_{CT} observed for the metallopolymer. This increase is shown in Table 6.2. For these dry nanocomposite films, the D_{CT} values are smaller than those obtained using cyclic voltammetry for the films in contact with aqueous electrolyte and with approximately 56% difference between these two methods. However, both D_{CT} values obtained are of the order of 10^{-13} cm^2 s^{-1} and this order of the D_{CT} values is consistent with that obtained in CV measurements. This may suggest that the effect of the movement of charge compensating counterions on the rate determining step is minimal. The same conclusion was drawn for the pure metallopolymer matrix, in which segmental polymer chain motion limits D_{CT}. However, for the nanocomposite film, the metallopolymers bind to gold nanoparticles by free pyridine moieties and this probably reduces segmental polymer chain motion. On the other hand, the gold nanoparticle may be loaded within several metallopolymer chains because of the large particle size of gold with 100 nm diameter and it is possible that the gold nanoparticles can mediate electron transfer between the redox centres. Therefore, this can cause a faster rate of homogeneous charge transport through the nanocomposite film as the nanoparticle loading is increased.

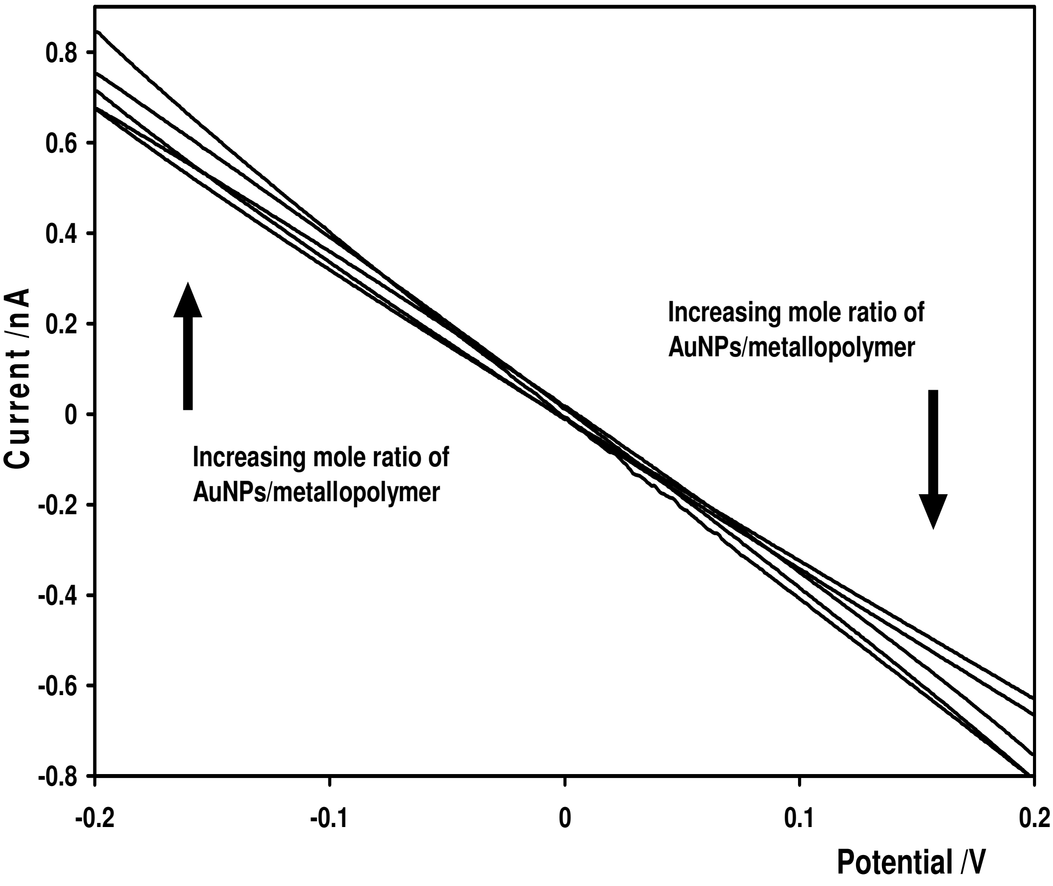

Figure 6.3. Dependence of the current on the applied potential for IDAs modified with [Ru(terpy)(box)PVP$_{20}$][PF$_6$]-AuNPs nanocomposite films equilibrated with air. The mole ration of AuNPs/metallopolymer increases from 1/600 to 1/120. In each case, one of the IDA combs was maintained at 0 V while the other was scanned at 50 mV/s.

Table 6.2. Summary of the conductivity and the charge transfer diffusion coefficient of nanocomposite films with the different mole ratio of AuNPs/metallopolymer on 3 mm glassy carbon electrodes in 0.1 M $LiClO_4$.

The mole ratio of AuNPs/metallopolymer	10^{-9} ***Slope*** **/Ω^{-1}**	10^{-10} ***Conductivity (σ)*** **/Ω^{-1} cm^{-1}**	10^{-13} D_{CT} **/cm^2 s^{-1}**
0	-	1.20±0.06	2.46±0.08
1/600	3.24	1.30±00.05	2.67±0.05
1/300	3.42	1.37±0.04	2.81±0.06
1/200	3.56	1.42±0.04	2.91±0.06
1/150	3.89	1.56±0.06	3.20±0.07
1/120	4.09	1.64±0.02	3.37±0.03

6.4 CONCLUSIONS

The preparation and enhanced electrochemical properties of nanocomposite film based on gold nanoparticles loaded [Ru(terpy)(box)PVP$_{20}$][PF$_6$] metallopolymer are reported. Cyclic voltammetry measurement reveals that the presence of AuNPs in the metallopolymer film improves the efficiency of the charge transport and the rate of homogeneous charge transport, D_{CT}, through the nanocomposite film depends on the gold nanoparticle loading. For the oxidation process, the D_{CT} value increases from 5.7×10^{-13} to 7.6×10^{-13} cm^2 s^{-1}, as the mole ration between AuNPs and metallopolymer in the composite film increases from 1/600 to 1/120. This observation suggests that the gold nanoparticles mediate electron transfer between adjacent metal centres. Also, investigations using thin nanocomposite films on IDA electrodes yield D_{CT} values that are consistent with those obtained using cyclic voltammetry. However, for both methods, the effect of AuNPs on the D_{CT} value is minor. It is probably due to the difficulty of obtaining the high mole ratio between AuNPs and metallopolymer in the nanocomposite solution. Taken together, these data indicate that the loading of gold nanoparticles into the metallopolymer may be used to control the rate of charge transport through the film but only close to the percolation threshold. However, some further research actions will need to be taken on this nanocomposite material including the effects of particles on the film structure, the rate determining step of charge transfer, and the importance of inter-particle percolation change.

6.5 REFERENCES

[1] A. C. Balazs, T. Emrick, T. P. Russell. Science. 314 (2006) 1107.

[2] R. Gangopadhyay, A. De. Chem. Mater. 12 (2000) 608.

[3] M. R. Bockstaller, R. A. Mickiewicz, E. L. Thomas. Adv. Mater. 17 (2005) 1331.

[4] S. Kuwabata, T. Idzu, C. R. Martin, H. Yoneyama. J. Electrochem. Soc. 145 (1998) 2707.

[5] P. K. Shen, H. T. Huang, A. C. C. Tseung, J. Electrochem. Soc. 139 (1992) 1840.

[6] R. J. Shan, M. Nuopponen, A. Niskanen, H. Jiang, E. I. Kauppinen, H. Tenhu. Langmuir 19 (2003) 3499.

[7] R. J. Forster, L. Keane. J. Electroanal. Chem. 554 (2003) 345.

[8] A. A. Argun, P. H. Aubert, B. C. Thompson, J. R. Reynolds. Chem. Mater. 16 (2004) 4401.

[9] R. J. Forster, J. G. Vos, M. E. G. Lyons, J. Chem. Soc. Faraday Trans. 87 (1991) 3761.

[10] R. J. Forster, J. G. Vos, J. Electroanal. Chem. 314 (1991) 135.

[11] A. M. Bond, F. J. Marken. Electroanal. Chem. 372 (1994) 125.

[12] P. J. Kuleszea, L. R. Faulkner. J. Am. Chem. Soc. 115 (1993) 11878.

[13] A. J. Bard, L. R. Faulkner. Electrochemical Methods: Fundamentals and Applications; 2 Ed.; Wiley: New York, 2001.

[14] E. W. Paul, A. J. Ricco, M. S. Wrighton. J. Phys. Chem. 89 (1985) 1441.

[15] J. W. Thackeray, H. S. White, M. S. Wrighton. J. Phys. Chem. 89 (1985) 5133.

[16] D. Ofer, R. M. Crooks, M. S. Wrighton. J. Am. Chem. Soc. 112 (1990) 7869.

[17] Q. Zeng, A. McNally, T. E. Keyes, R. J. Forster. Electrochim. Acta. 53 (2008) 7033.

CHAPTER 7

Conclusions

7.1 CONCLUSIONS

Electrochromic materials attract interests because they can exhibit redox states with distinct electronic (UV/visible) absorption spectra. These materials have been widely available in some applications, e.g. in cars as rear-view mirrors to increase driving safety and in architecture as colouration controlled windows to cut out solar infrared and save working environment costs.

In this thesis, there is a strong interest in Ruthenium- O^- coordinated phenolate ligands containing electrochromic metallopolymers because of strong σ donating ability of phenolate donor ligands, which can result in an increase of the electron density at the metal site. This metallopolymer also potentially offers many advantages in the practical electrochromic applications ranging from security to monitoring packaging integrity in foods and pharmaceuticals. Some of these advantages are shown as follows:

- Low metal centre redox potential at 0.1 V, which is much lower than that obtained from other Ru polypyridine complex system at 1.3 V.
- Rich spectroscopy from visible region MLCT, ILCT to NIR region LMCT.
- Intense colouration and multi-colour states
- Metallopolymer film is stable to electrochemical cycling.

Also, in practical applications the electrochromic materials are usually formed as a thin film to create an electrochromic electrode. It is very important to understand the dynamics of charge transport of this electrode by measuring the electrochromic switching rate, which is one of the key factors in evaluating an electrochromic material.

The metallopolymer containing Ru-phenolate complex shows that the electrochromic switching rate, D_{CT}, associated with oxidizing or reducing the ruthenium centres is of the order of 10^{-13} cm^2 s^{-1} and it would take approximately 90 s to fully oxidize the metallopolymer film with the thickness of 100 nm and regenerate the electrochromic centres. However, this rate is about two or three orders of magnitude lower that those found in other ruthenium metallopolymer systems. This observation is because the relatively low loading of ruthenium centres, 1 in 20 monomer units, makes the intersite separation large, of the order of 40 Å. This large distance means that movement of the polymer chain segments rather that the actual electron transfer itself, is likely to represent the rate determining step.

In order to improve the electron transfer efficiency, the simplest way is to increase the loading of ruthenium centres in the metallopolymer. The relatively high loading of ruthenium could make the intersite separation small and cause direct electron transfer between two ruthenium centres possible. Moreover, we took advantage of enhanced electrochemical properties of gold nanoparticles to form [Ru(terpy)(box)PVP_{20}][PF_6] metallopolymer nanocomposite. Cyclic voltammetry measurement indicated that the electron transfer rate of the metallopolymer depends on the gold nanoparticles loading. It increased with increasing gold nanoparticle loading in the nanocomposite film. However, future work on this nanocomposite material could include the effects of particles on the film structure, the rate determining step of charge transfer, and the importance of inter-particle percolation change. These data will be useful to better understand the rate of electron transfer between redox centres and through the nanocomposite film. These enhanced properties would give nanocomposites a better performance for potential applications in the electrochromic devices.

In [Ru(terpy)(box)PVP_{20}][PF_6] metallopolymer nanocomposite, the metallopolymer is bound to gold nanoparticle surface by the free PVP pyridine moieties. The well-defined and accessible interfacial structures are good model systems for studies of physical chemistry and statistical physics in two-dimensions, and the crossover to three dimensions. The binding ability of the host-guest inclusion between the immobilized CD monolayer on the electrode surface and electrochromic Os complex was investigated. Experimental data indicated that the association constant between adamantyl end group of the Os complex and CD monolayer was at the order of 10^4 M^{-1}, which was consistent with that in a CD-adamantane interaction reported previously. This inclusion could be used to build three dimensional structures due to its high host-guest binding ability. Therefore, a three dimensional gold nanoparticle multilayer via cyclodextrin-adamantane host–guest interaction has been developed in the thesis. The multilayer gives a model structure for the electrochromic materials because Os complexes can be replaced by other electrochromic guest molecules to obtain the different colouration. Moreover, interest in the gold nanoparticle multilayer is not only because of the high stability of self-assembly host monolayer on the AuNPs surface or electrochromic host-guest inclusion, but also due to the enhanced properties of AuNPs, including electrical conductivity, plasmon absorption, and interfacial electron transfer.

As reported previously, the plasmon absorption is influenced by the particle size. The absorption red shifts with increasing AuNPs size and the colour changes from red to light purple. For transparent application of the electrochromic materials, AuNPs plasmon absorption in the multilayer could be attractive to give a coloured background or sharp contrast by mixing the colour observed from electrochromic material.

APPENDIX A

Publications

Available online at www.sciencedirect.com
ScienceDirect
Electrochemistry Communications 10 (2008) 466–470
electrochemistry communications
www.elsevier.com/locate/elecom

Three colour electrochromic metallopolymer based on a ruthenium phenolate complex bound to poly(4-vinyl)pyridine

Qiang Zeng, Andrea McNally, Tia E. Keyes, Robert J. Forster *

National Centre for Sensor Research, Biomedical Diagnostics Institute, School of Chemical Sciences, Dublin City University, Dublin 9, Ireland

Received 13 December 2007; received in revised form 9 January 2008; accepted 10 January 2008
Available online 17 January 2008

Abstract

The photonic and electrochemical properties of a novel Ru–phenolate based metallopolymer are reported. The complex undergoes a ruthenium based reversible oxidation at approximately +0.400 V and irreversible box ligand oxidation at +0.800 V vs. Ag/AgCl. Oxidation of thin films in aqueous electrolyte at +0.500 V reversibly switches the colour from wine red to light green and a red orange colour is observed for mixed redox composition. In contrast, oxidation at potentials more positive than +1.500 V shows no visible colour change but produces a change in the near infra-red region. To determine the electrochromic switching rate and to identify the rate determining step of the, scan rate dependent cyclic voltammetry was performed under semi-infinite linear diffusion conditions in aqueous lithium perchlorate. These data reveal that the homogeneous charge transport diffusion coefficient, $D_{\mathrm{CT},}$ is $3.6 \pm 0.2 \times 10^{-13}$ cm^2 s^{-1}, i.e., under these conditions it takes approximately 90 s to fully oxidise a 100 nm thick film.

Keywords: Phenolate; Ruthenium; Metallopolymer; Electrochromic switching; Charge transport diffusion coefficient

1. Introduction

Electrochromic metallopolymers incorporating transition metal coordination complexes are potentially useful because of their intense colour and the possibility of accessing multiple oxidation states [1–3]. Electronic transitions in metal complexes typically involve valence electrons and oxidation or reduction of the complexes alters their optical properties [4,5]. In particular, Ruthenium–O$^-$ coordinated quinoid ligands and their metallopolymers are of interest as phenolate moieties are redox active and the complexes show rich visible–NIR spectroscopy [6–8]. As strong σ donors, phenolate bonds are capable of increasing the electron density at the metal site of Ru(II) complexes. This increased electron density reduces the oxidation potential of the metal centre which is attractive for low-power/voltage applications and extends the visible absorbance range of the material by making ILCT transitions possible [6].

Here, we report on a novel metallopolymer, [Ru(terpy)(box)PVP$_{20}$]PF$_6$, incorporating a Ru metal centre that is O, N coordinated to a phenolate donor ligand, terpy is 2,2$'$:6$'$,2$''$-terpyridine, box is 2-(2-hydroxyphenyl)benzoxazole, and PVP is poly(4-vinylpyridine) in which one in every 20 of the monomer units is labelled with the Ru(terpy)(box) (Chart 1). Metallopolymers based on pre-formed backbones offer the advantage of synthetic flexibility [9] and ease of characterisation. Moreover, by controlling the ruthenium loading the extent of interaction between the centres can be systematically varied so as to tune the absorbance change [10,11]. The metallopolymer exhibits a range of charge transfer transitions that generate electrochromic responses in the visible and NIR regions. The combination of colour changes, i.e., one that can be read visually and another that requires instrumentation, is particularly attractive for diverse applications ranging from

---

* Corresponding author. Tel.: +353 1 7005943; fax: +353 1 7005503.
E-mail address: Robert.Forster@DCU.ie (R.J. Forster).

1388-2481/$ - see front matter © 2008 Elsevier B.V. All rights reserved.
doi:10.1016/j.elecom.2008.01.009

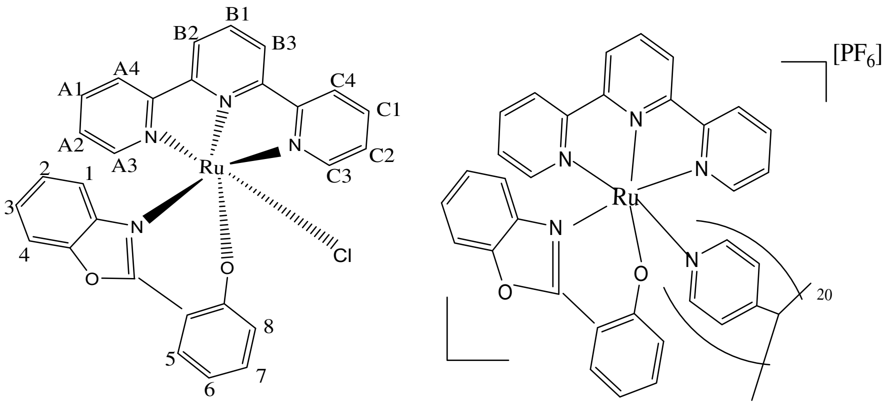

Chart 1.

security to monitoring packaging integrity in foods and pharmaceuticals. Detailed spectroscopic and electrochemical characterisation of these materials, are presented and resonance Raman spectroscopy is exploited to identify the nature of the optical transitions.

Cyclic voltammetry is a useful technique to measure the electrochromic switching rate of thin films under semi-infinite linear diffusion conditions [12]. Here, the optimal switching rate and the rate determining step have been identified by varying the concentration and anion of the supporting electrolyte.

2. Experimental

2.1. Materials

All reagents were analytical grade.

2.1.1. [Ru(terpy)Cl_3]

The complex was prepared using procedures described previously in the literature [13,14].

2.1.2. [Ru(terpy)(box)Cl]/[Ru(terpy)(box)PVP_{20}]PF_6

Modified methods [6,15] were employed for the synthesis of [Ru(terpy)(box)Cl] and [Ru(terpy)(box)PVP_{20}]PF_6. Anal. Calcd for [Ru(terpy)(box)Cl], $RuC_{28}H_{19}N_4O_2Cl$: C, 57.93; H, 3.28; N, 9.66. Found: C, 57.38; H, 3.47; N, 9.26. $_1$H NMR (400 MHz, DMSO-d) numbering scheme shown in Chart 1 H^{B2}, H^{B3}, 8.64–8.66 (d, 2 H); H^{A3}, H^{A4}, H^{C3}, H^{C4}, 8.54–8,59 (m, 4H); H^{A2}, H^{C2}, 7.94–7,96 (m, 2H); H^{B1}, 7.86–7.92 (m, 1H); H^8, 7.73–7,75 (d, 1H); H^{A1}, H^{C1}, 7.60–7,63 (m, 2H); H^1, H^6, 7.37–7.43 (m, 2H); H^5, 7.26–7.28 (d, 1H); H^2 6.97–7.01 (m, 1H); H^3 6.71–6.77 (m, 1H); H^7 6.48–6,52 (m, 1H); H^4 5.44–5.46 (d, 1H). ES MS m/z (calc) for the complex: 580 (580, [M]), 545 (545, [M-Cl]$^+$).

2.2. Instrumentation

Spectroelectrochemistry was carried out as using a custom built pyrex glass thin layer cell (1 mm), platinum gauze working electrode, Ag/AgCl non-aqueous reference and platinum wire auxiliary electrode. The electrolyte used was 0.1 M $TBABF_4$ (tetrabutylammonium tetrafluoroborate) dissolved in DMF. The metallopolymer dissolves completely in this solution. UV/visible/NIR spectra were recorded using the Shimadzu 3100 UV/NIR spectrometer. Raman spectroscopy was conducted using 785 nm excitation on a Dilor.Jobinyvon.Spex Labram. The x-axis was calibrated against silicon.

Electrochemistry was performed in conventional three-electrode cell with a CH Instruments Model 660a electrochemical workstation. All electrolyte solutions were deoxygenated and maintained under a nitrogen blanket during measurement. Cleaned glassy carbon working electrodes were modified by dropcasting the required volume of 1% metallopolymer in ACN/MeOH (1:1) followed by air-drying. The maximum concentration of ruthenium centres within the film was estimated at 0.5 M by flotation in non-swelling solvents, i.e., petroleum ether and chloroform.

3. Results and discussion

3.1. Spectroelectrochemistry

In systems with electrochemically active ligands it is important to establish if the redox processes are metal or ligand based. This issue can be conveniently probed using a combination of UV–vis spectroelectrochemistry and Raman spectroscopy. For the metallopolymer in the Ru^{2+} state, the wavelength of maximum absorbance, λ_{max}, is 480 nm, with a shoulder centred around 550 nm. The main absorbance is ascribed to a Ru(t_{2g}) to terpy(π^*) transition. The shoulder is assigned to an inter- or intra-ligand charge transfer transition (ILCT) π(box) to π^*(terpy). This behaviour has been reported previously in hydroquinone bound Ru(bpy) complexes [6–8]. Cyclic voltammetry of [Ru(terpy)(box)PVP_{20}]PF_6 reveals a reversible oxidation at +0.120 V and an irreversible oxidation at +0.781 V. Fig. 1 shows the changes in the absorbance spectrum of a solution of [Ru(terpy)(box)PVP_{20}]PF_6 following oxidation

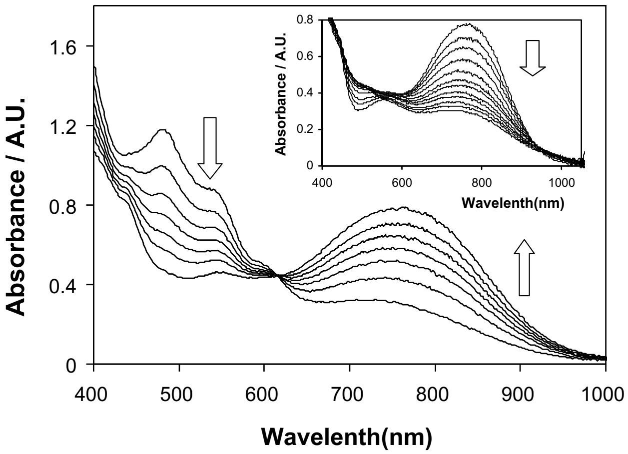

Fig. 1. Time dependent changes in the visible and near infra-red region of the spectrum of [Ru(terpy)(box)PVP$_{20}$][PF$_6$] dissolved in DMF containing 0.1 M TBAFB$_4$ as supporting electrolyte following application of +0.500 V (main figure) and +1.500 V (inset). Spectra were recorded at 2 min intervals.

at +0.500 V. As the metallopolymer is oxidised, the MLCT around 480 nm is gradually lost and the colour switches from wine red to light green. A red orange colour is also observed for mixed redox composition. Since the MLCT is lost, this observation strongly suggests that the first oxidation is Ru metal centre based. Oxidation also leads to a broad new feature centred at 760 nm. This is most likely an LMCT transition between phenolate and Ru(III)(dπ^*). Significantly, this redox induced colour switching is fully reversible over several hundred cycles.

As shown in the inset of Fig. 1, the LMCT transition is lost after electrolysis at 1.5 V suggesting that the most anodic oxidation is phenolate based and the phenolate is involved in the LMCT transition. The irreversibility of this process is most likely due to cleavage of the electron poor Ru(III)–O(phenoxy) bond [6]. Application of 1.5 V does not result in any visible colour changes because the LMCT lies in the NIR region. However, this combination of a reversible colour change in the visible region and a second irreversible change that cannot be discerned by eye is useful for many practical applications.

The assignment of oxidations as described above is entirely consistent with Raman spectroscopy. Raman spectra of the polymer following oxidation at +0.500 V ($\lambda_{ex} = 785$ nm, i.e., post-resonant with the new band at 760 nm present in the oxidised polymer) shows that the bands associated with the box ligand C–C and ring stretch modes (1596, 1312, 1140, 1012, and 856 cm^{-1}) and those attributed to Ru–O bridge coupled modes (676, 650, and 561 cm^{-1}) are resonantly enhanced. In sharp contrast, the terpy modes associated with the MLCT transition are not present. This observation suggests that the first oxidation of the metallopolymer is based on the Ru metal centre. Preliminary investigations indicate that reasonably stable films can be formed on optically transparent electrodes such as indium or fluorine doped tin oxide. Detailed investigations into the electrochemically induced spectral changes occurring within these thin films will be reported elsewhere, but are generally consistent with the solution phase behaviour.

3.2. Electrochemical properties

Fig. 2 illustrates voltammograms of a [Ru(terpy)(box)PVP$_{20}$]PF$_6$ film coated on 3 mm glassy carbon electrode recorded from 20 to 100 mV s^{-1} in aqueous 0.1 M LiClO$_4$. The formal potential, $E^{\circ\prime}$, for the Ru$^{2+/3+}$ couple is 0.380 V, and is significantly more positive that found in solution where $E^{\circ\prime}$ is 0.121 V indicating differences in the solvation shell or extents of ion pairing within the film compared to solution. The peak shape is independent of scan rate, υ, up to 100 mV s^{-1}, and as shown in Fig. 2 inset, i_p scales linearly with increasing υ. Repetitive cycling between 0.15 and 0.75 V over 1.5 h does not change the shape of the voltammograms and i_p decreases by less 5%. This indicates that the redox process is reversible and that metallopolymer film adheres strongly to the electrode surface.

For υ between 20 and 100 mV s^{-1}, ΔE_p is 92 ± 5 mV and the full width at half-maximum, FWHM, is 160 ± 8 mV. The observation that the peaks are broader than theoretically expected for an ideal Nernstian system indicates that there are destabilizing interactions between the metal centres [16]. The FWHM is larger than those found for other PVP based metallopolymers [17–19]. ΔE_p significantly exceeds that expected for reversible redox reactions under finite diffusion control. However, it is unaffected by υ for $2 < \upsilon < 50$ mV s^{-1} suggesting that slow heterogeneous electron transfer or ohmic drop are not responsible for the observed behaviour. Similar non-idealities in related

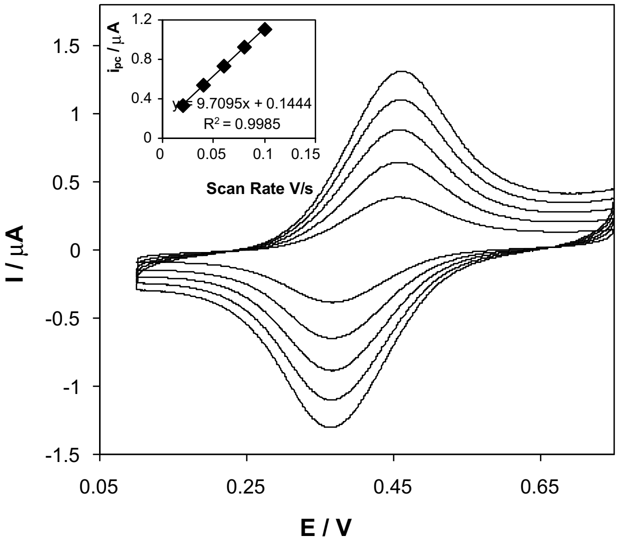

Fig. 2. Cyclic voltammograms of [Ru(terpy)(box)PVP$_{20}$][PF$_6$] metallopolymer film on 3 mm glassy carbon electrode in 0.1 M LiClO$_4$ electrolyte. $\upsilon = 20$, 40, 60, 80, and 100 mV s^{-1} (from bottom to top). $\Gamma = 4.9 \times 10^{-10}$ mol cm^{-2}. Inset: anodic i_p vs. υ.

systems have been interpreted in terms of Feldberg's unusual quasi-reversibility model [20].

Significantly, the system appears to be strongly ion-paired and increasing perchlorate concentration causes $E^{o'}$ of the $Ru^{2+/3+}$ couple to shift to more negative potentials by 52 ± 3 mV dec^{-1}, indicating that a single extra anion becomes bound to the metal centre in the oxidised state [21]. From the perspective of developing electrochromic films, this observation is important since it allows the drive voltage to be reduced.

3.3. Homogeneous charge transport rate of metallopolymer film

Beyond achieving a low switching voltage, reversible responses and intense colour changes, a key parameter influencing the utility of electrochromic materials is the switching rate, which can be determined from the homogeneous charge transfer diffusion coefficient, D_{CT} [22,23]. In fast scan cyclic voltammetry only a small fraction of the total amount of material immobilised is electrolysed and depletion zone remains well within the film. Under these conditions, linear diffusion predominates and the i_p varies linearly with $\upsilon^{1/2}$ [12].

Consistent with semi-infinite linear diffusion control, [24] the inset of Fig. 3 shows that the peak current, i_p, increases linearly with $\upsilon^{1/2}$ and the rate of homogeneous charge transport, D_{CT}, can be determined from the slope of using the Randles–Sevcik equation, which allows. D_{CT} is estimated for both the oxidation and reduction processes as $3.7 \pm 0.1 \times 10^{-13}$ $cm^2\,s^{-1}$. This is significantly lower than that found for other PVP based metallopolymers [17,18]. For example, in $[M(bpy)_2(PVP)_nCl]Cl$ films where M is Os or Ru, $25 \leqslant n \leqslant 5$, and bpy = 2,2′-bipyridyl D_{CT} is of the order of 10^{-9} $cm^2\,s^{-1}$ [17,18]. In Fig. 3, Γ is 5.1×10^{-9} mol cm^{-2} which corresponds to a minimum film thickness, δ, of approximately 100 nm. Given this value of D_{CT}, it takes approximately 90 s to fully oxidise the film. It is perhaps important to note that for practical electrochromic applications longer switching times may be observed because of the typically greater resistance of optically transparent electrodes and the need to use larger surface areas that may introduce greater ohmic drop.

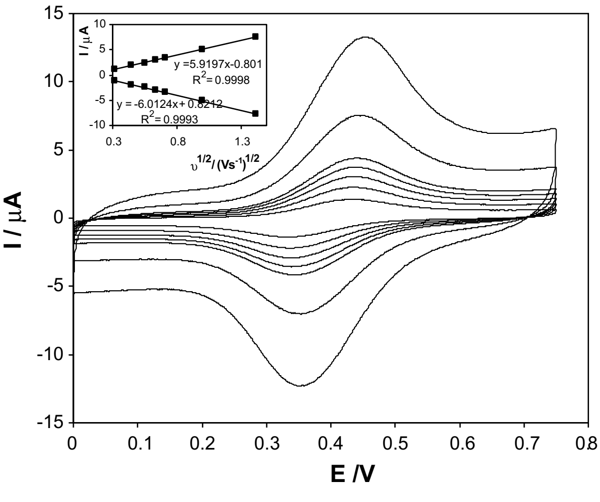

Fig. 3. Scan rate dependence of the voltammetric response of metallopolymer film on 3 mm glassy carbon electrode in 0.1 M $LiClO_4$. $\Gamma = 5.12 \times 10^{-9}$ mol cm^{-2}. υ = 2000, 1000, 500, 400, 300, 200, and 100 mV s^{-1} (from top to bottom). Inset: i_p vs. $\upsilon^{1/2}$ under same conditions.

3.4. Effect of electrolyte concentration on D_{CT}

To observe electron hopping as the rate determining step, charge-compensating counterions must be freely available within the structure. Under these circumstances, D_{CT} is expected to depend only weakly on the electrolyte concentration. Significantly, D_{CT} changes by less than 25% across the range from 0.1 to 1.0 M suggesting that electron hopping or segmental polymer chain movement rather than ion movement limits the overall rate of charge transport. Also, experiments in which the identity of the anions varies from perchlorate to nitrate, chloride and sulphate, reveal that D_{CT} changes by approximately a factor of three. Given that the Stokes radii of these ions ranges from 2.6 to 5.3 pm, this minor change indicates that electron hopping or segmental polymer chain movement limit the overall colour switching rate. Future investigations will determine the extent to which D_{CT} can be increased by decreasing the distance (currently of the order of 50 Å) between the metal centres by increasing the loading of $[Ru(terpy)(box)]^{2+}$ moieties.

4. Conclusions

A new electrochromic metallopolymer containing $Ru–O^-$ coordinated quinoid ligands has been synthesized and characterised. The metallopolymer exhibits rich electrochromic behaviour both in solution and within thin films. Oxidation at +0.5 V switches the colour from wine red to green while potentials above 1.0 V produce a change in the NIR region of the spectrum. The film can be oxidised at a rate of 10^{-13} $cm^2\,s^{-1}$ and is consistent with the colour switching rate being controlled by electron hopping or segmental polymer chain motion.

Acknowledgments

We appreciate the on-going financial support from Science Foundation Ireland under the Research Frontiers Programme (Award No.05/RFP/CHE0085) and the Biomedical Diagnostics Institute (Award No. 05/CE3/B754).

References

[1] R.J. Mortimer, Chem. Soc. Rev. 26 (1997) 147.
[2] R.J. Mortimer, N.M. Rowley, Metal complexes as dyes for optical data storage and electrochromic materials, in: J.A.

McCleverty, T.J. Meyer, M.D. Ward (Eds.), Comprehensive Coordination Chemistry – II: From Biology to Nanotechnology 9.2, Elsevier, Oxford, pp. 581–619.

[3] A. Juris, V. Balzani, F. Barigelletti, S. Campagna, P. Belser, A.V. Zelewsky, Coord. Chem. Rev. 84 (1988) 85.

[4] R.J. Mortimer, A.L. Dyer, J.R. Reynolds, Displays 27 (2006) 2.

[5] P.M.S. Monk, R.J. Mortimer, D.R. Rosseinsky, Electrochromism and Electrochromic Devices, Cambridge University Press, NY, 2007, p. 254.

[6] T.E. Keyes, D. Leane, R.J. Forster, C.G. Coates, J.J. McGarvey, M.N. Nieuwenhuyzen, E. Figgemeier, J.G. Vos, Inorg. Chem. 41 (2002) 5721.

[7] I. Brady, D. Leane, H.P. Hughes, R.J. Forster, T.E. Keyes, J. Chem. Soc., Dalton Trans. (2004) 334.

[8] T.E. Keyes, B. Evrard, J.G. Vos, C. Brady, J.J. McGarvey, P. Jayaweera, J. Chem. Soc., Dalton Trans. (2004) 2341.

[9] A.P. Clarke, J.G. Vos, Trends Electrochem. 1 (1992) 167.

[10] J.F. Rusling, R.J. Forster, J. Colloid Interface Sci. 262 (2003) 1.

[11] J.M. Calvert, R.H. Schmehl, B.P. Sullivan, J.S. Facci, T.J. Meyer, R.W. Murray, Inorg. Chem. 22 (1983) 2151.

[12] R.M. Wightman, D.O. Wipf, in: A.J. Bard (Ed.), Electroanalytical Chemistry, vol. 15, Marcel Dekker, NY, 1989.

[13] P.A. Adcock, F.R. Keene, R.S. Smythe, M.R. Snow, Inorg. Chem. 23 (1984) 2336.

[14] B.P. Sullivan, J.M. Calvert, T.J. Meyer, Inorg. Chem. 19 (1980) 1404.

[15] R.J. Forster, J.G. Vos, J. Electroanal. Chem. 314 (1991) 135.

[16] J. Hjelm, R.W. Handel, A. Hagfeldt, E.C. Constable, C.E. Housecroft, R.J. Forster, J. Phys. Chem. B 107 (2003) 10431.

[17] L. Dennany, C.F. Hogan, T.E. Keyes, R.J. Forster, Anal. Chem. 78 (2006) 1412.

[18] L. Dennany, R.J. Forster, B. White, M.R. Smyth, J.F. Rusling, J. Am. Chem. Soc. 126 (2004) 8835.

[19] R.J. Forster, D. Walsh, N. Mano, F. Mao, A.J. Heller, Langmuir 20 (2004) 862.

[20] S.W. Feldberg, I. Rubinstein, J. Electroanal. Chem. 240 (1988) 1.

[21] D.A. Buttry, Langmuir 6 (1990) 1319.

[22] A.M. Bond, F.J. Marken, Electroanal. Chem. 372 (1994) 125.

[23] P.J. Kuleszea, L.R. Faulkner, J. Am. Chem. Soc. 115 (1993) 11878.

[24] A.J. Bard, L.R. Faulkner, Electrochemical Methods: Fundamentals and Applications, second ed., Wiley, NY, 2001.

Electrochimica Acta 53 (2008) 7033–7038

Contents lists available at ScienceDirect

Electrochimica Acta

journal homepage: www.elsevier.com/locate/electacta

Redox induced switching dynamics of a three colour electrochromic metallopolymer film

Qiang Zeng, Andrea McNally, Tia E. Keyes, Robert J. Forster*

National Centre for Sensor Research, Biomedical Diagnostics Institute, School of Chemical Sciences, Dublin City University, Dublin 9, Ireland

ARTICLE INFO

Article history:
Received 4 April 2008
Received in revised form 8 May 2008
Accepted 9 May 2008
Available online 18 May 2008

Keywords:
Phenolate
Metallopolymer
Electrochromic switching rate
Rate-determining step
Charge transport diffusion coefficient

ABSTRACT

Thin films of a novel Ru-phenolate based metallopolymer, $[Ru(terpy)(box)PVP_{20}]PF_6$, in which one in every twenty of the 4-vinyl pyridine monomer units is labelled with the ruthenium complex have been formed on glassy carbon electrodes, terpy is 2,2′:6′,2″-terpyridine, box is 2-(2-hydroxyphenyl)benzoxazole, and PVP is poly(4-vinylpyridine). Cyclic voltammetry and Raman spectroscopy reveal that the $Ru^{2+/3+}$ couple is electrochemically reversible but that the phenolate ligand based oxidation is irreversible. These redox processes are associated with reversible colour changes from wine red (reduced) to red orange (mixed composition) then to light green (oxidized) in the visible region and an irreversible change in the near-IR region, respectively. Scanning electron microscopy reveals that repeated switching in $LiClO_4$ aqueous solution does not induce any significant structural change within the deposit films. Cyclic voltammetry has been used to determine the electrochromic switching rate under semi-infinite linear diffusion conditions. In aqueous $LiClO_4$, the homogeneous charge transport diffusion coefficient, D_{CT}, decreases from $3.6 \pm 0.3 \times 10^{-13}$ to $2.7 \pm 0.2 \times 10^{-13}$ cm^2 s^{-1} as the $LiClO_4$ concentration increases from 0.1 to 1.0 M. This weak dependence of D_{CT} on electrolyte concentration suggests that counterion availability is not rate-determining and that the overall rate of charge transport through the metallopolymer film is limited by the rate of segmental polymer chain motion necessary to bring adjacent centres sufficiently close to allow electron transfer to occur. Also the impact of changing the identity of the charge compensating anion of the redox electrochromic switching rate has been investigated. Finally, the electronic conductivity has been determined using interdigitated array electrodes (IDAs).

1. Introduction

Currently, there is significant interest in electrochromic metallopolymers incorporating transition metal coordination complexes because of the opportunity to couple electrochemical and optical processes leading to significant potential applications [1–3]. The visible absorbance of these materials typically arises from metal-to-ligand charge transfers that are lost upon their oxidation of the metal centre [4–6]. However, it is possible to produce metal complexes in which one or more ligands can be oxidised triggering additional colour changes. Ruthenium–O^- coordinated quinoid ligands containing complexes and their metallopolymers are of interest because of the strong σ donor ability of phenolate bonds, which increases the electron density at the metal site and results in a low oxidation potential and rich visible-NIR spectroscopy [7–9] of the complexes and their metallopolymers. For the practical application in display devices the switching rate is equally important [10]. Factors such as ionic conductivity of the contacting medium as well as ion and electron ion through thin films affect this switching rate.

We recently reported preliminary data on the colour changes that occur within a novel metallopolymer, $[Ru(terpy)(box)PVP_{20}]$-PF_6, incorporating a Ru metal centre that is O, N coordinated to a phenolate donor ligand, terpy is 2,2′:6′,2″-terpyridine, box is 2-(2-hydroxyphenyl)benzoxazole, and PVP is poly(4-vinylpyridine) in which one in every twenty of the monomer units is labelled with the ruthenium complex (Chart 1) [11]. This material exhibits a range of charge transfer transitions in the visible and NIR regions that can be changed by applying a potential capable of oxidising either the ruthenium or phenolate ligand.

In this contribution, we report on investigations using resonance Raman spectroscopy that probe the nature of the optical transitions. Moreover, the rate of charge transport through thin films deposited on glassy carbon electrodes has been measured as a function of electrolyte concentration and identity using cyclic voltammetry. In this way, insights into the nature of the rate-determining process

---

* Corresponding author. Tel.: +353 1 7005943.
E-mail address: robert.forster@dcu.ie (R.J. Forster).

0013-4686/$ – see front matter © 2008 Published by Elsevier Ltd.
doi:10.1016/j.electacta.2008.05.027

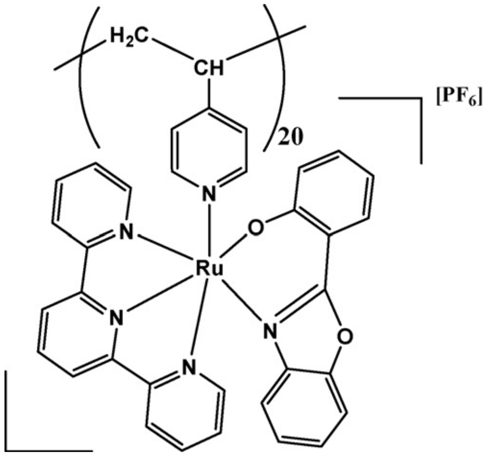

Chart 1.

for charge transport through the layer has been obtained. The significance of these findings for the design of intensely coloured, fast switching electrochromic films is discussed.

2. Experimental

The synthesis of the [Ru(terpy)(box)PVP$_{20}$][PF$_6$] metallopolymer has been described previously [11].

Spectroelectrochemistry was carried out using a homemade pyrex glass thin layer cell (1 mm), a platinum gauze as working electrode, an Ag/AgCl non-aqueous quasi-reference electrode and a platinum wire as auxiliary electrode. The electrolyte used was 0.1 M TBAFB$_4$ (tetraethyl ammonium tetrafluoroborate) in DMF and the UV/Visible/NIR spectra were recorded using the Shimadzu 3100 UV/NIR spectrometer. The working electrode was held at the required potential for 2 min before the first scan. A CH instrument Model 660a electrochemical workstation was used to control the applied potential.

Raman spectroscopy was obtained on a Dilor, Jobinyvon, Spex Labram, Argon ion and Helium–Neon lasers as well as a Ti-sapphire laser pumped by an Argon ion laser were available sources for excitation at 488, 632.8, and 785 nm, respectively. A backscattering geometry was used to collect scattered light by using an air cooled CCD array by one of two interchangeable gratings, 1800 lines/mm, which was used for 488 and 632.8 nm excitation with a spectral resolution of 1.5 cm^{-1} per pixel, or 600 lines/mm, which was employed for 785 nm excitation. Before use, the wavenumber axis of the Raman was calibrated with the silicon line at 521 cm^{-1}.

Electrochemistry was performed in conventional three-electrode cells using an Ag/AgCl electrode filled with 3 M KCl (aq) (CH instrument) as reference. Cyclic voltammetry (CV) was carried out using a CH instruments Model 660a electrochemical workstation. All electrolyte solutions were deoxygenated for at least 15 min using N$_2$ gas before use and maintained under a nitrogen blanket during measurement. Glassy carbon working electrodes were polished successively with 1.0, 0.3, and 0.05 μm alumina powder and modified by evaporating the required volume of a 1% metallopolymer solution in ACN/MeOH (1:1) followed by air-drying. The maximum concentration of ruthenium centres within the film was estimated as 0.5 M by flotation in non-swelling solvents, i.e., petroleum ether and chloroform.

For metallopolymer conductivity measurements, a CH instruments Model 760b electrochemical workstation was employed. Platinum interdigitated electrode arrays, IDAs, were purchased from Abtech Scientific. Inc. Metallopolymer films were prepared by evaporating the required volume of a 1% metallopolymer solution in ACN/MeOH (1:1) on the IDA fingers and gaps between fingers. In order to cover the IDA fingers and gaps completely, the metallopolymer solution were drop-cast on the IDA electrodes several times.

Scanning electron microscopy (SEM) was performed using a Hitachi S-3000N system to probe the physical characteristics of the deposits and to determine if voltammetric cycling results in any morphological changes in the deposit. In SEM investigations, films were formed on 3 mm radius carbon disks. To probe the effect of redox cycling, the modified disks were electrochemically cycled and then the films were washed in electrolyte free Milli-Q water and then dried in a vacuum desiccator for several hours.

3. Results and discussion

3.1. UV–vis spectroelectrochemistry and Raman spectroscopy

Systems of this kind are attractive for electrochromic applications in that both the metal centre and the phenolate ligand are electrochemically active. As reported previously, the complex undergoes a reversible oxidation at approximately +0.4 V and an irreversible oxidation at +0.8 V vs. Ag/AgCl. However, it is essential to establish whether the metal or box ligand is oxidised first. This issue can be conveniently probed using a combination of UV–vis spectroelectrochemistry and Raman spectroscopy. As shown in the inset of Fig. 1, for the metallopolymer in the reduced state, the wavelength of maximum absorbance is 480 nm corresponding to an MLCT transition, with a shoulder centred around 550 nm for an ILCT transition. As the metallopolymer is oxidised at +0.5 V, the MLCT transition is gradually lost and it leads to a broad new feature centred at 760 nm for an LMCT transition between phenolate and Ru(III) (dπ^*). The colour switches from wine red to light green and for the mixed redox composition a red orange colour is observed. The LMCT transition is lost after electrolysis at 1.5 V. But it does not result in any visible colour changes because the LMCT lies in the NIR region. These observations suggest that first oxidation is ruthenium based.

To better understand the absorption features of the metallopolymer, thin films of [Ru(terpy)(box)PVP$_{20}$][PF$_6$] were coated on a glassy carbon electrode and carried out Raman experi-

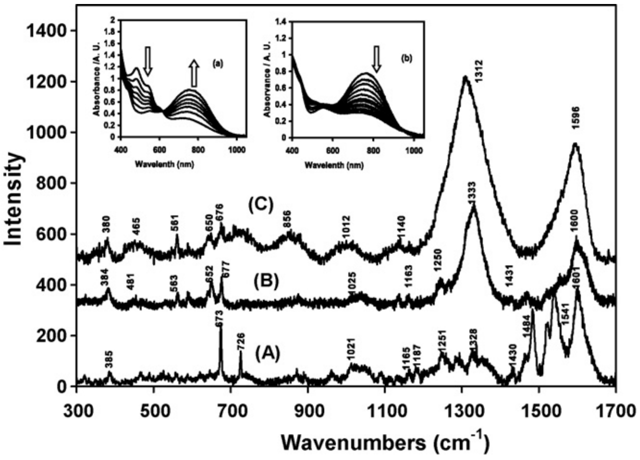

Fig. 1. Resonance Raman spectra of dry [Ru(terpy)(box)PVP$_{20}$][PF$_6$] metallopolymer film coated on 3 mm glassy carbon electrode (A) excited at 488 nm (B) excited at 632.8 nm and (C) excited at 785 nm. The insets show time dependent changes in the visible and near infra-red regions of the spectrum of the metallopolymer in DMF containing 0.1 M TBAFB$_4$ following application of +0.5 V (a) and +1.5 V (b). Spectra were recorded at every 2 min.

ments at 488 nm, 632.8 nm, and 785 nm. Fig. 1(A) shows the Raman spectra for [Ru(terpy)(box)PVP$_{20}$][PF$_6$] excited at 488 nm, which was used to investigate the MLCT absorption at around 480 nm. The features at 1601, 1541, 1484, 1328, 1251, 1187, 1165, 1021, 726, and 673 cm^{-1} are all characteristic of terpyridyl unit vibration [12] in a Ru (dπ)–terpy (π^*) MLCT transition. In the low frequency end of the spectrum, an Ru–N stretching vibration is also observed at 385 cm^{-1} [13]. The feature at 1430 cm^{-1} is thought to arise from the box ligand because it is not observed in the Raman spectrum for typical MLCT of Ru–terpy complexes.

Excitation at 632.8 nm is post-resonant with the low-energy ILCT absorbance shoulder at around 550 nm. This excitation wavelength was chosen to avoid the tail of the MLCT transition at 480 nm. As shown in Fig. 1(B), although the contribution from the MLCT is minimal, some terpy-based vibration features at 1600, 1333, 1250, 1163, and 1025 cm^{-1} are still evident. The feature at 1431 cm^{-1} associated with quinoid ligand is present. In the low energy region, the feature at 677 cm^{-1} and new features at 652, 563, and 481 cm^{-1} are apparent. The former, obscured by the terpy feature at 673 cm^{-1} excited at 488 nm, is attributed to the box ligand and the latter features are associated with Ru–O and box [7]. The intensity of the Ru–N feature at 384 cm^{-1} is significantly reduced suggesting that the longer wavelength absorbance is associated with an inter/intra ligand charge-transfer transition involving the phenolate and terpyridyl units. Such behaviour has been reported previously in hydroquinone bound Ru(bpy) units [7,14].

Fig. 1(C) shows the Raman spectrum excited at 785 nm. As described previously, oxidation of the Ru centre generates a new band around 760 nm, which is due to phenolate-to-Ru$_{(\mathrm{III})}$, LMCT, transition. The excitation at 785 nm is resonant with this feature. The terpy bands associated with the MLCT transition shown in Fig. 1(A) are completely lost under these conditions. However, bands associated with the box ligand still remain. Bands at 1596, 1312, 1140, 1012, and 856 cm^{-1} are attributed to the box ligand C–C and ring stretch modes. Bands at 676, 650, and 561 cm^{-1} are attributed to Ru–O bridge coupled modes. Also, these three bands are comparable to those observed for resonance Raman of the ILCT. The band at 465 cm^{-1} is attributed to Ru–O (box) and the band at 380 cm^{-1} is attributed to Ru(III)–N. The shift of the latter band from 385 cm^{-1} for Ru(II) to 380 cm^{-1} for Ru(III) is consistent with oxidation of the metal. All features of metal to ligand and metal to ligand bridge coupled modes in resonance Raman excited at 785 nm indicate that the metal is participating in the electronic transition. No terpy-based vibration evidence was found in this transition. Therefore, it strongly indicates that the transition at 760 nm is attributed to phenolate (π) to Ru$_{(\mathrm{III})}$ (dπ).

3.2. General electrochemical properties

Fig. 2 shows the initial voltammetric response of a [Ru(terpy)(box)PVP$_{20}$][PF$_6$] metallopolymer film deposits on a 3 mm glassy carbon electrode when it is first cycled in 0.1 M LiClO$_4$ aqueous solution. The response changes remarkable little during these initial scans. The changes of the anodic peak current and the cathodic peak current are approximately 15 and 2% respectively. The oxidation and reduction peak potentials remain constant at 458 ± 4 and 370 ± 4 mV. Significantly, after approximately 20 scans, the response no longer changes when the metallopolymer film is repeatedly cycled over 1000 scans and remains stable for at least 1.5 h.

Scanning electron microscopy (SEM) images have been obtained before and after voltammetric cycling to determine if voltammetric cycling results in any morphological changes in the deposit.

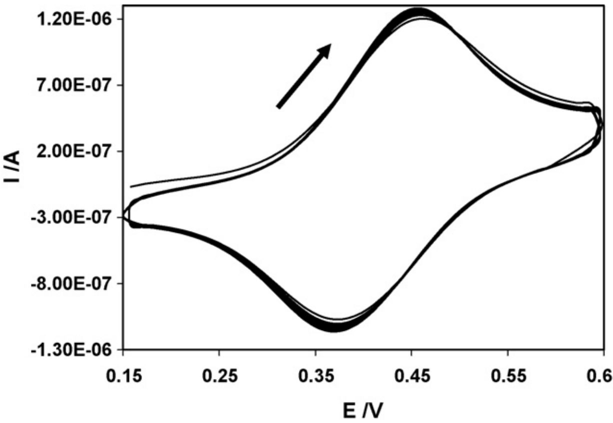

Fig. 2. First 30 voltammetric cycles for a solid state [Ru(terpy)(box)PVP$_{20}$][PF$_6$] metallopolymer film coated on 3 mm glassy carbon electrode in 0.1 M aqueous LiClO$_4$ electrolyte. The scan rate is 0.1 V s^{-1}.

Fig. 3A shows that prior to voltammetric cycling the film exists as a rather rough, amorphous coating. Consistent with the minor changes observed in the voltammetry following repeated cycling. Fig. 3B shows that voltammetric cycling does not significantly affect the structure of the film.

Fig. 4 shows that, once the voltammetry no longer changes with repetitive scanning, the response observed is similar to that expected for an ideal reversible redox reaction. Moreover, the inset of Fig. 4 shows that the voltammetric peak current depends linearly on the square root of the scan rate suggesting that the response is controlled by semi-infinite linear diffusion. The rate of homogeneous charge transport and the nature of the rate-determining step are presented in a later section.

3.3. Ion pairing effects

An important objective when developing electrochromic films is to minimize the voltage required to change the optical response. The formal potential of an immobilized electroactive group is sensitive to both the solvation shell of the redox centre and to the extent of ion-pairing [15–17]. Therefore, it ought to be possible to change the formal potential by changing the identity and concentration of the charge compensating counterion in solution [17,18].

The effect of electrolyte concentration on the formal potential of the Ru centres redox reaction has been examined for 0.1 M ≤ [LiClO$_4$] ≤ 1.0 M. A fixed background of 1.0 M Na$_2$SO$_4$ was used as a swamping electrolyte to avoid complications arising from changes in the ionic strength of the solution. Cyclic voltammetry is used to determine formal potential, and a scan rate of less than 0.5 V s^{-1} was used to avoid any influence from interfacial charge transfer kinetics. As shown in Fig. 5, $E^{o\prime}$ shifts in a negative potential direction with increasing LiClO$_4$ concentration indicating that the metal centre is easier to be oxidized. This response is consistent with ion-pairing between the electrolyte anions and the metal redox centres. This situation is summarized in the following Nernstian reaction,

$$[\mathrm{Ru(terpy)(box)PVP_{20}}]^{+}(X^{-})_{\zeta} - e^{-} + \rho(X^{-}) \leftrightarrow [\mathrm{Ru(terpy)(box)PVP_{20}}]^{2+}(X^{-})_{\zeta+\rho} \quad (1)$$

where both redox forms participate in the ion-paring equilibrium.

The slope observed for the metallopolymer film is 52 ± 3 mV, which is close to the theoretical (59/p) mV/decade, where p is the difference in the number of anions pairing with the oxidized and

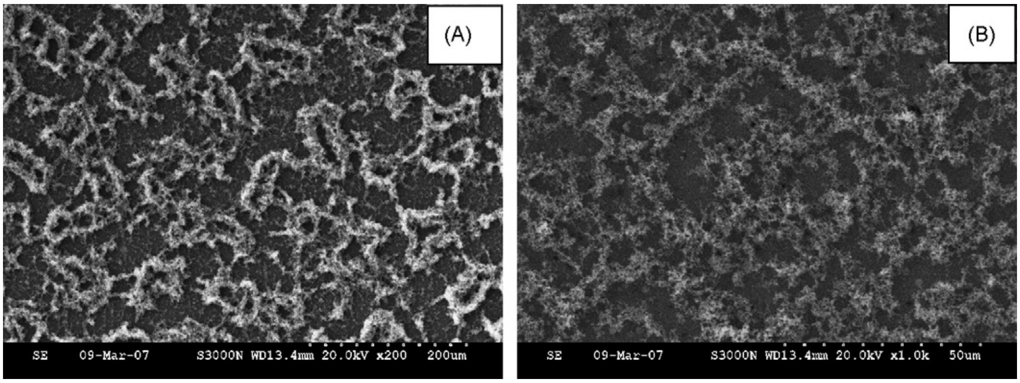

Fig. 3. Scanning electron microscopy images of a [Ru(terpy)(box)PVP$_{20}$][PF$_6$] metallopolymer film drop cast on a 3 mm glassy carbon electrode: (A) as deposited, before voltammetric cycling; (B) is after 100 voltammetric cycles between 0.10 and 0.75 V in 0.1 M LiClO$_4$ at a scan rate of 0.1 V s^{-1}.

reduced forms of the metal centre. It indicates that a single extra anion becomes bound to the metal centre in the oxidized state [19]. From the perspective of developing electrochromic films, this observation allows the drive voltage of the metallopolymer film to be reduced.

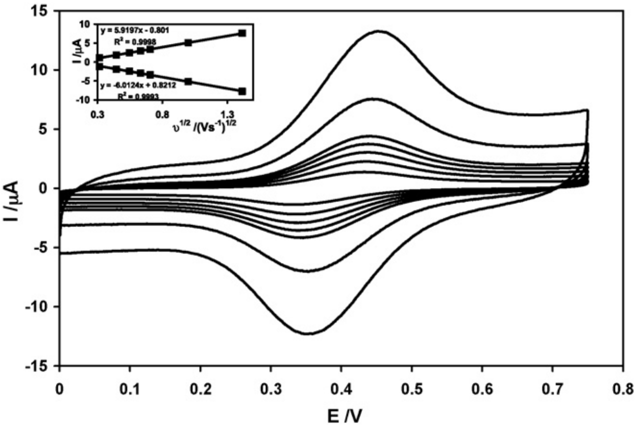

Fig. 4. Scan rate dependence of the voltammetric response of metallopolymer film on 3 mm glassy carbon electrode in 0.1 M LiClO$_4$. $\Gamma = 5.12 \times 10^{-9}$ mol cm^{-2}. υ = 2000, 1000, 500, 400, 300, 200, and 100 mV/s (from top to bottom). Inset: i_p vs. $\upsilon^{1/2}$ under same conditions.

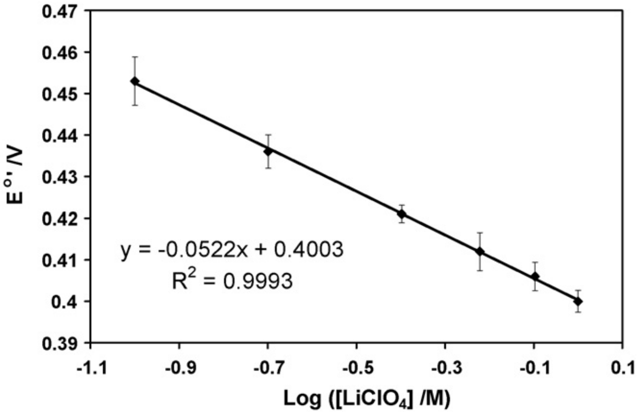

Fig. 5. Dependence of the formal potential for the Ru$^{2+/3+}$ couple within a [Ru(terpy)(box)PVP$_{20}$][PF$_6$] metallopolymer film on the log[LiClO$_4$] as supporting electrolyte. All measurements were performed in a constant-background electrolyte of 1.0 M Na$_2$SO$_4$.

3.4. Homogeneous charge transport rate and rate-determining step

The rate at which the colour of the polymer film can be switched can be quantified by measuring the homogeneous charge transfer diffusion coefficient, D_{CT} [20,21]. For $500 \geq \nu \geq 50$ mV s^{-1}, the voltammetric peak current increases linearly with the square root of the scan rate, υ, which is consistent with the response being under semi-infinite linear diffusion control. The peak current, i_p, can be expressed in terms of the Randles–Sevcik equation:

$$i_p = 2.96 \times 10^5 n^{3/2} A {D_{CT}}^{1/2} C_{eff} \nu^{1/2} \quad (2)$$

where n is the number of electrons transferred, A is the area of the working electrode, D_{CT} is the homogeneous charge transport diffusion coefficient, and C_{eff} is the effective fixed site concentration of the redox centre. The concentration of ruthenium centres within the metallopolymer has been determined from density measurements in non-swelling solvents as 0.5 M. Thus, Eq. (2) allows D_{CT} to be estimated for the oxidation and reduction processes as $3.7 \pm 0.1 \times 10^{-13}$ and $3.8 \pm 0.2 \times 10^{-13}$ cm^2 s^{-1}, respectively. Given the value of D_{CT} for the oxidation process, it takes approximately 90 s to fully oxidise a 100 nm metallopolymer film.

There are a number of processes that could contribute to homogeneous charge transport through films of this kind, including electron hopping, counterion diffusion/migration or movement of polymer chains or segments to bring adjacent redox centres sufficiently close to allow electron transfer to occur [22]. When charge-compensating counterions are freely available within the structure, electron hopping or the rate of segmental polymer chain motion is rate limiting and D_{CT} is expected to depend only weakly on the electrolyte concentration. Fig. 6 shows that D_{CT} for the anodic process, D_{CT} decreases from $3.6 \pm 0.3 \times 10^{-13}$ to $2.7 \pm 0.2 \times 10^{-13}$ cm^2 s^{-1} as the LiClO$_4$ concentration increases from 0.1 to 1.0 M. Taking into account the associated error bars, the overall change in D_{CT} observed is not significant and indicates that D_{CT} is at best very weakly dependent on the perchlorate concentration. This observation suggests that counterion availability is not rate determining and the overall rate of charge transport through the metallopolymer film is limited by electron hopping or segmental chain motion prior to electron transfer. The relatively low loading of ruthenium centres, one in twenty monomer units, makes the intersite separation large, of the order of 40 Å. This large distance means that movement of the polymer chain segments rather that the actual electron transfer itself, is likely to represent the rate-determining step. This conclusion is consistent with the fact that the D_{CT} measured here is at least two orders of magnitude lower that those found for electron hopping in related systems. The

Table 1
Charge transfer properties of the metallopolymer film coated on 3 mm glassy carbon electrode in 0.1 M of various aqueous supporting electrolytes

	Model radius	Strokes radius	Gibbs free energies (kJ mol^{-1})	$E^{o\prime}$ (V)	Peak separation (V)	10^{13} D_{CT} oxidation (cm^2 s^{-1})	10^{13} D_{CT} reduction (cm^2 s^{-1})
ClO_4^-	1.4	2.6	−1270	0.401	0.1	3.56	3.28
NO_3^-	2.0	3.3	−1362	0.474	0.111	2.83	2.12
Cl^-	2.0	3.9	−1403.5	0.498	0.127	2.44	1.70
SO_4^{2-}	3.1	5.3	−3202	0.519	0.144	1.01	0.72

The model and Strokes radius as well as the Gibbs free energies are from Ref. [24]. Potentials are vs. aqueous Ag/AgCl reference electrode and obtained using cyclic voltammetry at 0.1 V s^{-1}.

small decrease in D_{CT} most likely reflects a change in the film structure. For example, perchlorate is known to dehydrate PVP based polymer films making the layer more compact at higher electrolyte concentrations [23]. Additional insight into the nature of the rate-determining step can be obtained by changing the charge to volume ratio of the charge compensating counterion.

3.5. *Effect of anion identity*

Table 1 contains D_{CT} values measured in 0.1 M electrolytes where the anion is perchlorate, nitrate, chloride or sulphate. Significantly, D_{CT} changes by less than a factor of four across this range of anions despite the significant differences in Stokes radii suggesting that the ion size does not dramatically affect the rate of charge transport. However, perchlorate has the smallest Stokes radius [24] and exhibits the fastest charge transport rate. Compared to other anions, perchlorate is more hydrophobic which may facilitate permeation into the film [25]. The formal potential of the $Ru^{2+/3+}$ couple is significantly more positive where the supporting electrolyte contains the relatively hydrophilic SO_4^{2-} rather than ClO_4^-. This result suggests that the difference in Gibbs free energy of hydration for transfer of the anion from the aqueous to the solid phase is large and the film is thermodynamically hardest to oxidise when in contact with media containing strongly hydrated anions such as SO_4^{2-}.

3.6. *Electrical conductivity*

To address the issue of whether electron hopping or segmental polymer chain motion prior to electron transfer are rate limiting, the electronic conductivity has been determined using interdigitated array electrodes (IDAs) coated with the metallopolymer. As originally demonstrated by Wrighton and co-workers [26–28], the film conductivity is obtained from the slope $\partial i/\partial E$.

Fig. 7 shows that the current varies linearly with potential between −0.2 and +0.2 V and the slopes can be used in conjunction with Eq. (3) below to determine the conductivity, σ, where (d_G/A_{total}) is the Zaretsky cell constant. The constant of the IDAs used in this experiment is 0.04 cm^{-1}.

$$\sigma = \frac{d_G \partial i}{A_{total} \partial E} \tag{3}$$

The change of film conductivity has been measured in the presence of dry N_2 and an ACN/MeOH (1:1) solvent vapour bath at room temperature and pressure. The slopes of the best fit line to the data in Fig. 7 yield conductivities of $1.2 \times 10^{-10}\ \Omega^{-1}\ cm^{-1}$ for the film exposed to dry N_2 and $2.8 \times 10^{-10}\ \Omega^{-1}\ cm^{-1}$ for the film exposed to ACN/MeOH (1:1) vapour. Thus, exposure to solvent increases the conductivity of the film by a factor of approximately two perhaps reflecting plasticization of the layer.

When electron hopping represents the overall charge transport rate through the metallopolymer film, the Dahms–Ruff equation [29,30] can be used to calculate the electron self-exchange rate constant, k_{SE}, from the D_{CT} according to Eq. (4):

$$D_{CT} = D_{phys} + \frac{1}{6} k_{SE} \delta^2 C \tag{4}$$

where C is the concentration of Ru redox centres within the film, δ is the intersite separation between adjacent Ru redox centres, and D_{phys} describes physical diffusion in the absence of electron hopping. In this situation, D_{phys} is assumed to be zero, because the Ru centres are bound to the polymer chains. Therefore, Eq. (4) reduces to:

$$D_{CT} = \frac{1}{6} k_{SE} \delta^2 C \tag{5}$$

For a hypothetical cubic lattice model [31,32] applied to electron transport in redox polymers, the electron self-exchange rate

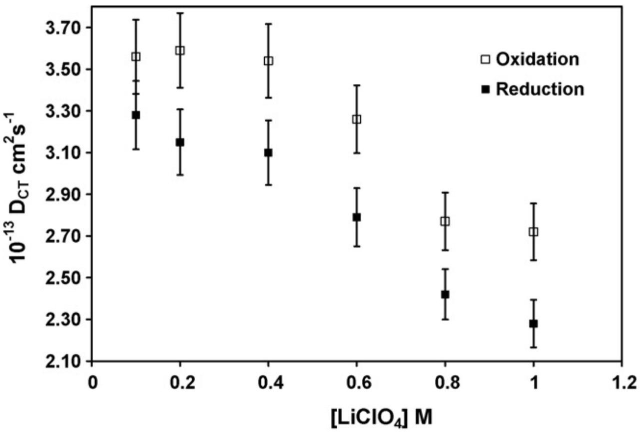

Fig. 6. Dependence of D_{CT} on the concentration of $LiClO_4$ as supporting electrolyte for a [Ru(terpy)(box)PVP_{20}][PF_6] metallopolymer film.

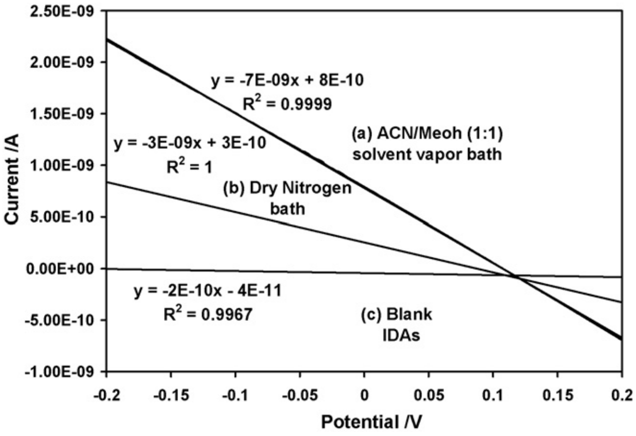

Fig. 7. Dependence of the current on the applied potential for blank IDAs in contact with air and IDAs modified with [Ru(terpy)(box)PVP_{20}][PF_6] metallopolymer films equilibrated with dry N_2 and ACN/MeOH (1:1) vapour. In each case, one of the IDA combs was maintained at 0 V while the other was scanned at 50 mV s^{-1}.

constant, k_{SE}, also can be calculated as Eq. (6),

$$k_{SE} = \frac{6RT\sigma}{10^{-3}F^2\delta^2[\mathrm{Ru}]^{2+}[\mathrm{Ru}]^{3+}} \tag{6}$$

where k_{SE} is the electron self-exchange rate constant, R is the gas constant, σ is the conductivity at temperature $T(K)$, F is the Faraday constant, and δ is the intersite separation between adjacent Ru redox centres. When we combine Eqs. (5) and (6), and make the concentration ratio $[\mathrm{Ru}]^{2+}/[\mathrm{Ru}]^{3+} = 1$, D_{CT} is given by Eq. (7):

$$D_{CT} = \frac{4RT\sigma}{10^{-3}F^2C} \tag{7}$$

For the dry film, the D_{CT} obtained is $2.5 \times 10^{-13}\,\mathrm{cm^2\,s^{-1}}$ while the value obtained for the solvent equilibrated film is $5.8 \times 10^{-13}\,\mathrm{cm^2\,s^{-1}}$. Significantly, both of these values are consistent with those obtained using cyclic voltammetry for the films in contact with aqueous electrolyte. Therefore, these IDA measurements confirm that the movement of charge compensating counterions does not represent the rate-determining step for homogeneous charge transport through these films. The fact that charge transport proceeds more rapidly when the films are exposed to acetonitrile/methanol vapour, coupled to the relatively large separation of the redox centres (of the order of 50–60 Å) suggests that segmental polymer chain motion limits D_{CT}.

4. Conclusions

A new electrochromic metallopolymer containing $\mathrm{Ru{-}O^-}$ coordinated quinoid ligands has been synthesized and characterized. The metallopolymer exhibits rich electrochromic behaviour both in solution and within thin films. For example, oxidation at +0.5 V switches the colour from wine red to green while oxidation at potentials above +1.0 V produces a change in the NIR region of the spectrum. The homogeneous charge transport diffusion coefficient, D_{CT}, associated with oxidizing or reducing the ruthenium centres is of the order of $10^{-13}\,\mathrm{cm^2\,s^{-1}}$ and varies by less than 25% on going from 0.1 to 1.0 M aqueous $\mathrm{LiClO_4}$ as supporting electrolyte. Also, D_{CT} changes by approximately a factor of three between sulphate (slowest) and perchlorate (fastest) based electrolytes. Investigations using thin films on IDA electrodes where ion movement does not contribute to the observed response yield D_{CT} values that are consistent with those obtained using cyclic voltammetry. Taken together, these data indicate that the redox switching rate is controlled by the segmental polymer chain movement necessary to bring adjacent ruthenium centres sufficiently close to allow electron hopping to occur.

Acknowledgment

We appreciate the on-going financial support from Science Foundation Ireland under the Research Frontiers Programme (Award No. 05/RFP/CHE0085) and the Biomedical Diagnostics Institute (Award No. 05/CE3/B754).

References

[1] R.J. Mortimer, Chem. Soc. Rev. 26 (1997) 147.
[2] R.J. Mortimer, N.M. Rowley, Metal Complexes as Dyes for Optical Data Storage and Electrochromic Materials, in: J.A. McCleverty, T.J. Meyer, M.D. Ward (Eds.), Comprehensive Coordination Chemistry. II. From Biology to Nanotechnology 9.2, Elsevier, Oxford, 2004, p. 581.
[3] A. Juris, V. Balzani, F. Barigelletti, S. Campagna, P. Belser, A.V. Zelewsky, Coord. Chem. Rev. 84 (1988) 85.
[4] R.J. Mortimer, A.L. Dyer, J.R. Reynolds, Displays 27 (2006) 2.
[5] P.M.S. Monk, R.J. Mortimer, D.R. Rosseinsky, Electrochromism and Electrochromic Devices, Cambridge University Press, New York, 2007, p. 254.
[6] F.S. Han, M. Higuchi, D.G. Kurth, J. Am. Chem. Soc. 130 (2008) 2073.
[7] T.E. Keyes, D. Leane, R.J. Forster, C.G. Coates, J.J. McGarvey, M.N. Nieuwenhuyzen, E. Figgemeier, J.G. Vos, Inorg. Chem. 41 (2002) 5721.
[8] I. Brady, D. Leane, H.P. Hughes, R.J. Forster, T.E. Keyes, J. Chem. Soc. Dalton Trans. (2004) 334.
[9] T.E. Keyes, B. Evrard, J.G. Vos, C. Brady, J.J. McGarvey, P. Jayaweera, J. Chem. Soc. Dalton Trans. (2004) 2341.
[10] A.A. Argun, P.H. Aubert, B.C. Thompson, J.R. Reynolds, Chem. Mater. 16 (2004) 4401.
[11] Q. Zeng, A. Mcnally, T.E. Keyes, R.J. Forster, Electrochem. Commun. 10 (2008) 466.
[12] S. Schneider, G. Brehm, C.J. Prenzel, J. Raman, Spectroscopy 27 (1996) 163.
[13] T.C. Strekas, H.D. Gafiney, S.A. Tysoe, R.P. Thumel, F. Lefoulon, Inorg. Chem. 28 (1989) 2964.
[14] T.E. Keyes, P.M. Jayaweera, J.J. McGarvey, J.G. Vos, J. Chem. Soc. Dalton Trans. (1997) 1627.
[15] S.E. Creager, G.K. Rowe, Anal. Chim. Acta 246 (1991) 233.
[16] G.K. Rowe, S.E. Creager, Langmuir 7 (1991) 2307.
[17] T. Nagamura, K. Sakai, J. Chem. Soc. Faraday Trans. 84 (1988) 3529.
[18] T. Nagamura, K. Sakai, Chem. Phys. Lett. 141 (1987) 553.
[19] D.A. Buttry, Langmuir 6 (1990) 1319.
[20] A.M. Bond, F.J. Marken, Electroanal. Chem. 372 (1994) 125.
[21] P.J. Kuleszea, L.R. Faulkner, J. Am. Chem. Soc. 115 (1993) 11878.
[22] R.J. Forster, J.G. Vos, in: G. Svehla (Ed.), Comprehensive Analytical Chemistry, XXVII, Elsevier, Amsterdam, 1992, p. 465.
[23] R.J. Forster, A.J. Kelly, J.G. Vos, J. Electroanal. Chem. 270 (1989) 365.
[24] Y. Marcus, Ion Properties, Marcel Dekker, New York, 1997.
[25] S.M. Oh, L.R. Faulkner, J. Am. Chem. Soc. 111 (1989) 5613.
[26] E.W. Paul, A.J. Ricco, M.S. Wrighton, J. Phys. Chem. 89 (1985) 1441.
[27] J.W. Thackeray, H.S. White, M.S. Wrighton, J. Phys. Chem. 89 (1985) 5133.
[28] D. Ofer, R.M. Crooks, M.S. Wrighton, J. Am. Chem. Soc. 112 (1990) 7869.
[29] H. Dahms, J. Phys. Chem. 72 (1968) 362.
[30] I. Ruff, V.J. Friedrich, K. Demeter, K. Csillag, J. Phys. Chem. 75 (1971) 3303.
[31] R.H. Terrill, J.E. Hutchinson, R.W. Murray, J. Phys. Chem. B 101 (1997) 1535.
[32] W.P. Wuelfing, S.J. Green, J.J. Pietron, D.E. Cliffel, R.W. Murray, J. Am. Chem. Soc. 122 (2000) 11465.